

Doctorat de l'Université de Toulouse

Étude de l'auto-couplage du boson de Higgs dans le canal $b\bar{b}\gamma\gamma$
à l'aide de la Méthode des Éléments de Matrice à NLO avec
l'expérience ATLAS auprès du collisionneur LHC au CERN

Thèse présentée et soutenue, le 30 septembre 2025 par
Matthias TARTARIN

École doctorale

SDM - SCIENCES DE LA MATIÈRE - Toulouse

Spécialité

Physique

Unité de recherche

L2IT - Laboratoire des 2 Infinis - Toulouse

Thèse dirigée par

Jan STARK et Catherine BISCARAT

Composition du jury

Mme Florencia CANELLI, Rapporteuse, University of Zurich, Physics Institute

M. Tilman PLEHN, Rapporteur, Heidelberg University

Mme Elisabeth PETIT, Examinatrice, CNRS, CPPM (Centre de Physique des Particules de Marseille)

M. Nicolas CHANON, Examineur, CNRS, IP2I (Institut de Physique des 2 Infinis - Lyon)

Mme Phuong Mai DINH, Examinatrice, Université de Toulouse, LPT (Laboratoire Physique Théorique)

M. Jan STARK, Directeur de thèse, CNRS, L2IT (Laboratoire des 2 Infinis - Toulouse)

Membres invités

Mme Catherine BISCARAT, co-encadrante, L2IT (Laboratoire des 2 Infinis - Toulouse)

Acknowledgements

First and foremost, I wish to warmly thank **Jan Stark**, my PhD supervisor, for accepting me as his doctoral student.

Despite the many responsibilities that come with directing the L2IT laboratory, he always found time for me, and our discussions were invariably stimulating and insightful. I greatly valued the dynamic we shared throughout these years, as our exchanges were always both engaging and challenging in the best sense, constantly pushing me to think deeper and work smarter. I learned a lot from his scientific and coding expertise, as well as from his clear, rigorous, and methodical approach to research. His guidance, combined with the trust he placed in me, allowed me to grow into the researcher I am today and to bring this work to its completion. For all this, I consider myself truly fortunate to have carried out my PhD under his supervision.

I am also very grateful to **Catherine Biscarat**, my co-supervisor, for her time, availability, and continuous support throughout this PhD. She always made sure that everything was going well, and ensuring that I never felt overwhelmed by the work. I very much appreciated the opportunity she gave me to collaborate with her on a major project outside the direct scope of my PhD, from which I learned a great deal through her guidance and supervision.

I am deeply grateful to **Charline Rougier**, the first PhD student of L2IT. She was always kind and ready to help me during my first year of PhD, even while finalizing her own research and manuscript during her last year. I am forever grateful to her for sharing the L^AT_EX manuscript template that I used to write this present manuscript.

I would also like to thank **Alexis Vallier** and **Paul Gessinger** for their supervision of my qualification task within the ATLAS collaboration and beyond. Alexis was also very present whenever I was at CERN, taking from his time to provide me with assistance and advice.

I would also like to express my sincere gratitude to all the members of the jury for accepting to evaluate my work. Their expertise, time, and thoughtful feedback have been invaluable, and I am deeply grateful for the attention they dedicated to this thesis.

It is a true privilege to have had **Florencia Canelli**, one of the pioneers of the Matrix Element Method, as a reviewer of this thesis. Her groundbreaking contributions laid the foundations of the approach that lies at the core of my own research, and having her take part in this jury is something I value deeply.

The presence of **Tilman Plehn** on the jury and as a reviewer is also particularly meaningful to me. His research has been a major source of learning, as I have often turned to his work and articles throughout this thesis. As someone who has always been drawn to the theoretical side of particle physics myself, I deeply value his contributions and consider his participation in my jury a true honor.

I am also very thankful to **Elisabeth Petit** and **Nicolas Chanon** for the interest and perspective they brought to this defense. Their insightful questions and thoughtful remarks made this moment both very enriching and intellectually stimulating, and I am extremely grateful for the time and attention they devoted to my work.

Finally, I am especially thankful to **Phuong Mai Dinh**, who served as president of the jury. I had the opportunity to work under her supervision during my first teaching assignment, where I came to appreciate her exceptional kindness and dedication to teaching. It was an absolute pleasure and a great honor to have her preside over this defense.

I would like to continue these acknowledgements by warmly thanking **Jeanette Thibaut** and **Jocelyne Gauthier**. Throughout these three years at L2IT they provided invaluable assistance with travel arrangements, conference participation, and the organizational aspects of the defense, always with an extreme kindness and warmth.

I also wish to thank **Gudrun Heinrich**. Her development of the POWHEG-BOX-V2/ggHH subrepository was crucial for the progress of my PhD. I had the chance to contact her by email and to meet her on several occasions during conferences. She was always extremely kind and provided valuable insights and directions to explore, for which I am very grateful.

My thanks also go to **Joany Manjarrés**, leader of the particle physics group at L2IT. Even though we did not work together directly, she always took the time to discuss with me whenever I asked for advice. She paid close attention to my work and presentations, and her feedbacks were always very helpful and greatly appreciated.

I also wish to acknowledge the institutions that supported this work. I am grateful to the **Université de Toulouse** and to the doctoral school **ED SdM** (*École Doctorale Sciences de la Matière*) for providing the support and framework for my doctoral studies.

I further thank our colleagues at the **IN2P3 Computing Centre** (CC-IN2P3) in Lyon (Villeurbanne) for the smooth operation of their computing farms.

Without this facility the present study would have not been possible.

I would like to express my deepest love and gratitude to the members of my **family**, who have been a constant source of support, encouragement, and affection throughout my entire life. I owe much of who I am today to them, for even my hardest efforts and moments of growth drew strength from their teaching and affection.

I would like to thank all of my **colleagues from the ATLAS Collaboration**. Working within such a large and dedicated community has been an extraordinary experience, both scientifically and personally.

I am also deeply grateful to my **colleagues and members of the L2IT** laboratory, past and present, with whom I had the chance to interact in various ways throughout these three years. The welcoming and collaborative atmosphere made these years of research both extremely enjoyable and fulfilling.

Finally, I wish to thank my **colleagues from the Université de Toulouse** for their support and kindness during my teaching duties over these three years of PhD. They contributed to make this experience deeply enriching and truly invaluable. This teaching experience also gave me the unique and memorable opportunity to work alongside some of my former teachers and mentors from the PARCOURS SPÉCIAL, which I enjoyed greatly.

Contents

Acknowledgements	3
Lists	13
List of Figures	13
List of Tables	24
List of Equations	29
List of Acronyms	31
Introduction	34
I Elements of theory	35
1 The Standard Model	37
1.1 Outline of the Standard Model	38
1.2 Symmetries in the Standard Model	43
1.2.1 Global Symmetries	44
1.2.2 Gauge Symmetries	44
1.2.3 Discrete Symmetries and their Violations	46
2 Higgs Physics	47
2.1 The Higgs Mechanism	47
2.2 Spontaneous Symmetry Breaking in the Standard Model	47
2.3 Higgs Boson Properties at the LHC	51
2.3.1 Production Mechanisms	51
2.3.2 Higgs Decay Channels and Branching Ratios	52
3 Higgs Self-Coupling and Di-Higgs Production	55
3.1 Theoretical Motivation	55
3.2 Di-Higgs Production in the Standard Model at the LHC	57

3.3	Experimental Access and Analysis Strategy	59
3.4	BSM Higgs Potential	61
3.4.1	Exploring Different Higgs Potentials:	61
3.4.2	Higgs Self-Coupling and Baryogenesis	63
3.5	Conclusion	63
II	Experimental setup	65
4	The Large Hadron Collider	69
4.1	The CERN Accelerator Complex and LHC Overview	69
4.2	Performance and Operation During Runs 1–3	71
4.3	Luminosity and Pile-Up Conditions	71
4.4	Physics Output Before HL-LHC	74
5	The ATLAS Detector and Physics Object Reconstruction Performance	75
5.1	General Overview and Design Principles	75
5.2	Coordinate System and Global Layout	78
5.3	The Inner Detector	78
5.4	The Electromagnetic Calorimeter: Photon Identification and Resolution	79
5.5	The Hadronic Calorimeter: Jet and b -Jet Reconstruction	81
5.6	Muon Spectrometer	81
5.7	Trigger and Data Acquisition System (DAQ)	81
5.8	Object reconstruction and performance	82
5.8.1	Photons γ	82
5.8.2	Jets and b -Tagging	83
5.9	Summary: Performance Milestones and Impact on LHC Analyses . .	85
6	Experimental Access to the Higgs Self-Coupling	87
6.1	Current Constraints and Effective Parameterization	87
6.2	Most Recent ATLAS non-resonant $HH \rightarrow b\bar{b}\gamma\gamma$ Analysis [‘25]	88
7	The High-Luminosity LHC and Future Prospects	93
7.1	HL-LHC Machine and Design Goals	93
7.2	ATLAS Detector Upgrades	93
7.2.1	The Inner Tracker (ITk): Capabilities, and Expected Performance	93
7.2.2	Calorimeter and Muon System Enhancements	98
7.3	Computing and Data Handling	98
7.4	ATLAS Qualification Task: ACTS Kalman Filter (KF) Integration in ATHENA	101
7.5	Future Sensitivity to Higgs Self-Coupling	104

III A statistically optimal method: The Matrix Element Method	105
8 General overview of the Matrix Element Method	109
8.1 Theoretical Foundations of the Matrix Element Method	109
8.1.1 Statistical Basis: Neyman-Pearson Lemma	109
8.1.2 Implementation in High Energy Physics	110
8.2 Evaluating methods discrimination power: ROC curves	113
8.3 Likelihood Formalism	115
8.3.1 Kinematic Likelihood Construction	115
8.3.2 Event Yield Likelihood	116
8.3.3 Extended Likelihood Framework	117
8.4 Method of Minimum Negative Log-Likelihood	117
9 Main Tools and Software for the Matrix Element Method	119
9.1 MadGraph5 (MadGraph5_aMC@NLO)	119
9.1.1 UFO Models	119
9.1.2 Core Functionality	120
9.2 MadWeight	120
9.3 MoMEMTA: Modular MEM Implementation	120
9.3.1 Architecture of MoMEMTA	120
9.3.2 Integration Algorithms within MoMEMTA	121
9.3.3 Main and Secondary Blocks	122
9.3.4 The MoMEMta-MaGMEE Module	125
9.4 POWHEG-BOX-V2: An alternative to MadGraph5	125
9.4.1 Main usage	125
9.4.2 Limitations for the MEM	126
10 Historical successes of the MEM	127
10.1 Major success of the Matrix Element Method: Top Quark Mass Measurements at DØ and CDF	127
10.2 Major applications and successes of the MEM at the LHC	128
10.2.1 Searches for the $t\bar{t}h$ process	128
10.2.2 Search for s-channel single Top quark production	129
10.2.3 Success in the measurement of $t\bar{t}$ spin correlation in the μ +jets channel	129
10.2.4 Discovery of the Higgs boson and spin-parity measurements in the $h \rightarrow 4l$ channel	129
11 Legacy analysis: Leading Order MEM Implementation in the $gg \rightarrow HH \rightarrow b\bar{b}\gamma\gamma$ channel	131
11.1 Matrix Element Construction and Effective Model Design	131
11.1.1 EFT Vertices and $gg \rightarrow HH$ Loop Approximation	131
11.1.2 UFO Model Merging and κ Parameterization	132
11.2 Event Simulation and Detector Smearing Framework	133
11.2.1 Parton-Level Generation and Background Channels	133
11.2.2 Detector Resolution and Simplified Transfer Functions	133

11.2.3	Pre-selection requirements at LO	133
11.3	Likelihood Evaluation with MADWEIGHT	134
11.4	Migration to MOMEMTA and Integration Strategy	134
11.4.1	Matrix Element Compatibility and C++ Translation	134
11.4.2	Lua Configuration and Parametrization Choices	136
11.5	Statistical Discrimination and Measurement of the Higgs Self-Coupling	137
11.5.1	MEM Likelihood Ratio (LHR) Versus Boosted Decision Tree (BDT) Performance	137
11.5.2	Extended Likelihood and κ Estimation	137
11.5.3	Treatment of Zero-Likelihood Events	140
11.6	Summary and Outlook Toward NLO Extensions	141

IV Developing a Matrix Element Method at NLO 143

12 Problem Statement and Motivation 147

12.1	Order of the Monte Carlo generated events and order of the MEM . .	148
12.2	Using NLO generated samples on MEM@LO	149
12.3	Problem statement	150

13 Theoretical considerations on the MEM at NLO 153

13.1	Existing Foundations of the NLO Formalism	153
13.2	Incorporating Initial-State Radiation to the Leading Order formalism	154
13.2.1	Boost Correction Method	154
13.2.2	Sudakov Reweighting	155
13.3	Extending the Matrix Element Method to Next-to-Leading Order . .	155
13.4	Variants of the Matrix Element Method at Next-to-Leading Order . .	157
13.5	Challenges Identified in the Literature	157
13.6	Conclusions	158

14 Our Contribution: A New MEM Formalism at NLO 159

14.1	Access to the Matrix Elements at NLO	159
14.2	Modifying POWHEG-BOX-V2	160
14.2.1	ggHH repository	160
14.2.2	$t\bar{t}H$ repository	161
14.3	Validation of the interface with matrix element comparison	161
14.3.1	Matrix element for $gg \rightarrow HH \rightarrow b\bar{b}\gamma\gamma$ at LO	161
14.3.2	Matrix Elements for $gg \rightarrow HH \rightarrow b\bar{b}\gamma\gamma$ at NLO	164
14.3.3	Matrix Elements for $t\bar{t}H$ at LO	165
14.3.4	Matrix Elements for $t\bar{t}H$ at NLO	166
14.4	Use of MADGRAPH5 for our MEM@NLO	167
14.5	Modifying MOMEMTA	168
14.5.1	Block N: Main Ideas	168
14.5.2	ExtraRadiation_3DOF: Main idea	173
14.5.3	Determination of the Infrared (IR) and Ultraviolet (UV) Limits	174
14.5.4	Updating Lua Steering Files	175
14.6	Summary of our Choice of MEM Integration Variables	177

14.7 Improving the Transfer Function for ATLAS fully simulated events . . .	178
14.8 Validation and Conclusion	180

V Results 181

15 Analysis Framework and Methodology 185

15.1 Monte Carlo Events Generated for this Analysis	185
15.1.1 Using the MADGRAPH5 software	185
15.1.2 Using the POWHEG-BOX-V2 software	188
15.2 Using official ATLAS fully simulated events	193
15.3 Pre-selection cuts and smearing	195
15.3.1 Pre-selection and cuts	195
15.3.2 Event smearing	195
15.4 Automated framework for MEM weight production	196
15.4.1 Motivation and file multiplicity	196
15.4.2 Computing time considerations	198
15.4.3 Schematic overview of the automated framework	200
15.5 Interpreting the results from the MEM: ROC Curves and Likelihoods	203
15.5.1 ROC Curves	203
15.5.2 Likelihood scans (as a function of κ_λ)	204

16 Results: With Our LO Matrix Element Method 211

16.1 ROC Curves using MEM@LO	212
16.1.1 $t\bar{t}H$ background	212
16.1.2 QCD di-photon background	215
16.1.3 Single-Higgs background	216
16.2 Likelihood Scans using LO generated samples	218
16.2.1 [LO] Signal-only	218
16.2.2 [LO] including $t\bar{t}H$ background	221
16.2.3 [LO] including QCD background	223
16.2.4 [LO] including singleHiggs background	225
16.2.5 [LO] including all three main backgrounds	227
16.3 Summary for the MEM@LO	230

17 Results: With Our New NLO Matrix Element Method 233

17.1 ROC Curves using MEM@NLO	234
17.1.1 $t\bar{t}H$ background	234
17.1.2 QCD di-photon background	236
17.1.3 Single-Higgs background	238
17.1.4 Impact of the radiation transverse momentum (p_T^{rad}) IR cut on the ROC	239
17.2 Likelihood Scan Performance: using NLO ISR generated samples . . .	242
17.2.1 [NLO ISR] Signal-only pseudo-data	242
17.2.2 [NLO ISR] including $t\bar{t}H$ background	245
17.2.3 [NLO ISR] including QCD background	247
17.2.4 [NLO ISR] including single-Higgs background	249

17.2.5	[NLO ISR] including all three main backgrounds	251
17.3	Likelihood Scan Performance: using ATLAS fully simulated events . .	254
17.3.1	[ATLAS fullsim] Signal-only pseudo-data	254
17.3.2	[ATLAS fullsim] including $t\bar{t}H$ background	257
17.3.3	[ATLAS fullsim] including QCD background	259
17.3.4	[ATLAS fullsim] including single-Higgs background	261
17.3.5	[ATLAS fullsim] including all three main backgrounds	263
17.4	Summary and Interpretation for the MEM@NLO	266
17.4.1	For the Monte Carlo NLO ISR generated events	266
17.4.2	For the ATLAS fully simulated events	268
Conclusion		271
VI Appendices		273
A	Dimension of the Matrix Element Method Likelihood Integral	273
A.1	General setting	273
A.2	Step-by-step illustration	274
A.3	Remarks on practical parameterizations	274
B	Follow-up on the validation of the Higgs decay	276
B.1	Boosted samples	278
B.2	Main Block M	282
B.3	Improving the Transfer Function for ATLAS Simulation: Ap- plication on ATLAS simulated n-tuples	284
C	Set-up for our work environment at CC-IN2P3	287
Résumé de la thèse obligatoire en français - Mandatory french summary [20 pages]		289
Bibliography		313

List of Figures

1.1	Fundamental particles included in the Standard Model, represented in the form of fundamental puzzle pieces (with non-contractual connecting parts). Original idea and creation, inspired by Ref. [14]. . . .	40
2.1	Illustration of the Higgs field potential $V(\phi)$, often called as ‘Mexican hat’ due to its shape. Taken from Ref. [22].	48
2.2	Other illustrations for the Higgs potential $V(\phi)$. (a) Before SSB, with $\mu^2 > 0$; (b) After SSB, with $\mu^2 < 0$. Point B marks the non-zero vacuum expectation value (VEV) v selected by the system once spontaneous symmetry breaking has occurred. Taken from Ref. [23]. .	49
2.3	Main Higgs boson production processes at leading order. (a) is the Feynman diagram of the triangle contribution for the ggF di-Higgs process; (b) is for the VBF process; (c) is the associated production with a vector boson at tree level, and (d) is the one at loop level; (e) is for the $t\bar{t}H$ process; (f and g) are the associated productions with a single top quark. Taken from Ref. [26].	51
2.4	Higgs boson branching ratios as a function of mass. Taken from Ref. [27].	52
2.5	Dominant one-loop contributions to the decay $H \rightarrow \gamma\gamma$: (a) a virtual W^\pm loop, and (b) a virtual top-quark loop. Diagrams produced using the https://feynman.aivazis.com/ website.	53
3.1	Feynman diagrams for the major production modes of two Higgs bosons: gluon fusion (ggF). (Left) Triangle diagram sensitive to the self-coupling vertex $\kappa_\lambda = \frac{\lambda_{3H}}{\lambda_{3H}^{SM}}$, (Right) Box diagram, which interferes destructively with the Triangle. Taken from Ref. [29].	57
3.2	Differential cross-section for Higgs boson pair production via gluon fusion as a function of m_{HH} , highlighting the distinct contributions of the triangle and box diagrams. The triangle diagram (red region) dominates at low invariant mass, while the box diagram (blue region) contributes more at higher m_{HH} . The resulting interference produces a characteristic shape sensitive to κ_λ . Taken from Ref. [30].	58
3.3	Depiction of Vector Boson Fusion (VBF) processes in Higgs boson pair production. Taken from [29].	59
3.4	Higgs branching ratio (BR) percentage for the different decay channels for $m_H = 125\text{GeV}$. Taken from Ref. [38].	59

3.5	Projections for the ongoing European Strategy for Particle Physics Update (ESPPU) 2026. (Top) Comparison of the BEH (Brout–Englert–Higgs) potentials for various BSM scenarios predicting a first-order phase transition, with respect to the Standard Model potential. (Middle) Difference between each potential $V(\phi)$ and the SM expectation $V_{\text{SM}}(\phi)$. (Bottom) A zoomed-in view of $V(\phi) - V_{\text{SM}}(\phi)$ around the potential minimum. Figure adapted from Ref. [39].	62
4.1	Schematic view of the CERN accelerator complex [44].	70
4.2	LHC plan for the Run 1 to Run 3 (last updated in January 2025). Taken from Ref. [49].	71
4.3	Delivered Luminosity \mathcal{L}_{int} versus time for 2011-2022 using proton-proton data only. Taken from Ref. [50].	73
4.4	Mean number of interactions per bunch crossing $\langle\mu\rangle$ for collisions recorded between 2011 and 2022, taken from Ref. [50]. The non-gaussian shape of all distributions is due to the luminosity leveling of the machine.	73
5.1	Schematic view of the ATLAS detector, from Ref. [7].	76
5.2	Schematic view of interactions of particles with the ATLAS subdetectors, from Ref. [51].	77
5.3	Schematic description of the coordinate system, taken from Ref. [52]. This figure has been created for the CMS experiment, but the coordinate system used in ATLAS is the exact same (except that the x -axis points toward CMS).	78
5.4	Cut-away view of the ATLAS calorimeter system. Taken from Ref. [7]	79
5.5	Schematic view of a barrel module of the ATLAS electromagnetic calorimeter. Taken from Ref. [7].	80
5.6	Pictures of the accordion-shaped electrodes of the ATLAS ECAL [54].	80
5.7	Tight-ID photon efficiency and data/MC scale factors versus E_{T} in four $ \eta $ regions, Taken from Ref. [59].	83
5.8	Reconstructed mass $m_{b\bar{b}}$ GeV with and without B-calibration. Taken from Ref. [63]	84
6.1	Predicted total cross-section for Higgs boson pair production via gluon-gluon fusion (ggF) as a function of the Higgs self-coupling modifier κ_{λ} , that we have computed using the HPAIR values at both Leading Order and Next-to-Leading Order in QCD. The κ_{λ} range spans from -3.5 to 10.0 . The LO prediction is shown in blue , and the NLO prediction in red	88
6.2	Observed and expected profile likelihood scans of κ_{λ} . All other relevant coupling modifiers are fixed to unity. Taken from Ref. [66]. . . .	92
6.3	Confidence level contours at 68% (solid line) and 95% (dashed line) in the $(\kappa_{\lambda}, \kappa_{2V})$ parameters space, when all other coupling modifiers are fixed to their SM predictions. The corresponding expected contours are shown by the inner and outershaded regions. The SM prediction is indicated by the star, while the best-fit value is denoted by the cross. Taken from Ref. [66].	92

7.1	An expanded version of Fig. 4.2, including additional HL-LHC plan (last update January 2025). Taken from Ref. [49].	94
7.2	Schematic view of the new ATLAS tracker ITk in the (z, r) plane, Layout 23-00-03 from Ref. [74]. Only active material is displayed. Red modules represent pixel modules and blue ones are strip modules.	95
7.3	Comparison of nuclear interaction length between ATLAS current inner detector used for Run 2 and ITk inclined duals. Taken from Ref. [75].	96
7.4	Track parameters resolution in d_0 and q/p_T as a function of true track η . Results are shown for single muons with p_T of 1, 10 or 100 GeV, for $< \mu > = 0$. Results for Run 2 are shown for comparison. Taken from Ref. [75].	97
7.5	Projected evolution of computing usage from 2020 until 2036. Taken from Ref. [77].	99
7.6	Projected evolution of disk (top) and tape (bottom) storage usage from 2020 until 2036. Taken from Ref. [77].	100
7.7	Representation of the new implementation of the uncalibrated (PRD-based) measurements fit between the ATHENA and ACTS frameworks. The top section outlines the four main steps of the interface. The ACTSKALMANFITTER class, implemented within ATHENA, now handles calibration internally during the fit (from Ref [78]).	102
7.8	Pull distributions of the transverse impact parameter d_0 as a function of η for the latest version of the ATHENA–ACTS interface. The histograms correspond to ACTS fits (red) and Athena fits (blue). The Gaussian fit (black) is performed on the ACTS distribution. The lower panel shows the ratio ACTS/Athena (from Ref [78]).	103
7.9	Width of the d_0 pull distribution as a function of η for the final implementation of the ATHENA–ACTS interface. The histograms correspond to ACTS fits (red) and Athena fits (blue). The lower panel shows the ratio ACTS/Athena (from Ref [78]).	104
8.1	Signal cross section (red -dashed) and maximum significance (black-solid) for observing anomalous Higgs self-coupling at the LHC with an integrated luminosity of 3 ab^{-1} . The significance from a cut-based rate measurement (black-dashed) using cuts is also shown. Taken from Ref. [86].	113
8.2	Schematic example of two ROC curves: example where the events are well discriminated between signal and background hypothesis (in green); example where the events are less strongly discriminated (in orange). Different points on a ROC curve correspond to different cuts on the discriminating variable. The line $x = y$ represents the performance of a random classification.	114

8.3	Method of minimum negative log-likelihood: Negative log-likelihood (NLL) function versus parameter κ . The cyan curve shows the observed NLL values, while the blue parabola represents the quadratic fit around the minimum. The green vertical line indicates the best-fit parameter value $\tilde{\kappa}$, with red lines marking the 1σ uncertainty interval $\sigma_{\kappa} = (\kappa_2 - \kappa_1)/2$, where κ_1 and κ_2 are the intersection points of the NLL curve with $\Delta\text{NLL} = 0.5$ (dashed horizontal line). The parabolic approximation (blue) becomes exact in the asymptotic limit around $\tilde{\kappa}$ per Wilks' theorem. Taken from Ref. [89].	118
9.1	Comparison between MADWEIGHT and MOMEMTA working principles. The lighter the color, the more the user has explicit control Taken from Ref. [89].	121
9.2	Illustration of the six MADWEIGHT Main Block configurations, also used within the MOMEMTA software. The integration variables of interest are labelled explicitly. Thick solid lines mark variables removed from the integration, while dashed lines indicate intermediate resonances added to it. Taken from Ref. [93].	123
9.3	Illustration of the four MADWEIGHT <i>secondary block</i> configurations, also used within the MOMEMTA software. The integration variables of interest are labelled explicitly. Thick solid lines mark variables removed from the integration, while dashed lines indicate intermediate resonances added to it. Taken from Ref. [93].	124
11.1	Gluon fusion di-Higgs history overview, from HTL to full picture (LO and NLO and higher order). Taken from a presentation by G.Heinrich at the Higgs Pair Workshop 2025, Ref. [119].	132
11.2	Visual representation of the MOMEMTA framework working principles. The lighter the color, the more the user has explicit control Taken from Ref. [89].	136
11.3	Likelihood scan of the negative logarithm of: the event kinematics likelihood (black), the event yield likelihood (green) and the extended likelihood (red) as a function of κ_{λ} for a sample of ggF signal events (generated at $\kappa_{\lambda} = 1$, with 16 pure signal events). The (blue) curve is a parabolic fit around the minimum of the extended likelihood (red), same as in Figure 8.3. Taken from Ref. [89].	138
11.4	Histograms of the measured value of (κ_{meas} , top), of the corresponding statistical uncertainty (κ_{unc} , middle) and of the pull value (ω , bottom) for signal events only. Taken from Ref. [89].	139
11.5	Negative logarithm of the event kinematics likelihood (black), the event yield likelihood (green) and the extended likelihood (red) as a function of κ_{λ} for a sample of 16 ggF signal events (generated at $\kappa_{\lambda} = 1$), and 290 non-resonant $b\bar{b}\gamma\gamma$ background events. The (blue) curve is a parabolic fit around the minimum of the extended likelihood (red), same as in Figure 8.3. Taken from Ref. [89].	140

12.1	Indicators used in the following of this manuscript to avoid any confusion about the order of the Matrix Element Method analysis. (Left) indicator for Leading Order MEM ; (Right) indicator for Next-to-Leading Order MEM.	148
12.2	Representation of all the different possible combination when LO and NLO MC generated events are studied under LO and NLO Matrix Element Methods. (a) LO MC events with LO MEM ; (b) LO MC events with NLO MEM ; (c) NLO MC events with LO MEM ; (d) NLO MC events with NLO MEM.	149
12.3	ROC curve of Leading-Order (LO, in black) and Next-to-Leading-Order (NLO, in red) MC generated events, using a LO Matrix Element Method (MEM@LO). This graph motivates the need for a MEM@NLO, and the results presented here will be discussed with a greater level of detail in Section 16.1 (<i>cf.</i> Figure 16.2).	150
13.1	Schematic depiction of the event topology for pair production of heavy particles X, together with initial-state radiation (ISR). Taken from Ref. [122].	154
13.2	Boost correction method used in Matrix Element Methods at Leading-Order. The left hand side depicts a collision that results in the production of four leptons (in red) that do not balance in the transverse plane. The resulting imbalance (X, in blue) represents the remaining event which is not modelled in the Born matrix element. A boost is applied to the event such that X has no components in the transverse plane, with the remaining longitudinal and energy components absorbed into the colliding partons. Taken from Ref. [125].	156
14.1	Histograms of the direct comparison between LO matrix elements for the process $gg \rightarrow HH$ from POWHEG-BOX-V2 and MadGraph@NLO for 10 000 different evaluations. Both x-axis correspond to the quantity $ME_{POWHEG} - ME_{MG}$ normalized by the ME_{POWHEG} value, and the y-axis correspond to the number of occurrences per bin.	163
14.2	Histogram of the direct comparison between LO matrix elements for the process $gg \rightarrow HH$ [from Magraph@NLO] with the addition of $H \rightarrow b\bar{b}$ and $H \rightarrow \gamma\gamma$ by hand [from Magraph@NLO], to the full $gg \rightarrow HH \rightarrow b\bar{b}\gamma\gamma$ [from Madgraph@NLO] for 10 000 different evaluations (with a fixed value of $\alpha_s = 0.1184$).	163
14.3	Histograms of the direct comparison between LO matrix elements for the process $t\bar{t}H$ from POWHEG-BOX-V2 and Madgraph@NLO for 5 193 different evaluations. Both x-axis correspond to the quantity $ME_{POWHEG} - ME_{MG}$ normalized by the ME_{POWHEG} value, and the y-axis correspond to the number of occurrences within each bins.	165
14.4	Histograms of the direct comparison between Real Matrix Elements for the process $t\bar{t}Hq$ from POWHEG-BOX-V2 and Magraph@NLO for 5 193 different evaluations. Both x-axis correspond to the quantity $ME_{POWHEG} - ME_{MG}$ normalized by the ME_{POWHEG} value, and the y-axis correspond to the number of occurrences within each bins.	166

14.5	Schematic representation of Block N, following the conventions used by MOMEMTA.	169
14.6	All curves area are normalized to unity in order to facilitate comparison. A discussion of these plots can be found in section 14.5.1	171
14.7	Distribution of the extra (real) radiation transverse momentum p_T for $gg \rightarrow HH$ NLO events generated with using the POWHEG-BOX-V2 software. The red dashed line indicates the mode (<i>i.e.</i> the most populated bin in the histogram) of the spectrum ($p_T^{\text{mode}} \simeq 16$ GeV), while the green dashed line marks the value below which 99 % of the entries lie ($p_T^{99\%} \simeq 2.6 \times 10^2$ GeV). These two points are used to define the lower and upper integration choices of ($p_T^{\text{min}}, p_T^{\text{max}}$) adopted for the MEM cuts in phase-space generation.	175
14.8	2D grid in $(E_{\text{reco}}, \eta_{\text{reco}})$ plane for ATLAS simulated n-tuples events, for the case of photons here. The procedure is the same for the b -jets.	178
14.9	Schematic overview on how the relative resolution σ/E_{reco} is obtained from the 2D Grid.	179
15.1	Feynman diagram for real QCD background, automatically generated by the MADGRAPH@NLO software.	187
15.2	Multiple definition of ‘NLO’ generated events, depending on the choices of the $b\bar{b}\gamma\gamma$ final state particles and how they are defined kinematically. We decided to name the different choices: ‘ ISR ’ (in red); ‘ FSRdr ’ (in green); and ‘ FSRend ’ (in orange).	190
15.3	Representation of the Higgs boson H decay into two particles of same nature p_1 and p_2 , within the Higgs rest frame.	192
15.4	Angular distributions of the Higgs boson decay daughters (named $\gamma_1, \gamma_2, b_1, b_2$). Top row: laboratory frame observables: azimuthal angle ϕ , polar angle θ , and $\cos(\theta)$. Bottom row: the same observables evaluated in the respective Higgs rest frames (denoted with a superscript star: $\phi^*, \theta^*, \cos(\theta^*)$). The four colored histograms are overlaid in each panel, with the legend displayed in the upper-right corner. . .	193
15.5	Comparison of the pseudo-rapidity (η) distributions for the four decay products of the Higgs boson in the $b\bar{b}\gamma\gamma$ final state. Blue markers represent events produced with the modified implementation, while red markers denote the reference sample from POWHEG-BOX-V2.	194
15.6	Wall-clock Time (in minutes) per event for a NLO signal sample evaluated under the corresponding NLO hypothesis before parallelisation. The mean, mode and maximum values of the distributions are indicated.	199
15.7	Wall-clock Time (in minutes) per event for a NLO signal sample evaluated under the corresponding NLO hypothesis after enabling CUBACORES parallelisation in MOMEMTA. The mean, mode and maximum values of the distributions are indicated.	199

15.8	Schematic overview of the automated MEM factory, organized and automated for result efficiency and clarity. We reproduced the idea behind Figure 11.2: the lighter the color, the clearer the computation for the user. With the addition of the green area which represents the workflow that is managed automatically. The green region encloses the part of the workflow that is executed entirely by the automation layer, from dataset ingestion to the production and validation of weight files.	200
15.9	Schematic overview of the automated workflow needed after MEM result production. We reproduced the idea behind the Figure 11.2: the lighter the color, the clearer the computation for the user. With the addition of the green area which represents the workflow that is managed automatically. The green region encloses the part of the workflow that is executed entirely by the automation layer.	202
15.10	Automatic fitting procedure on Matrix Element Method outcomes under the signal hypothesis to avoid ‘fluctuations’ for a small subset of κ_λ hypotheses caused by issues in the numerical integrator, and stabilize the likelihood scans.	205
15.11	Illustration of the theoretical cross-section as a function of κ_λ (top), compared to the (negative log) Yield likelihood $-\log \mathcal{L}_{\text{yield}}(\kappa_\lambda)$ at 300fb^{-1} (bottom). Both curves exhibit the well-known mirror symmetry between $\kappa_\lambda = 1.0$ and $\kappa_\lambda = 4.0$, highlighting a major challenge in extracting precise constraints on the Higgs self-coupling.	209
16.1	ROC curve obtained with MEM@LO when the dominant background is $t\bar{t}H$ (using the DIVONNE algorithm for both hypotheses). The dashed line indicates the expectation from a random classifier	212
16.2	ROC curve obtained with MEM@LO when the dominant background is $t\bar{t}H$ using the VEGAS integration algorithm for the background hypothesis. The dashed line indicates the expectation from a random classifier	213
16.3	ROC curve obtained with MEM@LO for the $b\bar{b}\gamma\gamma$ QCD background. The dashed line indicates the expectation from a random classifier	215
16.4	ROC curve obtained with MEM@LO against the single Higgs background. The dashed line indicates the expectation from a random classifier.	216
16.5	Example likelihood scan for one pseudo-dataset consisting of signal events ($\kappa_\lambda = 1.00$) analysed under MEM@LO. The graph shows $-\log \mathcal{L}$ as a function of the coupling modifier κ_λ for multiple likelihoods: Black: kinematic component only (\mathcal{L}_{Kin}). Green: yield term ($\mathcal{L}_{\text{yield}}$). Red: extended likelihood (\mathcal{L}_{ext}). Blue: quadratic fit to $-\log \mathcal{L}_{\text{ext}}$ used to extract the best-fit value and its statistical uncertainty.	218
16.6	Likelihood scan for a pure signal MC generated dataset.	219
16.7	Likelihood scan for MC generated dataset of both signal and $t\bar{t}H$ background.	221

16.8	Likelihood scan for MC generated dataset of both signal and QCD background.	223
16.9	Likelihood scan for MC generated dataset of both signal and single-Higgs background	225
16.10	Example likelihood scan for one pseudo-dataset consisting of a mix of all processes (including signal ggF generated for $\kappa_\lambda = 1.00$), analysed under MEM@LO. The graph shows $-\log \mathcal{L}$ as a function of the coupling modifier κ_λ for multiple likelihoods: Black: kinematic component only (\mathcal{L}_{Kin}). Green: yield term ($\mathcal{L}_{\text{yield}}$). Red: extended likelihood (\mathcal{L}_{ext}). Blue: quadratic fit to $-\log \mathcal{L}_{\text{ext}}$ used to extract the best-fit value and its statistical uncertainty.	227
16.11	Likelihood scan for MC generated dataset of signal and all of the backgrounds, altogether.	228
16.12	Summary of the MEM@LO profile likelihood performance for the $b\bar{b}\gamma\gamma$ final state at $\sqrt{s} = 14$ TeV, for an integrated luminosity of 300fb^{-1} . For each pseudo-datasets ensemble the black dot marks the measured Higgs self-coupling modifier κ_λ , while the dashed grey line indicates the SM value ($\kappa_\lambda = 1.00$). The turquoise (orange) regions give the $\pm 1\sigma$ ($\pm 2\sigma$) expected bands obtained from toy fluctuations.	230
17.1	ROC curve obtained with MEM@NLO when the dominant background is $t\bar{t}H$ (using the DIVONNE algorithm for both hypotheses). The dashed line indicates the expectation from a random classifier.	234
17.2	ROC curve obtained with MEM@NLO for the $b\bar{b}\gamma\gamma$ QCD background. The dashed line indicates the expectation from a random classifier	236
17.3	ROC curve obtained with MEM@NLO when the dominant background is singleHiggs. The dashed line indicates the expectation from a random classifier	238
17.4	Comparison of different ROC curves for different choices of cuts on the transverse momentum p_T for the generation of the phase-space of the signal ggF extra radiation. No change has been made on the $t\bar{t}H$ background MEM to keep consistency between plots and only study the impact of this change on the signal. The ROC curve in Figure 17.4.c corresponds to our reference choice of cut.	240
17.5	Evolution of the AUC value depending on the choice of p_T cut (for the signal ggF extra radiation), using values from Figure 17.4	241
17.6	Example likelihood scan for one pseudo-dataset consisting of NLO ISR signal events ($\kappa_\lambda = 1.00$) analysed under MEM@NLO. The graph shows $-\log \mathcal{L}$ as a function of the coupling modifier κ_λ for multiple likelihoods: Black: kinematic component only (\mathcal{L}_{Kin}). Green: yield term ($\mathcal{L}_{\text{yield}}$). Red: extended likelihood (\mathcal{L}_{ext}). Blue: quadratic fit to $-\log \mathcal{L}_{\text{ext}}$ used to extract the best-fit value and its statistical uncertainty.	242
17.7	Likelihood scan for a pure signal sample using MEM@NLO weights.	243

- 17.8 Histograms of the performance of the likelihood scans with $t\bar{t}H$ background included. **Top:** distribution of the best-fit coupling parameter $\hat{\kappa}_\lambda$, with Gaussian fit overlaid. **Middle:** distribution of the estimated uncertainty σ_{measured} . **Bottom:** distribution of the pull values, defined as $(\hat{\kappa}_\lambda - \kappa_{\text{true}})/\sigma_{\text{measured}}$ 245
- 17.9 Histograms of the performance of the likelihood scans with QCD background included. **Top:** distribution of the best-fit coupling parameter $\hat{\kappa}_\lambda$, with Gaussian fit overlaid. **Middle:** distribution of the estimated uncertainty σ_{measured} . **Bottom:** distribution of the pull values, defined as $(\hat{\kappa}_\lambda - \kappa_{\text{true}})/\sigma_{\text{measured}}$ 247
- 17.10 Histograms of the performance of the likelihood scans with single-Higgs background included. **Top:** distribution of the best-fit coupling parameter $\hat{\kappa}_\lambda$, with Gaussian fit overlaid. **Middle:** distribution of the estimated uncertainty σ_{measured} . **Bottom:** distribution of the pull values, defined as $(\hat{\kappa}_\lambda - \kappa_{\text{true}})/\sigma_{\text{measured}}$ 249
- 17.11 Example likelihood scan for one pseudo-dataset consisting of a combination of NLO ISR signal events ($\kappa_\lambda = 1.00$) and backgrounds, analysed under MEM@NLO. The graph shows $-\log \mathcal{L}$ as a function of the coupling modifier κ_λ for multiple likelihoods: **Black:** kinematic component only (\mathcal{L}_{Kin}). **Green:** yield term ($\mathcal{L}_{\text{yield}}$). **Red:** extended likelihood (\mathcal{L}_{ext}). **Blue:** quadratic fit to $-\log \mathcal{L}_{\text{ext}}$ used to extract the best-fit value and its statistical uncertainty. 251
- 17.12 Histograms of the performance of the likelihood scans with all background included. **Top:** distribution of the best-fit coupling parameter $\hat{\kappa}_\lambda$, with Gaussian fit overlaid. **Middle:** distribution of the estimated uncertainty σ_{measured} . **Bottom:** distribution of the pull values, defined as $(\hat{\kappa}_\lambda - \kappa_{\text{true}})/\sigma_{\text{measured}}$ 252
- 17.13 Example likelihood scan for one pseudo-dataset consisting of ATLAS simulated n-tuples signal events ($\kappa_\lambda = 1.00$) analysed under MEM@NLO. The graph shows $-\log \mathcal{L}$ as a function of the coupling modifier κ_λ for multiple likelihoods: **Black:** kinematic component only (\mathcal{L}_{Kin}). **Green:** yield term ($\mathcal{L}_{\text{yield}}$). **Red:** extended likelihood (\mathcal{L}_{ext}). **Blue:** quadratic fit to $-\log \mathcal{L}_{\text{ext}}$ used to extract the best-fit value and its statistical uncertainty. 254
- 17.14 Likelihood scan for a pure signal sample of ATLAS simulated n-tuples using MEM@NLO weights. 255
- 17.15 Histograms of the performance of the likelihood scans with $t\bar{t}H$ background included. **Top:** distribution of the best-fit coupling parameter $\hat{\kappa}_\lambda$, with Gaussian fit overlaid. **Middle:** distribution of the estimated uncertainty σ_{measured} . **Bottom:** distribution of the pull values, defined as $(\hat{\kappa}_\lambda - \kappa_{\text{true}})/\sigma_{\text{measured}}$ 257
- 17.16 Histograms of the performance of the likelihood scans with QCD background included. **Top:** distribution of the best-fit coupling parameter $\hat{\kappa}_\lambda$, with Gaussian fit overlaid. **Middle:** distribution of the estimated uncertainty σ_{measured} . **Bottom:** distribution of the pull values, defined as $(\hat{\kappa}_\lambda - \kappa_{\text{true}})/\sigma_{\text{measured}}$ 259

17.17	Histograms of the performance of the likelihood scans with single-Higgs background included. Top: distribution of the best-fit coupling parameter $\hat{\kappa}_\lambda$, with Gaussian fit overlaid. Middle: distribution of the estimated uncertainty σ_{measured} . Bottom: distribution of the pull values, defined as $(\hat{\kappa}_\lambda - \kappa_{\text{true}})/\sigma_{\text{measured}}$	261
17.18	Example likelihood scan for one pseudo-dataset consisting of a combination of ATLAS simulated n-tuples signal events ($\kappa_\lambda = 1.00$) and backgrounds, analysed under MEM@NLO. The graph shows $-\log \mathcal{L}$ as a function of the coupling modifier κ_λ for multiple likelihoods: Black: kinematic component only (\mathcal{L}_{Kin}). Green: yield term ($\mathcal{L}_{\text{yield}}$). Red: extended likelihood (\mathcal{L}_{ext}). Blue: quadratic fit to $-\log \mathcal{L}_{\text{ext}}$ used to extract the best-fit value and its statistical uncertainty. . . .	263
17.19	Histograms of the performance of the likelihood scans for all background sample combined together (with the signal). Top: distribution of the best-fit coupling parameter $\hat{\kappa}_\lambda$, with Gaussian fit overlaid. Middle: distribution of the estimated uncertainty σ_{measured} . Bottom: distribution of the pull values, defined as $(\hat{\kappa}_\lambda - \kappa_{\text{true}})/\sigma_{\text{measured}}$	264
17.20	Summary of the MEM@NLO profile likelihood performance for the $b\bar{b}\gamma\gamma$ final state at $\sqrt{s} = 14$ TeV for an integrated luminosity of 300 fb^{-1} . For each pseudo-datasets ensemble the black dot marks the measured Higgs self-coupling modifier κ_λ , while the dashed grey line indicates the SM value ($\kappa_\lambda = 1.00$). The turquoise (orange) regions give the $\pm 1\sigma$ ($\pm 2\sigma$) expected bands obtained from toy fluctuations.	266
17.21	Summary of the MEM@NLO profile likelihood performance for the $b\bar{b}\gamma\gamma$ final state at $\sqrt{s} = 14$ TeV for an integrated luminosity of 300 fb^{-1} . We use the same convention as from Figure 17.20. Public ATLAS limits are shown for indication context only, where ‘ATLAS bbyy 25’ refers to Ref. [66] and ‘ATLAS ’24’ refers to Ref. [64].	268
22	Step-by-step illustration for the counting of the dimension of the MEM Likelihood integral, written by hand.	275
23	Validity of the θ^* distribution using a sine function fit.	276
24	Comparison of the transverse momentum p_T distributions for the four decay products of the Higgs boson in the $b\bar{b}\gamma\gamma$ final state. Blue markers represent events produced with the modified POWHEG-BOX-V2 implementation, while red markers denote the reference sample.	277
25	Comparison of the energy E distributions for the four decay products of the Higgs boson in the $b\bar{b}\gamma\gamma$ final state. Same conventions as Figure 24	277
26	ROC curve obtained with MEM@LO against the $t\bar{t}H$ background to see the impact of boosted kinematic events.	278
27	Example likelihood scan for one pseudo-dataset consisting of boosted NLO events ($\kappa_\lambda = 1.00$) analysed under MEM@LO with $t\bar{t}H$ background. The graph shows $-\log \mathcal{L}$ as a function of the coupling modifier κ_λ for multiple likelihoods: Black: kinematic component only (\mathcal{L}_{Kin}). Green: yield term ($\mathcal{L}_{\text{yield}}$). Red: extended likelihood (\mathcal{L}_{ext}). Blue: quadratic fit to $-\log \mathcal{L}_{\text{ext}}$ used to extract the best-fit value and its statistical uncertainty.	280
28	Likelihood scan with $t\bar{t}H$ background included, for boosted NLO events.	281

29	Schematic representation of Block M, following the conventions used by MoMEMTA.	282
30	ROC curves of the same ATLAS simulated n-tuples (gluon-fusion signal and $t\bar{t}H$ background under different transfer function W using the MEM@NLO.)	284
31	Likelihood scan with $t\bar{t}H$ background included, for NLO events using the MEM@NLO and the grid W transfer function.	285

List of Tables

1.1	Properties of fermions (quarks and leptons) grouped into generations: the charge Q is in electron units q_e and the mass in GeV. They all have spin- $\frac{1}{2}$ [13].	39
1.2	Properties of the gauge bosons in the Standard Model: the electric charge Q in electron charge unit q_e , the mass value or mass limit in GeV, the spin and the type of mediated force. Taken from Ref. [13]. .	39
1.3	Quantum numbers of fermions: P - chirality, Q - electric charge, T - weak isospin, T_3 - third component of weak isospin, $Y_W = 2(Q - T_3)$ - weak hypercharge, C - colour charge. The index $i = 1, 2, 3$ denotes fermion generations, <i>e.g.</i> u_L^i denotes left-handed up-type quarks: $u_L^1 = u_L$, $u_L^2 = c_L$, and $u_L^3 = t_L$	44
2.1	Properties of the Higgs boson in the Standard Model. The Higgs is the only elementary scalar particle (i.e spin 0), electrically neutral, with a precisely measured mass of about 125 GeV [25].	50
3.1	Cross-section at $\sqrt{s} = 14$ TeV for Higgs boson pair production from gluon fusion at different perturbative orders, using full theory or different approximations. The infinite top mass approximation is referred as Heavy Top Limit (<i>HTL</i>), and the finite top mass approximation is referred as FTAPPROX.	58
6.1	Summary of Monte Carlo (MC) configurations used for signal and background processes. Reproduced from Ref. [66].	91
8.1	Confusion matrix illustrating the definitions of true and false positives and negatives. Green cells correspond to correct predictions, while red cells indicate misclassifications.	115
14.1	Choice of integration limits for the kinematic variables of interest for the additional real radiation in the MEM phase-space.	174
14.2	Summary of integration dimensions and variable choices across Leading and Next-to-Leading Order processes. Values in parentheses indicate possible dimensionality reduction after constraining the width of off-shell particles (<i>e.g.</i> the Higgs boson).	177

15.1	Summary of cross-sections σ [in pb], pre-selection efficiencies ε , and their product $\sigma \cdot \varepsilon$ [in pb] computed and used for all processes under study (at both LO and NLO). The signal process is shown here for $\kappa_\lambda = 1.00$ as an example. Note: The specific branching ratios (BR) have not been included in the cross-sections σ values, for transparency purposes.	206
15.2	Branching ratios (BR) used in this analysis. The values for the Higgs decays are taken mainly from the HPAIR software and compared to the literature. The top-quark branching ratio is close to unity and plays a minor role here, but is included for completeness.	206
16.1	Table for the values of interest hidden in Figure 16.1 and 16.2. The MEM integration algorithm is (DIVONNE) unless stated otherwise. Are indicated in this table: the area under the curve (AUC) (in %); the number of signal events that have zero weights values for both hypothesis at the same time (in %); and the number of background events that have zero weights values for both hypothesis at the same time (in %).	213
16.2	Table for the values of interest hidden in Figure 16.3. The MEM integration algorithm is (DIVONNE) unless stated otherwise. Are indicated in this table: the area under the curve (AUC) (in %); the number of signal events that have zero weights values for both hypothesis at the same time (in %); and the number of background events that have zero weights values for both hypothesis at the same time (in %). . .	215
16.3	Table for the values of interest hidden in Figure 16.4. The MEM integration algorithm is (DIVONNE) unless stated otherwise. Are indicated in this table: the area under the curve (AUC) (in %); the number of signal events that have zero weights values for both hypothesis at the same time (in %); and the number of background events that have zero weights values for both hypothesis at the same time (in %). . .	216
16.4	Fraction of ‘ill’ events (zero weight for their own hypothesis) removed before the likelihood scan of Figure 16.6.	219
16.5	Fraction of ‘ill’ events (zero weight for their own hypothesis) removed before the likelihood scan of Figure 16.7.	221
16.6	Fraction of ‘ill’ events (zero weight for their own hypothesis) removed before the likelihood scan of Figure 16.8.	223
16.7	Fraction of ‘ill’ events (zero weight for their own hypothesis) removed before the likelihood scan of Figure 16.9.	225
16.8	Fraction of ‘ill’ events (zero weight for their own hypothesis) removed before the likelihood scan of Figure 16.11.	228
16.9	Summary of likelihood-scan performance for each process (MEM@LO). The “best-fit” column quotes the Gaussian mean from the top histogram of each figure (κ_{mean}), and σ_κ is the corresponding width. The measured uncertainty is the mean of the green histogram, and the pull parameters come from the Gaussian fit to the bottom histogram (ω_{mean}).	231

17.1	Table for the values of interest hidden in Figure 17.1. The MEM integration algorithm is (DIVONNE) unless stated otherwise. Are indicated in this table: the area under the curve (AUC) (in %); the number of signal events that have zero weights values for both hypothesis at the same time (in %); and the number of background events that have zero weights values for both hypothesis at the same time (in %). . .	235
17.2	Table for the values of interest hidden in Figure 17.2. The MEM integration algorithm is (DIVONNE) unless stated otherwise. Are indicated in this table: the area under the curve (AUC) (in %); the number of signal events that have zero weights values for both hypothesis at the same time (in %); and the number of background events that have zero weights values for both hypothesis at the same time (in %). . .	237
17.3	Table for the values of interest hidden in Figure 17.3. The MEM integration algorithm is (DIVONNE) unless stated otherwise. Are indicated in this table: the area under the curve (AUC) (in %); the number of signal events that have zero weights values for both hypothesis at the same time (in %); and the number of background events that have zero weights values for both hypothesis at the same time (in %). . .	239
17.4	Fraction of ‘ill’ events (zero weight for their own hypothesis) removed before the likelihood scan of Figure 17.7. For the special case of signal files, if the weight is zero for any of the κ_λ hypothesis it is removed from the list completely.	243
17.5	Fraction of ‘ill’ events (zero weight for their own hypothesis) removed before the likelihood scan of Figure 17.8.	246
17.6	Fraction of ‘ill’ events (zero weight for their own hypothesis) removed before the likelihood scan of Figure 17.9.	248
17.7	Fraction of ‘ill’ events (zero weight for their own hypothesis) removed before the likelihood scan of Figure 17.10.	250
17.8	Fraction of ‘ill’ events (zero weight for their own hypothesis) removed before the likelihood scan of Figure 17.12.	251
17.9	Fraction of ‘ill’ events (zero weight for their own hypothesis) removed before the likelihood scan of Figure 17.14.	255
17.10	Fraction of ‘ill’ events (zero weight for their own hypothesis) removed before the likelihood scan of Figure 17.16.	258
17.11	Fraction of ‘ill’ events (zero weight for their own hypothesis) removed before the likelihood scan of Figure 17.16.	260
17.12	Fraction of ‘ill’ events (zero weight for their own hypothesis) removed before the likelihood scan of Figure 17.17.	262
17.13	Fraction of ‘ill’ events (zero weight for their own hypothesis) removed before the likelihood scan of Figure 17.19.	265
17.14	Summary of likelihood-scan performance for each process for NLO ISR generated events analysed using MEM@NLO. The best-fit entries list the Gaussian mean (κ_{mean}) and width (σ_κ) of the blue histogram at the top. The measured uncertainty is the mean of the green histogram in the middle panel, while the pull parameters are taken from the Gaussian fit to the bottom panel.	267

17.15	Summary of likelihood-scan performance for ATLAS simulated $b\bar{b}\gamma\gamma$ samples analysed with MEM@NLO. We use the same convention as from Table 17.20.	269
16	Table for the values of interest hidden in Fig. 26. The MEM integration algorithm is (DIVONNE). Are indicated in this table: the area under the curve (AUC) (in %); the number of signal events that have zero weights values for both hypothesis at the same time (in %); and the number of background events that have zero weights values for both hypothesis at the same time (in %).	279
17	Fraction of "ill" events (zero weight for their own hypothesis) removed before the likelihood scan of Fig. 28.	279
18	Table for the values of interest hidden in Fig. 30. The MEM integration algorithm is (DIVONNE). Are indicated in this table: the area under the curve (AUC) (in %); the number of signal events that have zero weights values for both hypothesis at the same time (in %); and the number of background events that have zero weights values for both hypothesis at the same time (in %).	284
19	Fraction of "ill" events (zero weight for their own hypothesis) removed before the likelihood scan of Fig. 31.	286

List of Equations

1.4 Free Lagrangian equation	41
1.5 SM Lagrangian equation	41
1.10QED Lagrangian equation	43
2.1 Higgs field potential equation	48
3.2 Higgs boson potential equation	56
5.2 Energy resolution formula for photons	80
5.3 Energy resolution formula for b-jets	81
8.5 Matrix Element Method master equation: Likelihood Process	112
8.6 MadMax prediction for HL-LHC on constraining the Higgs self-coupling λ_{3H}	113
8.8 Event likelihood formula	116
8.9 Sample Likelihood formula	116
8.10Yield Likelihood formula	116
8.11Extended Likelihood formula	117
8.12Negative Log-likelihood (NLL) equation	117
9.1 POWHEG-BOX-V2 Born kinematic generation formula	126
12.1NLO cross-section contributions equation	151
13.2FBPS generation equation	157
14.3Block N Jacobian final result	170
.2 Remaining degrees of freedom DoF for the MEM depending on the process	274

List of Acronyms

LHC	Large Hadron Collider
HL-LHC	High-Luminosity Large Hadron Collider
ATLAS	A Toroidal LHC ApparatuS
CMS	Compact Muon Solenoid
ALICE	A Large Ion Collider Experiment
LHCb	Large Hadron Collider beauty
LEP	Large Electron–Positron Collider
SPS	Super Proton Synchrotron
PS	Proton Synchrotron
PSB	Proton Synchrotron Booster
Linac	Linear Accelerator
IRRAD	Proton Irradiation Facility
GIF++	Gamma Irradiation Facility at CERN
SM	Standard Model
BSM	Beyond the Standard Model
BEH	Brout–Englert–Higgs
EFT	Effective Field Theory
SMEFT	Standard Model Effective Field Theory
QCD	Quantum Chromodynamics
EWK	Electroweak
VEV	Vacuum Expectation Value
IR	Infrared
UV	Ultraviolet

VBF	Vector Boson Fusion
ggF	Gluon–Gluon Fusion
tH	Single-top associated Higgs production
ttH	Top–Antitop associated Higgs production
BR	Branching Ratio
HTL	Heavy Top Limit
FTapprox	Finite Top-Mass Approximation
MEM	Matrix Element Method
MEM@LO	Matrix Element Method at Leading Order
MEM@NLO	Matrix Element Method at Next-to-Leading Order
MoMEMta	Modular Matrix Element Method Analysis
MC	Monte Carlo
MC@NLO	Monte Carlo at Next-to-Leading Order
NLO	Next-to-Leading Order
LO	Leading Order
NNLO	Next-to-Next-to-Leading Order
ISR	Initial-State Radiation
FSR	Final-State Radiation
FSRdr	Final-State Radiation with ΔR recombination
FSRend	Final-State Radiation (end of the chain)
PDF	Parton Distribution Function
PDF4LHC	PDF recommendations from the LHC working group
POWHEG	Positive Weight Hardest Emission Generator
MadGraph	MadGraph5_aMC@NLO Monte Carlo generator
PYTHIA	Monte Carlo event generator for parton showers
FastJet	Jet clustering software package
LHAPDF	Library for High Energy Physics PDFs
HepMC	High Energy Physics Monte Carlo event record
ROOT	CERN Data Analysis Framework

Athena	ATLAS Reconstruction Framework
ACTS	A Common Tracking Software
KF	Kalman Filter
BDT	Boosted Decision Tree
ROC	Receiver Operating Characteristic
AUC	Area Under the Curve
NLL	Negative Log-Likelihood
CPU	Central Processing Unit
GPU	Graphics Processing Unit

Introduction

The precise measurement of the Higgs boson trilinear self-coupling λ_{3H} stands among the primary goals of the Large Hadron Collider (LHC) program at CERN, as it would offer a direct experimental probe of the Higgs mechanism, its underlying dynamics, and the way in which all fundamental particles acquire their mass.

Current measurements by the ATLAS and CMS collaborations still allow sizeable deviations from the Standard Model (SM) prediction. Tighter limits on the scale factor κ_λ (defined as $\lambda_{3H}/\lambda_{3H}^{\text{SM}}$), are therefore essential to confirm the SM or to uncover signs of new physics.

Higgs boson pair production is dominated by gluon fusion at LHC. Among its many decay modes, the $b\bar{b}\gamma\gamma$ final state offers a good balance between the high rate production and purity of the signal. Because Higgs boson pair production is extremely rare at the LHC, it demands a method that extracts the full information from every available event, with minimal cuts on the data.

The *Matrix Element Method* (MEM) meets this challenge in a statistically optimal way, according to the Neyman–Pearson lemma. It converts matrix element amplitudes derived from first principles into event-by-event likelihoods (while keeping nearly the entire dataset, avoiding strict selection requirements).

Historically, the MEM delivered some of the most precise top-quark mass determinations at the Tevatron. However, most subsequent MEM analyses have continued to rely on Leading Order (LO) matrix elements. As a result, important QCD radiative corrections present in real LHC events are neglected. These corrections are known to modify the final-state kinematics and therefore bias the accuracy of the method.

This thesis addresses this limitation and goes further. It delivers the first Next-to-Leading Order MEM (**MEM@NLO**) for the $gg \rightarrow HH \rightarrow b\bar{b}\gamma\gamma$ channel with a newly developed implementation within the MOMEMTA software.

This new framework has been validated against two realistic pseudo-datasets, in analyses combining all three dominant backgrounds together (i.e. $t\bar{t}H$, single Higgs, and QCD di-photon backgrounds), assuming the injected hypothesis $\kappa_\lambda = 1.00$.

For the NLO (ISR) pseudo-events, we find:

$$\kappa_\lambda = 1.14, \quad \text{with the associated uncertainty } \sigma_\kappa = 0.50.$$

whereas the study on fully simulated ATLAS $b\bar{b}\gamma\gamma$ n -tuples gives:

$$\kappa_\lambda = 1.22, \quad \text{with the associated uncertainty } \sigma_\kappa = 0.41.$$

The focus of this work is on demonstrating the theoretical soundness, numerical stability, and practical feasibility of such an approach in a realistic LHC environment. These results show that the MEM@NLO can constrain the Higgs self-coupling with great accuracy (under full detector and background conditions) while also providing a statistically competitive constraint, underscoring the method’s suitability for future precision studies at the LHC.

Part I

Elements of theory

THE HIGGS BOSON



This chapter provides a structured and self-contained overview of the theoretical framework relevant to this thesis.

While it is not intended as a lecture on quantum field theory, it delivers an extensive presentation of the Standard Model, with a particular focus on its gauge structure, the Higgs sector, and the mechanism of electroweak symmetry breaking.

The discussion begins in **Chapter 1** with the formulation of the SM Lagrangian and the central role of symmetry principles in determining particle interactions and conservation laws.

Chapter 2 introduces spontaneous symmetry breaking in the context of gauge theories, leading to the Higgs mechanism, which reconciles gauge invariance with the observed masses of the weak bosons.

The final part of this section, **Chapter 3**, is dedicated to the scalar potential and the Higgs boson self-interactions which remain among the least experimentally constrained parameters of the SM.

Content

1	The Standard Model	37
1.1	Outline of the Standard Model	38
1.2	Symmetries in the Standard Model	43
1.2.1	Global Symmetries	44
1.2.2	Gauge Symmetries	44
1.2.3	Discrete Symmetries and their Violations	46
2	Higgs Physics	47
2.1	The Higgs Mechanism	47
2.2	Spontaneous Symmetry Breaking in the Standard Model	47
2.3	Higgs Boson Properties at the LHC	51
2.3.1	Production Mechanisms	51
2.3.2	Higgs Decay Channels and Branching Ratios	52
3	Higgs Self-Coupling and Di-Higgs Production	55
3.1	Theoretical Motivation	55
3.2	Di-Higgs Production in the Standard Model at the LHC	57
3.3	Experimental Access and Analysis Strategy	59
3.4	BSM Higgs Potential	61
3.4.1	Exploring Different Higgs Potentials:	61
3.4.2	Higgs Self-Coupling and Baryogenesis	63
3.5	Conclusion	63

Chapter 1

The Standard Model

The Standard Model (SM) of particle physics is the theoretical framework that currently provides the most accurate and comprehensive description of the known elementary particles and their interactions, with the exception of gravity.

It is built on foundational principles such as gauge symmetry, Lorentz invariance, and the mathematical structure of quantum field theory. The SM successfully accounts for three of the four fundamental forces in nature: the electromagnetic, weak, and strong interactions.

A key achievement of the SM is the unification of the electromagnetic and weak forces into a single electroweak interaction, formalized through the Glashow–Weinberg–Salam (GWS) framework [2–4], an accomplishment recognized by the Nobel Prize in Physics in 1979.

The validity of the Standard Model has been confirmed by numerous experiments with high precision, culminating in the discovery of the Higgs boson at the Large Hadron Collider (LHC) in 2012 [5, 6] by the ATLAS [7] and CMS [8] experiments. The SM is a remarkable synthesis of decades of theoretical insight and experimental discovery, which formulation relies on the language of group theory, providing a precise mathematical framework to describe internal symmetries of the theory. The SM of particles physics is a (spontaneously broken) gauge theory based on the following gauge group:

$$\mathcal{G} = SU(3)_C \times SU(2)_L \times U(1)_Y, \quad (1.1)$$

where each component corresponds to one of the interactions discussed earlier: $SU(3)_C$ for the strong force (Quantum Chromodynamics, or QCD), $SU(2)_L$ for the weak force, and $U(1)_Y$ for the hypercharge associated with electromagnetism before electroweak unification [9].

Despite its experimental success, the SM is known to be incomplete. Its large number of arbitrary parameters might be an indication that this might not be a complete theory yet [10]. There are 19 arbitrary free parameters:

- 3 gauge couplings g_s , g and g' ,
- 9 fermion masses,
- 3 CKM matrix mixing angles and 1 phase,
- 2 Higgs parameters v and λ ,
- 1 mixing angle θ associated with the QCD ground state.

All 19 parameters are now precisely measured experimentally, yet the Standard Model offers no principle that predicts (or even motivates) their specific numerical values.

Furthermore, with the confirmation of neutrino oscillations (which is an indirect proof of non-zero neutrino masses [11, 12]) at least 7 more parameters should be added to the list: 3 masses, 3 mixing angles, 1 Dirac CP -phase (and possibly 2 Majorana phases).

Despite describing observed phenomena with remarkable precision, the SM does not provide answers to some fundamental questions, such as the reason why there is exactly three generations of fermions (*cf.* Table 1.1), or what is the origin of the values for the fermion masses and mixing angles.

The SM also does not incorporate gravity, fails to account for dark matter, and cannot explain the observed baryon asymmetry of the universe.

These open questions motivate searches for physics beyond the Standard Model (BSM), and the need to measure each of these parameters with an extreme precision.

In this chapter we introduce the structure of the Standard Model and highlight the symmetry principles that govern it. The aim is not to reproduce a full derivation, but to establish a working theoretical foundation relevant for this PhD manuscript.

1.1 Outline of the Standard Model

The particle content of the SM is divided into fermions and bosons, which are all illustrated in Figure 1.1.

Fermions, which constitute matter, are spin- $\frac{1}{2}$ particles and are grouped into three generations of quarks and leptons (*cf.* Table 1.1). Within each family, the particles share identical gauge quantum numbers and interactions, differing only in their masses (which increase across the three generations). Contrary to leptons, quarks are also described by a color charge making them sensitive to the strong interactions (QCD).

Bosons are force carriers with integer spin, mediating interactions among fermions.

Gen.	Quark	Q/q_e	mass [GeV]	Lepton	Q/q_e	mass [GeV]
1	up (u)	$\frac{2}{3}$	$(2.16^{+0.49}_{-0.26}) \times 10^{-3}$	electron (e^-)	-1	0.511×10^{-3}
	down (d)	$-\frac{1}{3}$	$(4.67^{+0.48}_{-0.17}) \times 10^{-3}$	electron neutrino (ν_e)	0	$< 2 \times 10^{-9}$
2	charm (c)	$\frac{2}{3}$	$1.27^{+0.02}_{-0.02}$	muon (μ^-)	-1	0.106
	strange (s)	$-\frac{1}{3}$	$(93.4^{+8.6}_{-3.4}) \times 10^{-3}$	muon neutrino (ν_μ)	0	$< 0.19 \times 10^{-3}$
3	top (t)	$\frac{2}{3}$	$172.69^{+0.3}_{-0.3}$	tau (τ^-)	-1	1.777
	bottom (b)	$-\frac{1}{3}$	$4.18^{+0.03}_{-0.02}$	tau neutrino (ν_τ)	0	$< 18.2 \times 10^{-3}$

Table 1.1: Properties of fermions (quarks and leptons) grouped into generations: the charge Q is in electron units q_e and the mass in GeV. They all have spin- $\frac{1}{2}$ [13].

The gauge bosons include the photon (γ), W^\pm and Z bosons, and gluon (g) (*cf.* Table 1.2).

Boson	Q/q_e	mass [GeV]	spin	force
Photon (γ)	0	$< 10^{-27}$	1	Electromagnetic
W boson (W)	± 1	80.377 ± 0.012	1	Weak
Z boson (Z)	0	91.1876 ± 0.0021	1	Weak
Gluon (g)	0	$\leq 10^{-3}$	1	Strong

Table 1.2: Properties of the gauge bosons in the Standard Model: the electric charge Q in electron charge unit q_e , the mass value or mass limit in GeV, the spin and the type of mediated force. Taken from Ref. [13].

The **Higgs boson** (H) will be considered separately from the other bosons of the Standard Model (*cf.* Table 2.1).

It is the only fundamental scalar particle (*i.e.* with spin 0), which plays a unique role by explaining how elementary particles acquire mass through a mechanism called *spontaneous symmetry breaking*.

The dynamics of this mechanism, together with the structure of the Higgs sector, will be examined in detail in Chapter 2 and Chapter 3.

Lagrangians: Origins

All the dynamics of the Standard Model (including particle interactions, propagation, and mass generation) are encapsulated in its Lagrangian $\mathcal{L}_{(\text{SM})}$.

In quantum field theory (QFT), the *Lagrangian density* \mathcal{L} is the central object from which the entire dynamics of a physical system can be derived.

It is a function of the fields $\psi(x)$ present in the theory, their derivatives $\partial_\mu \psi(x)$, and the spacetime coordinates x^μ .

The origin of the Lagrangian density lies in a more fundamental quantity known as the *action* S , which governs the dynamics of physical systems in both classical and quantum field theory.

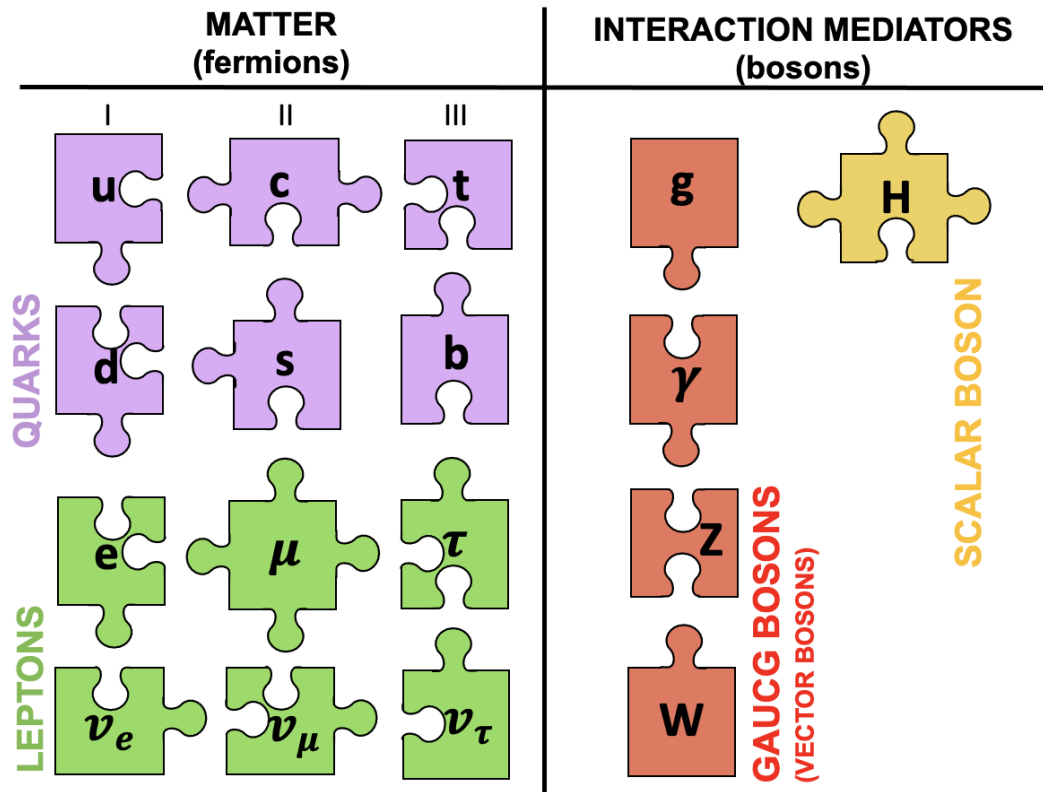


Figure 1.1: Fundamental particles included in the Standard Model, represented in the form of fundamental puzzle pieces (with non-contractual connecting parts). Original idea and creation, inspired by Ref. [14].

In field theory, the action S is a scalar functional that depends on the configuration of fields and is defined as the integral of the Lagrangian density over four-dimensional Minkowski spacetime:

$$S[\psi] = \int d^4x \mathcal{L}(\psi, \partial_\mu \psi, x) . \quad (1.2)$$

Under some additional conditions (namely that the variation $\delta\psi(x)$ vanishes at the boundary of spacetime and that the action integral is finite), one can derive from the action S the ‘Euler–Lagrange equations’:

$$\partial_\mu \left(\frac{\delta \mathcal{L}}{\delta(\partial_\mu \psi)} \right) - \frac{\delta \mathcal{L}}{\delta \psi} = 0 \quad (1.3)$$

which encode the fundamental field equations determining the dynamics of the system.

A simple example of a Lagrangian density is the *free Lagrangian* (*i.e.* in the absence of interactions). Take for instance the free Lagrangian describing a spin- $\frac{1}{2}$ fermion field (such as an electron or a quark), without interactions. The Lagrangian density from the action for a free fermion $\psi(x)$ with mass m is:

$$\mathcal{L}_{\text{free}} = \bar{\psi} (i\gamma^\mu \partial_\mu - m) \psi, \quad (1.4)$$

where γ^μ are the Dirac gamma matrices, $\psi(x)$ is the fermion spinor field, and $\bar{\psi} = \psi^\dagger \gamma^0$ is its Dirac adjoint.

In QFT, the Lagrangian \mathcal{L} determines how quantum fields evolve and interact, serving as the foundation for calculating observable quantities like scattering amplitudes (by providing the appropriate matrix elements) and correlation functions.

The requirement of local gauge invariance, renormalizability, Lorentz invariance, and minimal field content places strong constraints on the allowed form of \mathcal{L} . These principles uniquely determine the full Lagrangian (for the SM), up to a finite set of input parameters.

All measurable predictions in the Standard Model (from cross-sections and decay widths to particle masses and coupling strengths) stem directly from this single function \mathcal{L} .

Its structure is the most concise encapsulation of the Standard Model's physical content, rendering it both a summary and a generator of the theory's phenomenology.

Each term in the SM Lagrangian can be associated to a given physical phenomenon: gauge boson dynamics, fermion propagation and interactions, spontaneous symmetry breaking via the Higgs field, and mass generation through Yukawa couplings.

Standard Model Lagrangian: Full picture

As already mentioned in the introduction, the Standard Model is based on the $SU(3)_C \times SU(2)_L \times U(1)_Y$ gauge symmetry. The SM Lagrangian is composed of multiple distinct terms, each encoding fundamental sectors of the SM theory:

$$\mathcal{L}_{\text{SM}} = \mathcal{L}_{\text{Gauge}} + \mathcal{L}_{\text{Matter}} + \mathcal{L}_{\text{Yukawa}} + \mathcal{L}_{\text{Higgs}} \quad (1.5)$$

where:

- $\mathcal{L}_{\text{Gauge}}$ contains the kinetic energy of the gauge fields (bosons) and describes their self-interactions:

$$\mathcal{L}_{\text{Gauge}} = \frac{1}{2g_s^2} \text{Tr } G^{\mu\nu} G_{\mu\nu} + \frac{1}{2g^2} \text{Tr } W^{\mu\nu} W_{\mu\nu} - \frac{1}{4g'^2} B^{\mu\nu} B_{\mu\nu}. \quad (1.5)$$

where g_s , g , g' are the gauge coupling constants for $SU(3)_C$, $SU(2)_L$, and $U(1)_Y$, respectively. Their values will be later discussed in Chapter 2. $G_{\mu\nu} = G_{\mu\nu}^a T^a$ is the gluon field strength tensor:

$$G_{\mu\nu}^a = \partial_\mu G_\nu^a - \partial_\nu G_\mu^a + g_s f^{abc} G_\mu^b G_\nu^c,$$

where G_μ^a are the eight $SU(3)_C$ gauge fields (gluons), T^a are $SU(3)$ generators in the fundamental representation, and f^{abc} are the $SU(3)$ structure constants. $W_{\mu\nu} = W_{\mu\nu}^j \sigma^j / 2$ is the weak $SU(2)_L$ field strength tensor:

$$W_{\mu\nu}^j = \partial_\mu W_\nu^j - \partial_\nu W_\mu^j + g \epsilon^{jkl} W_\mu^k W_\nu^l,$$

where W_μ^j are the three weak gauge bosons, σ^j are the Pauli matrices, and ϵ^{jkl} is the Levi-Civita symbol.

$B_{\mu\nu}$ is the $U(1)_Y$ hypercharge field strength tensor:

$$B_{\mu\nu} = \partial_\mu B_\nu - \partial_\nu B_\mu,$$

where B_μ is the $U(1)$ gauge field.

- $\mathcal{L}_{\text{Matter}}$ contains the kinetic energy of the matter particles (fermions) and describes their interactions with the gauge bosons via the covariant derivatives. Its general form is:

$$\mathcal{L}_{\text{Matter}} = \sum_{\psi} \bar{\psi} i \gamma^\mu D_\mu \psi, \quad (1.6)$$

where the sum runs over all fermion fields in the Standard Model: left-handed quark and lepton doublets, and right-handed singlets for each fermion type.

The covariant derivative D_μ encodes all gauge interactions: color ($SU(3)_C$), weak isospin ($SU(2)_L$), and hypercharge ($U(1)_Y$).

For clarity, $\mathcal{L}_{\text{Matter}}$ can be further decomposed into QCD and electroweak components:

$$\mathcal{L}_{\text{Matter}} = \mathcal{L}_{\text{QCD}} + \mathcal{L}_{\text{EW}} \quad (1.7)$$

The first term is based on the $SU(3)_C$ symmetry and can be written as:

$$\mathcal{L}_{\text{QCD}} = \sum_{\text{quarks } \psi} \bar{\psi} i \gamma^\mu D_\mu^{\text{QCD}} \psi, \quad (1.8)$$

and developed into:

$$\mathcal{L}_{\text{QCD}} = - \sum_{\text{quarks } \psi} \bar{\psi} \gamma^\mu g_s T_a G_\mu^a \psi, \quad (1.2)$$

where ψ represents quark fields $\psi = Q_L^i, u_R^i, d_R^i$ (*cf.* Table 1.3), γ^μ are Dirac matrices, G_μ^a are the $SU(3)$ gauge fields containing gluons, T_a are the $SU(3)$ generators and g_s is the strong coupling constant.

The second term correspond to the unified theory of electroweak (EW), based on the $SU(2)_L \times U(1)_Y$ symmetry:

$$\mathcal{L}_{\text{EW}} = \sum_{\text{fermions } \psi} \bar{\psi} i \gamma^\mu D_\mu^{\text{EW}} \psi, \quad (1.9)$$

which can be developed as:

$$\mathcal{L}_{\text{EW}} = \sum_{\text{fermions } \psi} \bar{\psi} \gamma^\mu \left(-g' \frac{1}{2} Y_W B_\mu - g \frac{1}{2} \sigma_j W_\mu^j \right) \psi, \quad (1.3)$$

where ψ represents fermion fields $\psi = L_L^i, e_R^i, Q_L^i, u_R^i, d_R^i$ (*cf.* Table 1.3), Y_W is the weak hypercharge, B_μ is the $U(1)$ gauge field, σ_j are Pauli matrices, which are $SU(2)$ generators and act only on left-handed particles, W_μ^j represents the three $SU(2)$ gauge fields: W^\pm and Z , and g and g' are coupling constants.

After the breaking of the electroweak symmetry (*cf.* Chapter 2), the covariant derivative will reduce to the QED Lagrangian as part of the residual $U(1)_{\text{EM}}$ symmetry, with the photon field A_μ as its gauge boson. It describes the interaction of charged fermions with the photon fields. The part of \mathcal{L}_{SM} that forms the QED Lagrangian is given by:

$$\mathcal{L}_{\text{QED}} = \bar{\psi}(i\gamma^\mu D_\mu - m)\psi - \frac{1}{4}F_{\mu\nu}F^{\mu\nu} , \quad (1.10)$$

with $F_{\mu\nu} = \partial_\mu A_\nu - \partial_\nu A_\mu$ the electromagnetic field strength tensor, and m the associated fermion mass,.

- $\mathcal{L}_{\text{Yukawa}}$ describes the interaction of the Higgs boson with fermions. The Yukawa Lagrangian can be written as:

$$\mathcal{L}_{\text{Yukawa}} = -\Gamma_u^{ij}\bar{Q}_L^i\epsilon\phi^*u_R^j - \Gamma_d^{ij}\bar{Q}_L^i\phi d_R^j - \Gamma_\ell^{ij}\bar{L}_L^i\epsilon\phi e_R^j + h.c. \quad (1.11)$$

where Q_L^i/L_L^i denote the quark/lepton left-handed doublets and $u_R^j/d_R^j/e_R^j$ the right-handed singlets (*cf.* Table 1.3).

The indices $i, j = 1, 2, 3$ represent three generations of fermions. Γ_u^{ij} are Yukawa couplings represented by 3×3 complex arbitrary matrices in the fermion generation space. They are not diagonal and provide mixing between generations. ϵ is the totally antisymmetric tensor related to the σ_2 Pauli matrix by $\epsilon = i\sigma_2$.

- $\mathcal{L}_{\text{Higgs}}$ describes the kinetic energy of the Higgs field, its gauge interactions, and the Higgs potential. It will be discussed in greater detail in its dedicated chapter (*cf.* Chapter 2).

1.2 Symmetries in the Standard Model

Symmetries play a foundational role in the construction and interpretation of modern physical theories. They do not only dictate the allowed structure of Lagrangians through invariance requirements, but also are at the origin of the conservation laws that constrain the dynamics of physical systems.

The formal link between continuous symmetries and conservation laws is provided by Noether's theorem, first formulated by Emmy Noether in 1918 [15].

In its most general form, Noether's theorem states that for every continuous symmetry of the action, there exists a corresponding conserved current.

More precisely, if the variation of the fields $\delta\psi(x)$ under an infinitesimal transformation leaves the action invariant (*i.e.* $\delta S = 0$), then there exists a current $j^\mu(x)$ such that:

$$\partial_\mu j^\mu(x) = 0 , \quad (1.12)$$

expressing local conservation of the corresponding quantity.

	Field	P	Q	T	T_3	Y_W	C
Quarks	$Q_L^i = \begin{pmatrix} u^i \\ d^i \end{pmatrix}_L$	L	$+2/3$ $-1/3$	$\frac{1}{2}$	$+\frac{1}{2}$ $-\frac{1}{2}$	$\frac{1}{3}$	$b/g/r$
	u_R^i	R	$+2/3$	0	0	$4/3$	
	d_R^i	R	$-1/3$	0	0	$-2/3$	
Leptons	$L_L^i = \begin{pmatrix} \nu^i \\ e^i \end{pmatrix}_L$	L	0 -1	$\frac{1}{2}$	$+\frac{1}{2}$ $-\frac{1}{2}$	-1	$-$
	ν_R^i	R	0	0	0	0	
	e_R^i	R	-1	0	0	-2	

Table 1.3: Quantum numbers of fermions: P - chirality,

Q - electric charge,

T - weak isospin,

T_3 - third component of weak isospin,

$Y_W = 2(Q - T_3)$ - weak hypercharge,

C - colour charge.

The index $i = 1, 2, 3$ denotes fermion generations, *e.g.* u_L^i denotes left-handed up-type quarks: $u_L^1 = u_L$, $u_L^2 = c_L$, and $u_L^3 = t_L$.

1.2.1 Global Symmetries

Global spacetime symmetries such as translations, rotations, and Lorentz boosts, play a fundamental role in the formulation of any relativistic quantum field theory. These symmetries reflect the homogeneity and isotropy of spacetime, and are mathematically described by the Poincaré group \mathcal{P} (*i.e.* the group of Minkowski spacetime isometries, with $\mathcal{P} \equiv \text{ISO}(1, 3)$).

Noether's theorem relates each continuous global symmetry with a conserved quantity. For example the invariance under spatial rotations corresponds to the conservation of angular momentum.

Their invariance must be preserved by both the Lagrangian and the quantization procedure to ensure physical consistency. All Standard Model fields and interactions are constructed to transform covariantly under the full Poincaré group, ensuring relativistic invariance of the theory at every stage.

1.2.2 Gauge Symmetries

Gauge symmetries are fundamentally distinct from global symmetries in both their interpretation and their physical consequences. Whereas global symmetries correspond to physically observable transformations that generate conserved quantities via Noether's theorem, gauge symmetries reflect a redundancy in the mathematical description of a physical system. They express an invariance under local changes of variables in field space, which leave all observable quantities unchanged.

In this sense, *gauge symmetries are not symmetries of nature itself, but of our description of nature*. They arise because we choose to formulate quantum field theories in terms of fields that contain more degrees of freedom than what is physically necessary.

This is particularly evident in electrodynamics. To illustrate this, consider a theory of a complex fermion field $\psi(x)$, invariant under global phase rotations: $\psi(x) \rightarrow e^{i\alpha}\psi(x)$, with constant α .

This global $U(1)$ symmetry leads, via Noether's theorem, to conservation of electric charge.

However if one attempts to promote this symmetry to a local one $\psi(x) \rightarrow e^{i\alpha(x)}\psi(x)$ with $\alpha(x)$ now depending on the space-time coordinate x , a problem arises: the kinetic term in the free Lagrangian (*cf.* Eq.(1.4)) is no longer invariant under the transformation, since derivatives of $\alpha(x)$ introduce additional terms.

To restore local gauge invariance, one must introduce a new vector field $A_\mu(x)$ (the gauge field) which transforms as

$$A_\mu(x) \rightarrow A_\mu(x) - \frac{1}{e}\partial_\mu\alpha(x) . \quad (1.13)$$

The ordinary derivative is then replaced by the *covariant derivative*,

$$D_\mu = \partial_\mu + ieA_\mu(x) , \quad (1.14)$$

which ensures that $D_\mu\psi(x)$ transforms in the same way as $\psi(x)$ under the local $U(1)$ transformation.

This modified Lagrangian

$$\mathcal{L}_{\text{QED}} = \bar{\psi}(i\gamma^\mu D_\mu - m)\psi - \frac{1}{4}F_{\mu\nu}F^{\mu\nu} , \quad (1.15)$$

is now invariant under local $U(1)$ symmetry, and describes the full dynamics of Quantum Electrodynamics (QED). It corresponds to the one already introduced in Eq.(1.10).

In other words, the requirement of local gauge invariance *forces* the introduction of interaction: the gauge field A_μ is interpreted as the photon, which couples to electric charge.

In fact, requiring local gauge invariance determines the interaction structure of the theory. Gauge bosons arise as necessary degrees of freedom introduced to preserve local symmetry. The electromagnetic, weak, and strong interactions all emerge from imposing local invariance under their respective symmetry groups.

Gauge symmetries thus differ fundamentally from global symmetries: while global symmetries imply conservation laws, local gauge symmetries dictate the existence of interaction-mediating fields and fully determine the dynamical structure of the theory.

1.2.3 Discrete Symmetries and their Violations

In addition to continuous spacetime and gauge symmetries, the Standard Model has three fundamental *discrete* symmetries defined as: charge conjugation (C), parity (P), and time reversal (T).

These three symmetries are defined by their action on quantum (Dirac) fields $\psi(t, \vec{x})$ as follows:

- **Charge conjugation** (\mathcal{C}): $\psi(x) \rightarrow \psi^c(x)$, where $\psi^c = C\bar{\psi}^T$ replaces a particle with its antiparticle.
- **Parity** (\mathcal{P}): $\psi(t, \vec{x}) \rightarrow \gamma^0\psi(t, -\vec{x})$, reflecting spatial coordinates.
- **Time reversal** (\mathcal{T}): $\psi(t, \vec{x}) \rightarrow T\psi(-t, \vec{x})$, reversing the time coordinate (with T anti-unitary).

These transformations involve the Dirac gamma matrices γ^μ , which encode the spinor structure of the theory, and play a central role in expressing the discrete operations. These symmetries can be considered individually or in combination.

The *CPT theorem* states that any local, Lorentz-invariant, and unitary quantum field theory must be invariant under the full \mathcal{CPT} transformation.

This result is deeply rooted in the structure of relativistic quantum mechanics and is believed to be exact. Under CPT, a (Dirac) field $\psi(t, \vec{x})$ transforms as:

$$\psi(t, \vec{x}) \xrightarrow{CPT} \gamma_5\psi^*(-t, -\vec{x}) . \quad (1.16)$$

Experimental observations confirm that \mathcal{CPT} symmetry holds to extremely high precision. Any violation would signal physics beyond the Standard Model and possibly a breakdown of locality or Lorentz invariance.

Individually, however, the discrete symmetries \mathcal{C} , \mathcal{P} , and \mathcal{T} are *not* preserved by all interactions.

The electromagnetic and strong interactions respect each of these symmetries, the weak interaction violates both \mathcal{C} and \mathcal{P} maximally. Even the combined \mathcal{CP} transformation is not an exact symmetry of nature.

This was first observed in the neutral kaon system in 1964 [16], and later confirmed in the B -meson sector at the B-factories: BaBar (SLAC) [17] and Belle (KEK) [18].

Discrete symmetries (though once assumed fundamental) are now understood as approximate, with their violations providing some of the most sensitive tests of the Standard Model's completeness.

Chapter 2

Higgs Physics

2.1 The Higgs Mechanism

The Higgs mechanism is an elegant theoretical solution to an apparent inconsistency in particle physics.

The photon (γ), mediator of the electromagnetic interaction, and the gluons (g), mediators of the strong interaction, have been established experimentally to be massless to high precision, consistent with their successful quantum field theoretical descriptions.

Weak interactions, on the other hand, were understood from low-energy phenomenology to have a very limited range (about $\sim 10^{-18}$ m), which in field theory implies the exchange of heavy vector bosons (denoted by W and Z). However, adding explicit mass terms for these bosons breaks the underlying gauge symmetry of the theory.

This sharp contrast between gauge mediators raised profound theoretical questions in the scientific community.

This conceptual challenge was resolved in the 1960s by Brout, Englert, and Higgs [19–21]. They introduced the concept of *Spontaneous Symmetry Breaking* (SSB), where a broken symmetry generates a mass term for weak bosons while leaving the underlying gauge symmetry intact (so that photons and gluons, whose gauge generators are unbroken, necessarily remain massless).

This framework, known as the Higgs mechanism, is realized in the Standard Model via a complex scalar field: The Higgs Field.

2.2 Spontaneous Symmetry Breaking in the Standard Model

At the heart of the mechanism lies the phenomenon of spontaneous symmetry breaking: although the Lagrangian possesses a continuous symmetry, the vacuum state does not.

This occurs when a (scalar) potential V exhibits a set of degenerate minima. The

system settles into one of these minima, defining a specific direction in field space that serves as the physical vacuum.

In quantum field theory, this phenomenon can be modeled for a complex scalar doublet ϕ using a potential of the form:

$$V(\phi) = \mu^2(\phi^\dagger\phi) + \lambda(\phi^\dagger\phi)^2, \quad (2.1)$$

where $\lambda > 0$ ensures boundedness from below, and $\mu^2 < 0$ leads to a non-zero vacuum expectation value (VEV) v .

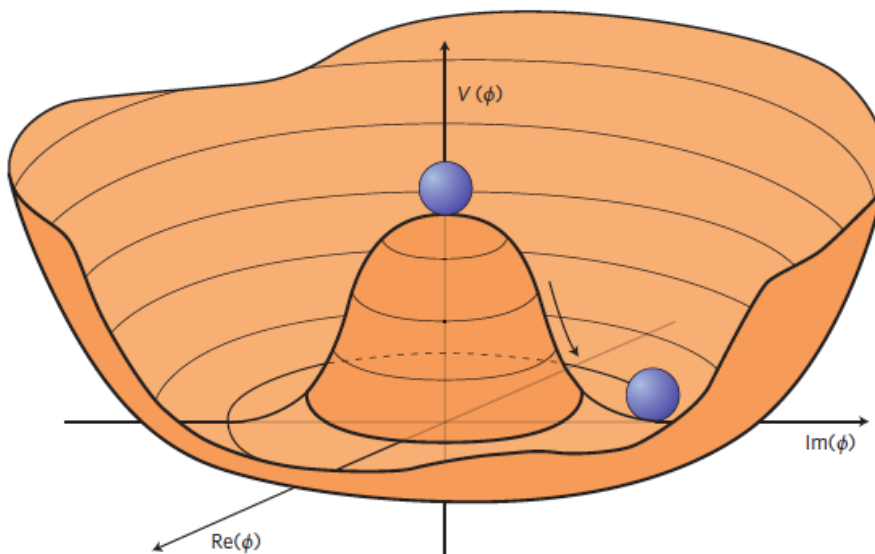


Figure 2.1: Illustration of the Higgs field potential $V(\phi)$, often called as ‘Mexican hat’ due to its shape. Taken from Ref. [22].

The resulting vacuum manifold forms a circle in the complex ϕ plane, illustrated in Figure 2.1 and Figure 2.2, and choosing any point on this circle spontaneously breaks the original symmetry.

In a theory with global symmetry, this breaking gives rise to massless scalar excitations known as the Goldstone bosons [24].

However, if the symmetry is local (*i.e.* gauged), the Goldstone bosons are “eaten” by the corresponding gauge fields, endowing them with mass and providing the longitudinal degrees of freedom of the massive vector bosons.

The Higgs mechanism

This absorption mechanism is the essence of the Higgs mechanism: it preserves gauge invariance while explaining the origin of mass for gauge bosons.

In the Standard Model, the Higgs field is introduced as a complex scalar doublet under $SU(2)_L$:

$$\phi = \begin{pmatrix} \phi^+ \\ \phi^0 \end{pmatrix}. \quad (2.2)$$

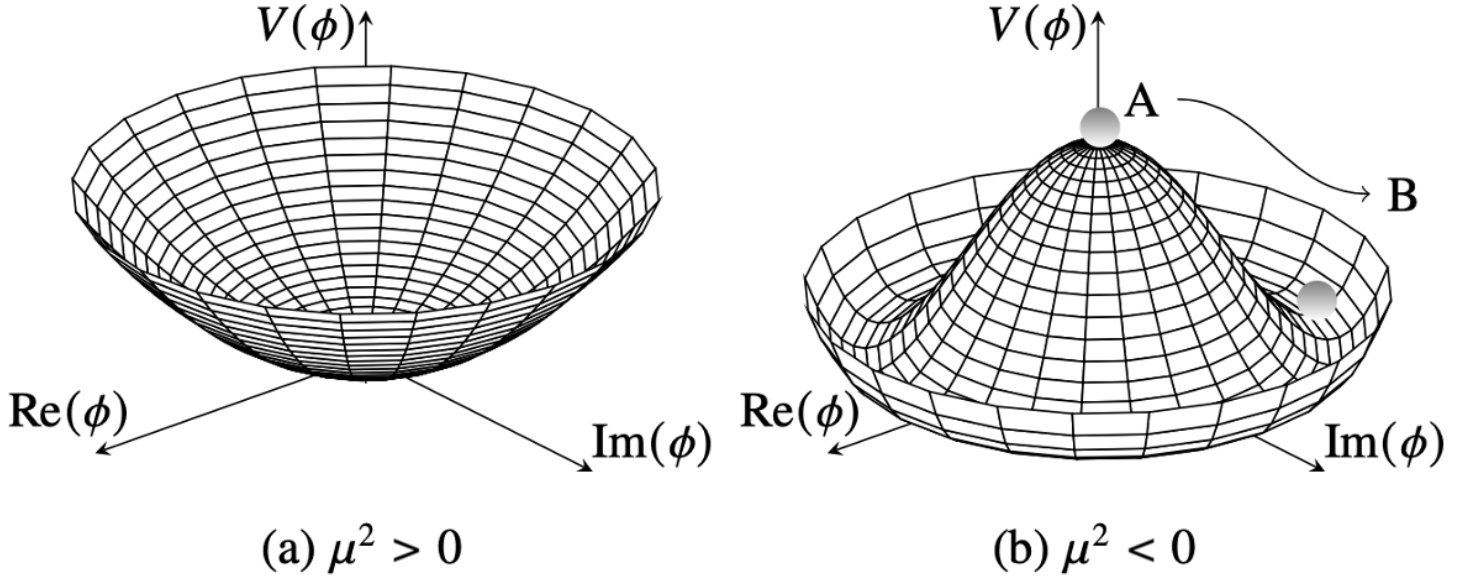


Figure 2.2: Other illustrations for the Higgs potential $V(\phi)$.

(a) Before SSB, with $\mu^2 > 0$;

(b) After SSB, with $\mu^2 < 0$.

Point B marks the non-zero vacuum expectation value (VEV) v selected by the system once spontaneous symmetry breaking has occurred. Taken from Ref. [23].

Its dynamics are governed by the Lagrangian:

$$\mathcal{L}_{\text{Higgs}} = (D_\mu \phi)^\dagger (D^\mu \phi) - V(\phi) , \quad (2.3)$$

where the covariant derivative is:

$$D_\mu = \partial_\mu - ig \frac{\tau^a}{2} W_\mu^a - ig' \frac{Y}{2} B_\mu , \quad (2.4)$$

with g and g' the gauge couplings of $SU(2)_L$ and $U(1)_Y$ respectively, τ^a the Pauli matrices, and W_μ^a , B_μ the corresponding gauge fields.

Recall from Eq. (2.1) the expression of the most general form of the scalar potential $V(\phi)$ for the Higgs field. For $\mu^2 < 0$, the Higgs field acquires a non-zero vacuum expectation value in the neutral direction:

$$\langle \phi \rangle = \frac{1}{\sqrt{2}} \begin{pmatrix} 0 \\ v \end{pmatrix} , \quad (2.5)$$

where $v = \sqrt{-\mu^2/\lambda} \approx 246$ GeV is fixed from the measured value of the Fermi constant G_F .

The Electroweak Symmetry breaking (EWSB)

The non-zero value of the VEV v breaks the electroweak symmetry group $SU(2)_L \times U(1)_Y$ down to the electromagnetic subgroup $U(1)_{\text{EM}}$.

Since the vacuum is invariant under $U(1)_{\text{EM}}$, the associated gauge boson (the photon) remains massless. This is a crucial consistency requirement: electromagnetism is a long-range force, and the photon has been measured to be massless to very high precision.

Upon EWSB, the Higgs vacuum expectation value v breaks three of the four generators of $SU(2)_L \times U(1)_Y$ producing three would-be Goldstone bosons that are absorbed to give mass (and longitudinal polarization) to the W^\pm and Z^0 gauge bosons.

The remaining physical degree of freedom in the Higgs field manifests itself as a scalar particle: the Higgs boson.

Boson	Q/q_e	mass [GeV]	spin	role
Higgs boson (H)	0	125.09 ± 0.21	0	Mass generation

Table 2.1: Properties of the Higgs boson in the Standard Model. The Higgs is the only elementary scalar particle (i.e spin 0), electrically neutral, with a precisely measured mass of about 125 GeV [25].

Diagonalizing the mass matrix of the neutral gauge fields yields the photon A_μ and the Z boson:

$$A_\mu = \cos \theta_W B_\mu + \sin \theta_W W_\mu^3 , \quad (2.6)$$

$$Z_\mu = -\sin \theta_W B_\mu + \cos \theta_W W_\mu^3 , \quad (2.7)$$

where the weak mixing angle θ_W is defined via:

$$\tan \theta_W = \frac{g'}{g} . \quad (2.8)$$

The resulting gauge boson masses are:

$$m_W = \frac{1}{2} g v , \quad (2.9)$$

$$m_Z = \frac{1}{2} \sqrt{g^2 + g'^2} v , \quad (2.10)$$

$$m_\gamma = 0 . \quad (2.11)$$

The photon being massless reflects the unbroken $U(1)_{\text{EM}}$ gauge invariance, while the masses of the W and Z bosons encode the effects of electroweak symmetry breaking.

This mass pattern with $m_W < m_Z$ and $m_\gamma = 0$ is a robust prediction of the Standard Model.

2.3 Higgs Boson Properties at the LHC

2.3.1 Production Mechanisms

The dominant Higgs production modes at the LHC are illustrated in Figure 2.3:

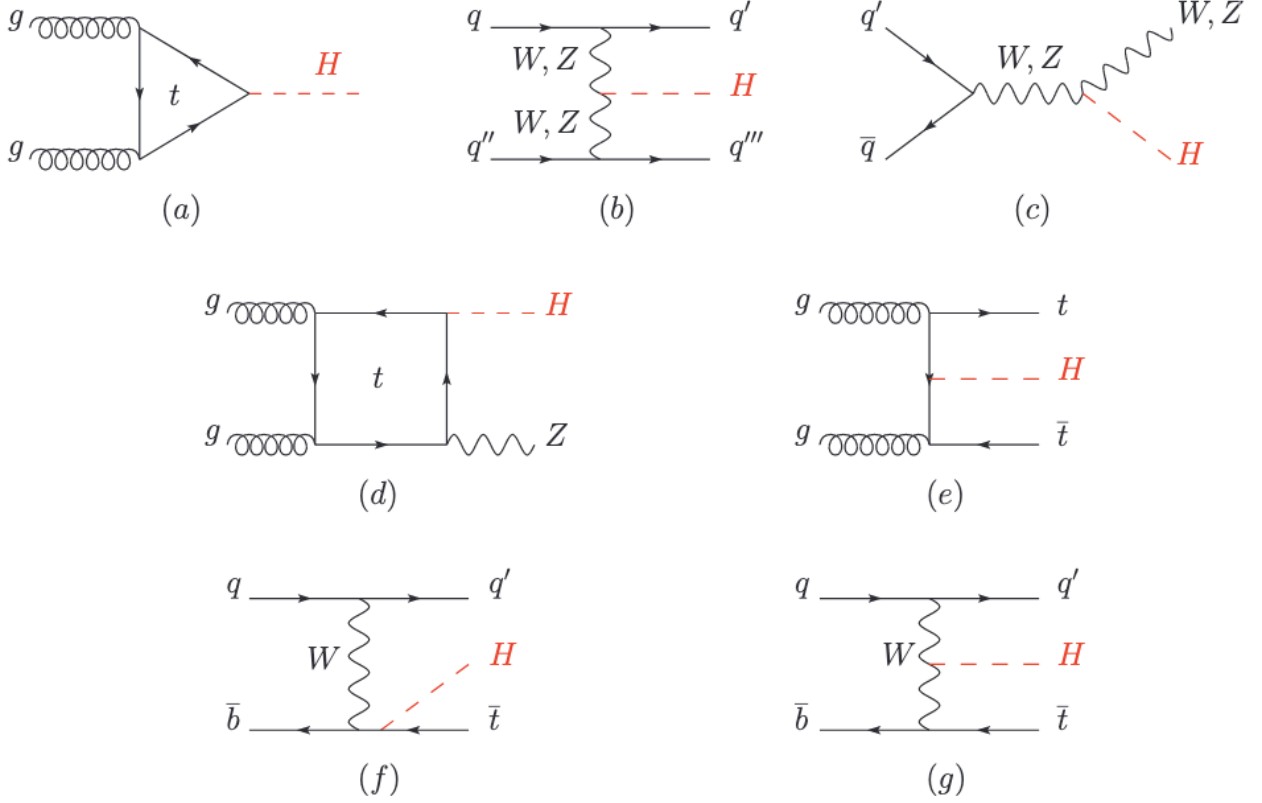


Figure 2.3: Main Higgs boson production processes at leading order.

(a) is the Feynman diagram of the triangle contribution for the ggF di-Higgs process; (b) is for the VBF process; (c) is the associated production with a vector boson at tree level, and (d) is the one at loop level; (e) is for the $t\bar{t}H$ process; (f and g) are the associated productions with a single top quark. Taken from Ref. [26].

- **Gluon-gluon fusion (ggF, Figure 2.3.a)**: is the dominant Higgs production mechanism at the LHC, despite being a loop-induced process.
- **Vector boson fusion (VBF, Figure 2.3.b)**: A process in which two quarks exchange a W or Z boson and emit a Higgs boson. Although its cross-section is smaller than ggF, the clean topology provides high sensitivity in certain final states.
- **Associated production (VH, $t\bar{t}H$)**: The Higgs boson can be produced in association with a vector boson (W^\pm or Z), known as VH production (Figure 2.3.c and Figure 2.3.d), or with a top-quark pair ($t\bar{t}H$, Figure 2.3.e).

2.3.2 Higgs Decay Channels and Branching Ratios

The branching ratios for the main decays of the Standard Model Higgs boson are presented in Figure 2.4 (as a function of the Higgs boson mass).

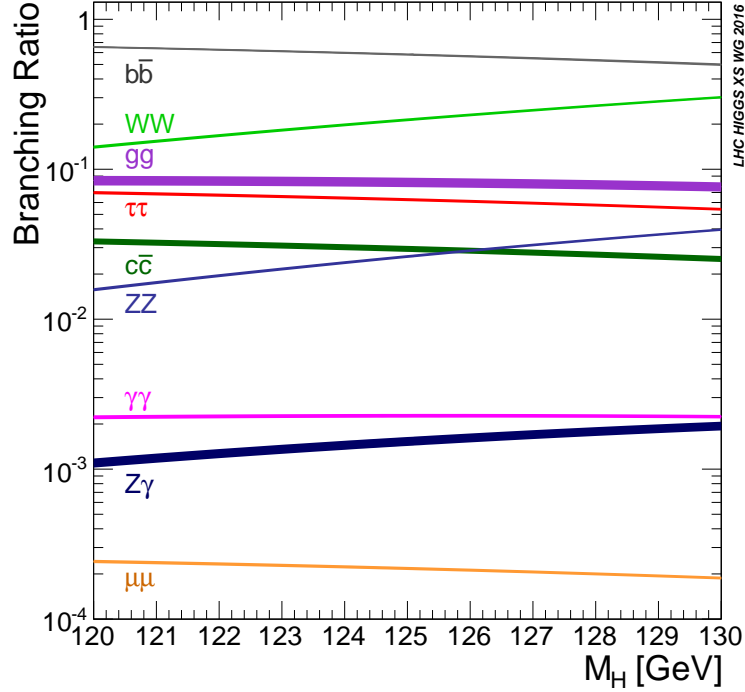


Figure 2.4: Higgs boson branching ratios as a function of mass. Taken from Ref. [27].

$H \rightarrow b\bar{b}$ channel: The $H \rightarrow b\bar{b}$ channel has the highest branching ratio. However, experimentally this channel suffers from large QCD backgrounds and limited jet identification efficiency, making the observation of the Higgs boson in this channel difficult. Similar experimental challenges are encountered in the $H \rightarrow c\bar{c}$, $H \rightarrow \tau\tau$, and $H \rightarrow gg$ channels.

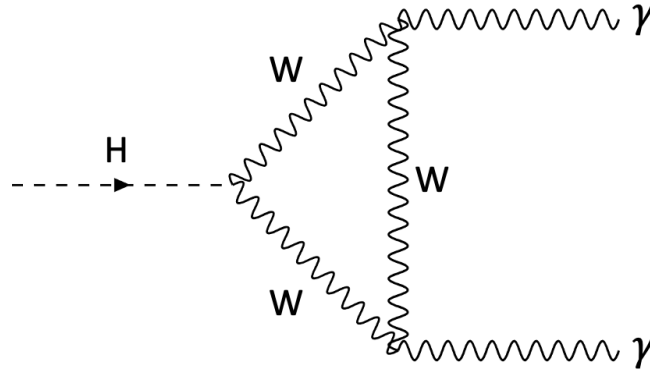
$H \rightarrow WW$ channel: The decay channel $H \rightarrow WW$ has the second highest branching ratio. The W bosons decay to quarks with a branching ratio of about 67%, but this final state is difficult to use due to the overwhelming QCD background. Therefore, the leptonic channel is preferred. However, the two neutrinos in this final state escape detection, preventing full reconstruction of the Higgs boson invariant mass. This leads to poor mass resolution and makes background rejection in this channel challenging.

$H \rightarrow ZZ$ channel: The $H \rightarrow ZZ$ channel is considered one of the two “golden channels” for observing the Higgs boson. The Z bosons are selected in the decay mode $ZZ \rightarrow (ll)(ll)$ (where $l = e, \mu$). This channel yields a final state with a clean resonance appearing over a continuous background, facilitating the observation of the Higgs boson.

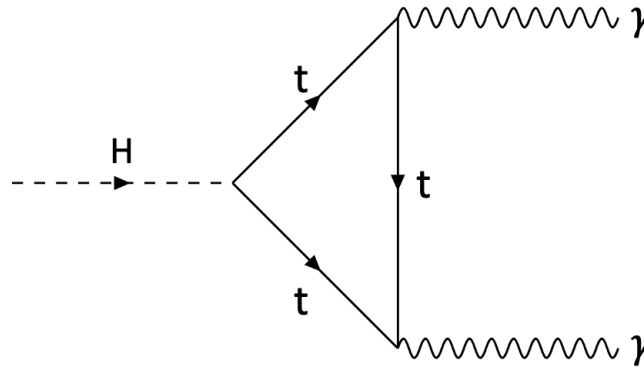
$H \rightarrow \gamma\gamma$ **Channel:** The $H \rightarrow \gamma\gamma$ channel is the other golden channel for Higgs observation. The branching ratio for this process is about 0.22% (*cf.* Figure 2.4). Despite the small branching ratio, this channel benefits from a very clean experimental signature: a narrow resonance dominated by the detector's electromagnetic calorimeter resolution, sitting over a continuum background of QCD diphoton production.

The dominant background arises from the QCD diphoton production, whose cross-section is roughly three orders of magnitude larger than that of the Higgs signal. Other background sources include associated photon production with jets. Additional background arises from jets produced in association with a quark or gluons, creating a jet that can mistakenly be reconstructed as a photon. Electrons misidentified as photons also contribute to the background.

The Higgs boson decays into two photons through loop processes, dominated by the W boson loop or a top quark triangle diagram (*cf.* Figure 2.5).



(a) W^\pm boson loop



(b) Top quark triangle

Figure 2.5: Dominant one-loop contributions to the decay $H \rightarrow \gamma\gamma$: (a) a virtual W^\pm loop, and (b) a virtual top-quark loop.

Diagrams produced using the <https://feynman.aivazis.com/> website.

Chapter 3

Higgs Self-Coupling and Di-Higgs Production

Among the few remaining parts of the Standard Model that need experimental confirmation, the self-interaction of the Higgs boson holds exceptional theoretical and experimental significance.

While the scalar potential responsible for electroweak symmetry breaking (EWSB) is conceptually simple, experimental verification of its full structure remains incomplete.

In the Standard Model, Higgs-boson pair production occurs primarily through gluon–gluon fusion, mediated by both triangle and box top-quark loops.

The two amplitudes interfere destructively (drastically reducing the production cross-section) and the final states are overwhelmed by substantial backgrounds, making the signal difficult to isolate.

This chapter introduces the Higgs boson trilinear coupling λ_{3H} , the key to double Higgs production. It will motivate the need for precision tools such as the Matrix Element Method (see Part III of this manuscript) to fully exploit the available kinematic information in a data-driven measurement of λ_{3H} .

3.1 Theoretical Motivation

Recall that in the SM, the Higgs potential is expressed as:

$$V(\phi) = \mu^2 \phi^\dagger \phi + \lambda (\phi^\dagger \phi)^2, \quad (3.1)$$

where ϕ is the Higgs field, μ^2 is a dimensional parameter, and λ is the self-interaction strength.

Expanding the potential around the vacuum expectation value (vev) v , this leads to a scalar potential in terms of the physical Higgs boson H (not to be confused with the Higgs field ϕ):

$$V(H) = \lambda v^2 H^2 + \lambda v H^3 + \frac{\lambda}{4} H^4, \quad (3.2)$$

which can be rewritten as:

$$V(H) = \frac{1}{2} m_H^2 H^2 + \frac{\lambda_{3H}}{3!} H^3 + \frac{\lambda_{4H}}{4!} H^4, \quad (3.3)$$

where:

- $m_H^2 = 2\lambda v^2$ is the squared mass of the Higgs boson,
- $\lambda_{3H} = \frac{3m_H^2}{v}$ is the trilinear Higgs self-coupling,
- $\lambda_{4H} = \frac{3m_H^2}{v^2}$ is the quartic Higgs self-coupling.

The experimental measurement of this trilinear Higgs self-coupling λ_{3H} from LHC data is a central goal of contemporary LHC physics, and the focus of this thesis.

The Higgs boson was jointly discovered by the ATLAS [7] and CMS [8] experiments at the Large Hadron Collider (LHC) in 2012 [5, 6]. Since then, its mass has been precisely measured [25] to be:

$$m_H = 125.09 \pm 0.21 \text{ (stat)} \pm 0.11 \text{ (syst)} \text{ GeV}. \quad (3.4)$$

Given the measured values for $v \approx 246$ GeV, one can predict the value of the self-interaction strength λ parameter (using Eq. (3.1))

$$\lambda = \frac{m_H^2}{2v^2} \approx 0.13. \quad (3.5)$$

The SM value for trilinear Higgs self-coupling λ_{3H} is therefore:

$$\lambda_{3H}^{\text{SM}} = 6\lambda v = \frac{3m_H^2}{v} \approx 190 \text{ GeV}. \quad (3.6)$$

A precise determination of λ_{3H} is essential for completing the experimental test of the SM Higgs sector. Any departure from the SM value would impact electroweak baryogenesis scenarios, where modified Higgs self-interactions might help explain the matter–antimatter asymmetry of the Universe [28].

3.2 Di-Higgs Production in the Standard Model at the LHC

The primary process sensitive to the trilinear Higgs coupling at LHC in proton-proton collisions is non-resonant Higgs boson pair production, dominated by gluon-gluon fusion (ggF) (*cf.* Figure 3.1).

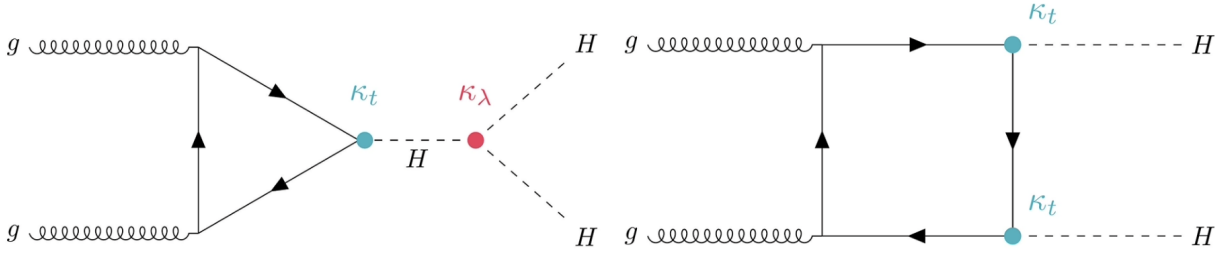


Figure 3.1: Feynman diagrams for the major production modes of two Higgs bosons: gluon fusion (ggF).

(Left) Triangle diagram sensitive to the self-coupling vertex $\kappa_\lambda = \frac{\lambda_{3H}}{\lambda_{3H}^{SM}}$,

(Right) Box diagram, which interferes destructively with the Triangle.

Taken from Ref. [29].

The gluon-gluon fusion is mediated by heavy quark loops, primarily the top quark. At leading order, two classes of Feynman diagrams contribute destructively:

1. **Triangle diagram:** a process dominated by top-quark loop where a single off-shell Higgs boson decays into two on-shell Higgs bosons. This diagram contains the trilinear self-coupling vertex and its amplitude is proportional to λ_{3H} .
2. **Box diagram:** a process dominated by top-quark loop where two Higgs bosons are produced without a self-coupling vertex.

The interference between these diagrams is destructive in the SM, suppressing the total cross-section and giving rise to a well-studied dependence of the total cross-section on $\kappa_\lambda = \frac{\lambda_{3H}}{\lambda_{3H}^{SM}}$.

This interference not only affects the total rate but also imprints a characteristic structure in the invariant mass distribution of the Higgs boson pair (m_{HH}). As illustrated in Figure 3.2, the two diagrams contribute to distinct kinematic regions: the triangle diagram (proportional to κ_λ) enhances the low- m_{HH} region, while the box diagram dominates at higher invariant masses.

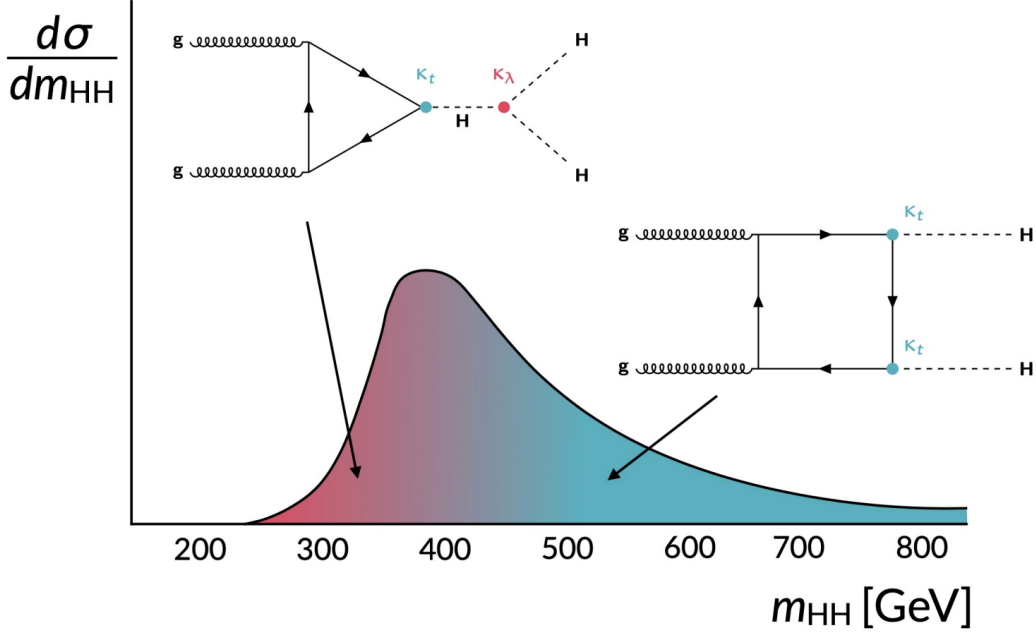


Figure 3.2: Differential cross-section for Higgs boson pair production via gluon fusion as a function of m_{HH} , highlighting the distinct contributions of the triangle and box diagrams. The triangle diagram (red region) dominates at low invariant mass, while the box diagram (blue region) contributes more at higher m_{HH} . The resulting interference produces a characteristic shape sensitive to κ_λ .
Taken from Ref. [30].

The SM cross-section for ggF di-Higgs is approximately 32.88 fb (at NLO full theory, for $\sqrt{s} = 14$ TeV). The values of the cross-section for processes with Higgs receive large Next-to-Leading Order (NLO) and Next-to-Next-to-Leading Order (NNLO) corrections, as we can see in Table 3.1.

	σ_{LO} (fb)	σ_{NLO} (fb)	σ_{NNLO} (fb)
Basic HTL	$17.07^{+30.9\%}_{-22.2\%}$ [31, 32]	$31.93^{+17.6\%}_{-15.2\%}$ [31, 32]	$37.52^{+5.2\%}_{-7.6\%}$ [33]
B-i/proj HTL	$19.85^{+27.6\%}_{-20.5\%}$ [31, 32]	$38.32^{+18.1\%}_{-14.9\%}$ [31, 32]	$39.58^{+1.4\%}_{-4.7\%}$ [34]
FTapprox	$19.85^{+27.6\%}_{-20.5\%}$ [35]	$34.25^{+14.7\%}_{-13.2\%}$ [35]	$36.69^{+2.1\%}_{-4.9\%}$ [34]
Full Theory	$19.85^{+27.6\%}_{-20.5\%}$ [31, 32]	$32.88^{+13.5\%}_{-12.5\%}$ [36]	—

Table 3.1: Cross-section at $\sqrt{s} = 14$ TeV for Higgs boson pair production from gluon fusion at different perturbative orders, using full theory or different approximations. The infinite top mass approximation is referred as Heavy Top Limit (HTL), and the finite top mass approximation is referred as FTAPPROX.

Other production mechanisms such as vector boson fusion (VBF) (*cf.* Figure 3.3), top-associated ($t\bar{t}HH$) and vector-associated (VHH) production channels contribute less than 10% of the total cross-section [37], but are complementary in constraining other effective couplings (*e.g.* κ_{2V}).

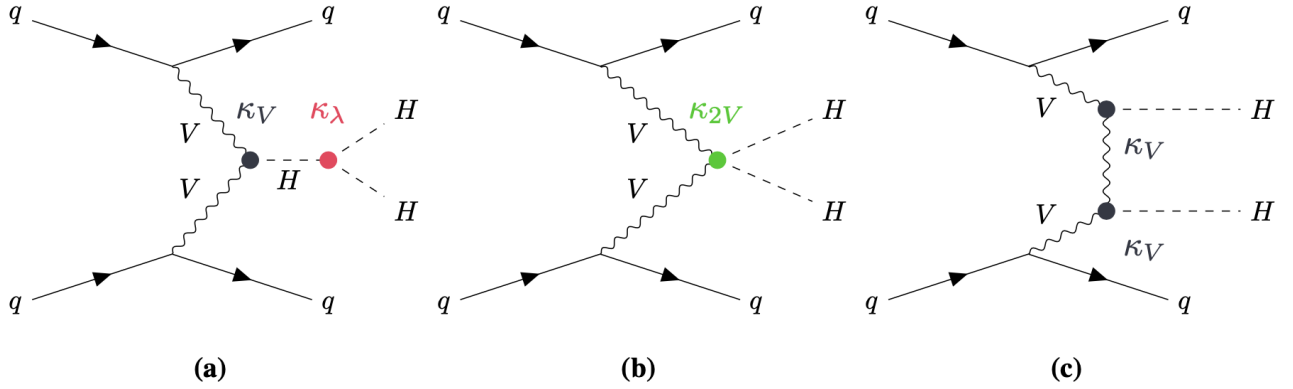


Figure 3.3: Depiction of Vector Boson Fusion (VBF) processes in Higgs boson pair production. Taken from [29].

3.3 Experimental Access and Analysis Strategy

The LHC experiments have performed extensive searches for di-Higgs production. The rarity of the signal, combined with significant backgrounds, requires careful channel selection and sophisticated analysis techniques.

	bb	WW	$\tau\tau$	ZZ	$\gamma\gamma$
bb	34%				
WW	25%	4.6%			
$\tau\tau$	7.3%	2.7%	0.39%		
ZZ	3.1%	1.1%	0.33%	0.069%	
$\gamma\gamma$	0.26%	0.10%	0.028%	0.012%	0.0005%

Figure 3.4: Higgs branching ratio (BR) percentage for the different decay channels for $m_H = 125\text{GeV}$. Taken from Ref. [38].

Several final states have been studied, with varying balances of signal purity and branching fraction (*cf.* Fig 3.4):

- $HH \rightarrow b\bar{b}\gamma\gamma$: This is considered the ‘golden channel’ for the study of the Higgs self-coupling. It is the perfect compromise between the excellent mass

resolution in the $\gamma\gamma$ system and the very high b -jet branching fraction in Higgs boson decay.

- $HH \rightarrow b\bar{b}\tau^+\tau^-$ and $b\bar{b}WW^*$: These provide larger yields but face more difficult backgrounds and poorer mass resolution.
- $HH \rightarrow b\bar{b}b\bar{b}$: This channel has the largest branching ratio but suffers from poor b -jet resolution, overwhelming QCD multijet backgrounds and combinatorics.

3.4 BSM Higgs Potential

The parameter κ_λ affects not only the rate and kinematics of di-Higgs production but also encodes critical information about the shape of the Higgs scalar potential beyond its curvature at the minimum. This has direct implications for the global structure and stability of the electroweak vacuum.

We recall from Eq. (3.3) the form of the scalar potential for the Higgs boson in the SM:

$$V(H) = \frac{1}{2}m_H^2 H^2 + \lambda_{3H}vH^3 + \frac{1}{4}\lambda_{4H}H^4, \quad (3.7)$$

and the associated SM predictions for the trilinear and quartic Higgs couplings:

$$\lambda_{3H}^{\text{SM}} = \frac{3m_H^2}{v} \quad \text{and} \quad \lambda_{4H}^{\text{SM}} = \frac{3m_H^2}{v^2}.$$

3.4.1 Exploring Different Higgs Potentials:

The study presented in Ref. [39] (by both the ATLAS and CMS collaborations) examines four electroweak symmetry breaking (EWSB) scenarios that may arise in realistic beyond the Standard Model (BSM) frameworks. These scenarios were considered for a dedicated high-luminosity LHC (HL-LHC) sensitivity study at $\sqrt{s} = 3 \text{ ab}^{-1}$, and predict a strong first-order phase transition (FOPT) in the early universe [40,41], which is not realized in the SM [42].

Within the context of the Standard Model Effective Field Theory (SMEFT), both a dimension-6 (SMEFT 6) and a dimension-8 (SMEFT 8) extension of the Higgs potential are explored. Additionally, two scenarios introducing small modifications to the low-energy SM Brout–Englert–Higgs (BEH) potential are discussed: one with a logarithmic term and one with an exponential term, both expressed as functions of the scalar doublet inner product $\Phi^\dagger\Phi$. Full technical details can be found in [39].

A graphical representation of the different Higgs potentials is provided in Figure 3.5. The associated values of k_3 (*i.e.* $\kappa_{\lambda_{3H}}$) for each scenario are indicated in the top panel.

At $\sqrt{s} = 3 \text{ ab}^{-1}$, Figure 3.5 shows that the 95% confidence level (CL) exclusion band, shown in red, rules out nearly all scenarios featuring a strong first-order phase transition. In contrast, at $\sqrt{s} = 2 \text{ ab}^{-1}$, certain regions of parameter space remain unconstrained.

While current experimental data still allow sizeable deviations from the SM expectation, a precise determination of κ_λ is crucial. Such a measurement would not only validate the electroweak symmetry breaking mechanism but also constrain the possible forms of the scalar potential at higher energy scales. Achieving this level of precision by the end of HL-LHC operations would constitute a milestone result for the field, with significant implications for our understanding of the early universe.

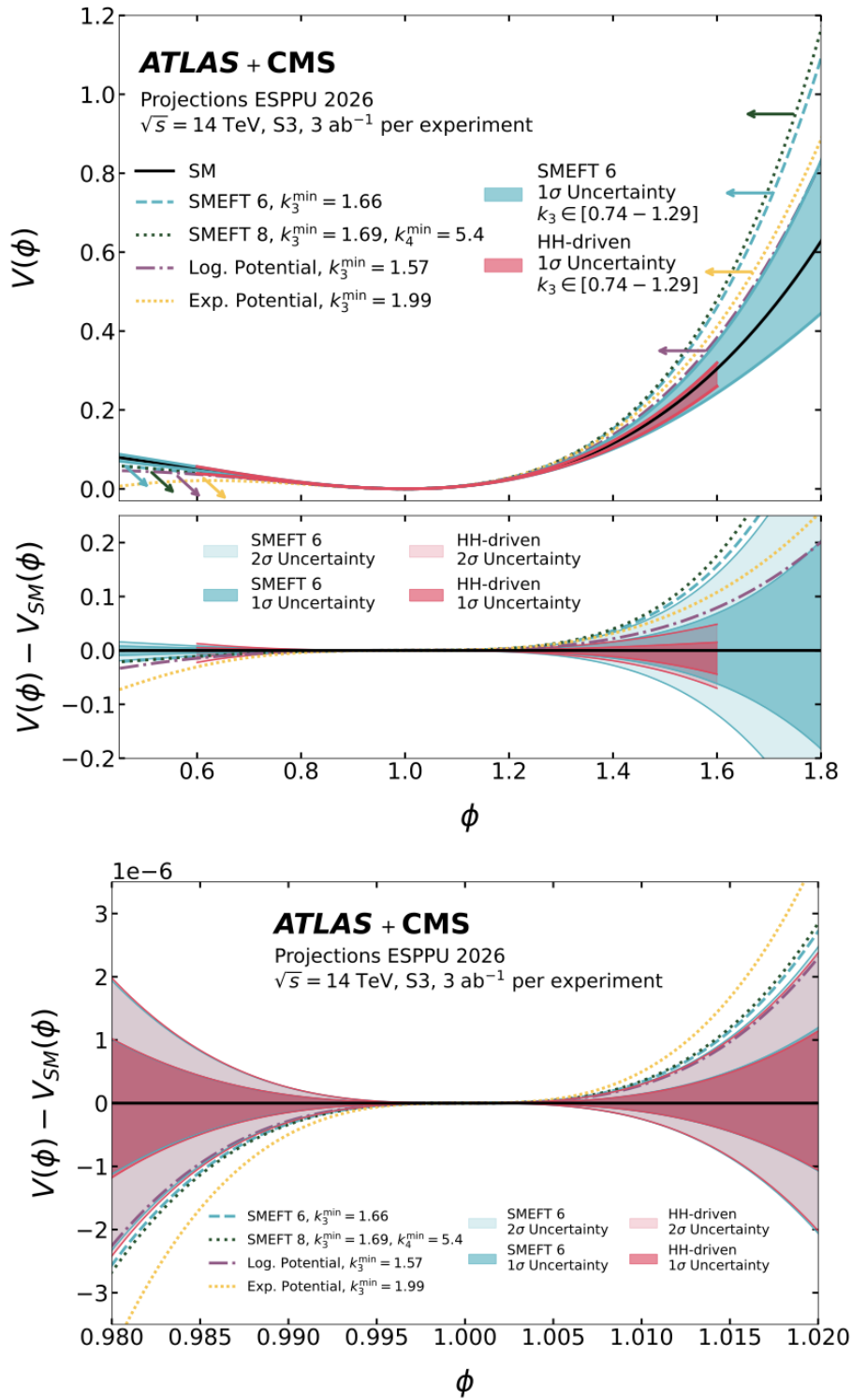


Figure 3.5: Projections for the ongoing European Strategy for Particle Physics Update (ESPPU) 2026.

(Top) Comparison of the BEH (Brout–Englert–Higgs) potentials for various BSM scenarios predicting a first-order phase transition, with respect to the Standard Model potential.

(Middle) Difference between each potential $V(\phi)$ and the SM expectation $V_{SM}(\phi)$.

(Bottom) A zoomed-in view of $V(\phi) - V_{SM}(\phi)$ around the potential minimum.

Figure adapted from Ref. [39].

3.4.2 Higgs Self-Coupling and Baryogenesis

The cosmological relevance of the Higgs potential arises from its role in the electroweak phase transition, which may have triggered baryogenesis in the early Universe.

As shown in Ref. [28], a strong first-order electroweak phase transition (one of the three necessary Sakharov conditions for baryogenesis) requires a significant deformation of the scalar potential, typically resulting in an enhanced Higgs self-coupling.

Using non-perturbative functional renormalization group methods, the study explores both extensions of the Higgs potential and finds that scenarios supporting electroweak baryogenesis consistently predict $\lambda_{3H} \gtrsim 1.5 \lambda_{3H}^{\text{SM}}$, corresponding to $\kappa_\lambda \gtrsim 1.5$.

This result should be interpreted in light of the projected sensitivity of the LHC to the Higgs self-coupling (*cf.* Eq. (8.6)).

This enhancement is not limited to effective field theory expansions with dimension-6 operators, but persists in broader classes of potentials where simple Taylor expansions fail to capture the relevant vacuum structure. The observed link between a strong phase transition and measurable deviations in the Higgs self-coupling suggests that collider experiments (especially those probing di-Higgs production) can serve as indirect probes of the early-Universe baryogenesis.

In this context, a precision determination of κ_λ , as pursued in this thesis via the Matrix Element Method at NLO, offers not only insights into electroweak symmetry breaking but also critical constraints on the dynamics responsible for the matter–antimatter asymmetry observed today.

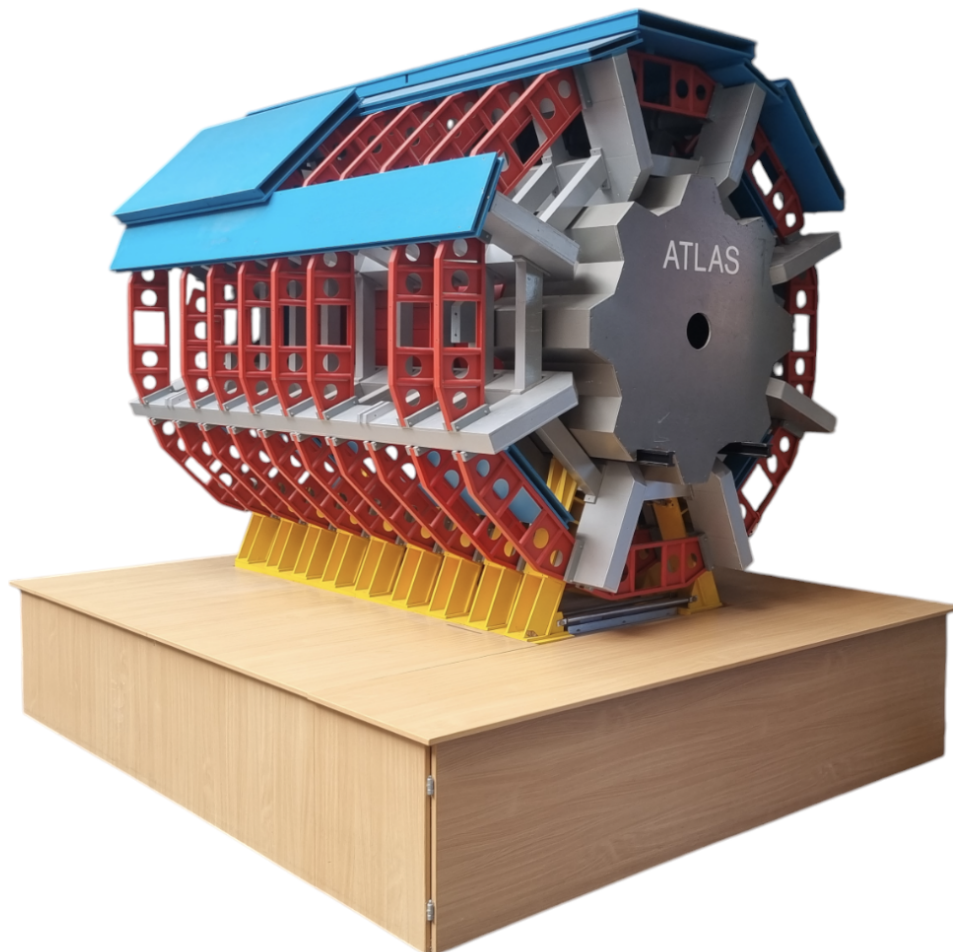
3.5 Conclusion

The measurement of the Higgs boson self-coupling λ_{3H} is a cornerstone objective in the post-discovery phase of Higgs physics. While the SM provides a concrete prediction, verifying this experimentally is both a test of the SM and a probe for new physics.

The interplay of triangle and box diagrams in di-Higgs production (resulting in destructive interference) makes this measurement challenging but uniquely informative. As data accumulate and analysis techniques improve, significant progress toward measuring λ_{3H} is expected in the coming years, particularly at the HL-LHC and future colliders.

Part II

Experimental setup



The previous part of this manuscript presented the theoretical framework of the Standard Model (SM), with particular emphasis on the Higgs mechanism, the scalar potential, and the role of the trilinear self-coupling λ_{3H} in particle physics.

While theoretical predictions are essential to define the parameters of interest and motivate new physics searches, their validation relies fundamentally on our experimental capabilities.

This second part introduces the experimental foundation upon which the measurement of the Higgs boson self-coupling is based, with a focus on the $gg \rightarrow HH \rightarrow b\bar{b}\gamma\gamma$ channel studied within the ATLAS experiment.

The discussion continues in **Chapter 4**, which presents the Large Hadron Collider (LHC), the most powerful particle accelerator ever constructed (to date). The chapter outlines its operational history from Runs 1 to 3, with particular emphasis on delivered luminosity, pile-up conditions, and their implications for precision measurements.

Chapter 5 describes the ATLAS detector, one of the two general-purpose experiments at the LHC. Beyond a technical overview, this chapter emphasizes the performance of ATLAS across its operational lifespan, including the evolution of key components such as the tracking system, calorimeters, and trigger. Special attention is given to the reconstruction performance of photons and b -jets, which are critical to the final state under study in this thesis.

Chapter 6 focuses on the experimental access to Higgs boson pair production at the LHC. While the theoretical motivation has already been discussed, this chapter reviews how di-Higgs production manifests itself in LHC collisions, the experimental strategies employed to isolate it, and the current status of searches in various final states. The specific role of the $b\bar{b}\gamma\gamma$ channel is highlighted as one of the most sensitive probes due to its clean signature and excellent mass resolution.

Finally, **Chapter 7** introduces the High-Luminosity LHC (HL-LHC) upgrade, which aims to increase the LHC's dataset by an order of magnitude. It outlines the major accelerator improvements and the extensive upgrade program of the ATLAS detector. Expected performance for key observables, including photon and b -jet identification in high pile-up environments, is discussed in the context of future sensitivity to the Higgs self-coupling. We will also present the software developments carried out as part of my ATLAS authorship qualification project (QP, or "qualification task" QT) focusing on the upgraded Inner Tracker (ITk).

Content

4	The Large Hadron Collider	69
4.1	The CERN Accelerator Complex and LHC Overview	69
4.2	Performance and Operation During Runs 1–3	71
4.3	Luminosity and Pile-Up Conditions	71
4.4	Physics Output Before HL-LHC	74
5	The ATLAS Detector and Physics Object Reconstruction Performance	75
5.1	General Overview and Design Principles	75
5.2	Coordinate System and Global Layout	78
5.3	The Inner Detector	78
5.4	The Electromagnetic Calorimeter: Photon Identification and Resolution	79
5.5	The Hadronic Calorimeter: Jet and b -Jet Reconstruction	81
5.6	Muon Spectrometer	81
5.7	Trigger and Data Acquisition System (DAQ)	81
5.8	Object reconstruction and performance	82
5.8.1	Photons γ	82
5.8.2	Jets and b -Tagging	83
5.9	Summary: Performance Milestones and Impact on LHC Analyses . .	85
6	Experimental Access to the Higgs Self-Coupling	87
6.1	Current Constraints and Effective Parameterization	87
6.2	Most Recent ATLAS non-resonant $HH \rightarrow b\bar{b}\gamma\gamma$ Analysis [’25]	88
7	The High-Luminosity LHC and Future Prospects	93
7.1	HL-LHC Machine and Design Goals	93
7.2	ATLAS Detector Upgrades	93
7.2.1	The Inner Tracker (ITk): Capabilities, and Expected Performance	93
7.2.2	Calorimeter and Muon System Enhancements	98
7.3	Computing and Data Handling	98
7.4	ATLAS Qualification Task: ACTS Kalman Filter (KF) Integration in ATHENA	101
7.5	Future Sensitivity to Higgs Self-Coupling	104

Chapter 4

The Large Hadron Collider

The discovery and exploration of the Higgs boson properties, and more broadly the entire programme of precision tests of the Standard Model (SM) at the TeV scale, has been made possible by the capabilities of the Large Hadron Collider (LHC).

The Large Hadron Collider (LHC) [43] is a circular particle accelerator located at the European Centre of Nuclear Research (CERN), near Geneva (Switzerland). The LHC is the most powerful particle accelerator ever built to this day.

This chapter provides an overview of the LHC's design, operational performance, and physics output during its first three major data-taking periods (Runs 1–3), establishing the experimental context for Higgs physics analyses at ATLAS.

4.1 The CERN Accelerator Complex and LHC Overview

The LHC is the final stage of a complex acceleration chain at CERN. To date, it is the highest energy operating proton-proton (p-p) collider at a center of mass energy of $\sqrt{s}=13$ TeV at the end of Run 2 (and $\sqrt{s}=13.6$ TeV for Run 3).

The LHC consists of a 27 km circumference ring where protons (or heavy ions) circulate in opposite directions.

Protons are first accelerated by Linac-4 to 160 MeV, then injected into the Proton Synchrotron Booster (PSB), where they reach 2 GeV. They are subsequently transferred to the Proton Synchrotron (PS) and accelerated to 25 GeV, followed by injection into the Super Proton Synchrotron (SPS), which delivers beams at 450 GeV to the LHC ring [45].

The LHC contains a complex system of superconducting magnets that are cooled to a temperature of 1.9 K. These magnets generate an 8.3 T magnetic field that bends and confines the proton bunches within beam pipes maintained under high vacuum. To collide protons, hydrogen plasma is first injected into secondary accelerators,

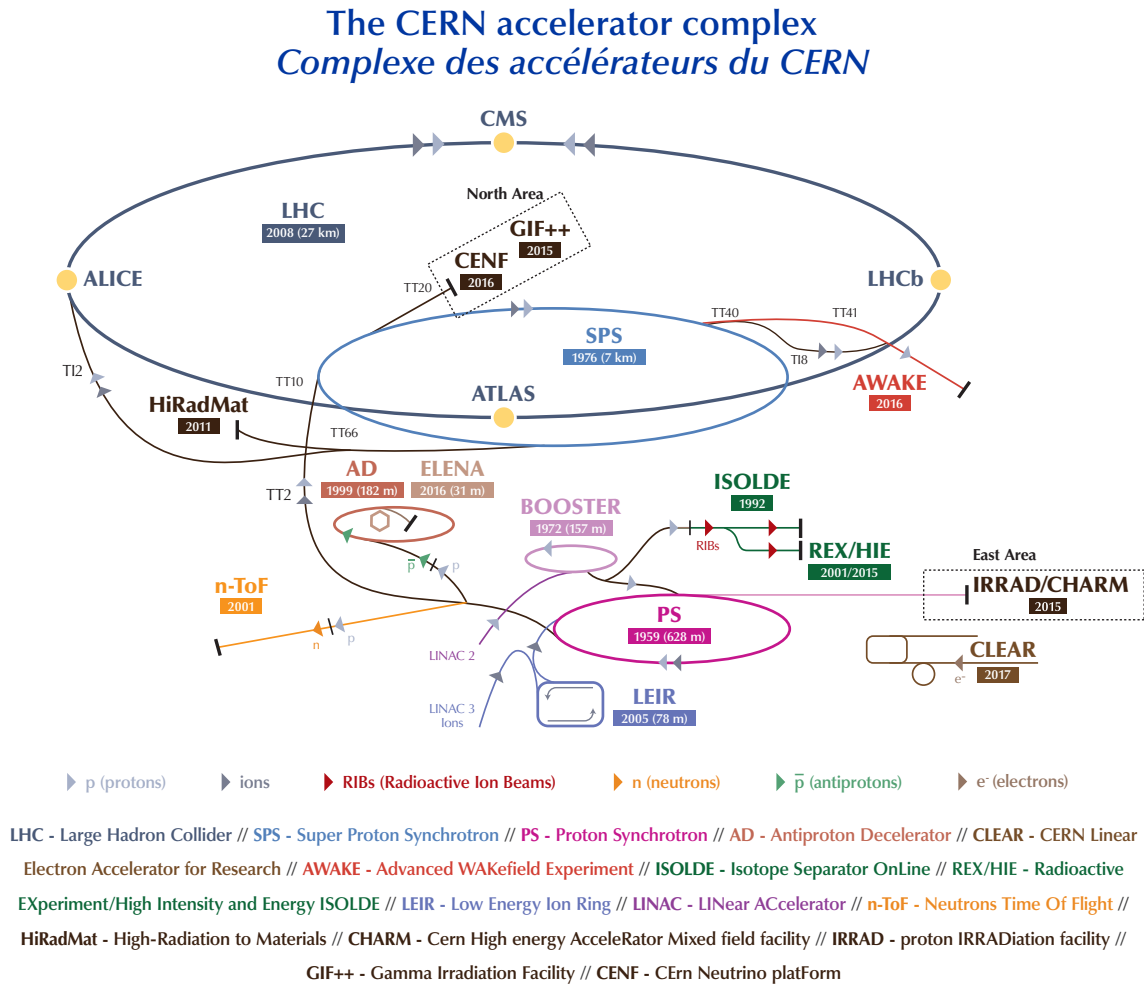


Figure 4.1: Schematic view of the CERN accelerator complex [44].

forming bunches of approximately 10^{11} protons, which are then gradually accelerated. These protons are passed through a sequence of accelerators, increasing in size and energy, before being injected into the LHC (the main accelerator) where they reach an energy of 6.5 TeV per bunch during Run 2 [46].

The LHC ring is equipped with four collision points, hosting the ATLAS (A Toroidal LHC Apparatus) [7], CMS (Compact Muon Solenoid) [8], LHCb (Large Hadron Collider beauty) [47], and ALICE (A Large Ion Collider Experiment) [48] experiments. A schematic of the LHC and its chain of secondary accelerators, along with the locations of the main experiments, is shown in Figure 4.1.

4.2 Performance and Operation During Runs 1–3

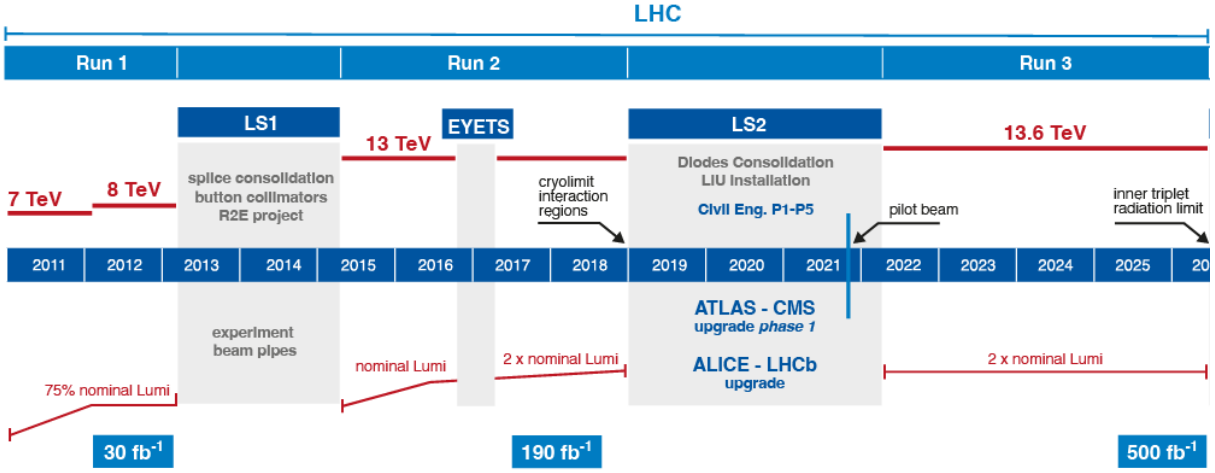


Figure 4.2: LHC plan for the Run 1 to Run 3 (last updated in January 2025). Taken from Ref. [49].

The LHC was constructed in the same tunnel that had previously housed the LEP (Large Electron-Positron Collider) experiment, and has undergone several running periods, punctuated by long shutdowns for upgrades (*cf.* Figure 4.2):

- **Run 1 (2011–2012):** Delivered pp collisions at $\sqrt{s} = 7$ and 8 TeV, accumulating a total of about 25 fb^{-1} .
- **Run 2 (2015–2018):** Operated at $\sqrt{s} = 13$ TeV, with 139 fb^{-1} recorded by ATLAS after data-quality filtering [45, 46].
- **Run 3 (2022–2025, ongoing):** Operates at 13.6 TeV with a target integrated luminosity exceeding 170 fb^{-1} [39].

Key upgrades between runs included higher beam intensities, improved injector performance, and a transition from Linac2 to Linac4 [46].

These runs have enabled the LHC experiments to conduct increasingly sensitive measurements of Higgs boson properties and probe for rare and exotic processes.

4.3 Luminosity and Pile-Up Conditions

One of the most important characteristics of a collider is its luminosity, which quantifies the ability of the machine to produce interactions between the two colliding beams. In scattering theory and accelerator physics, the luminosity \mathcal{L} is defined as the ratio of the number of interactions per unit time to the cross-section of the process under consideration:

$$\mathcal{L} = \frac{1}{\sigma} \frac{dN}{dt}, \quad (4.1)$$

where dN/dt is the interaction rate and σ is the corresponding interaction cross-section. Luminosity is typically expressed in units of $\text{cm}^{-2} \text{s}^{-1}$ or, equivalently,

$\text{fb}^{-1} \text{s}^{-1}$, with $1 \text{ fb}^{-1} = 10^{39} \text{ cm}^{-2}$ (i.e using femtobarn, a sub-unit of barn).

In the context of the LHC, the *instantaneous luminosity* can be related directly to beam parameters. For two colliding proton bunches, the expression reads:

$$\mathcal{L} = \frac{f_{\text{rev}} n_b N_1 N_2}{4\pi\sigma_x\sigma_y} F, \quad (4.2)$$

where f_{rev} is the revolution frequency of the beams in the LHC ring, n_b is the number of bunches per beam, $N_{1,2}$ are the numbers of protons per bunch in each beam, $\sigma_{x,y}$ denote the transverse beam sizes, and F is a geometric reduction factor that accounts for the finite crossing angle of the bunches [46].

The *integrated luminosity* is defined as the time integral of the *instantaneous luminosity* over the data-taking period:

$$\mathcal{L}_{\text{int}} = \int \mathcal{L}(t) dt, \quad (4.3)$$

and is the key figure of merit for comparing datasets collected over long periods. It effectively measures the total number of potential collisions delivered by the accelerator and is therefore the standard metric used to express the physics reach of an experiment.

The delivered Luminosity \mathcal{L}_{int} (over time) at LHC using proton-proton data only is given in Figure 4.3.

During Run 2 the LHC delivered up to 2 808 bunches per beam, with a bunch spacing of 25 ns, and each bunch containing around 1.2×10^{11} protons. This configuration led to an average pile-up $\langle\mu\rangle$ (*i.e.* the mean number of inelastic proton-proton interactions per bunch crossing) reaching 37.8 in 2017 and 33.7 over the entire run [46]. The mean number of interactions per bunch crossing $\langle\mu\rangle$ for collisions recorded between 2011 and 2022 is represented in Figure 4.4.

Such conditions are particularly challenging for the reconstruction of photons and b -jets, which are crucial in analyses of the $b\bar{b}\gamma\gamma$ final state.

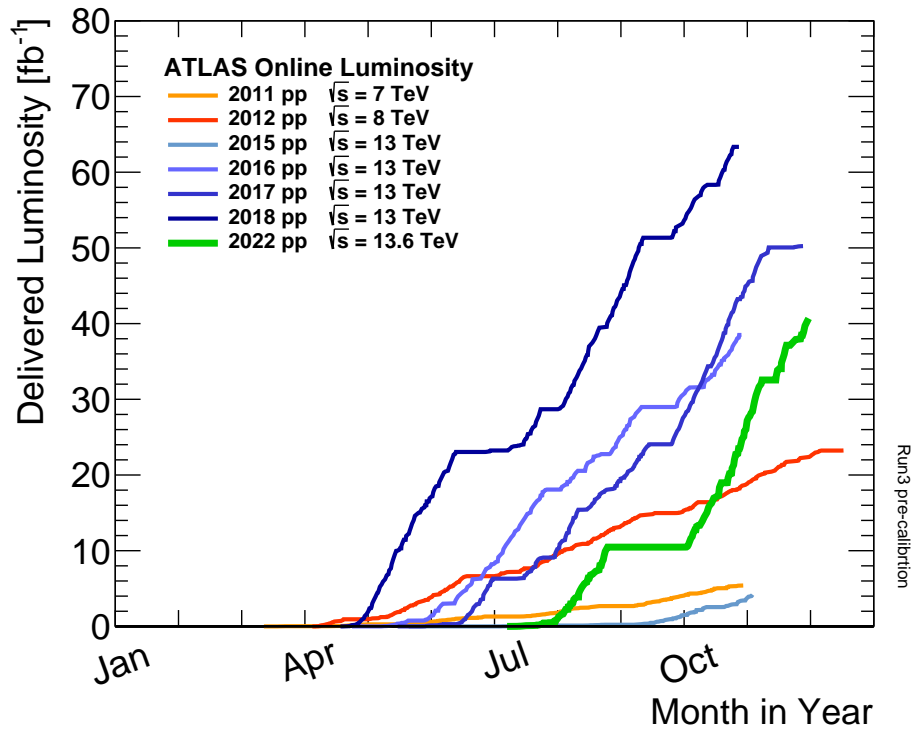


Figure 4.3: Delivered Luminosity \mathcal{L}_{int} versus time for 2011-2022 using proton-proton data only. Taken from Ref. [50].

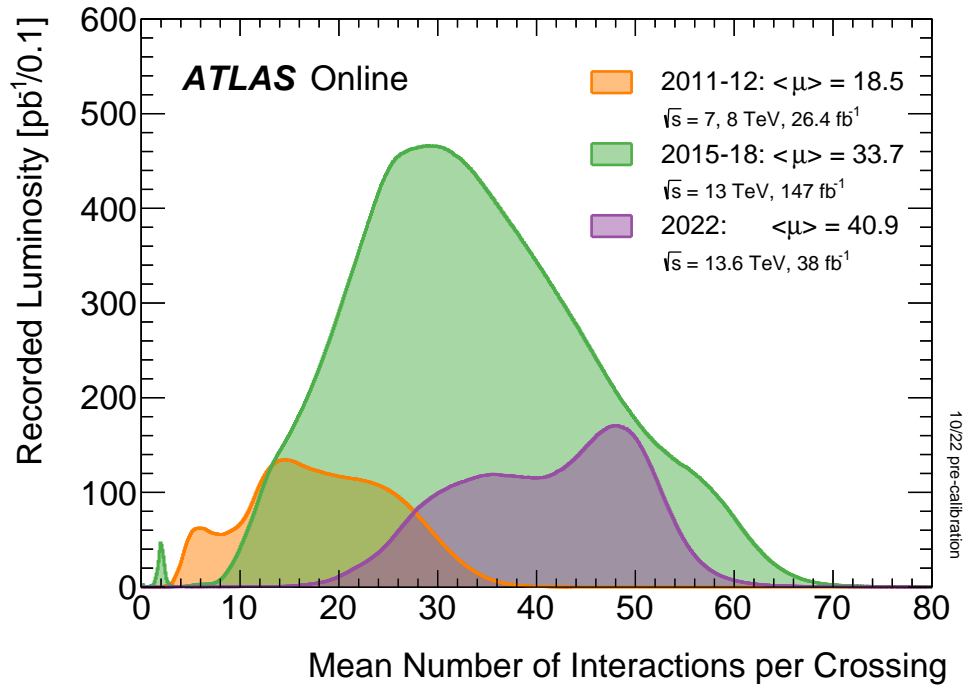


Figure 4.4: Mean number of interactions per bunch crossing $\langle\mu\rangle$ for collisions recorded between 2011 and 2022, taken from Ref. [50]. The non-gaussian shape of all distributions is due to the luminosity leveling of the machine.

4.4 Physics Output Before HL-LHC

The LHC has enabled a transformative era of particle physics. Among its most significant achievements is the discovery of the Higgs boson (in 2012), confirming the last missing cornerstone of the Standard Model. The study of rare processes such as $t\bar{t}H$ production, $H \rightarrow \mu^+\mu^-$, and $H \rightarrow Z\gamma$ decays further confirmed the Higgs sector's consistency with the Standard Model expectations [39].

Beyond the single Higgs sector, the search for Higgs boson pair production (central to probing the shape of the scalar potential and the trilinear self-coupling λ_{3H}) has become one of the key focuses of particle physics. Dedicated analyses in multiple final states, including $b\bar{b}b\bar{b}$, $b\bar{b}\tau^+\tau^-$, and $b\bar{b}\gamma\gamma$, have been performed by ATLAS and will be discussed in section 6.2.

While no significant excess over the Standard Model prediction has been observed so far, these analyses have placed the most stringent constraints to date on di-Higgs production cross-sections and the allowed range of the ratio κ_λ .

The accumulated experience from these LHC campaigns, both in data analysis techniques and in understanding detector performance, has set the stage for the High-Luminosity LHC which will be discussed later on in Chapter 7.

Chapter 5

The ATLAS Detector and Physics Object Reconstruction Performance

Precision physics at the energy frontier relies not only on energy and luminosity reach of the collider, but critically on the performance of the detectors. The ATLAS experiment [7] is one of two general-purpose detectors at the LHC (along with CMS [8]), and is designed to study a wide range of physics.

This chapter presents the architecture of the ATLAS detector and highlights its performance during LHC Runs 1 to 3, with particular focus on components and observables relevant to the reconstruction of photons and b -jets, central to the $HH \rightarrow b\bar{b}\gamma\gamma$ final state analysis that is at the center of this manuscript.

5.1 General Overview and Design Principles

The ATLAS detector is a forward-backward symmetric, cylindrical apparatus with nearly 4π coverage in solid angle. It consists of several concentric subsystems: an inner tracking detector (ID) within a 2 T solenoidal magnet; electromagnetic and hadronic calorimeters; and a muon spectrometer with air-core toroidal magnets (*cf.* Fig. 5.1).

As illustrated in Figure 5.2, each subdetector is optimized for different physics objects [46]:

- **Inner tracking detector** is the innermost system surrounding the interaction point. It reconstructs charged particle trajectories. A solenoidal magnetic field bends the tracks, allowing a measurement of the transverse momentum p_T and charge identification.
- **Calorimeter system** is a two-stage subdetector that measures particle energies with high precision. The electromagnetic calorimeter is deep enough to fully contain electron and photon showers, while hadrons begin showering there but release most of their energy in the subsequent hadronic calorimeter.

- **Muon spectrometer** is the outermost detector, tasked with reconstructing particles that traverse the calorimeters without significant energy loss, namely the muons.
- **Online event-selection (trigger) system** is a procedure designed to refine the data rate to a level compatible with recording and offline analysis. It must retain high efficiency for the broad spectrum of physics signatures under investigation while respecting bandwidth and computing constraints. At design luminosity, the LHC delivers proton-proton collisions at a rate of 40 MHz.

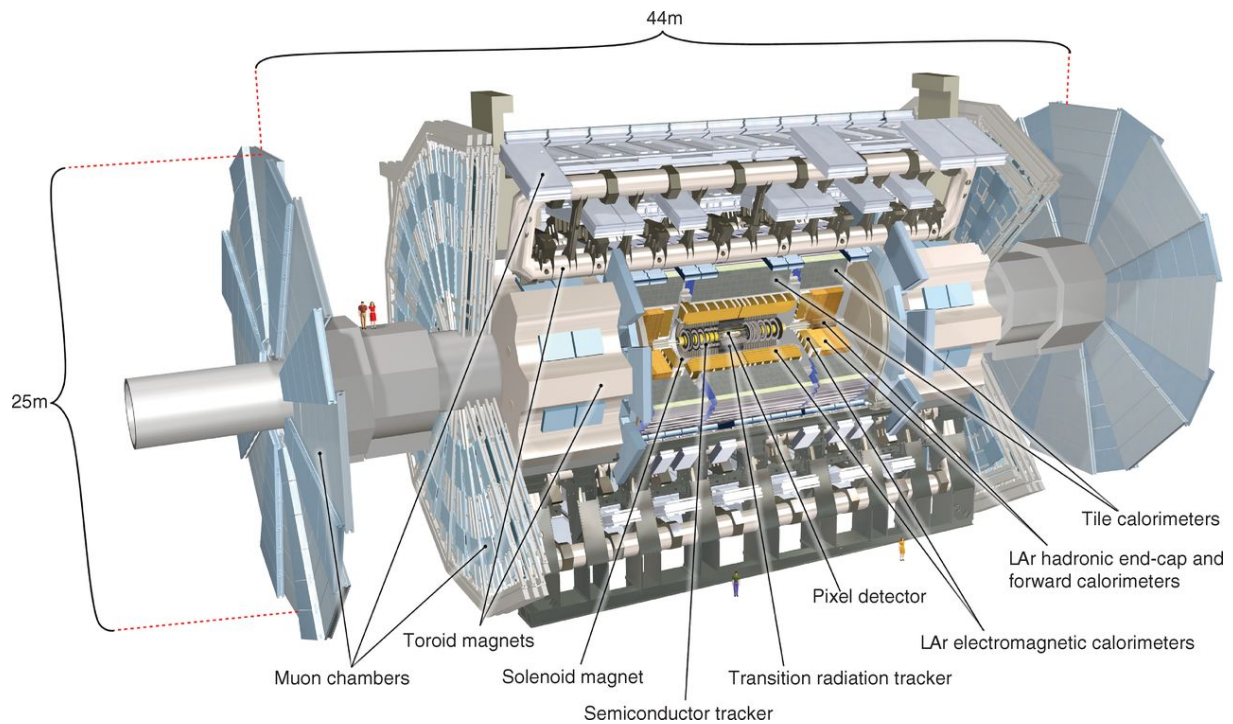


Figure 5.1: Schematic view of the ATLAS detector, from Ref. [7].

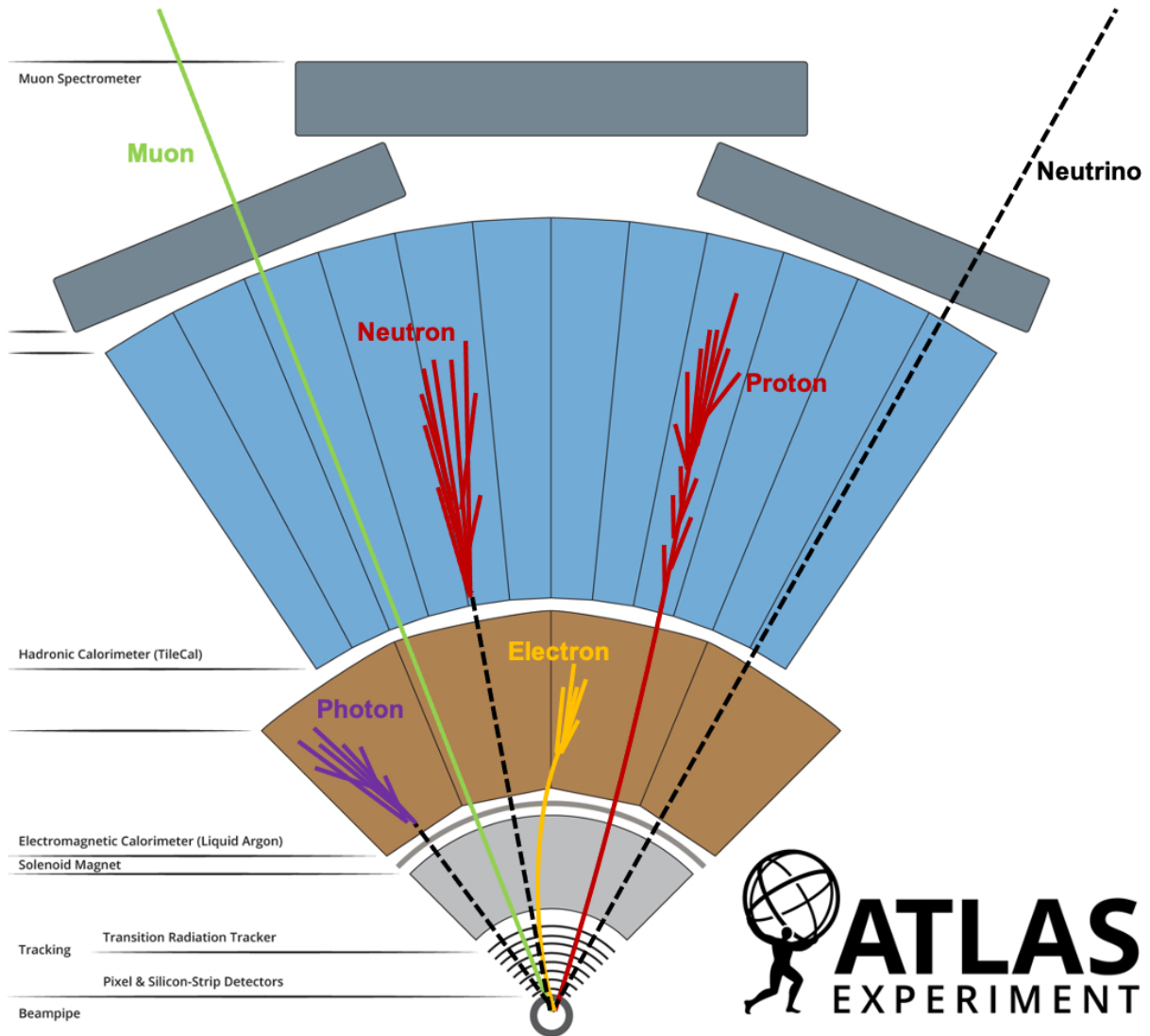


Figure 5.2: Schematic view of interactions of particles with the ATLAS subdetectors, from Ref. [51].

5.2 Coordinate System and Global Layout

The ATLAS Collaboration uses a right-handed coordinate system with the origin at the nominal interaction point. The z -axis is defined along the beam pipe, the x -axis points from the interaction point toward the center of the LHC ring, and the y -axis points upward (*cf.* Figure 5.3).

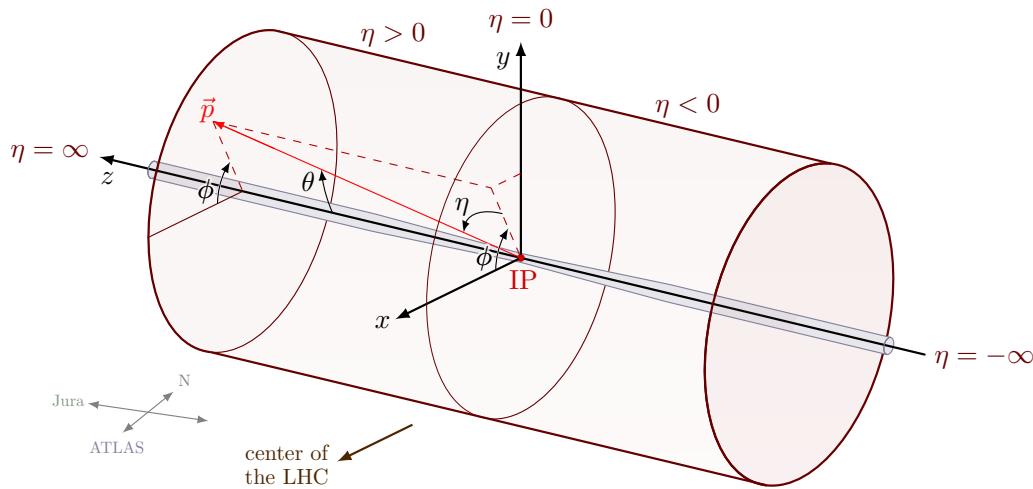


Figure 5.3: Schematic description of the coordinate system, taken from Ref. [52].

This figure has been created for the CMS experiment, but the coordinate system used in ATLAS is the exact same (except that the x -axis points toward CMS).

The azimuthal angle ϕ is measured in the x - y plane, and the polar angle θ is measured from the z -axis (where $\theta = 0$ is parallel to the beampipe).

It is more common to define and use the *pseudorapidity* η as:

$$\eta = -\ln \tan(\theta/2) \quad (5.1)$$

as well as the angular distance $\Delta R = \sqrt{(\Delta\eta)^2 + (\Delta\phi)^2}$ which is used to describe the angular separation between reconstructed objects [45].

5.3 The Inner Detector

The Inner Detector (ID) [53] is used to identify the precise interaction point and trajectory of charged particles.

The ID is segmented into barrel and end-cap sections along the beam axis. The barrel extends 1.6 m, covering $|\eta| < 1$, and the end-cap sections cover the remainder of the 7 m length. With this setup, the ID provides precision tracking up to $|\eta| = 2.5$. It is composed of three subsystems, the Pixel Detector, the Semiconductor Tracker (SCT, a silicon strip detector), and the Transition Radiation Tracker (TRT).

The Insertable B-Layer (IBL), added before Run 2, significantly improved impact parameter resolution and flavor tagging efficiency.

5.4 The Electromagnetic Calorimeter: Photon Identification and Resolution

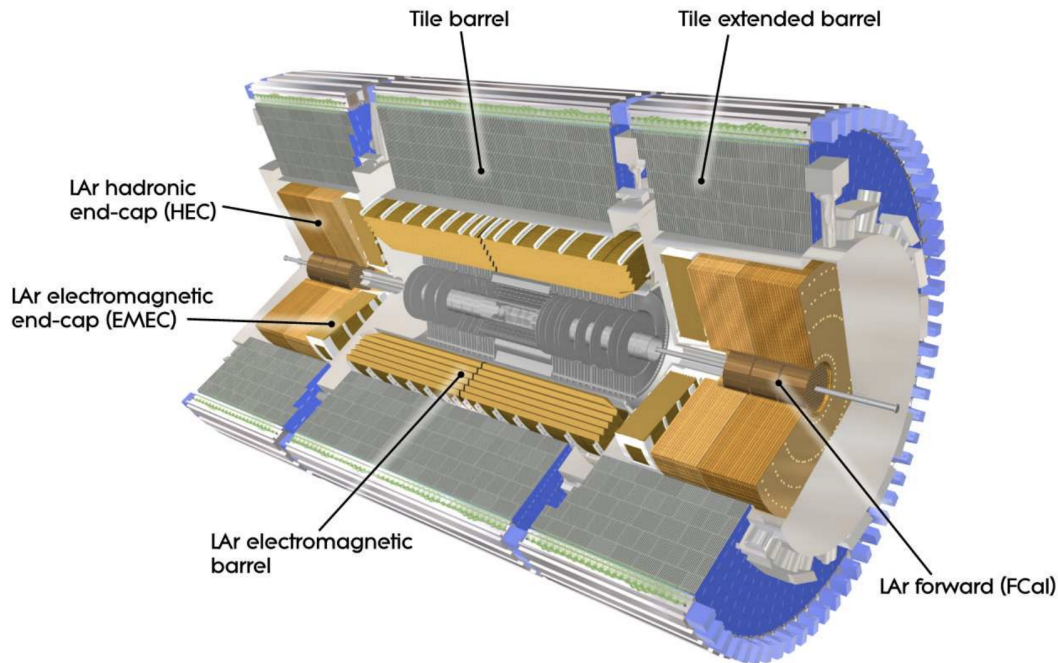


Figure 5.4: Cut-away view of the ATLAS calorimeter system. Taken from Ref. [7]

The calorimeter system in ATLAS measures the energy of particles absorbed by the material. ATLAS employs calorimeters targeting different types of particle showering: the electromagnetic calorimeter (ECAL) targets EM showers from photons and electrons, while the hadronic Tile calorimeter targets hadronic showers. The ECAL lies outside the ID and central solenoid, and the hadronic calorimeter is outside of the ECAL. A schematic of the calorimeter can be found in Figure 5.4, and one of a barrel module of the ECAL in Figure 5.5.

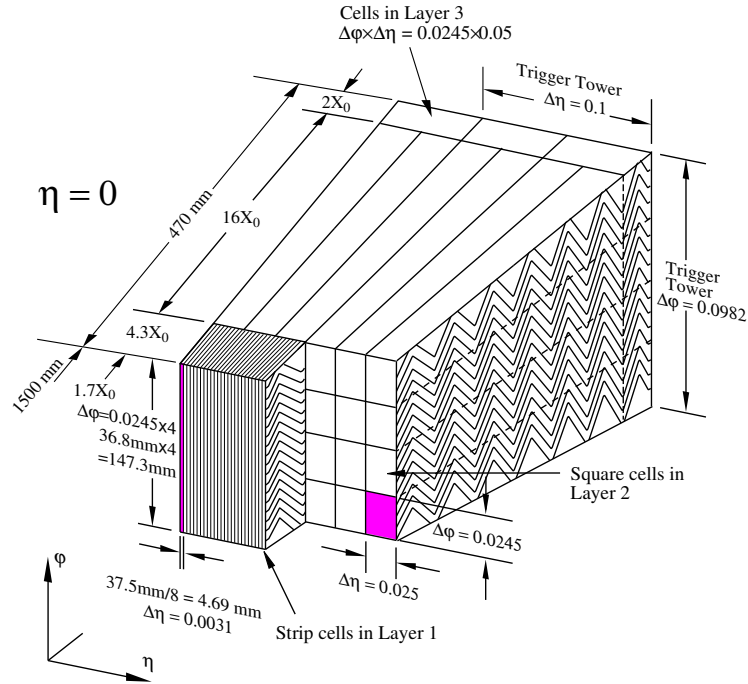


Figure 5.5: Schematic view of a barrel module of the ATLAS electromagnetic calorimeter. Taken from Ref. [7].

The ATLAS LAr ECAL is a lead-liquid argon (LAr) sampling calorimeter with accordion-shaped electrodes, covering $|\eta| < 3.2$ as can be seen in Figure 5.6.

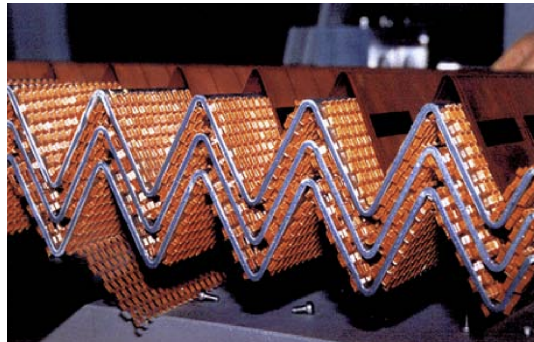


Figure 5.6: Pictures of the accordion-shaped electrodes of the ATLAS ECAL [54].

It features high granularity in η and three longitudinal layers, optimized for shower shape identification and position resolution. The ECAL achieves an energy resolution of

$$\frac{\sigma_E}{E} = \frac{10\%}{\sqrt{E \text{ (GeV)}}} + 0.7\% \quad (5.2)$$

in the barrel and end-cap regions [46].

Photon identification relies on a combination of calorimeter-based variables and leakage into the hadronic calorimeter.

The Inner Detector (ID) tracking plays a key role in distinguishing photons from electrons by rejecting candidates associated with a well-reconstructed track, and

by identifying early photon conversions (i.e the detection of electron–positron track pairs originating the interaction of the photon with the ID material).

5.5 The Hadronic Calorimeter: Jet and b -Jet Reconstruction

Hadrons naturally tend to produce additional hadronic particles when interacting with dense material in a phenomenon known as a hadronic shower, and continue until the energy of the decay products is small enough to be halted by ionization energy loss or absorbed in a nuclear process.

The hadronic calorimeter consists of two main subsystems: the Tile calorimeter (iron/scintillator, $|\eta| < 1.7$) and the LAr hadronic end-cap and forward calorimeters (LAr/Cu or LAr/W, $1.5 < |\eta| < 4.9$).

The combined system offers an energy resolution of

$$\frac{\sigma_E}{E} = \frac{50\%}{\sqrt{E \text{ (GeV)}}} + 3\% \quad (5.3)$$

for central jets, degrading at forward η (*cf.* Ref. [46]).

The identification of b -jet, or b -tagging, combines inner detector tracking with secondary vertex reconstruction. The high-granularity ID and presence of the IBL allow identification of displaced vertices with high resolution. For a 70% b -jet efficiency working point, the light-flavor rejection exceeds a factor of 300 [55].

5.6 Muon Spectrometer

The ATLAS Muon Spectrometer (MS) is the outermost layer of the ATLAS detector, aiming to track muons via independent triggering (within $|\eta| < 2.7$).

The MS uses Monitored Drift Tubes (MDTs) and Cathode Strip Chambers (CSCs) for precision tracking, and Resistive Plate Chambers (RPCs) and Thin Gap Chambers (TGCs) for triggering. The spatial resolution of MDTs reaches $35 \mu\text{m}$ in the z direction, while CSCs provide $40 \mu\text{m}$ in R [46].

5.7 Trigger and Data Acquisition System (DAQ)

Dataflow and storage are a major challenge for ATLAS. Bunches of protons interact every 25 ns, a rate of 40 MHz. On average, a raw event contains about 1.6 MB [56]. Recording all of those interactions would not be possible, nor desirable since they are dominated by soft collisions processes which do not yield interesting physics. To isolate events which are desirable to record, ATLAS utilizes a two-stage trigger system [57] that evolved significantly between Runs 1 and 3:

The Level-1 (L1) trigger uses coarse-granularity calorimeter and muon information with a latency of $2.5\ \mu\text{s}$, operating at rates of up to 100 kHz in Run 3.

The second stage of the trigger is software-based. Events passing L1 are processed by the High-Level Trigger (HLT), implemented in software and running on a scalable computing farm, which refines decisions using full detector granularity. The final output rate is reduced to 1–2 kHz [46].

The Data Acquisition System (DAQ) integrates readout, event building, and storage. Its performance and flexibility are crucial for adapting to increasing luminosity and pile-up conditions.

5.8 Object reconstruction and performance

The final state particles for our analysis are $b\bar{b}\gamma\gamma$ (i.e two different pairs of objects: b-jets and photons). We will focus this section on the ATLAS detector’s ability to reconstruct them, and its performance.

5.8.1 Photons γ

Reconstruction chain. Photon candidates start as clusters in the electromagnetic calorimeter (ECAL) with $E_T > 400\ \text{MeV}$. Each cluster is extrapolated to the Inner Detector (ID). If no ID track is found the object is labelled *unconverted*, and one or two tracks forming a vertex within $r < 80\ \text{cm}$ mark it as *converted* [58]. Run-2 “region-of-interest” tracking and improved Transition Radiation Tracker (TRT) pattern recognition lift the true-conversion efficiency above 70 % for $E_T > 20\ \text{GeV}$ while keeping fake conversions below 9 % even at $\langle\mu\rangle \simeq 40$ [58].

Energy calibration and resolution. Raw ECAL energies are corrected for upstream material as well as lateral and longitudinal leakage. A multivariate regression, re-trained after the Insertable B-Layer (IBL) upgrade, then refines the response for *unconverted* and *converted* photons separately [58]. The resulting resolution satisfies Eq. (5.2), narrowing the $m_{\gamma\gamma}$ peak that underpins Di-Higgs analyses.

Efficiency measurements and scale factors. Three data-driven methods anchor the Run-2 photon identification efficiency: radiative $Z \rightarrow \ell\ell\gamma$ decays, an electron-extrapolation from $Z \rightarrow e^+e^-$, and an inclusive matrix method (not to be confused with Matrix Element Methods, MEM) that extends to $E_T \approx 1.5\ \text{TeV}$. The techniques agree within 1 % in the regions of energy where they overlap [58].

Figure 5.7 (from Ref. [59]) shows that the tight-ID efficiency rises from 55 % at $E_T = 10\ \text{GeV}$ to 98 % above 250 GeV. Converted photons trail by only a few percent. Data/MC scale factors remain within 1 % of unity for $E_T > 40\ \text{GeV}$ and within 5 % below.

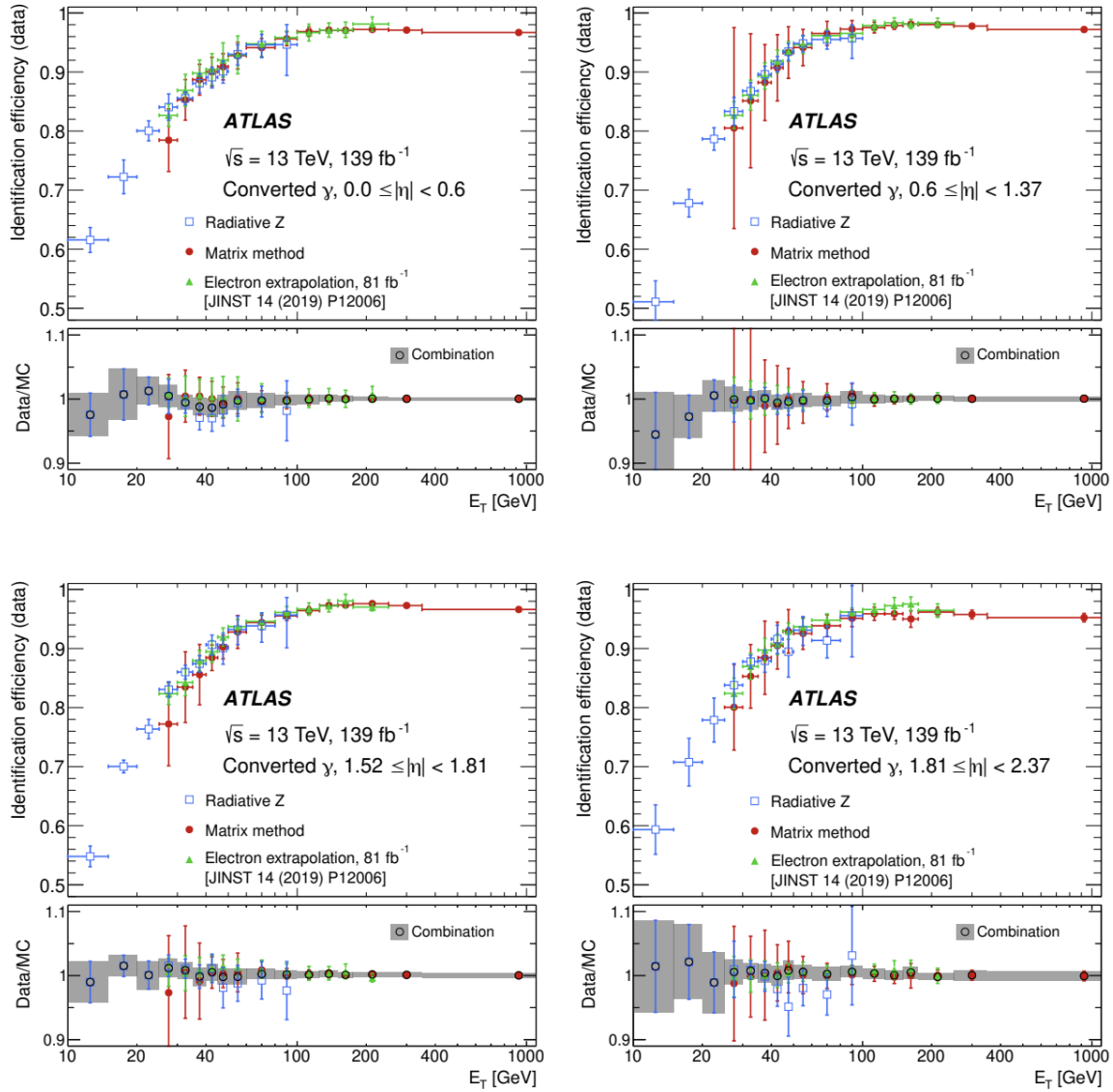


Figure 5.7: Tight-ID photon efficiency and data/MC scale factors versus E_T in four $|\eta|$ regions, Taken from Ref. [59].

5.8.2 Jets and b -Tagging

Jet reconstruction and energy scale. The hadronization of a b -quark creates a collimated stream of particles, a *jet*, made of several hadrons enclosed in a cone. Reconstructing a jet at particle level would require identifying each individual hadron that constitutes it and grouping them into a single object. This is not experimental possible as the calorimeter only measures the total energy from the collection of particles inside the jet.

Hadrons are reconstructed using the track candidates reconstructed in the tracker and matched to compatible topo-clusters. A jet reconstruction algorithm named the anti- k_t algorithm [60], is then used to combine particles composing a jet sequentially. To prevent the jets to be affected by noise cells of the calorimeters, a quality selection requirement (called *LooseBad*) removes the calorimeter noise while the *Jet-Vertex*

Tagger (JVT) rejects pile-up jets with $> 90\%$ efficiency for $p_T < 60$ GeV, falling smoothly to 60% at higher pile-up. The Run-2 jet-energy scale (JES) is known to 1% for $30 < p_T < 1$ TeV, rising to 4% below 30 GeV [61].

***b*-tagging algorithms.** The current ATLAS flavor tagger is based on a deep-learning neural network named DL1R, which merges four low-level taggers (IP2D, IP3D, SV1, JETFITTER) [62]. The algorithm assigns every jet a *b*-tagging score w . A threshold on w sets the *working point* (WP) (with typical choices 60% , 70% , 77% and 85%) fix the accepted *b*-jet efficiency at those values and thereby determine the light- and charm-jet rejection.

For instance the 77% working point delivers a light-jet rejection of ≈ 170 , meaning that only one out of about 170 light-flavour jets (u, d, s -quark or gluon jets) is misidentified as a *b*-jet. For the charm-jet, the rejection is of ~ 5 in simulated $t\bar{t}$ events. As for the photons, more than two *b*-jets can be reconstructed in a single event. We defined the *b*-jets candidates considered for this analysis as the two ones having the highest *b*-tagging score.

***b*-jets calibration.** To improve the mass resolution of the $b\bar{b}$ system, calibration corrections are applied. For *b*-jets an additional *B-calibration* adds the four-momentum of any muon inside the jet and corrects for the undetected neutrino, improving the $m_{b\bar{b}}$ resolution by $\sim 10\%$ (*cf.* Figure 5.8).

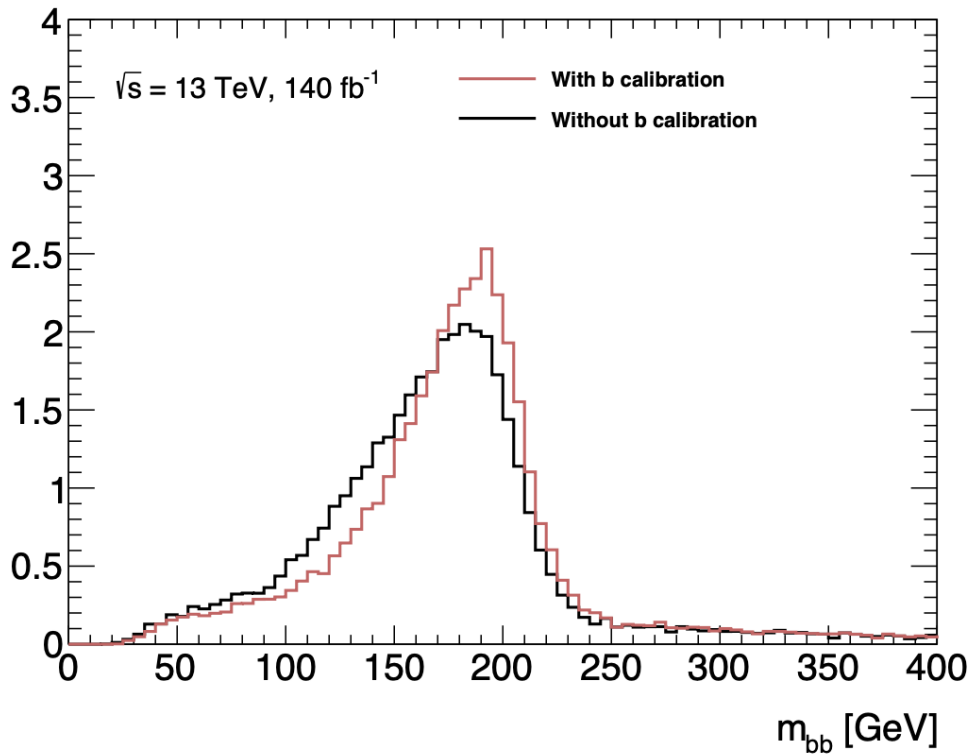


Figure 5.8: Reconstructed mass $m_{b\bar{b}}$ GeV with and without B-calibration. Taken from Ref. [63]

5.9 Summary: Performance Milestones and Impact on LHC Analyses

Over the first three LHC runs, the ATLAS detector has met or exceeded all design goals.

The Insertable B-Layer sharpened track-impact and secondary-vertex resolution; the liquid-argon calorimeter maintained a photon energy resolution of 1% (at $E_\gamma \gtrsim 50$ GeV) and deep-learning flavor taggers such as DL1R provides strong light-jet rejection at the working points used in Higgs analyses.

Parallel continuous trigger upgrades kept pace with the rising luminosity, while preserving low thresholds for photons and b -jets.

These advances provide the experimental foundation for precision Higgs studies. In particular with the sharp $m_{\gamma\gamma}$ peak, the 10 %-improved m_{bb} resolution from b -jet calibration, and the percent-level photon and b -tag scale factors which combine to maximise the sensitivity of the $HH \rightarrow b\bar{b}\gamma\gamma$ channel to the trilinear Higgs self-coupling.

Chapter 6

Experimental Access to the Higgs Self-Coupling

Following the theoretical overview of the Higgs sector presented in Chapter 3, this chapter focuses on the experimental approach to probing the trilinear Higgs boson self-coupling λ_{3H} with a particular emphasis on di-Higgs production at the LHC.

6.1 Current Constraints and Effective Parameterization

Experimental results are typically interpreted in terms of a scale factor:

$$\kappa_\lambda = \frac{\lambda_{3H}}{\lambda_{3H}^{\text{SM}}}, \quad (6.1)$$

which parameterizes deviations from the SM expectation. A value of $\kappa_\lambda = 1$ corresponds to the SM.

The ATLAS and CMS collaborations have conducted a common combination of all major di-Higgs searches using the full Run 2 dataset (with the inclusion of the final states $b\bar{b}b\bar{b}$, $b\bar{b}\tau^+\tau^-$, $b\bar{b}\gamma\gamma$, and multileptons).

For the ATLAS Collaboration, the observed (expected) 95% CL constraint on the di-Higgs signal strength $\mu_{HH} = \frac{\sigma_{HH}}{\sigma_{HH}^{\text{SM}}}$ is 2.9 (2.4), which translates to a constraint on the self-coupling [64]:

$$-1.2 < \kappa_\lambda < 7.2 \quad (95\% \text{ CL}). \quad (6.2)$$

The extraction of the trilinear Higgs self-coupling (or equivalently its deviation from the Standard Model κ_λ) relies on the strong dependence of the di-Higgs production cross-section on κ_λ (*cf.* Figure 6.1).

This is the basis of so-called *yield-based* or *event-counting* analyses, where the total observed di-Higgs event yield is compared to the predicted Standard Model rate as a function of κ_λ (with a detailed discussion about this point in Section 15.5.2).

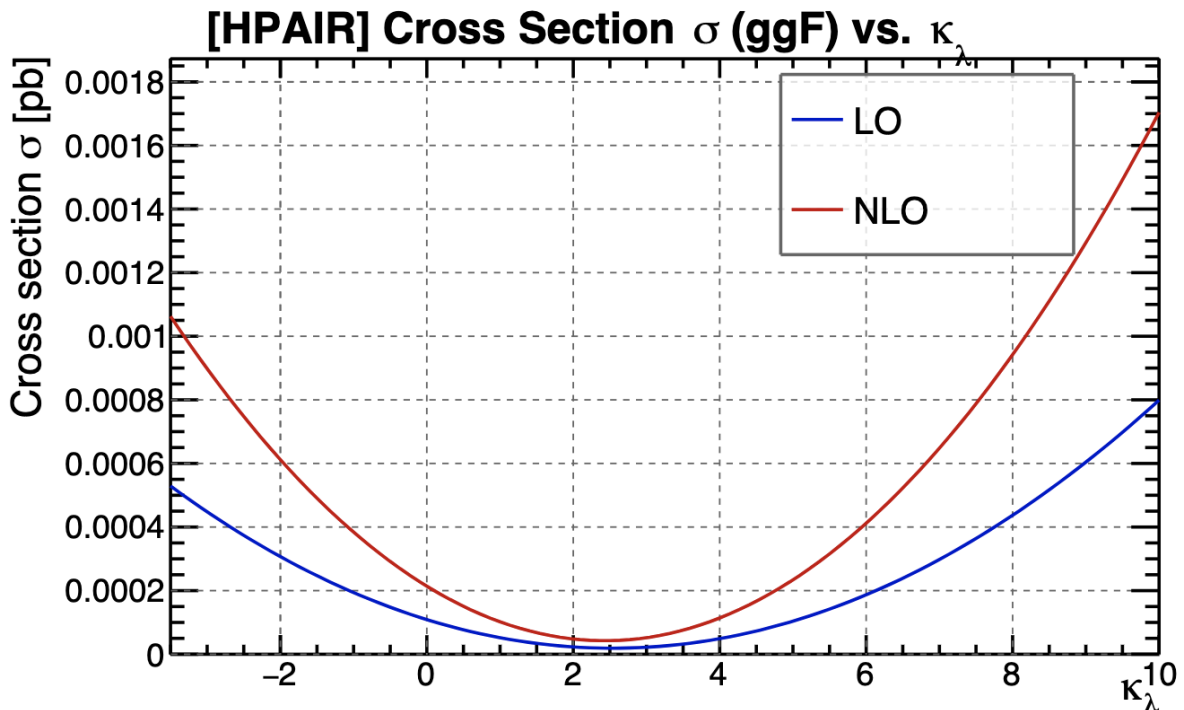


Figure 6.1: Predicted total cross-section for Higgs boson pair production via gluon-gluon fusion (ggF) as a function of the Higgs self-coupling modifier κ_λ , that we have computed using the HPAIR values at both Leading Order and Next-to-Leading Order in QCD.

The κ_λ range spans from -3.5 to 10.0 .

The LO prediction is shown in **blue**, and the NLO prediction in **red**.

As a matter of comparison, we also include the results found by CMS: The observed (expected) 95% CL constraint on the di-Higgs signal strength μ_{HH} is 3.5 (2.5), which translates to a constraint on the self-coupling [65]:

$$-1.4 < \kappa_\lambda < 7.0 \quad (95\% \text{ CL}). \quad (6.3)$$

In many analyses, an effective field theory (EFT) (or Higgs effective field theory HEFT) framework is used to describe possible new physics contributions. These include modifications to the top-Higgs coupling, additional higher-dimensional operators, or contact interactions involving gluons and the Higgs field. Such contributions can significantly alter both the cross-section and the kinematic properties of di-Higgs events.

6.2 Most Recent ATLAS non-resonant $HH \rightarrow b\bar{b}\gamma\gamma$ Analysis [’25]

The search for non-resonant Higgs boson pair production in the $HH \rightarrow b\bar{b}\gamma\gamma$ final state represents one of the most sensitive direct probes of the Higgs boson self-coupling at the LHC.

This final state combines the large branching ratio of $H \rightarrow b\bar{b}$ with the excellent

mass resolution of $H \rightarrow \gamma\gamma$, leading to a high signal-to-background discriminating power despite the small cross-section expected in the Standard Model.

The most recent analysis, presented in Ref. [66], uses both the Run 2 and beginning of Run 3 data collected by the ATLAS detector (which correspond to data taking between 2015 and 2024). The first sample is at $\sqrt{s} = 13$ TeV, corresponding to an integrated luminosity of 140 fb^{-1} . The second is at $\sqrt{s} = 13.6$ TeV, corresponding to an integrated luminosity of 168 fb^{-1} . This work constitutes the most up-to-date ATLAS result in this channel and defines the current benchmark for experimental sensitivity to κ_λ using the $b\bar{b}\gamma\gamma$ final state.

This analysis is exactly the subject of this thesis, which focuses on improving sensitivity to κ_λ in the $gg \rightarrow HH$ to $b\bar{b}\gamma\gamma$ channel, but the methods used are very different.

For this analysis events are selected by requiring two isolated photons and at least two jets, with at least one of the jets passing a b -tagging requirement based on multivariate classifiers. The two leading photons passing the selection are required to have an invariant mass $m_{\gamma\gamma}$ within the range $[105, 160]$ GeV, and transverse momenta greater than 35% and 25% of $m_{\gamma\gamma}$, respectively.

The signal region is defined by $120 < m_{\gamma\gamma} < 130$ GeV, while the sidebands correspond to the remaining entries in the interval $m_{\gamma\gamma} \in [105, 160]$ GeV outside the signal region.

Additional kinematic selections are applied to improve background suppression, including cuts on the transverse momenta of the diphoton and dijet systems, as well as their angular separations $\Delta R(b, b)$ and $\Delta R(\gamma, \gamma)$.

The analysis indicates that this pre-selection choice helps to suppress the background while keeping good signal efficiency.

Additionally a new method called the Kinematic Fit (KF) has been developed to improve the resolution of $m_{b\bar{b}}$ by balancing the transverse momentum with the diphoton system, and the invariant mass of the system with two photons and two bjets ($m_{\gamma\gamma b\bar{b}}$) in a two-step process. This is a new feature, developed for this analysis.

Event discrimination using Boosted Decision Trees [BDTs]

To enhance the sensitivity of the analysis, events are categorized based on the number of b -tagged jets, typically into 1-tag and 2-tag signal-rich regions. Within each category, a multivariate technique based on Boosted Decision Trees (BDTs) is employed to discriminate the non-resonant Higgs boson pair signal from the dominant background processes.

Boosted Decision Trees (BDTs) are machine learning algorithms that build an ensemble of decision trees sequentially. Each tree is trained to correct the classification errors made by the previous ones, giving more weight to misclassified events. The final output is a weighted combination of all trees, resulting in a robust discriminator that captures complex correlations among input variables and improves

signal–background separation.

In high energy physics, BDTs are widely used to exploit correlations among input observables that may not be fully captured by sequential or cut-based approaches.

In this analysis, the BDTs are trained using a set of high-level kinematic variables that are sensitive to the kinematic structure of Higgs boson pair production. The inputs include the invariant masses $m_{b\bar{b}}$ and $m_{\gamma\gamma}$, the transverse momenta $p_T^{b\bar{b}}$ and $p_T^{\gamma\gamma}$ of the reconstructed Higgs candidates, the scalar sum of the jet transverse momenta, and angular variables such as $\Delta R(b, b)$, $\Delta R(\gamma, \gamma)$, and $\Delta\phi(H, H)$ between the Higgs decay products. These variables capture the distinctive topology of the HH signal relative to the smoothly distributed background.

The output of the BDT classifier is used to define signal-rich and background-rich bins.

Validation of the models: Monte Carlo simulations

Monte Carlo (MC) simulations are essential for particle physics analysis. They use probabilistic algorithms to generate artificial high energy collision events based on quantum field theory and phenomenological models (often combined with models of the detector response).

In the context of collider physics, this process begins with the generation of hard-scattering matrix elements, typically computed at leading order (LO) or next-to-leading order (NLO) in perturbative QCD, for a given process. These matrix elements are calculated using generators such as MADGRAPH@NLO, POWHEG–BOX–V2, or MCFM ([clickable links](#)).

Monte Carlo (MC) simulation are used to model signal and background processes, evaluate detector acceptance and selection efficiencies, optimize event selection strategies, train multivariate classifiers, and estimate systematic uncertainties. Its accuracy is continuously validated by comparing key distributions in control regions between simulation and data. MC simulation provides the theoretical templates against which observed data are compared.

The generated partons can be evolved through parton showering, which accounts for soft and collinear QCD radiation using approximations valid in the infrared limit. This is often followed by hadronization, where partons form color-neutral hadrons, and a modeling of the underlying event, which describes soft multiple parton interactions and beam remnants. These steps are performed using general-purpose event generators such as PYTHIA [67], HERWIG [68], or SHERPA [69], which incorporate tunable models constrained by experimental data.

For the analysis discussed here, all signal and background generated samples are passed through a detailed Monte Carlo (MC) simulation of the ATLAS detector response [70] based on Geant4 [71], with the exception of BSM signal samples (*i.e.* where the value of at least one of the coupling modifiers κ_λ , κ_{2V} or κ_{3V} is not set to 1.00).

The non-resonant di-photon samples ($\gamma\gamma$ +jets and $b\bar{b}\gamma\gamma$) on the other hand are interfaced to a fast detector simulation based on a parametric description of the calorimeter response [72]. Additional inelastic pp collisions, defined as pileup, are also included in the simulations.

The Higgs boson mass value of 125 GeV has been used in all simulations, a value consistent with the latest measurements [73].

We have reproduced the summary of all simulated processes used in the analysis in Table.6.1.

Process	Generator	PDF set	Showering	Tune	Accuracy	Order of σ calculation
ggF HH	POWHEG Box v2	PDF4LHC21	PYTHIA 8.309	A14	NLO	NNLO
VBF HH	MADGRAPH5_AMC@NLO	NNPDF3.0NLO	PYTHIA 8.309	A14	LO	N ³ LO
ggF H	NNLOPS	PDF4LHC15nlo (PDF4LHC21)	PYTHIA 8.309	AZNLO (A14)	NNLO	N ³ LO
VBF H	POWHEG Box v2	PDF4LHC15nlo (PDF4LHC21)	PYTHIA 8.309	AZNLO (A14)	NLO	NNLO
WH	POWHEG Box v2	PDF4LHC15nlo (PDF4LHC21)	PYTHIA 8.309	AZNLO (A14)	NLO	NNLO
$qq \rightarrow ZH$	POWHEG Box v2	PDF4LHC15nlo (PDF4LHC21)	PYTHIA 8.309	AZNLO (A14)	NLO	NNLO
$gg \rightarrow ZH$	POWHEG Box v2	PDF4LHC15nlo (PDF4LHC21)	PYTHIA 8.309	A14	LO	NLO
ttH	POWHEG Box v2	NNPDF3.0NLO (PDF4LHC21)	PYTHIA 8.309	A14	NLO	NNLO
bbH	POWHEG Box v2	NNPDF3.0NLO (PDF4LHC21)	PYTHIA 8.309	A14	NLO	NNLO
tHq	MADGRAPH5_AMC@NLO	NNPDF3.0NLO	PYTHIA 8.309	A14	NLO	NLO
tHW	MADGRAPH5_AMC@NLO	NNPDF3.0NLO	PYTHIA 8.309	A14	NLO	NLO
$\gamma\gamma$ +jets	SHERPA 2.2.14	NNPDF3.0NNLO	SHERPA 2.2.14	–	–	–
$\gamma\gamma b\bar{b}$	SHERPA 2.2.14	NNPDF3.0NNLO	SHERPA 2.2.14	–	–	–

Table 6.1: Summary of Monte Carlo (MC) configurations used for signal and background processes.

Reproduced from Ref. [66].

Results on real ATLAS data

The analysis presented in Ref. [66] uses pp collision data collected by the ATLAS experiment during the LHC Run 2 and 3. No significant evidence for di-Higgs production is observed over the expected Standard Model.

The analysis sets a 95% confidence level upper limit on the non-resonant Higgs pair production cross-section at 3.7 (observed) and 2.9 (expected) times the Standard Model prediction.

This translates into a constraint on the Higgs boson self-coupling modifier κ_λ . The parameter space outside the interval $[-1.4, 6.8]$ is excluded at 95% CL (*cf.* Figures 6.2 and 6.3), providing the most stringent limits to date in this final state.

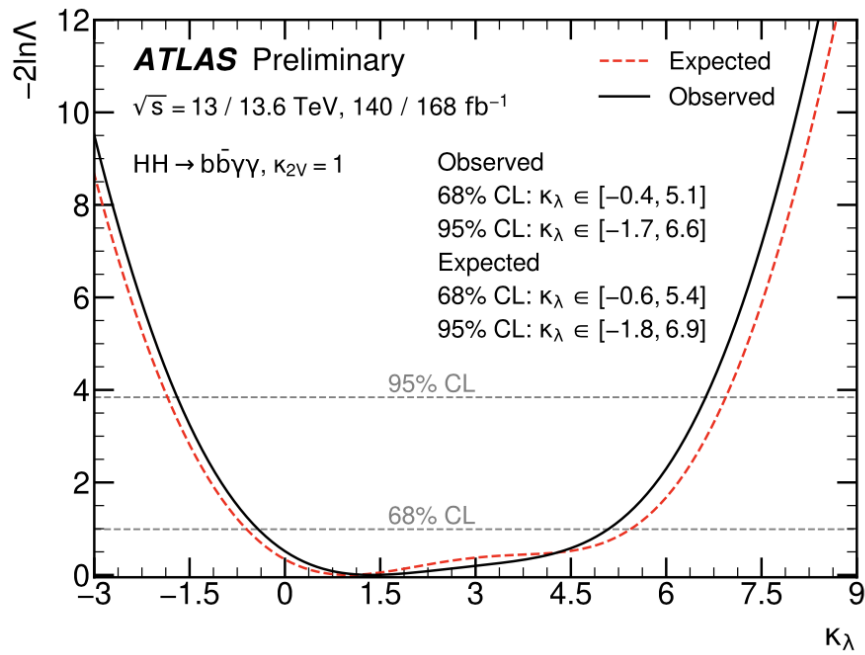


Figure 6.2: Observed and expected profile likelihood scans of κ_λ . All other relevant coupling modifiers are fixed to unity. Taken from Ref. [66].

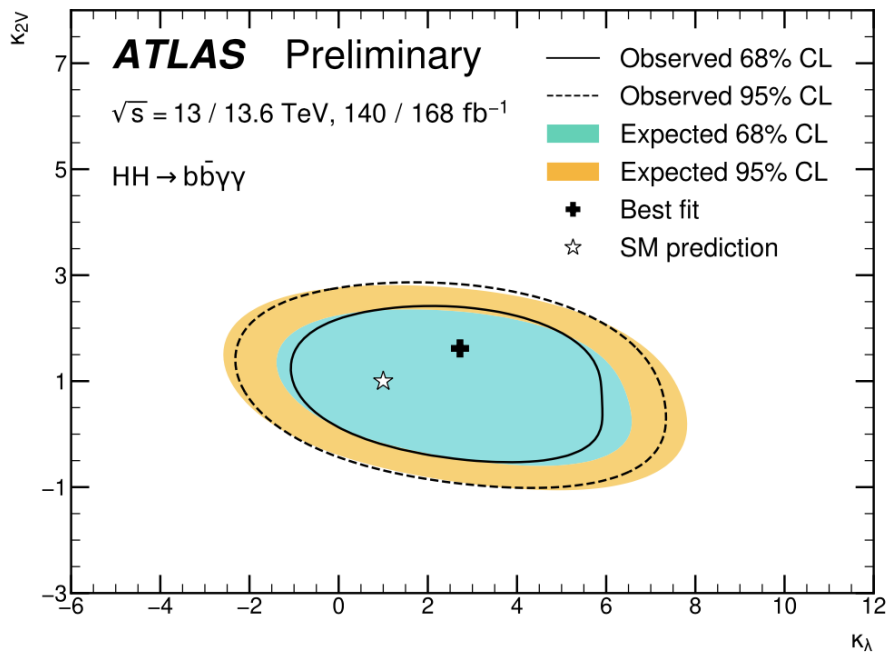


Figure 6.3: Confidence level contours at 68% (solid line) and 95% (dashed line) in the $(\kappa_\lambda, \kappa_{2V})$ parameters space, when all other coupling modifiers are fixed to their SM predictions. The corresponding expected contours are shown by the inner and outershaded regions. The SM prediction is indicated by the star, while the best-fit value is denoted by the cross. Taken from Ref. [66].

Chapter 7

The High-Luminosity LHC and Future Prospects

The High-Luminosity Large Hadron Collider (HL-LHC) is the next big upgrade of the LHC and its detectors, giving us about ten times more collisions to study. This larger dataset will let us look closely at very rare events such as Higgs-boson pair production, test the Standard Model with higher accuracy, and widen the search for new physics.

This chapter provides a concise overview of the High-Luminosity Large Hadron Collider (HL-LHC), without delving into its full technical depth as it lies outside the core scope of this manuscript.

7.1 HL-LHC Machine and Design Goals

The HL-LHC is designed to deliver at least 3000 fb^{-1} (i.e. 3 ab^{-1} , with scenarios going up to 4 ab^{-1}) of data to both ATLAS and CMS by the end of 2040 (*cf.* Figure 7.1).

It will operate at a peak instantaneous luminosity \mathcal{L} of $7.5 \times 10^{34} \text{ cm}^{-2}\text{s}^{-1}$, resulting in an average pile-up of 140 (up to 200) interactions per bunch crossing.

These extreme conditions require significant upgrades to both the accelerator and detectors.

7.2 ATLAS Detector Upgrades

7.2.1 The Inner Tracker (ITk): Capabilities, and Expected Performance

The High-Luminosity upgrade of the LHC (HL-LHC) will present unprecedented experimental challenges.

To meet the tracking demands of this high-occupancy environment (high pile-up discussed earlier), the ATLAS Inner Detector will be entirely replaced by the all-silicon Inner Tracker (ITk), specifically engineered for high granularity, radiation tolerance, and extended pseudorapidity coverage.



Figure 7.1: An expanded version of Fig. 4.2, including additional HL-LHC plan (last update January 2025). Taken from Ref. [49].

Detector architecture The ITk is composed of two main sub-detectors (*cf.* Figure 7.2): the Pixel and the Strip detectors. Both systems are modular and organized into a central barrel and forward end-cap regions.

The Pixel system (in red) is located closest to the beam pipe and is responsible for the most precise spatial measurements. For the first time in an ATLAS tracker, the pixel modules are deliberately tilted so that charged particle tracks strike the sensors as orthogonal as possible.

The Strip system (in blue) surrounds the Pixel layers and contributes to robust pattern recognition and momentum reconstruction over the full acceptance.

Layout and acceptance The final layout adopted for the ITk is the so-called 23-00-03 geometry, as shown in Fig. 7.2, which includes five Pixel barrel layers and four Strip barrel layers, along with corresponding disks in the end-cap regions on both sides of the detector. The coverage extends to $|\eta| < 4$, a significant improvement compared to the current Inner Detector limit of $|\eta| < 2.5$. This extended reach is particularly important for forward physics and precision vertexing in high pile-up.

Material budget. A direct comparison of the number of nuclear interaction lengths as a function of pseudorapidity between the Run 2 detector and the ITk shows substantial reductions, as illustrated in Fig. 7.3.

Tracking performance From a performance standpoint, tracking resolution with ITk is expected to outperform the current Inner Detector. Parameters like track

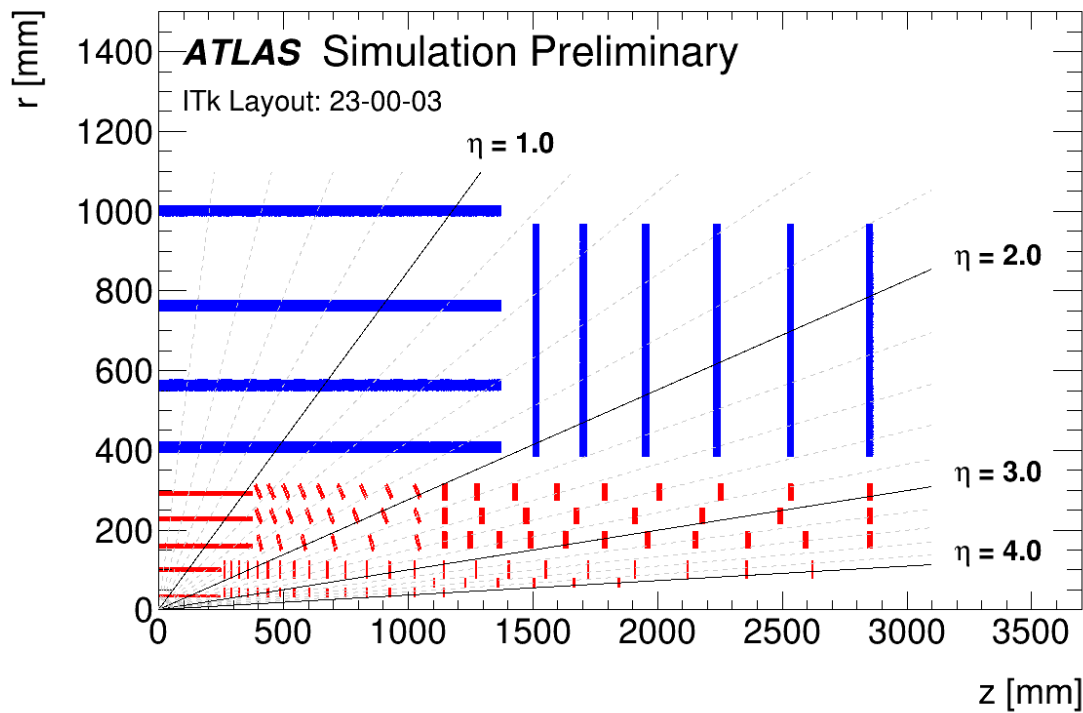


Figure 7.2: Schematic view of the new ATLAS tracker ITk in the (z, r) plane, Layout 23-00-03 from Ref. [74]. Only active material is displayed. Red modules represent pixel modules and blue ones are strip modules.

parameter resolutions in transverse impact parameter (d_0) and transverse momentum (p_T) have been evaluated with single-muon simulations.

The transverse impact parameter d_0 is a variable specific to tracking inside detectors, and is defined as the distance of closest approach of the track to the primary vertex point.

Figures 7.4a and 7.4b compare the track impact parameter resolution in d_0 (top) and the relative transverse momentum resolution in p_T (bottom) as a function of the true track pseudorapidity η , for different p_T values and both ITk and Run 2 configurations.

For high-momentum tracks ($p_T = 100$ GeV), where multiple scattering effects are negligible, the d_0 resolution in the ITk remains below $10 \mu\text{m}$ up to $|\eta| \approx 3.0$. This performance, although about 20-30% worse than Run 2 across most of the η range, reflects the design trade-offs of the ITk: the adoption of digital clustering technology and a larger innermost pixel layer radius.

For lower p_T tracks (1 GeV and 10 GeV), where multiple scattering dominates, the d_0 resolution of the ITk remains broadly comparable to Run 2 up to $|\eta| < 2.5$, with even moderate degradation beyond this point.

Similarly, the p_T resolution shows good agreement between ITk and Run 2 at central pseudorapidity for $p_T = 1$ and 10 GeV. At $p_T = 100$ GeV, the ITk benefits from its extended tracking coverage and improved pattern recognition, maintaining

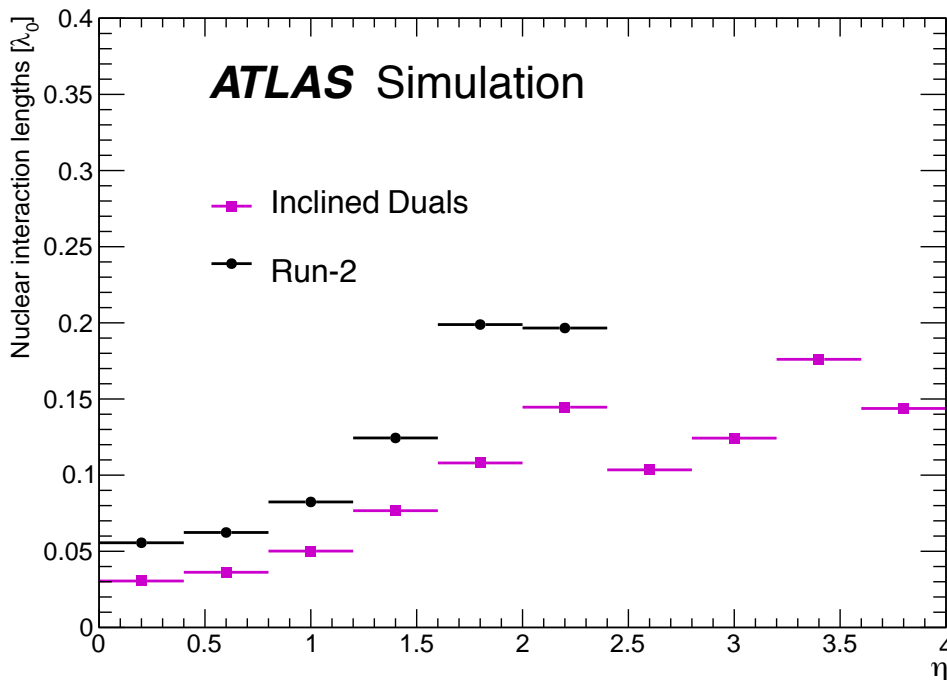


Figure 7.3: Comparison of nuclear interaction length between ATLAS current inner detector used for Run 2 and ITk inclined duals. Taken from Ref. [75].

better resolution than Run 2 up to $|\eta| \approx 2.5$, despite the harsher HL-LHC conditions.

Overall, these results indicate that the ITk will continue to provide high-quality track reconstruction, even in the forward region, and will retain sufficient resolution for precision measurements and performance-critical tasks such as b -tagging.

A crucial ingredient of ITk is its resilience against radiation damage. The sensor and readout technologies were specifically selected to withstand doses expected over 3000 fb^{-1} of integrated luminosity, with minimal degradation in signal-to-noise ratio or charge collection efficiency throughout the experiment's lifetime. Cooling systems and support structures were redesigned to maintain thermal and mechanical stability, while minimizing material within the tracking volume.

The ACTS framework Another major element of the ATLAS tracking upgrade concerns the software infrastructure. The ACTS [76] (A Common Tracking Software) framework has been developed as a modular, experiment-independent toolkit, designed to provide a unified and efficient tracking framework for the HL-LHC era. Within the ATLAS collaboration, it will serve as the backbone of the reconstruction software for the Inner Tracker (ITk).

At the core of the track-fitting procedure in ACTS lies a new implementation of the *Kalman Filter* (KF). In this context, the Kalman Filter refers to a recursive

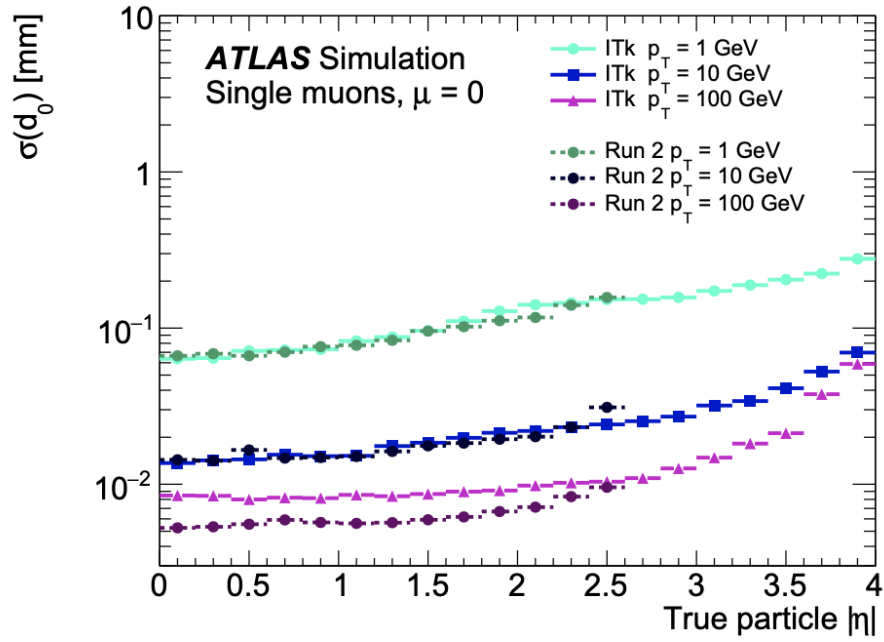
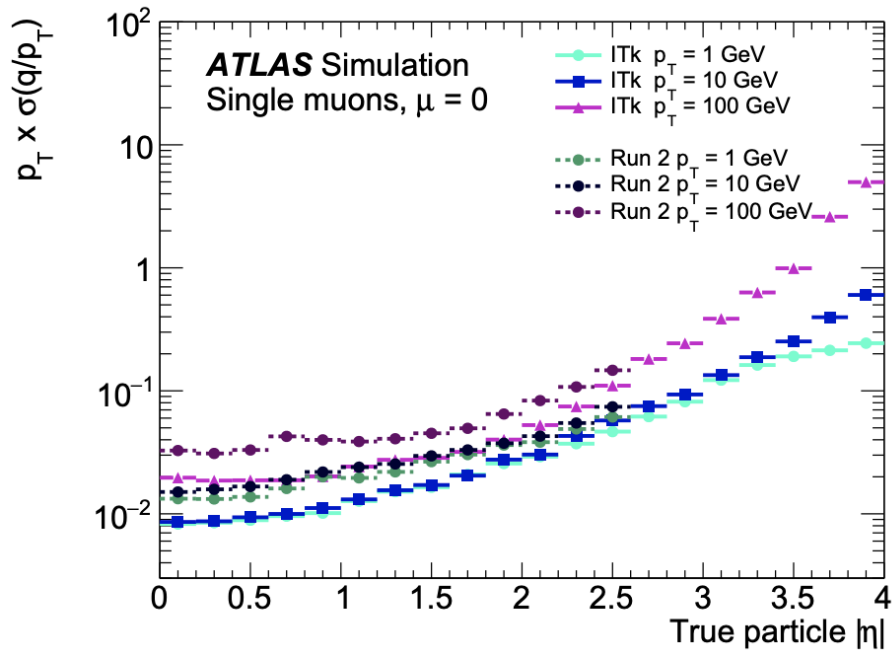
(a) Track resolution in d_0 as a function of η .(b) Track resolution in p_T as a function of η .

Figure 7.4: Track parameters resolution in d_0 and q/p_T as a function of true track η . Results are shown for single muons with p_T of 1, 10 or 100 GeV, for $\langle \mu \rangle = 0$. Results for Run 2 are shown for comparison. Taken from Ref. [75].

algorithm that estimates the most probable trajectory of a charged particle as it propagates through the detector. The algorithm iteratively updates the track parameters and their covariance matrix, providing an optimal fit in the least-squares sense under Gaussian assumptions.

The new KF implementation within ACTS has demonstrated excellent agreement with existing fits performed in the ATLAS ATHENA software when tested on both simulated and refitted tracks in data. The qualification task presented in this thesis involved refitting tracks using ACTS with the ITk geometry and confirmed consistency across multiple configurations and datasets (*cf.* Section 7.4).

7.2.2 Calorimeter and Muon System Enhancements

The readout electronics of both the electromagnetic and hadronic calorimeters will be replaced to enable full-granularity information to be used at the Level-1 trigger. Upgrades to the muon system include new trigger chambers and frontend electronics, ensuring efficiency and robustness at high pile-up.

7.3 Computing and Data Handling

The transition to the HL-LHC era will not only challenge the detector hardware and reconstruction algorithms, but also place unprecedented demands on computing infrastructure. The expected increase in instantaneous luminosity and pile-up will result in significantly larger event sizes and higher trigger rates, requiring a re-evaluation of data processing, storage, and access strategies across the ATLAS computing model.

The computing model foresees a tenfold increase in CPU and disk capacity by the end of HL-LHC operations. The projected usage is shown in Figures 7.5 and 7.6, with CPU demand expected to reach several tens of millions of HS06-equivalent units, and disk/tape storage growing by hundreds of petabytes per year.

This growth in resource demand is driven not only by increased data volume, but also by the complexity of reconstruction algorithms such as those involving precision timing information, track pattern recognition under high occupancy, and large-scale simulation campaigns for systematic uncertainty evaluations.

To address these challenges, ATLAS is developing a new data processing model (real-time calibration to reduce the storage of data, Machine Learning acceleration in trigger decision-making and reconstruction, etc...).

Another strategic area is software optimization. Code modernisation, vectorisation, and algorithm redesign are being actively pursued to reduce per-event CPU consumption and memory usage (*cf.* R&D efforts in Figure 7.5).

Overall, ATLAS computing for HL-LHC represents a coordinated transformation across software, infrastructure, and physics workflows, ensuring the experiment can fully exploit the large and complex datasets expected in the next phase of LHC operations.

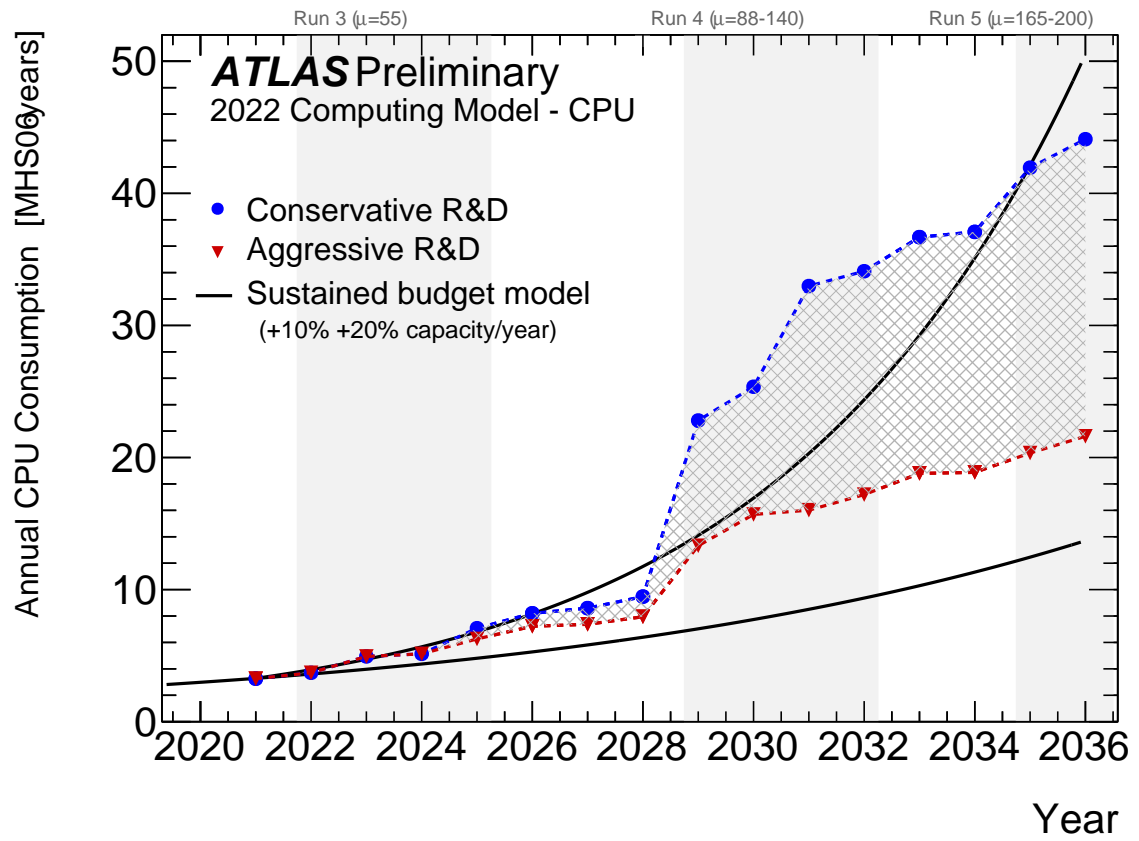
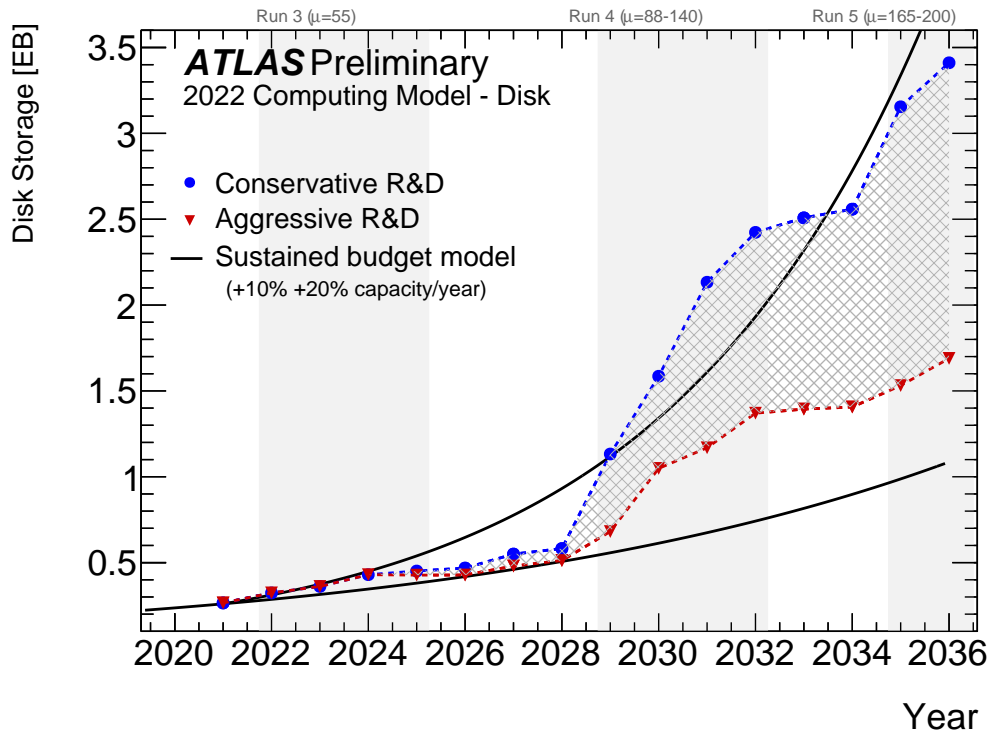
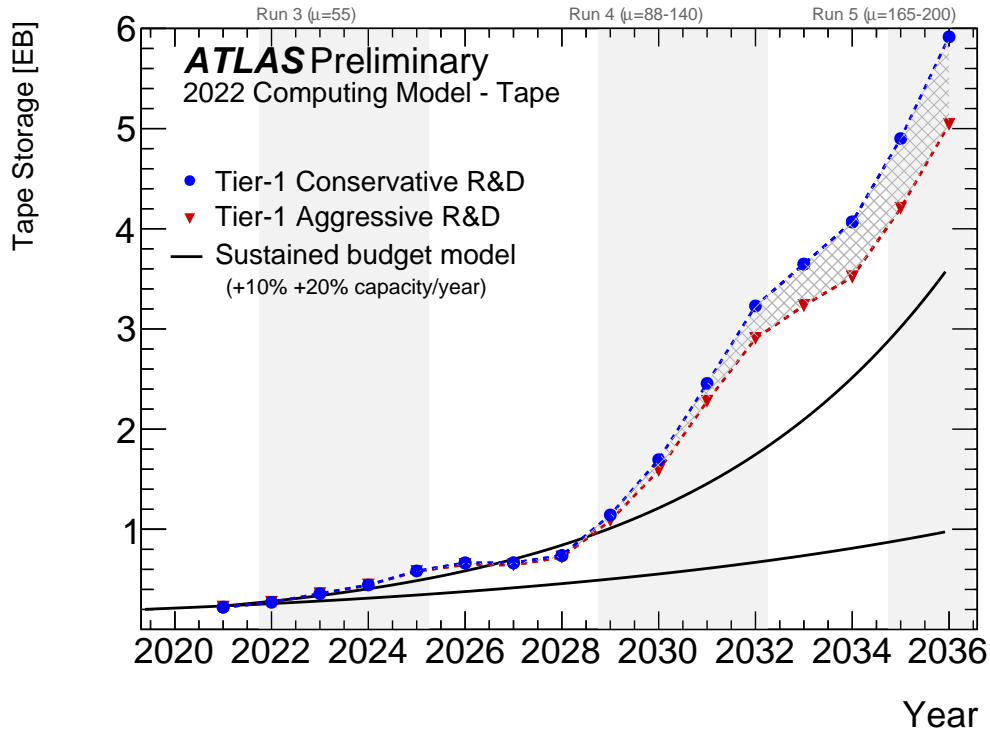


Figure 7.5: Projected evolution of computing usage from 2020 until 2036. Taken from Ref. [77].



(a) Evolution of disk usage



(b) Evolution of tape usage

Figure 7.6: Projected evolution of disk (top) and tape (bottom) storage usage from 2020 until 2036. Taken from Ref. [77].

7.4 ATLAS Qualification Task: ACTS Kalman Filter (KF) Integration in Athena

The ATLAS authorship qualification process is specific to the collaboration, and requires each new member to contribute to a technical task of broad relevance to the ATLAS Collaboration. This work aims to support the long-term development and operation of the ATLAS detector and its software infrastructure.

My qualification task [78] focused on the integration of the ACTS Kalman Filter (KF) [79] into the ATLAS reconstruction framework *ATHENA*, a critical step for enabling precision tracking with the upgraded Inner Tracker (ITk) at the HL-LHC. This project was carried out from November 2022 to November 2023, under the supervision of Paul Gessinger-Befurt and Alexis Vallier.

ACTS is a modern, experiment-independent C++ toolkit designed for modular and high-performance track reconstruction. It provides a flexible geometry description, alignment tools, and advanced algorithms such as the KF and Gaussian Sum Filter (the latter being used for the reconstruction of electron tracks). The integration of ACTS into *ATHENA* is part of a broader transition of the ATLAS tracking software toward a more maintainable, experiment-independent, and performant framework in preparation for HL-LHC data-taking.

The qualification project began with validation studies of existing ACTS Kalman refits using calibrated RIO On Track (ROT) measurements and later extended to the development of a new interface enabling refits directly from uncalibrated PrepRawData (PRD) hits.

In the ATLAS reconstruction chain, the distinction between PRDs and ROTs is essential:

- **PrepRawData (PRD):** detector-level measurements derived from raw read-out. They serve as the basic inputs to the tracking reconstruction but are not yet associated with a specific track hypothesis.
- **RIO On Track (ROT):** a measurement derived from a PRD once it has been assigned to a track. The hit is expressed in the local coordinate system of the detector surface, associated to a detector element, and corrected using the appropriate error matrix. RIO stands for “Readout (or Reconstructed) Input Object.”

In this context, **calibration** will refer to the transformation of PRD measurements into ROTs (*i.e.* the determination of the spatial position and uncertainty after accounting for detector alignment and response).

This required the design and implementation of a calibration pathway capable of operating within the ACTS Kalman Fitter itself. A new data structure, the `PRDSourceLink`, was introduced to carry the necessary contextual information for the PRD-to-ROT transformation inside ACTS. The resulting integration was finalized in a merge request that was successfully included in the ATLAS main *ATHENA* repository.

My key contribution to the ATHENA software was the development and validation of this first fully functional PRD-based track refitting using ACTS.

To achieve this, the ATHENA–ACTS interface was extended to:

- Access the detector-element context from PRDs stored within ATHENA.
- Invoke the local calibration tools using the ATLAS conditions database.
- Ensure full compatibility with both barrel and end-cap geometries of the ITk layout.

A schematic representation of the new (and final) interface is shown in Fig. 7.7.

1. Start from **PRD** (PrepRawData) stored tracks.
2. Fit the track from the **PRD**.
3. Go into calibration as **PRD**.
4. Transform into **ROT** during calibration + use fit-updated parameters.

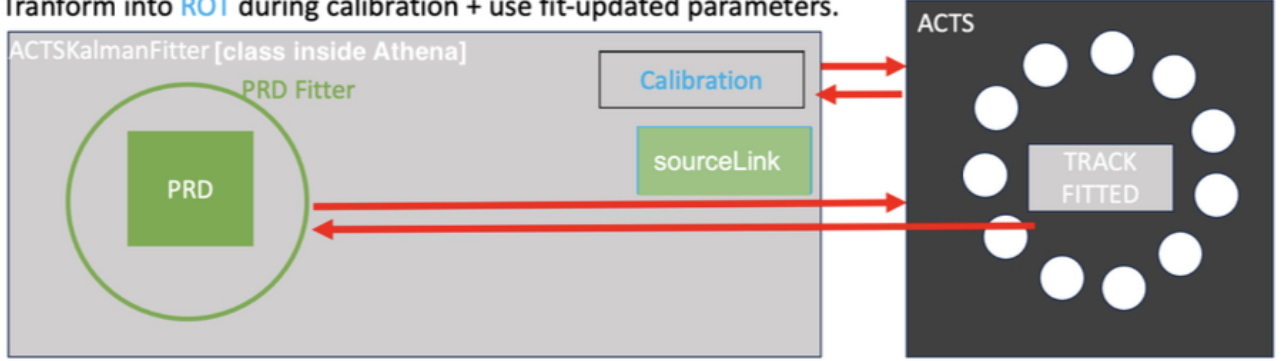


Figure 7.7: Representation of the new implementation of the uncalibrated (PRD-based) measurements fit between the ATHENA and ACTS frameworks. The top section outlines the four main steps of the interface. The ACTSKALMANFITTER class, implemented within ATHENA, now handles calibration internally during the fit (from Ref [78]).

The final implementation was tested on multiple Monte Carlo samples using the ITk geometry, including single-particle and full simulated event samples. The performance was evaluated through pull distributions, residuals, and resolutions of tracking parameters such as d_0 , z_0 , p_T , and η .

The plots presented below (*cf.* fig.7.8 and 7.9) correspond to the final version of the interface, which demonstrated full consistency and validated the integration of ACTS inside Athena. Earlier stages of the development and intermediate results are documented in more detail in the corresponding ATLAS Note [78].

The results show excellent agreement between ACTS and ATHENA refits, confirming the stability and robustness of the implementation.

This work was successfully merged into the main ATHENA software repository, marking its completion and integration into the ATLAS reconstruction framework.

The successful outcome of this qualification task demonstrates the readiness of

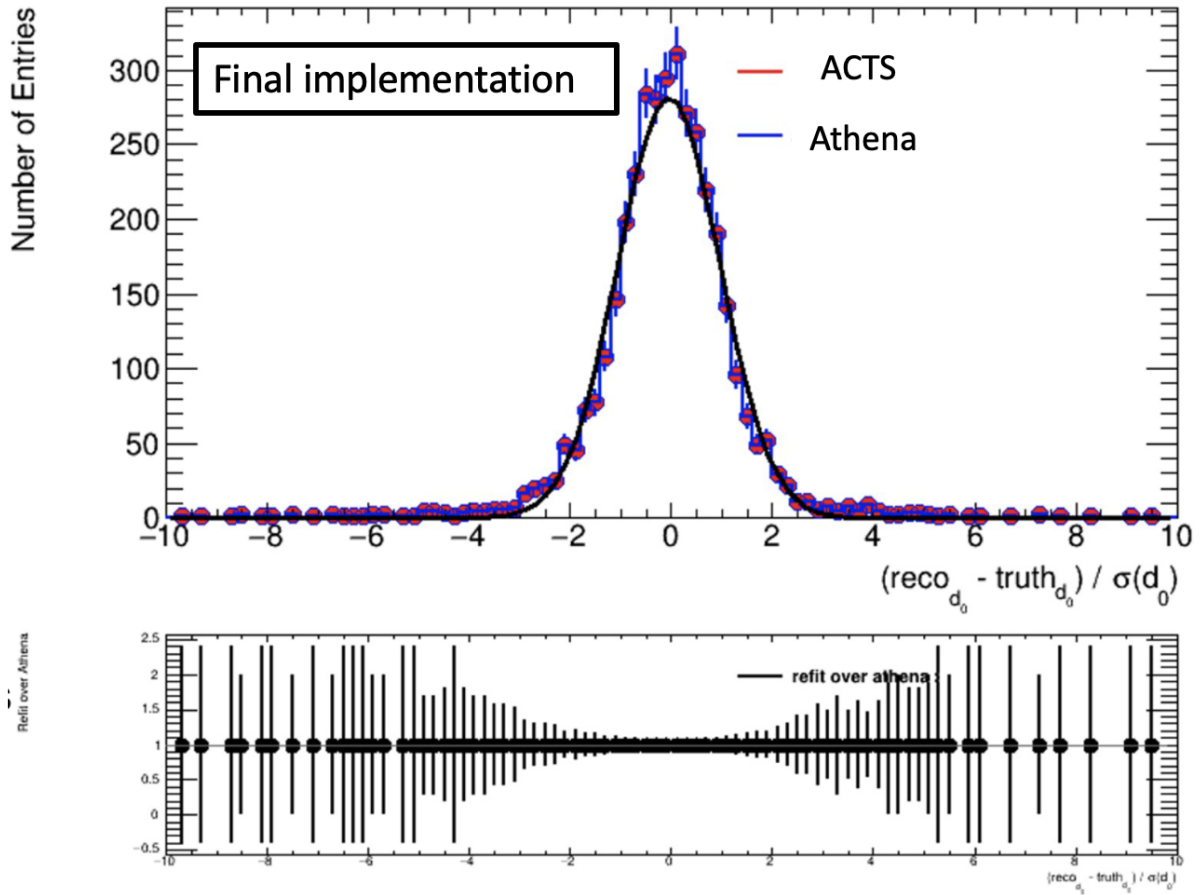


Figure 7.8: Pull distributions of the transverse impact parameter d_0 as a function of η for the latest version of the ATHENA–ACTS interface. The histograms correspond to ACTS fits (red) and Athena fits (blue). The Gaussian fit (black) is performed on the ACTS distribution. The lower panel shows the ratio ACTS/Athena (from Ref [78]).

ACTS-based reconstruction for HL-LHC data-taking and represents a concrete step toward modernizing the ATLAS tracking software stack.

It directly supports the tracking performance goals described in Section 7.2.1, ensuring that the ITk’s high-granularity tracking data can be reconstructed efficiently and with optimal precision.

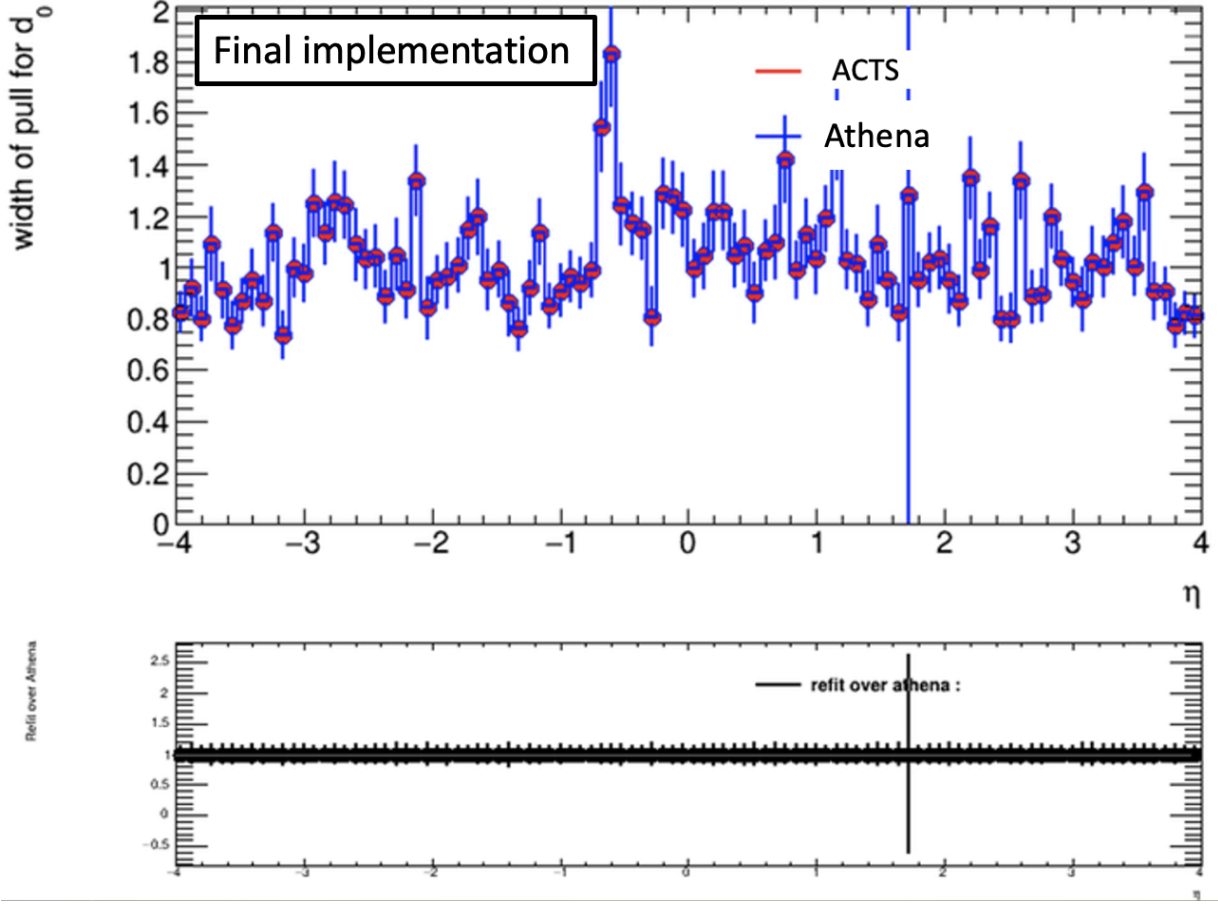


Figure 7.9: Width of the d_0 pull distribution as a function of η for the final implementation of the ATHENA–ACTS interface. The histograms correspond to ACTS fits (red) and Athena fits (blue). The lower panel shows the ratio ACTS/Athena (from Ref [78]).

7.5 Future Sensitivity to Higgs Self-Coupling

The HL-LHC will dramatically extend the sensitivity to the trilinear Higgs self-coupling λ_{3H} through a combination of significantly increased integrated luminosity and improvements in detector performance. In particular, the $HH \rightarrow b\bar{b}\gamma\gamma$ final state is projected to remain one of the most powerful channels owing to its balance between manageable backgrounds, good mass resolution, and sufficient signal yield.

With 3000 fb^{-1} of data, the ATLAS experiment is expected to constrain the signal strength μ_{HH} with a relative uncertainty of roughly 50% when using the $b\bar{b}\gamma\gamma$ channel alone [80]. This corresponds to a projected 95% confidence interval on the self-coupling modifier κ_λ of approximately $[-0.5, 2.0]$ (assuming all other couplings are fixed to their Standard Model values).

This precision would allow ATLAS to confirm or exclude a wide class of new physics models that predict deviations from the SM Higgs potential.

Part III

A statistically optimal method: The Matrix Element Method



We dedicated the previous section to the review of the experimental setup of the ATLAS experiment at the LHC and the effort in the study of the Higgs sector. We presented one multivariate analysis method used in many analyses at LHC: the Boosted Decision Trees (BDT) (in Section 6.2).

Yet many other methods are used for analysis. One can mention for instance the very popular cut-based methods (i.e where the event-selection technique relies on a fixed set of specific threshold cuts on discriminating observables), or event-counting methods (quickly introduced in Section 6.1).

Part III of this manuscript introduces another multivariate method (**at the center of this doctoral research**): The Matrix Element Method.

That will set the necessary foundations for the next parts focused on the development of the Matrix Element Method at Next-to-Leading order (NLO) (discussed in the dedicated Parts IV and V).

The opening **Chapter 8** focuses on the derivation and comprehensive review of the Matrix Element Method at Leading-Order (LO).

Chapter 9 will examine the most prominent software used in the community for the Matrix Element Method implementations.

The following **Chapter 10** will cover key successes of the Matrix Element Method, including both widely recognized applications across experiments and notable results unique to the LHC.

The final **Chapter 11** of this set will revisit a master's thesis that provides the primary motivation for the present doctoral research.

Content

8	General overview of the Matrix Element Method	109
8.1	Theoretical Foundations of the Matrix Element Method	109
8.1.1	Statistical Basis: Neyman-Pearson Lemma	109
8.1.2	Implementation in High Energy Physics	110
8.2	Evaluating methods discrimination power: ROC curves	113
8.3	Likelihood Formalism	115
8.3.1	Kinematic Likelihood Construction	115
8.3.2	Event Yield Likelihood	116
8.3.3	Extended Likelihood Framework	117
8.4	Method of Minimum Negative Log-Likelihood	117
9	Main Tools and Software for the Matrix Element Method	119
9.1	MadGraph5 (MadGraph5_aMC@NLO)	119
9.1.1	UFO Models	119
9.1.2	Core Functionality	120
9.2	MadWeight	120
9.3	MOMEMTA: Modular MEM Implementation	120
9.3.1	Architecture of MOMEMTA	120

9.3.2	Integration Algorithms within MoMEMTA	121
9.3.3	Main and Secondary Blocks	122
9.3.4	The MoMEMta-MaGMEE Module	125
9.4	POWHEG-BOX-V2: An alternative to MadGraph5	125
9.4.1	Main usage	125
9.4.2	Limitations for the MEM	126
10	Historical successes of the MEM	127
10.1	Major success of the Matrix Element Method: Top Quark Mass Measurements at DØ and CDF	127
10.2	Major applications and successes of the MEM at the LHC	128
10.2.1	Searches for the $t\bar{t}h$ process	128
10.2.2	Search for s-channel single Top quark production	129
10.2.3	Success in the measurement of $t\bar{t}$ spin correlation in the μ +jets channel	129
10.2.4	Discovery of the Higgs boson and spin-parity measurements in the $h \rightarrow 4l$ channel	129
11	Legacy analysis: Leading Order MEM Implementation in the $gg \rightarrow HH \rightarrow b\bar{b}\gamma\gamma$ channel	131
11.1	Matrix Element Construction and Effective Model Design	131
11.1.1	EFT Vertices and $gg \rightarrow HH$ Loop Approximation	131
11.1.2	UFO Model Merging and κ Parameterization	132
11.2	Event Simulation and Detector Smearing Framework	133
11.2.1	Parton-Level Generation and Background Channels	133
11.2.2	Detector Resolution and Simplified Transfer Functions	133
11.2.3	Pre-selection requirements at LO	133
11.3	Likelihood Evaluation with MADWEIGHT	134
11.4	Migration to MoMEMTA and Integration Strategy	134
11.4.1	Matrix Element Compatibility and C++ Translation	134
11.4.2	Lua Configuration and Parametrization Choices	136
11.5	Statistical Discrimination and Measurement of the Higgs Self-Coupling	137
11.5.1	MEM Likelihood Ratio (LHR) Versus Boosted Decision Tree (BDT) Performance	137
11.5.2	Extended Likelihood and κ Estimation	137
11.5.3	Treatment of Zero-Likelihood Events	140
11.6	Summary and Outlook Toward NLO Extensions	141

Chapter 8

General overview of the Matrix Element Method

We begin this set of chapters with a comprehensive overview of the Matrix Element Method (MEM) in its most general form.

8.1 Theoretical Foundations of the Matrix Element Method

8.1.1 Statistical Basis: Neyman-Pearson Lemma

The Matrix Element Method is rooted in the Neyman-Pearson lemma [82], a cornerstone of statistical hypothesis testing since 1933.

For two simple hypotheses H_0 (null hypothesis) and H_1 (alternative hypothesis), the lemma states that among all possible tests of H_0 versus H_1 at a fixed significance level α , the most powerful test is obtained by rejecting H_0 in favor of H_1 whenever the ratio of their probability densities

$$\Lambda(\mathbf{x}^i) = \frac{f(\mathbf{x}^i | H_0)}{f(\mathbf{x}^i | H_1)}$$

falls below a threshold $\eta(\alpha)$. Here x denotes the observed data, and $f(\mathbf{x}^i | H_i)$ is the probability density (or mass function) under hypothesis H_i .

In their original paper, Neyman and Pearson expressed the lemma in terms of probability densities. In modern usage it is often written with likelihood functions $\mathcal{L}(H_i | \mathbf{x}^i)$.

It is important to distinguish the roles of probabilities and likelihoods:

- **Probabilities:** Given a fixed hypothesis H (i.e. fixed parameters), they describe the distribution of all possible data \mathbf{x}^i (the “forward” problem).

- **Likelihoods:** Given fixed observed data \mathbf{x}^i , they quantify the relative compatibility of different hypotheses H (the “inverse” problem).

For the purpose of our analysis we will adopt the likelihood formulation, and write the test statistic as

$$\Lambda(\mathbf{x}) = \frac{\mathcal{L}(\mathbf{x} | H_1)}{\mathcal{L}(\mathbf{x} | H_0)}. \quad (8.1)$$

8.1.2 Implementation in High Energy Physics

Foundational Work

The application of the Neyman-Pearson lemma with the use of likelihoods to particle physics was pioneered in Refs. [83–85], and the result that emerged from this work will be discussed in more detail in Section 10.1.

In this part we will explain how the Neyman-Pearson lemma can be used to its full potential in particle physics analysis.

Definition

It is possible to derive the expression of the likelihood \mathcal{L} from first principle for the particular case of high-energy hadronic collisions.

The corresponding method, called the **Matrix Element Method**, assigns a likelihood $\mathcal{L}(\mathbf{x}^i; \mathbf{h})$ to each experimental event \mathbf{x}^i based on a theoretical model (or hypothesis \mathbf{h}) one is interested in testing.

It is a statistically optimal (from using the Neyman–Pearson lemma), multivariate technique, which aims to determine how well an observed event agrees with a theoretical model, by maximizing the use of all the experimental and theoretical information available in an analysis with minimal cuts on the data \mathbf{x} .

Because of this very unique property of reducing information loss as much as possible, the MEM is often used to isolate rare signals from backgrounds in searches for new physics, or for measurements of Standard Model observables in rare processes.

Constructing the likelihood $\mathcal{L}(\mathbf{x}^i; \mathbf{h})$ from first principles

In a collision between two partons a_1 and a_2 (given a good detector resolution and known beam energies), the likelihood \mathcal{L} of the n final state partons of an event to be *produced* with the four-momenta $\mathbf{y} = (y_1, \dots, y_n)$ by the process p with the assumed parameter values \mathbf{h} is proportional to the partonic differential cross-section of the corresponding process $d\sigma_p(a_1 a_2 \rightarrow \mathbf{y}; \mathbf{h})$ defined as:

$$d\sigma_p(a_1 a_2 \rightarrow \mathbf{y}; \mathbf{h}) = \frac{(2\pi)^4 |\mathcal{M}_p(a_1 a_2 \rightarrow \mathbf{y}; \mathbf{h})|^2}{q_1 q_2 s} \delta \left(a_1 + a_2 - \sum_{j=1}^n y_j \right) d^{4n} \mathbf{y} \quad (8.2)$$

where:

- $\mathcal{M}_p(a_1 a_2 \rightarrow \mathbf{y}; \mathbf{h})$ denotes the Matrix Element of $a_1 a_2 \rightarrow \mathbf{y}$ for the process p and the hypothesis \mathbf{h} , obtained from first principles,
- q_1 and q_2 are the momentum fractions of partons a_1 and a_2 (also referred to as Bjorken x scaling variables),
- s is the Mandelstam variable corresponding to the squared center-of-mass energy of the proton-proton collision,
- $\delta(a_1 + a_2 - \sum_{j=1}^n y_j)$ represents the energy-momentum conservation,
- $d^{4n}\mathbf{y}$ is an element of the phase space of the n final-state partons.

When the incoming particles are from inside a proton, and detector smearing (i.e the detector resolution) is no longer negligible, the observable cross-section must be written as a convolution of the partonic cross-section with the parton-distribution functions (PDFs) and with the detector response, followed by an integration over all unobservable partonic variables (eg. final state particles that are not detected).

We can compute the differential cross-section of proton-proton collisions as the convolution of the partonic differential cross-section given in Eq. (8.2) with the PDF, summed over all possible flavors a_1 and a_2 of the colliding partons:

$$d\sigma_p(pp \rightarrow \mathbf{y}; \mathbf{h}) = \int_{q_1, q_2} \sum_{a_1, a_2} f_{a_1}(q_1) f_{a_2}(q_2) d\sigma_p(a_1 a_2 \rightarrow \mathbf{y}; \mathbf{h}) dq_1 dq_2, \quad (8.3)$$

where $f_a(q)$ is the probability density to find a parton of flavor a and momentum fraction q in the proton.

The resolution of the detector is taken into account by convoluting this differential cross-section with the transfer function $W(\mathbf{x}^i, \mathbf{y})$ (which describes the probability for a partonic final state \mathbf{y} to be reconstructed as \mathbf{x}^i in the detector). It is commonly assumed that the transfer function is "factorable" and can be written as the product of single-particle resolution functions (which themselves can be written as the product of the resolution functions associated with the physical quantities measured). These transfer functions can be seen as a parametrised model of the resolution of the detector.

To take detector effects into account, we need to modify the expression of the differential cross-section accordingly:

$$d\sigma_p(pp \rightarrow \mathbf{x}^i; \mathbf{h}, W) = \int_{\mathbf{y}} d\sigma_p(pp \rightarrow \mathbf{y}; \mathbf{h}) W(\mathbf{x}^i, \mathbf{y}). \quad (8.4)$$

Very simple implementations of W are often found to be sufficient. For example a δ distribution for variables that are well defined and very well measured (for example the angles), or Gaussian distribution when the detector resolution has to be taken into account (typically for energy measurements).

$W(\mathbf{x}^i, \mathbf{y})$ must satisfy the normalization condition $\int_{\mathbf{y}} W(\mathbf{x}^i, \mathbf{y}) = 1$.

Likelihood $\mathcal{L}_{\text{process}}^{\text{p}}(\mathbf{h}|\mathbf{x}^i)$ The Likelihood of interest for the Neyman–Pearson lemma is defined as follow:

$$\begin{aligned}\mathcal{L}_{\text{process}}^{\text{p}}(\mathbf{h}|\mathbf{x}^i) &= \frac{d\sigma_p(pp \rightarrow \mathbf{x}^i; \mathbf{h}, W)}{\sigma_p^{\text{obs}}(pp \rightarrow F)} \\ &= \frac{(2\pi)^4}{\sigma_p^{\text{obs}}(pp \rightarrow F)} \int_{\mathbf{y}} \int_{q_1, q_2} \sum_{a_1, a_2} f_{a_1}(q_1) f_{a_2}(q_2) \frac{|\mathcal{M}_p(a_1 a_2 \rightarrow \mathbf{y}; \mathbf{h})|^2}{q_1 q_2 s} \\ &\quad \times W(\mathbf{y}, \mathbf{x}^i) \delta\left(a_1 + a_2 - \sum_{j=1}^n y_j\right) dq_1 dq_2 d^{4n} \mathbf{y}\end{aligned}\quad (8.5)$$

The observed integrated cross-section $\sigma_p^{\text{obs}}(pp \rightarrow F)$ to produce the final state partons F , in the denominator, normalizes $\mathcal{L}_{\text{process}}^{\text{p}}(\mathbf{h}|\mathbf{x}^i)$ as one would expect from a probability (or rather likelihood here).

This cross-section is often multiplied by an extra factor (the efficiency ϵ) to account for pre-selection requirements.

$\mathcal{L}_{\text{process}}^{\text{p}}(\mathbf{h}|\mathbf{x}^i)$ is a multi-dimensional integral, which can be computationally very intensive in resources and time.

The direct computation of the multivariate likelihood in the Matrix Element Method presents significant challenges, involving high-dimensional phase space integration and complex matrix element calculations.

Specialized software tools have been developed to handle these computationally intensive tasks efficiently. A detailed discussion of these computational tools and their implementation follows in the next Chapter 9.

Optimal Discrimination and MadMax: Sensitivity to κ_λ at the LHC

An important question in Higgs pair production is determining the maximum achievable sensitivity to deviations in the Higgs self-coupling parameter κ_λ from its Standard Model value.

This has been studied with the MadMax framework [86], directly grounded in the Neyman–Pearson lemma.

MadMax employs the log-likelihood ratio test introduced previously, leveraging detailed Monte Carlo simulations to identify regions in kinematic phase space that maximize sensitivity to κ_λ .

In particular, it has been found that two kinematic regions provide significant information: near the Higgs pair production threshold (low m_{HH}), and the boosted regime (high $p_{T,H}$), where interference effects between triangle and box diagrams depend strongly on κ_λ .

Using this approach, MadMax predicts that the High-Luminosity LHC (HL-LHC) with an integrated luminosity of 3 ab^{-1} could constrain the Higgs self-coupling λ_{3H}

as follows:

$$\frac{\lambda_{3H}}{\lambda_{3H}^{\text{SM}}} = 0.4\text{--}1.7 \quad \text{at 68\% CL (3 ab}^{-1}\text{).} \quad (8.6)$$

Figure 8.1 illustrates the expected significance and cross section for observing deviations from the Standard Model self-coupling at the HL-LHC, as derived using MadMax [86].

This sensitivity represents an idealized benchmark achievable under optimal conditions, assuming controlled theoretical and systematic uncertainties.

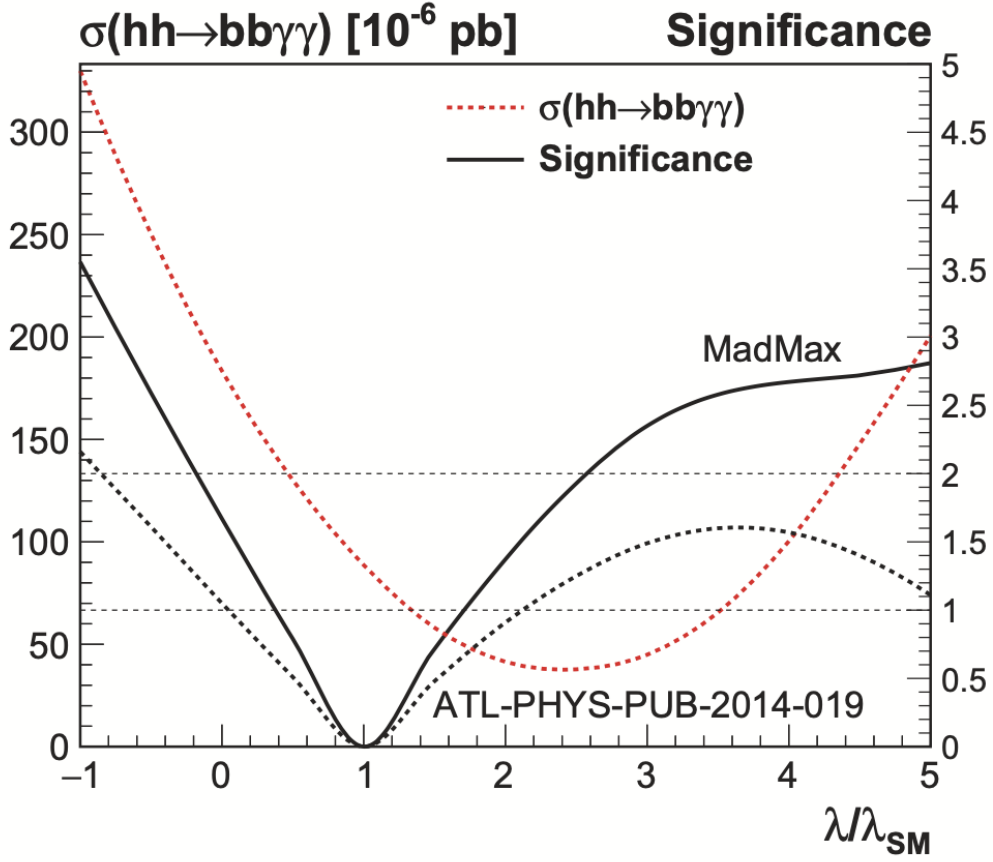


Figure 8.1: Signal cross section (red-dashed) and maximum significance (black-solid) for observing anomalous Higgs self-coupling at the LHC with an integrated luminosity of 3 ab⁻¹.

The significance from a cut-based rate measurement (black-dashed) using cuts is also shown.

Taken from Ref. [86].

8.2 Evaluating methods discrimination power: ROC curves

The **ROC curve**, or **rejection curve**, first developed by electrical and radar engineers during World War II (which explains the origin of its name ‘Receiver Operating

Characteristic' [87]) is a choice of graphical representation that illustrates the performance in terms of signal efficiency and background rejection for a given discriminant variable (*cf.* Figure 8.2).

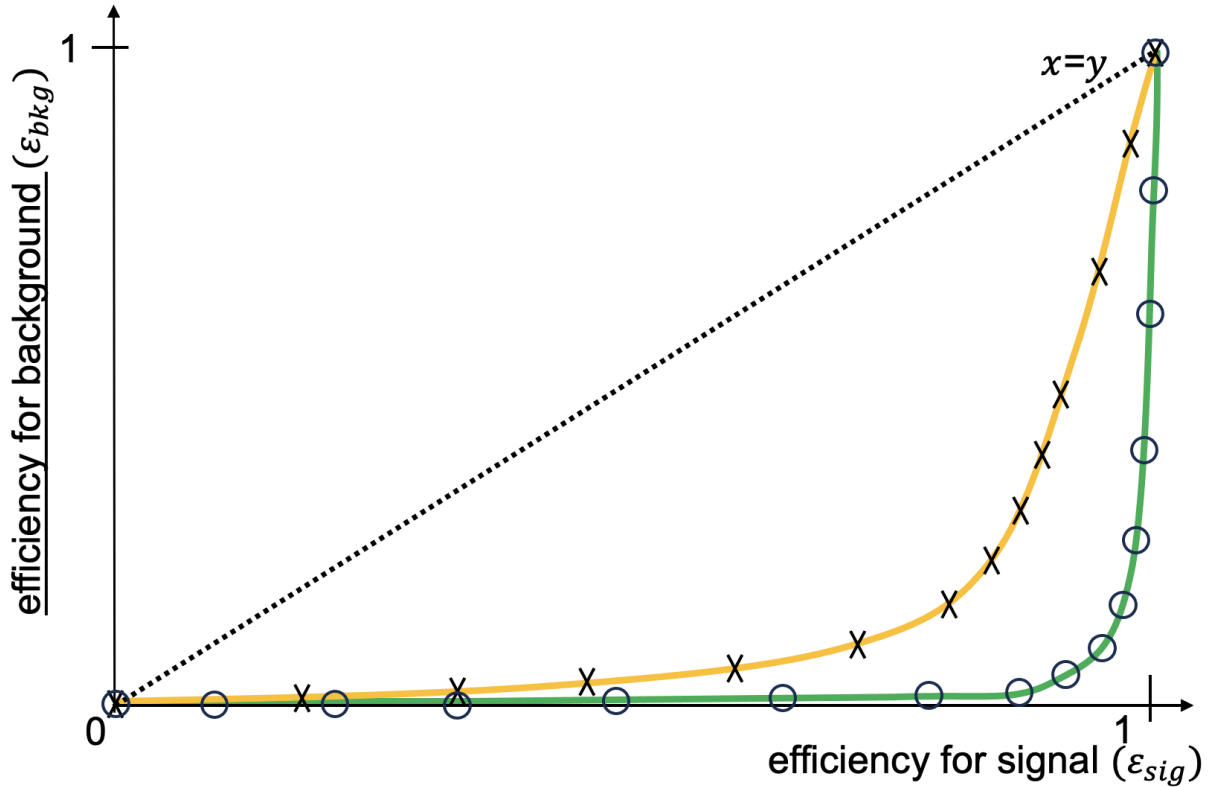


Figure 8.2: Schematic example of two ROC curves: example where the events are well discriminated between signal and background hypothesis (in green); example where the events are less strongly discriminated (in orange). Different points on a ROC curve correspond to different cuts on the discriminating variable. The line $x = y$ represents the performance of a random classification.

Rejection curves are a good general purpose metric, and serve as a visual diagnostic of a method's ability to distinguish between two hypotheses. Given the conventions of Figure 8.2, it is defined as a plot of the selection efficiency for the background (ϵ_{bkg}) as a function of the selection efficiency for the signal (ϵ_{sig}), where:

- Selection efficiency for signal: ϵ_{sig} is the fraction of true signal events retained after applying a selection on the discriminant (i.e the computation of the ratio $\frac{TP}{TP+FN}$ in terms of the confusion matrix (*cf.* Table 8.1), for a given dataset of events),
- Selection efficiency for background: ϵ_{bkg} is the corresponding fraction of background events retained after applying a selection on the discriminant (i.e the computation of the ratio $\frac{FP}{FP+TN}$ in terms of the confusion matrix (*cf.* Table 8.1), for a given dataset of events).

		Predicted Condition	
		Positive	Negative
Actual	Positive	True Positive (TP)	False Negative (FN)
	Negative	False Positive (FP)	True Negative (TN)

TP: True Positive (correctly predicted positive case).

FN: False Negative (incorrectly predicted negative case).

FP: False Positive (incorrectly predicted positive case).

TN: True Negative (correctly predicted negative case).

Table 8.1: Confusion matrix illustrating the definitions of true and false positives and negatives. Green cells correspond to correct predictions, while red cells indicate misclassifications.

As illustrated in figure 8.2, a ROC curve that is close to the lower-right border of the plane has a more optimal separation power. The area under the curve (AUC) offers a concise reference measurement of the discriminating power of the method. Because the vertical axis is defined as the error rate ($1 - \text{efficiency}$), a **smaller** AUC corresponds to a **better** discrimination between the competing hypotheses in our analysis.

Some other conventions for the ROC curve replaces the vertical axis with the background rejection rate, $1 - \epsilon_{\text{bkg}}$, instead of the background efficiency ϵ_{bkg} .

This change only affects the graphical appearance of the ROC and reverses the numerical interpretation of the AUC (larger is therefore better), but leaves the underlying classifier output (and therefore the physics conclusions) unchanged.

8.3 Likelihood Formalism

8.3.1 Kinematic Likelihood Construction

The Matrix Element Method employs a hierarchical likelihood structure to combine event-level kinematic information.

Let's consider a dataset $\mathcal{D} = \{\mathbf{x}^i\}_{i=1}^N$ of N events, and n_P different processes. Here again \mathbf{x}^i denotes the kinematic observables for the i -th event and \mathbf{h} represents the theoretical parameters of interest for our analysis (*e.g.* Higgs couplings κ_λ).

Process Likelihood

For each event \mathbf{x}^i , recall from Section 8.1.2 that the likelihood obtained from first principles for a given process p can be computed as follow:

$$\mathcal{L}_{\text{process}}^p(\mathbf{h}|\mathbf{x}^i) = \frac{1}{\sigma_p^{\text{obs}}(pp \rightarrow F)} \int_{\mathbf{y}} d\sigma_p(pp \rightarrow y; \mathbf{h}) W(\mathbf{y}, \mathbf{x}^i) \quad (8.7)$$

We will call this likelihood as the **process** likelihood to avoid future confusions.

Event Likelihood

Once the contributions of the event \mathbf{x}^i have been computed for each of the n_p processes (signal and backgrounds), we can construct the **event likelihood**:

$$\mathcal{L}_{\text{event}}(\mathbf{h}|\mathbf{x}^i) = \sum_{p=1}^{n_p} f_p(\mathbf{h}) \mathcal{L}_{\text{process}}^p(\mathbf{h}|\mathbf{x}^i), \quad (8.8)$$

where f_p is the fraction of events from process p in the entire event sample (satisfying $\sum_p f_p = 1$). One can consider these fractions to be unknown (*i.e.* treating them as additional free parameters in the likelihood maximization), or they can be fixed using prior knowledge about the sample composition.

Sample Likelihood (or Kinematic Likelihood)

And finally, given a dataset $\mathcal{D} = \{\mathbf{x}^i\}_{i=1}^N$ of N events, the total sample likelihood is the product of (per-)event likelihoods:

$$\mathcal{L}_{\text{sample}}(\mathbf{h}|\mathcal{D}) = \mathcal{L}_{\text{kinematic}}(\mathbf{h}|\mathcal{D}) = \prod_{i=1}^N \mathcal{L}_{\text{event}}(\mathbf{h}|\mathbf{x}^i) \quad (8.9)$$

Throughout this manuscript we will mostly refer to this quantity as the **kinematic** likelihood $\mathcal{L}_{\text{kinematic}}$ to emphasize that this is the likelihood obtained from the Matrix Element Method outputs, using the kinematic properties of the reconstructed final state particles (after a given event pre-selection).

8.3.2 Event Yield Likelihood

Given the strong dependence of the di-Higgs production cross-section on κ_λ (*cf.* Figure 6.1), the number of events observed (after applying a given set of event selection) is a valuable piece of information for its the extraction.

Assuming that the number of observed events N_{obs} follows a Poisson distribution, the event yield likelihood $\mathcal{L}_{\text{yield}}$ is the Poisson probability with parameter $\lambda(\kappa)$ to observe N_{obs} events (for a given integrated luminosity):

$$\mathcal{L}_{\text{yield}}(\kappa) = \frac{\lambda(\kappa)^{N_{\text{obs}}} e^{-\lambda(\kappa)}}{N_{\text{obs}}!}, \quad \lambda(\kappa) = N_{\text{sig}}(\kappa) + N_{\text{bkg}} \quad (8.10)$$

where $N_{\text{sig}}(\kappa)$ and N_{bkg} correspond to the theoretically expected number of respectively signal and background events (given the value of κ).

8.3.3 Extended Likelihood Framework

The extended likelihood combines two complementary sources of information: kinematic details from the Matrix Element Method and yield expectations derived from theoretical cross sections.

It is mathematically defined as the product of the kinematic likelihood and the yield likelihood:

$$\mathcal{L}_{\text{ext}}(\kappa) = \underbrace{\prod_{i=1}^{N_{\text{obs}}} \mathcal{L}_{\text{event}}(\kappa|\mathbf{x}^i)}_{\text{Kinematic term}} \times \underbrace{\mathcal{L}_{\text{yield}}(\kappa)}_{\text{Yield term}} \quad (8.11)$$

The corresponding negative log-likelihood (NLL) becomes:

$$\begin{aligned} -\ln \mathcal{L}_{\text{ext}}(\kappa) &= -\sum_{i=1}^{N_{\text{obs}}} \ln \mathcal{L}_{\text{event}}(\kappa|\mathbf{x}^i) \\ &\quad + \lambda(\kappa) - N_{\text{obs}} \ln \lambda(\kappa) + C \end{aligned} \quad (8.12)$$

where C is a constant term, and can be removed in any minimization of the NLL since it does not depend on κ_λ .

8.4 Method of Minimum Negative Log-Likelihood

Description

The Method of Minimum Negative Log-Likelihood (NLL) provides a robust statistical framework for parameter estimation in high-energy physics analyses. Given a likelihood function $\mathcal{L}(\mathbf{h}|\mathbf{x})$ for parameters \mathbf{h} and observed data \mathbf{x} , the estimator $\hat{\mathbf{h}}$ is obtained through:

$$\hat{\mathbf{h}} = \underset{\mathbf{h}}{\text{argmin}} [-\ln \mathcal{L}(\mathbf{h}|\mathbf{x})] \quad (8.13)$$

Numerical Stability

One of the advantage of using NLL instead of the simple Likelihood computed from the MEM is numerical stability, and the fact that product likelihoods $\mathcal{L} = \prod_i p_i$ with $p_i \ll 1$ suffer from floating-point underflow. The log transform converts this to a stable sum:

$$-\ln \mathcal{L} = -\sum_i \ln p_i \quad (8.14)$$

Statistical Uncertainty Extraction from NLL Profiles

Another great advantage comes from the quick computation of the statistical uncertainty σ_h for a parameter h , which is determined by examining the behavior of the negative log-likelihood (NLL) function around its minimum. This procedure

exploits the asymptotic properties of maximum likelihood estimators under Wilks' theorem [88].

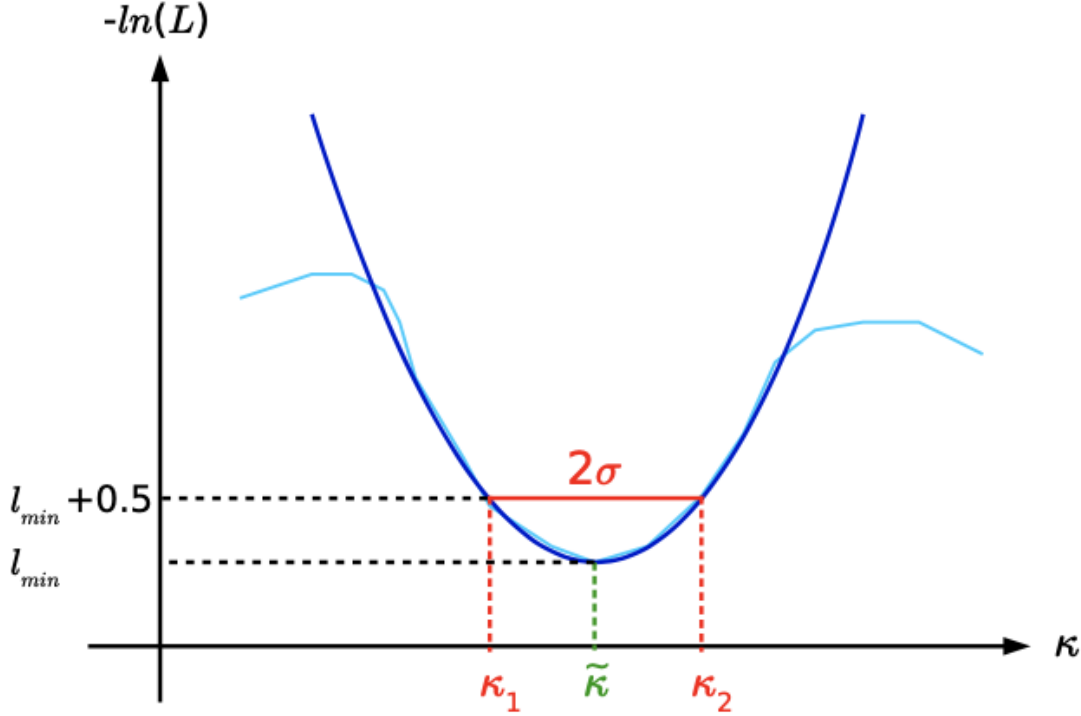


Figure 8.3: Method of minimum negative log-likelihood: Negative log-likelihood (NLL) function versus parameter κ . The cyan curve shows the observed NLL values, while the blue parabola represents the quadratic fit around the minimum. The green vertical line indicates the best-fit parameter value $\tilde{\kappa}$, with red lines marking the 1σ uncertainty interval $\sigma_\kappa = (\kappa_2 - \kappa_1)/2$, where κ_1 and κ_2 are the intersection points of the NLL curve with $\Delta\text{NLL} = 0.5$ (dashed horizontal line). The parabolic approximation (blue) becomes exact in the asymptotic limit around $\tilde{\kappa}$ per Wilks' theorem. Taken from Ref. [89].

For a single parameter of interest h , the 1σ confidence interval is defined by the criterion:

$$\Delta(-\ln \mathcal{L}) \equiv -\ln \mathcal{L}(h) - (-\ln \mathcal{L}(\hat{h})) = 0.5 \quad (8.15)$$

where \hat{h} is the best-fit value minimizing the NLL. This is graphically represented in Figure 8.3.

The uncertainty σ_h is then obtained by solving:

$$-\ln \mathcal{L}(\hat{h} \pm \sigma_h) = -\ln \mathcal{L}(\hat{h}) + 0.5. \quad (8.16)$$

Chapter 9

Main Tools and Software for the Matrix Element Method

The Matrix Element Method requires sophisticated software tools for the purpose of the computation of the multi-dimensional integral of the phase space and to handle the theoretically complex matrix elements and detector response modeling (*cf.* Eq. (8.5)).

This chapter reviews the key frameworks used in modern MEM analyses, focusing on their capabilities, limitations, and possible interfaces.

9.1 MadGraph5 (MadGraph5_aMC@NLO)

MadGraph5_aMC@NLO [90] (shortened to MADGRAPH5) is a cornerstone of modern high-energy phenomenology.

Starting from a user-supplied Lagrangian in UFO format, it automatically generates all contributing Feynman diagrams, builds the corresponding matrix elements, and performs the multi-dimensional phase-space integration needed to obtain differential or total cross-sections.

Its most common practical use is the production of parton-level Monte-Carlo samples (weighted or unweighted LHE files) that seed the subsequent shower, hadronisation and detector-simulation steps.

9.1.1 UFO Models

The UNIVERSAL FEYNRULES OUTPUT (UFO) format [91] is the bridge between FEYNRULES (where a model Lagrangian is encoded symbolically) and event generators such as MADGRAPH5.

By packaging the field content, interactions, coupling orders, and running parameters altogether, a UFO file can be generated, enabling MADGRAPH5 to handle *any* renormalisable or effective theory without manual recoding of Feynman rules.

This flexibility is very useful for Matrix Element Methods: one can scan anomalous Higgs couplings (κ_t , κ_g , κ_λ , ...) or switch to an EFT basis with higher-dimensional

operators simply by swapping the UFO directory, leaving the downstream weight-calculation machinery untouched.

9.1.2 Core Functionality

MADGRAPH5 provides:

- An automatic generation of Feynman diagrams and amplitudes at Leading Order or Next-to-Leading Order in QCD (given there is a corresponding UFO model available),
- An interface to parton shower programs (PYTHIA [67], HERWIG [68]) and detector simulators,
- A phase-space integration via VEGAS [92] which is an algorithm, developed by G. Peter Lepage. It is an *adaptive Monte Carlo integration* package that uses importance sampling to concentrate evaluation points where the integrand is largest.

MadGraph5_aMC@NLO is a powerful software for matrix element generation, cross-section computation and Monte Carlo simulated event generations, which are all very important for any MEM analysis.

9.2 MadWeight

MADWEIGHT [93] is a module of the MADGRAPH5 framework that automates MEM likelihood calculations by carrying out the required phase-space integrations. It has been widely adopted by experimental collaborations, including CMS, for precision measurements and hypothesis testing.

Key Features of MadWeight MADWEIGHT provides a robust implementation of the Matrix Element Method through several critical technical advancements. At its core, the framework seamlessly integrates leading-order matrix elements generated by MADGRAPH5 with detector response models through transfer functions. This integration preserves all quantum correlations in the matrix elements while properly accounting for detector resolution effects.

9.3 MoMEMta: Modular MEM Implementation

MoMEMTA [94] is a C++/Python framework designed as MADWEIGHT's successor, offering greater flexibility. Specifically, the user has full control over the choice of integration variables (i.e the choice of blocks from Section 9.3.3).

9.3.1 Architecture of MoMEMta

MoMEMTA implements a modular computational pipeline that rigorously separates the three core components of the Matrix Element Method: matrix element evaluation, detector response modeling, and phase-space integration.

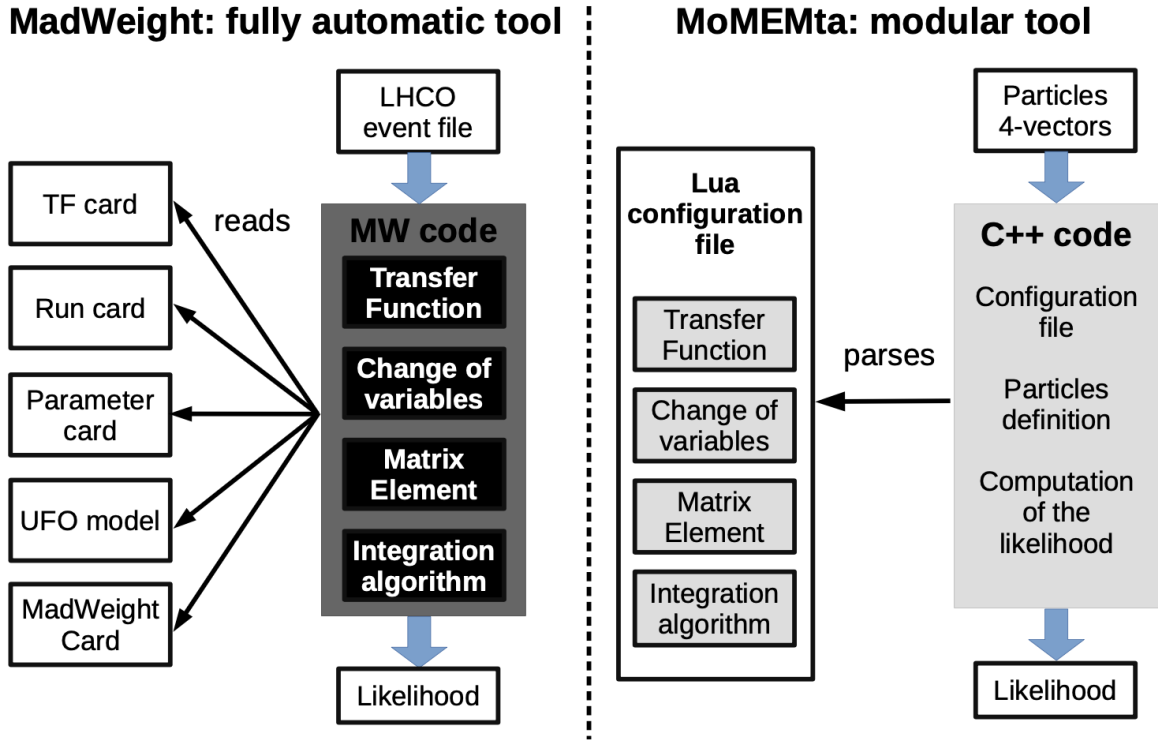


Figure 9.1: Comparison between MADWEIGHT and MOMEMTA working principles. The lighter the color, the more the user has explicit control
Taken from Ref. [89].

This decomposition, illustrated in Fig. 9.1, allows independent optimization of each component while maintaining strict bookkeeping of physical correlations. The framework's C++ core handles numerical integration, with MADGRAPH5 generated matrix elements (in the default workflow) provided as shared libraries.

9.3.2 Integration Algorithms within MoMEMta

MOMEMTA supports several multi-dimensional integration algorithms through the CUBA library [95], which is widely used in particle physics for numerical phase-space integration.

The available algorithms include:

- **VEGAS**: an adaptive Monte Carlo integrator that learns the shape of the integrand and biases sampling toward regions of higher weight. It is particularly efficient when the integrand exhibits localized peaks, which is often the case for resonant processes.
- **DIVONNE**: a stratified sampling algorithm that recursively subdivides the integration domain. It is better adapted to high-dimensional integrals and cases where the integrand is sharply peaked along complicated manifolds.
- **SUAVE**: a hybrid of importance sampling and stratified sampling. It is rarely used in MEM applications, but may be helpful in cases with complex but smooth integrands.

- **CUHRE**: a deterministic cubature rule suited for smooth and low-dimensional integrals. In practice, it is rarely used in MEM computations due to the presence of resonant structures and sharp features.

All of these algorithms are accessible via the MOMEMTA steering Lua files, and can be configured by the user with parameters such as the number of iterations, convergence thresholds, and error tolerances.

The choice of integration algorithm strongly depends on the topology of the process, the number of invisible or unconstrained particles, and the complexity of the matrix element. In this thesis, we mainly used DIVONNE as the default integration algorithm.

9.3.3 Main and Secondary Blocks

Most of the analytic phase-space mappings that MADWEIGHT designates as **Blocks** were imported into the first public release of MOMEMTA.

The blocks are designed to reduce the dimensionality of the multi-dimensional integral in Eq. (8.5) by exploiting the conservation constraints (mostly carried by the δ -functions).

Carefully chosen changes of variables absorb these constraints and isolate each resonant structure of the process into a dedicated integration variable, making the integrand both lower in dimension and more sharply distributed.

These mappings are organised into two categories: the *MainBlock*, which covers the primary kinematic degrees of freedom, and one or several *SecondaryBlocks* for the remaining variables (*cf.* Figures 9.2 and 9.3 for a visual representation of these building blocks).

Contrary to the MADWEIGHT software which automatically selects those substitutions, MOMEMTA give users the flexibility to choose among the available models. The Main Blocks are defined by a list of specific variables to be removed from the integration. These variables are adjusted as a function of all other kinematic quantities associated with the decay chain to enforce the conservation of energy and momentum.

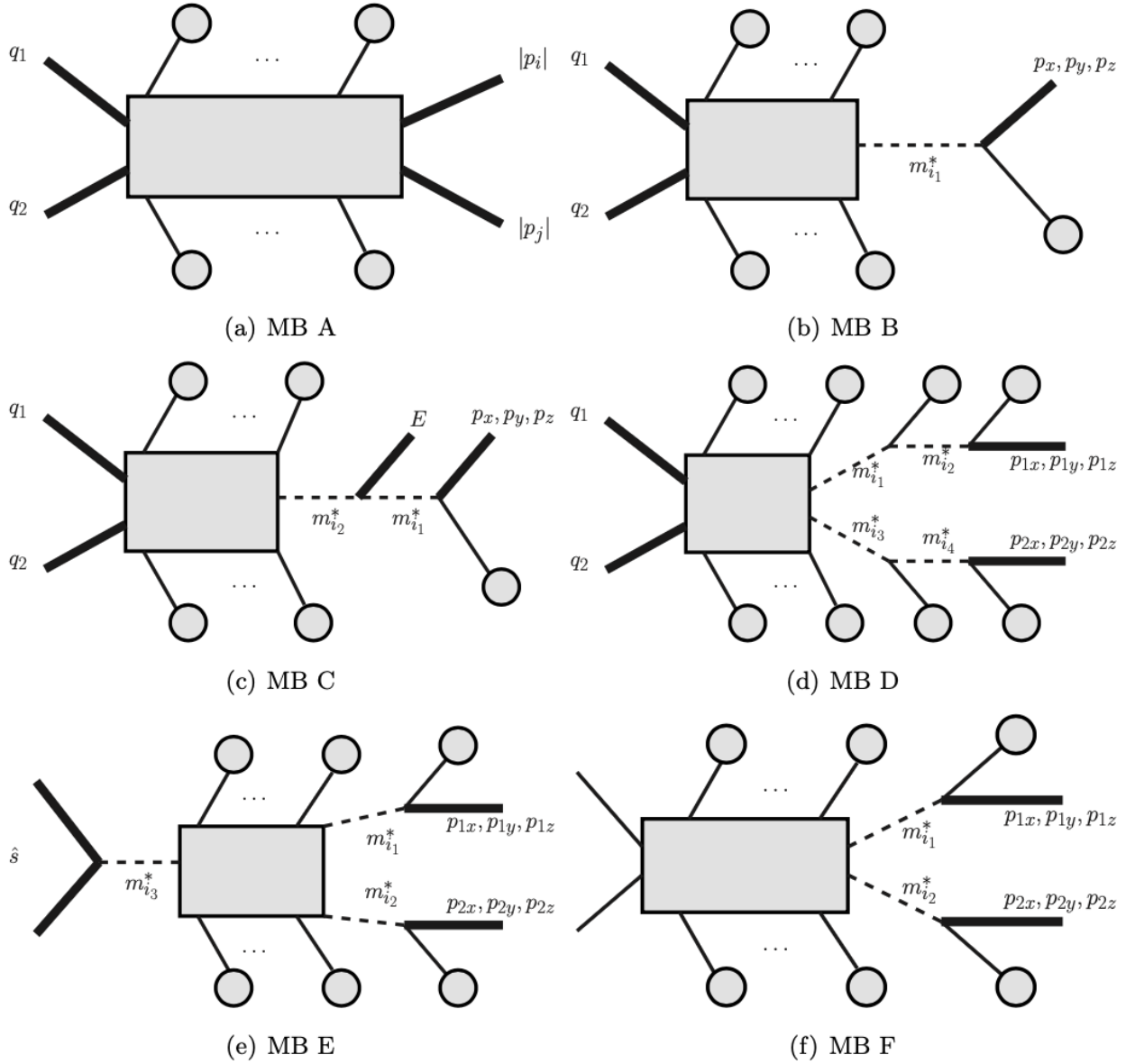


Figure 9.2: Illustration of the six MADWEIGHT Main Block configurations, also used within the MOMEMTA software.

The integration variables of interest are labelled explicitly.

Thick solid lines mark variables removed from the integration, while **dashed lines** indicate intermediate resonances added to it. Taken from Ref. [93].

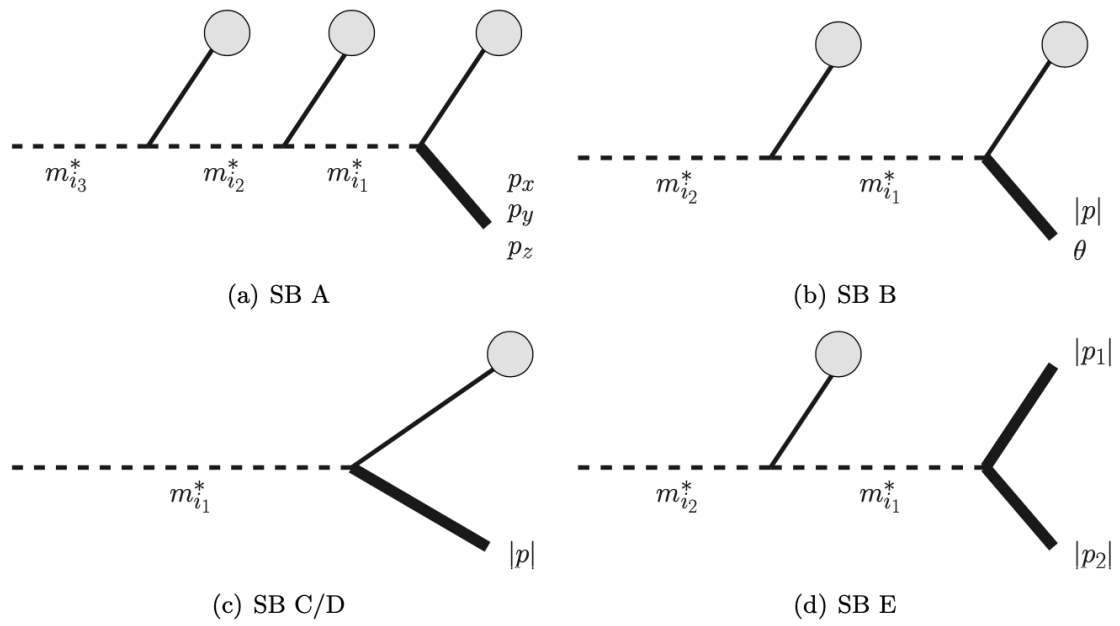


Figure 9.3: Illustration of the four MADWEIGHT *secondary block* configurations, also used within the MOMEMTA software.

The integration variables of interest are labelled explicitly.

Thick solid lines mark variables removed from the integration, while **dashed lines** indicate intermediate resonances added to it. Taken from Ref. [93].

9.3.4 The MoMEMta-MaGMEE Module

The Matrix Element Generator for MadGraph Experiments Extension (MaGMEE) constitutes MoMEMta's interface to translate the matrix element codes automatically generated in Fortran by MADGRAPH5 given the user needs, to C++ MoMEMta-friendly files.

This is a very important addition to MadGraph5_aMC@NLO, to easily access the matrix element for the integration from MoMEMta. Some translations from the Fortran codes into the C++ results might fail, so extra attention is required (and some by-hand translations might be needed).

The source code is openly accessible online in the MoMEMta-MaGMEE ¹ webpage (by clicking on the link).

9.4 POWHEG-BOX-V2: An alternative to MadGraph5

The POWHEG-BOX-V2 framework [96] plays a crucial role in particle physics analysis through its implementation of NLO QCD corrections matched to parton showers.

For each subrepository dedicated to a given process, POWHEG-BOX-V2 computes all of the Next-to-Leading Order contributions to the matrix elements (*i.e.* both the virtual loop contributions and real emission diagrams). But unlike MadGraph, it is not adequate for inclusion to the Matrix Element Method, as it has not been designed or thought for that purpose at all.

It is important that we present this software among the other ones in this present section, as it will be very important for the development of the MEM at NLO (*cf.* Section.15.4.3).

9.4.1 Main usage

The POWHEG-BOX-V2 performs two primary functions for particle physics analysis:

1. **Cross-section calculation:** The framework computes fully differential NLO cross-sections through numerical integration. All the different subprocesses included in POWHEG-BOX-V2 share the same structure, defined and clearly described by the POWHEG-BOX-V2 manual [96].

2. **Event generation:** POWHEG-BOX-V2 can produce weighted or unweighted events at Next-to-Leading accuracy and include an interface to hadronization models (by softwares like PYTHIA [67] or HERWIG [68]) for additional parton showering. The function used for Born kinematic generation is defined [96] as:

¹<https://github.com/MoMEMta/MoMEMta-MaGMEE> (link verified June 2025).

$$\begin{aligned}
\bar{B}^{f_b}(\Phi_n) &= [B(\Phi_n) + V(\Phi_n)]_{f_b} \\
&+ \sum_{\alpha_r \in \{\alpha_r | f_b\}} \int [d\Phi_{\text{rad}} \hat{R}(\Phi_{n+1})]_{\bar{\Phi}_n^{\alpha_r} = \Phi_n, \alpha_r} \\
&+ \sum_{\alpha_\oplus \in \{\alpha_\oplus | f_b\}} \int \frac{dz}{z} G^{\alpha_\oplus}(\Phi_{n,\oplus}) \\
&+ \sum_{\alpha_\ominus \in \{\alpha_\ominus | f_b\}} \int \frac{dz}{z} G^{\alpha_\ominus}(\Phi_{n,\ominus}).
\end{aligned} \tag{9.1}$$

where the square brackets with a suffix represent a context: everything inside the brackets is evaluated relative to that suffix.

The symbol f_b labels a Born flavor structure. Thus, due to this context notation, B and V inside the square brackets refer to the contributions of the Born and soft-virtual cross-section having the flavor structure f_b .

The suffix in the first summation runs over all α_r that have f_b as their underlying Born flavor. The corresponding square bracket under the integral sign means that we integrate over the radiation phase space of the current α_r , keeping the underlying Born variables $\bar{\Phi}_n^{\alpha_r}$ fixed and equal to Φ_n .

The real contribution R has been properly regularized using plus distributions so that it is written with a hat and has to be handled properly (more information in Ref. [96]).

The event files generated by POWHEG-BOX-V2 are in the Les Houches (LHE) format.

9.4.2 Limitations for the MEM

As highlighted previously, and despite its many advantages over MADGRAPH5, the POWHEG-BOX-V2 is not made to be used within existing Matrix Element Methods.

The core limitation lies in the framework itself: POWHEG-BOX-V2 was never intended to expose matrix-element values at given phase-space points or to give non-experts the control needed to do so.

Because it lacks this flexibility where MEM requires it most, the package is inherently ill-suited for direct integration into a Matrix Element Method analysis.

Chapter 10

Historical successes of the MEM

We have defined the Matrix Element Method in the previous chapters, and presented the main softwares developed and commonly used in the community. We will now focus on some of the method's biggest successes.

A lot of what will be discussed here has been greatly inspired by the article ‘The Matrix Element Method in the LHC era’ [97], which has been written in 2017 by Sébastien Wertz (one of the major contributors of the MoMEMta software).

We will split the main successes in two categories: Major successes in High Energy Physics, and those specific to the LHC.

10.1 Major success of the Matrix Element Method: Top Quark Mass Measurements at DØ and CDF

We start this section with the first and main historical success of the Matrix Element Method in the most precise measurement of the mass of the top quark at the DØ and CDF experiments at the Tevatron Collider (Fermilab) [85, 98–100].

The precise measurement of the top quark mass m_t has been a cornerstone of high-energy physics since its discovery in 1995 by the CDF and DØ collaborations. Among the various techniques employed for the measurement of m_t , the MEM emerged as a revolutionary approach, outperforming traditional methods in both statistical precision and control of systematic uncertainties.

Its adoption by the DØ and CDF collaborations marked a fundamental shift in top quark analyses, setting new standards for precision and reliability in collider physics.

Prior to MEM, top mass measurements relied on Template Methods (comparing reconstructed kinematic distributions to Monte Carlo (MC) templates) and Kinematic Fitting (minimizing a χ^2 based on assumed decay kinematics). But these methods had key limitations: there was still an important ambiguity between signal and background (as the discrimination from these methods was weak, and the combinatorial backgrounds in jet pairing and neutrino reconstruction introduced

large uncertainties), and also systematic biases as the methods heavily relied on MC modeling (for fragmentation, detector effects, and background shapes). It is also important to point out that reducing events to a single observable (as done in the Template Methods) lead to loss of information.

The $t\bar{t}$ channel (the one used for the top mass measurement) was a rare process at the DØ and CDF experiments at the time. This is no longer the case at LHC, but its rarity back then made any information loss an important issue in the search for precise measurements of the top quark mass.

The Matrix Element Method addressed all of these issues, by being statistically optimal by construction. It used the full event information, including all of the hidden correlations between observables (unlike template methods). The MC dependence was also greatly reduced due to the fact that the MEM factorized physics (matrix elements) from detector effects (transfer functions), minimizing modeling biases.

The DØ collaboration performed a pioneering measurement in 2004 using the MEM [85], significantly reducing the statistical uncertainty from to previous techniques, and demonstrated its robustness against QCD radiation effects.

10.2 Major applications and successes of the MEM at the LHC

The MEM's success in top mass measurements cemented its role as the gold standard for precision collider physics, influencing later applications by the general-purpose LHC experiments ATLAS and CMS that we will discuss in this part of the chapter.

10.2.1 Searches for the $t\bar{t}h$ process

In addition to the top quark mass, an other crucial parameter of the SM is the Top-Higgs coupling. The discovery of the production of Standard Model (SM) Higgs bosons in association with Top quark pairs ($t\bar{t}h$ process) is the natural approach to get access to direct measurements of this coupling.

This discovery is extremely challenging due to the the small signal-to-background (S/B) ratio. Data collected at the time of the writing of Ref. [97] only allowed to set upper limits on the signal strength, and it was expected that LHC Run 2 would allow the discovery of the process.

The ATLAS and CMS experiments have performed searches for the $t\bar{t}h$ process in many different final states. Some analyses featured MEM-based discriminants: on the one hand in final states with $H \rightarrow b\bar{b}$ and semi-/fully-leptonic $t\bar{t}h$ decays [101–104], on the other in multi-lepton final states with $H \rightarrow VV$ [105, 106].

In these analyses, the MEM likelihoods were combined with non-kinematical information (such as quantities related to object reconstruction and identification) to further increase the sensitivity to the signal.

10.2.2 Search for s-channel single Top quark production

The s-channel single top is the rarest top quark production mode. While being rather difficult to detect at the LHC (due to a less-favorable initial state, at least at the time at the writing of Ref. [97]), upper limits on its cross-section have been set by the ATLAS [107] and CMS [108] collaborations. BDTs were used in both these analysis to enhance the sensitivity to the signal.

ATLAS had repeated the search for this process by re-analysing its 8 TeV dataset using updated calibrations and a in-house implementation of the Matrix Element Method [109], and was able to substantially increase the expected/observed significance for the process in the background-only hypothesis, up from 1.4/1.3 σ in [107] to 3.9/3.3 σ .

The ATLAS Collaboration now reports 4 σ evidence for s-channel single-top production using the full Run 2 statistics at $\sqrt{s} = 13$ TeV [110].

10.2.3 Success in the measurement of $t\bar{t}$ spin correlation in the μ +jets channel

In the SM, top-quark pairs are produced with correlated spins, and decay quickly enough for this correlation to manifest itself in their decay products. A measurement of this correlation provides an important test of the SM, as well as sensitivity to possible indirect effects from physics beyond the SM.

CMS performed such a measurement [111] in the μ +jets channel using a Matrix Element Method, achieving the most precise determination of the $t\bar{t}$ spin correlation in this final state to date.

Beyond parameter extraction, the MEM was also used for hypothesis testing by comparing the compatibility of the observed data with the ‘correlated’ versus ‘uncorrelated’ spin scenarios. The computation of event likelihoods in this analysis was performed using the MADWEIGHT package [93].

10.2.4 Discovery of the Higgs boson and spin-parity measurements in the $h \rightarrow 4l$ channel

Matrix Element techniques (notably the ‘MELA’ approach) were employed by CMS during the discovery of the SM Higgs boson to enhance the sensitivity of the $H \rightarrow ZZ^* \rightarrow 4l$ search [112]. Similar tools were later adopted by both ATLAS and CMS to constrain the spin-parity properties of the newly discovered resonance [113–118].

Unlike the previous examples discussed in this section, no multidimensional phase-space integration was required here: the final state contains only visible particles, with no neutrinos or missing energy, and the detector resolutions on electron and muon kinematics are sufficiently small that transfer functions can be approximated as delta functions. As a result, the event likelihood reduces to a direct evaluation of the matrix element at the reconstructed four-momenta of the final-state leptons.

Chapter 11

Legacy analysis: Leading Order MEM Implementation in the $gg \rightarrow HH \rightarrow b\bar{b}\gamma\gamma$ channel

Among various techniques developed to measure Higgs boson tri-linear coupling constant λ_{3H} , the Matrix Element Method stands out for its statistical optimality and event-by-event sensitivity.

By evaluating the likelihood of each observed final state under different theoretical hypotheses, the MEM allows to maximally exploit the multidimensional structure of phase-space.

Such an approach is particularly powerful in channels like $gg \rightarrow HH \rightarrow b\bar{b}\gamma\gamma$, where the signal is rare and the backgrounds are overwhelming.

Motivated by this potential, a pioneering study aiming to implement the MEM at Leading Order for this di-Higgs production channel within the ATLAS experiment was performed in Ref. [89]. It represents the first complete application of the MEM for process and provides a crucial baseline for any further developments, including the Next-to-Leading Order formalism that this thesis aims to establish.

11.1 Matrix Element Construction and Effective Model Design

11.1.1 EFT Vertices and $gg \rightarrow HH$ Loop Approximation

Remember that the process $gg \rightarrow HH$ at LO is loop-induced and dominated by top-quark loops (*cf.* Figure 2.3.a).

The progress in the its theoretical description is described in Figure 11.1.

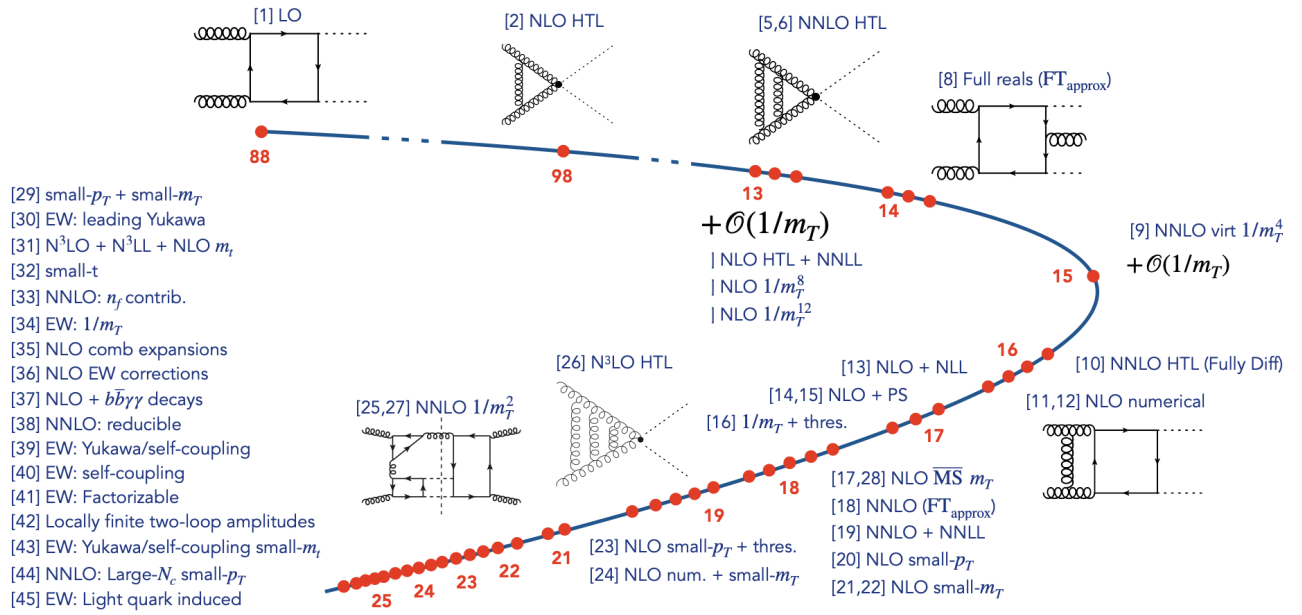


Figure 11.1: Gluon fusion di-Higgs history overview, from HTL to full picture (LO and NLO and higher order).

Taken from a presentation by G.Heinrich at the Higgs Pair Workshop 2025, Ref. [119].

Due to the computational cost of loop evaluation within matrix element integration, ref. [89] adopted the effective field theory (EFT) approximation, where the heavy top-quark loops are replaced by point-like effective vertices: ggH , $ggHH$, and $H\gamma\gamma$. These operators allow one to represent the complex loop structure via simplified tree-level vertices suitable for MEM integration.

11.1.2 UFO Model Merging and κ Parameterization

The legacy analysis faced several challenges, starting with the absence of a single UFO model containing all the necessary effective vertices. The HEFT model available in MadGraph5_aMC@NLO included the ggH and $H\gamma\gamma$ couplings but lacked the $ggHH$ vertex, while the SM_EFT_FF_bt model provided ggH and $ggHH$ interactions but omitted $H\gamma\gamma$.

To solve this, the authors of Ref. [89] constructed a new custom UFO model (named SM_EFT_FF_bt_haa_kappa), by merging the components of the two existing models and manually verifying the Lorentz structures.

Another key feature of this new custom UFO model was the inclusion of a free parameter $\kappa_\lambda = \lambda_{3H}/\lambda_{3H}^{SM}$, allowing hypothesis testing of BSM self-coupling strengths. The implementation was validated by comparing the total cross-section at $\sqrt{s} = 14$ TeV against theoretical predictions from HPAIR¹.

HPAIR is a public Fortran program that computes Leading and Next-to-Leading Or-

¹<http://tiger.web.psi.ch/hpair> (link verified June 2025).

der (LO/NLO) cross-sections for Higgs-boson pair production via gluon fusion at hadron colliders for different values of κ_λ .

11.2 Event Simulation and Detector Smearing Framework

11.2.1 Parton-Level Generation and Background Channels

The authors generated parton-level events at Leading Order for both signal and background using MADGRAPH5.

Two dominant backgrounds were simulated: continuum $b\bar{b}\gamma\gamma$ production and $t\bar{t}H$ with $H \rightarrow \gamma\gamma$, both of which mimic the final state and challenge the signal discrimination.

11.2.2 Detector Resolution and Simplified Transfer Functions

To model the detector response, a simplified smearing scheme was implemented: 1% Gaussian smearing on photon energies and 10% on b -quark energies. No angular smearing or fake rates were included.

This decision was motivated by computational constraints and the proof-of-concept nature of the study.

11.2.3 Pre-selection requirements at LO

As the computation of the likelihood in the MEM is very CPU consuming, pre-selection cuts mimicking the ATLAS detector's acceptance (and diphoton triggers thresholds) were applied at generator level, including thresholds on p_T , $|\eta|$, invariant masses, and angular separations.

Specifically, the pre-selection requirements for the final state particles (consisting of photons γ and b -jets) are:

Objects pre-selection requirements

- **Photon selection**
 - $p_T(\text{leading } \gamma) > 43 \text{ GeV}$
 - $p_T(\text{subleading } \gamma) > 30 \text{ GeV}$
 - $|\eta_\gamma| < 2.37$, excluding $1.37 < |\eta_\gamma| < 1.52$
- **b -jet selection**
 - $p_T(b \text{ jet}) > 35 \text{ GeV}$
 - $|\eta_b| < 2.5$
- **Separation and invariant mass**
 - $\Delta R(\gamma, b) > 0.2$
 - $123 < m_{\gamma\gamma} < 127 \text{ GeV}$

where p_T refers to the transverse momentum, η is the pseudorapidity, and ΔR denotes the angular separation between objects.

Subscripts such as *leading* and *subleading* refer to the ordering in transverse momentum, *leading* being the highest.

11.3 Likelihood Evaluation with MadWeight

Integration Setup and Custom Transfer Functions

Their first implementation of the MEM was done using MADWEIGHT, a component of MadGraph5 designed for likelihood integration (*cf.* Section 9.2).

MADWEIGHT evaluates the probability of an observed event by integrating the squared matrix element over phase space, convoluted with PDFs and transfer functions.

Complications came from MADWEIGHT's fixed input structure, and the VEGAS integrator used by MADWEIGHT showed instability, especially for background hypotheses.

11.4 Migration to MoMEMta and Integration Strategy

11.4.1 Matrix Element Compatibility and C++ Translation

Due to the limitations of MADWEIGHT, the authors migrated the analysis to MO-MEMTA, a modular C++ toolkit offering more flexibility.

However, the migration was not straightforward. The matrix elements exported through the MOMEMTA-MAGMEE plugin were not always translated consistently: in some cases, parts of the matrix element files originally implemented in Fortran were not propagated into the C++ structures expected by MOMEMTA. This issue occurred in particular for the main process of interest, gluon-fusion di-Higgs production, where some specific components of the matrix element was missing after translation.

To solve this issue, the authors translated the relevant Fortran routines into C++ by hand.

Another issue that required attention was the occurrence of floating-point instabilities in MOMEMTA, which occasionally led to invalid event flags. In particular, events with two photons could yield negative values for the squared invariant mass due to rounding errors inherent in double-precision arithmetic. The authors corrected this problem by introducing infinitesimal shifts in the photon energies, thereby restoring a strictly positive mass value $m_\gamma > 0$.

11.4.2 Lua Configuration and Parametrization Choices

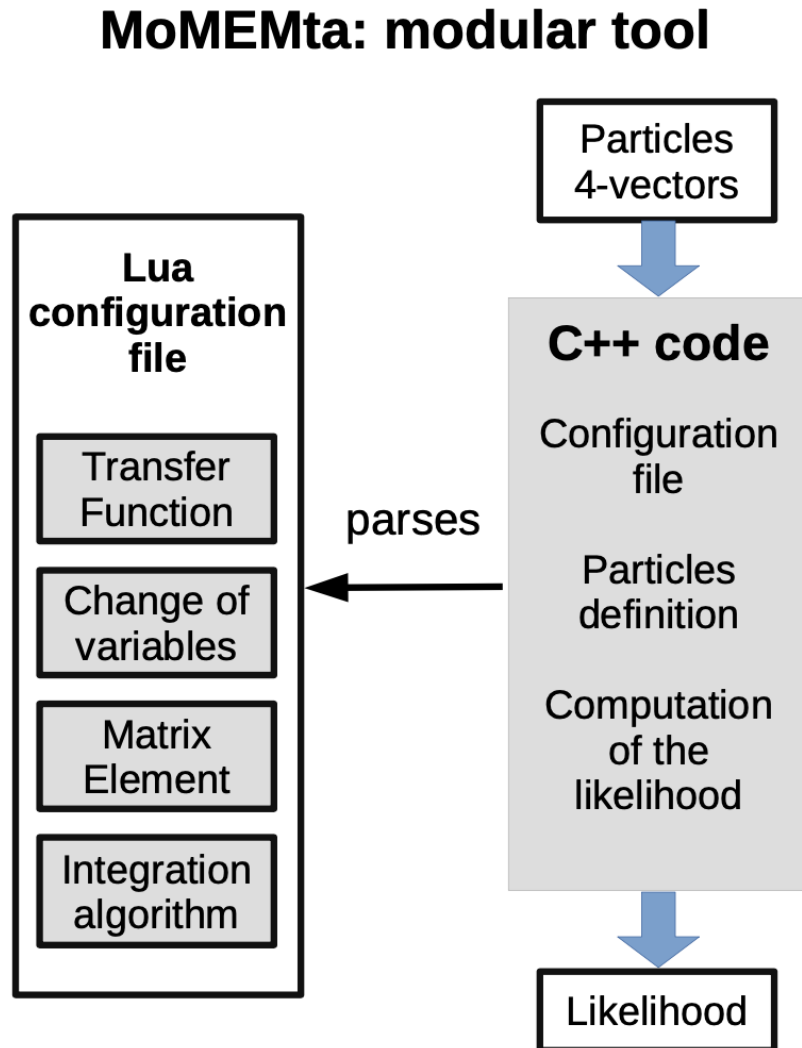


Figure 11.2: Visual representation of the MoMEMTA framework working principles. The lighter the color, the more the user has explicit control Taken from Ref. [89].

Because MoMEMTA is fully modular, every process is steered by a dedicated Lua configuration file (see Fig. 11.2).

Within a single Lua script, the user can specify

- **variable transformations** via “Main” and “Secondary” blocks,
- **transfer functions** $W(\mathbf{x}^i, \mathbf{y})$ for each reconstructed object,
- the **matrix element path** for the file corresponding the the process of interest,
- the **multi-dimensional integrator**: VEGAS, DIVONNE, or SUAVE.

For gluon-fusion Higgs pair production, the author used the MOMEMTA Main Block A to parameterize the phase space. This choice removes the Bjorken variable from the set of integration parameters, along with two of the final-state particle energies. They decided to remove the energies of one photon energy and one b -jet (any pair among the four $b\bar{b}\gamma\gamma$ final-state particle energies could equivalently have been chosen).

Another key module used is `GaussianTransferFunctionOnEnergy`, which models the detector resolution for the selected objects, and corresponds to the transfer function(s) W introduced in eq. 8.5

11.5 Statistical Discrimination and Measurement of the Higgs Self-Coupling

11.5.1 MEM Likelihood Ratio (LHR) Versus Boosted Decision Tree (BDT) Performance

To evaluate performance, the authors computed ROC curves comparing the MEM likelihood ratio to a Boosted Decision Tree (BDT) trained on the same sample.

MOMEMTA's output outperformed both the BDT and MADWEIGHT's, particularly in low signal-to-background regions.

This demonstrated that the MEM is able to capture more physically meaningful correlations than BDT machine learning models, especially in kinematically constrained final states with narrow resonances.

11.5.2 Extended Likelihood and κ Estimation

The strategy adopted to obtain likelihood scans proceeds as follows:

For a given dataset that contains N_{evt} reconstructed events, let κ denote the parameter of interest (in this work the Higgs self-coupling modifier κ_λ).

A *likelihood scan* is produced by computing the negative log Likelihood (NLL) of interest for many discrete values of κ_λ in a given range.

The minimum attained at $\kappa = \hat{\kappa}$ defines the best-fit estimate, and the statistical uncertainty σ is estimated using the procedure described in Section 8.4 using Wilk's theorem.

To assess statistical consistency, we generate a large ensemble of pseudo-datasets under the null hypothesis $\kappa_{\text{test}} = 1.00$. For each pseudo-dataset, we perform the full profiling procedure again, drawing the total number of events from a Poisson distribution centered on the expected yield. All of the resulting best-fit values $\hat{\kappa}_k$ from each pseudo-datasets are then collected into a histogram to build the pull distribution.

The pull for each pseudo-datasets is computed as:

$$\omega_k = \frac{\hat{\kappa}_k - \kappa_{\text{test}}}{\sigma_k},$$

where σ_k is the profiled uncertainty computed from Wilk's theorem for the k -th fit. An unbiased and well-calibrated estimator yields a pull distribution that is Gaussian with a mean at zero and unit width.

The κ_λ extraction is performed using the *extended likelihood* formalism, that combines the per-event likelihood \mathcal{L}_{Kin} with a Poisson likelihood for the expected signal yield $\mathcal{L}_{\text{Yield}}$ as discussed in Section 8.3.3.

This exploits both the differential shape of the kinematic discriminator and the overall event rate, maximizing the sensitivity of the κ_λ extraction (*cf.* Figure 11.3).

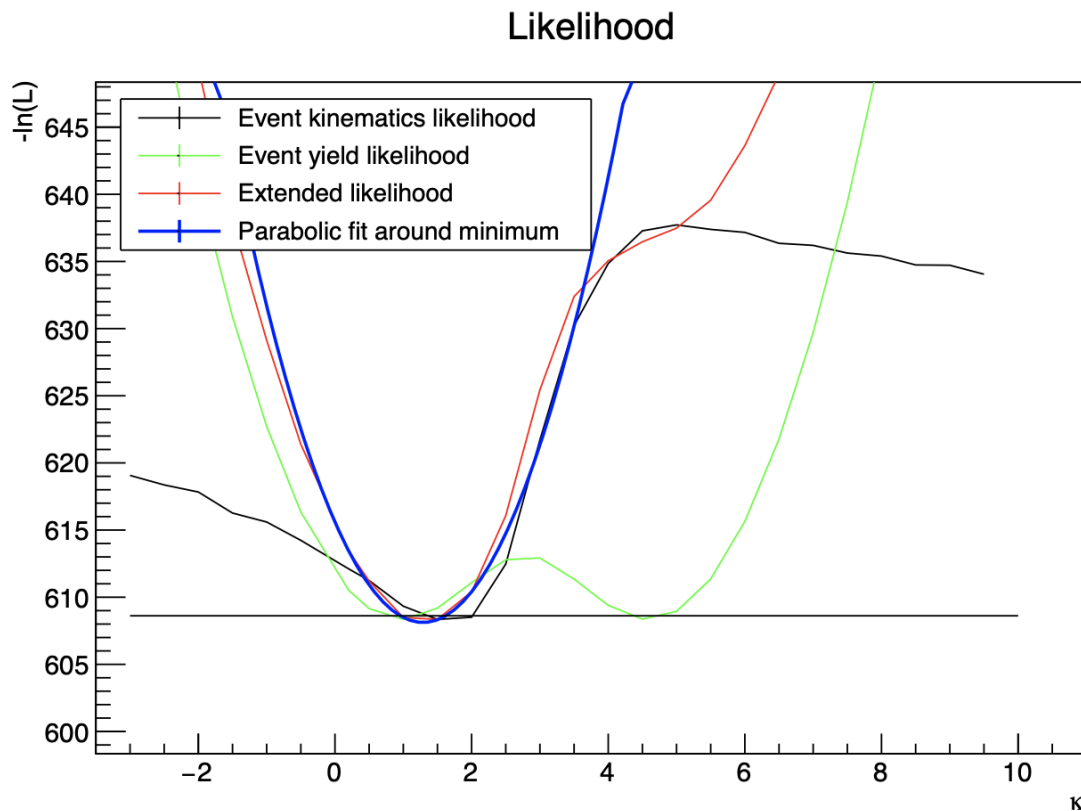


Figure 11.3: Likelihood scan of the negative logarithm of: the event kinematics likelihood (black), the event yield likelihood (green) and the extended likelihood (red) as a function of κ_λ for a sample of ggF signal events (generated at $\kappa_\lambda = 1$, with 16 pure signal events).

The (blue) curve is a parabolic fit around the minimum of the extended likelihood (red), same as in Figure 8.3. Taken from Ref. [89].

An ensemble of $N=124$ signal only pseudo-datasets have been studied by the authors, and the best-fit result obtained was $\kappa_\lambda = 1.017 \pm 0.3149$ (*cf.* Figure 11.4), where we estimate the error on κ_λ from the theoretical uncertainty σ and the number of pseudo-datasets N using the formula: $\frac{\sigma}{\sqrt{N}}$.

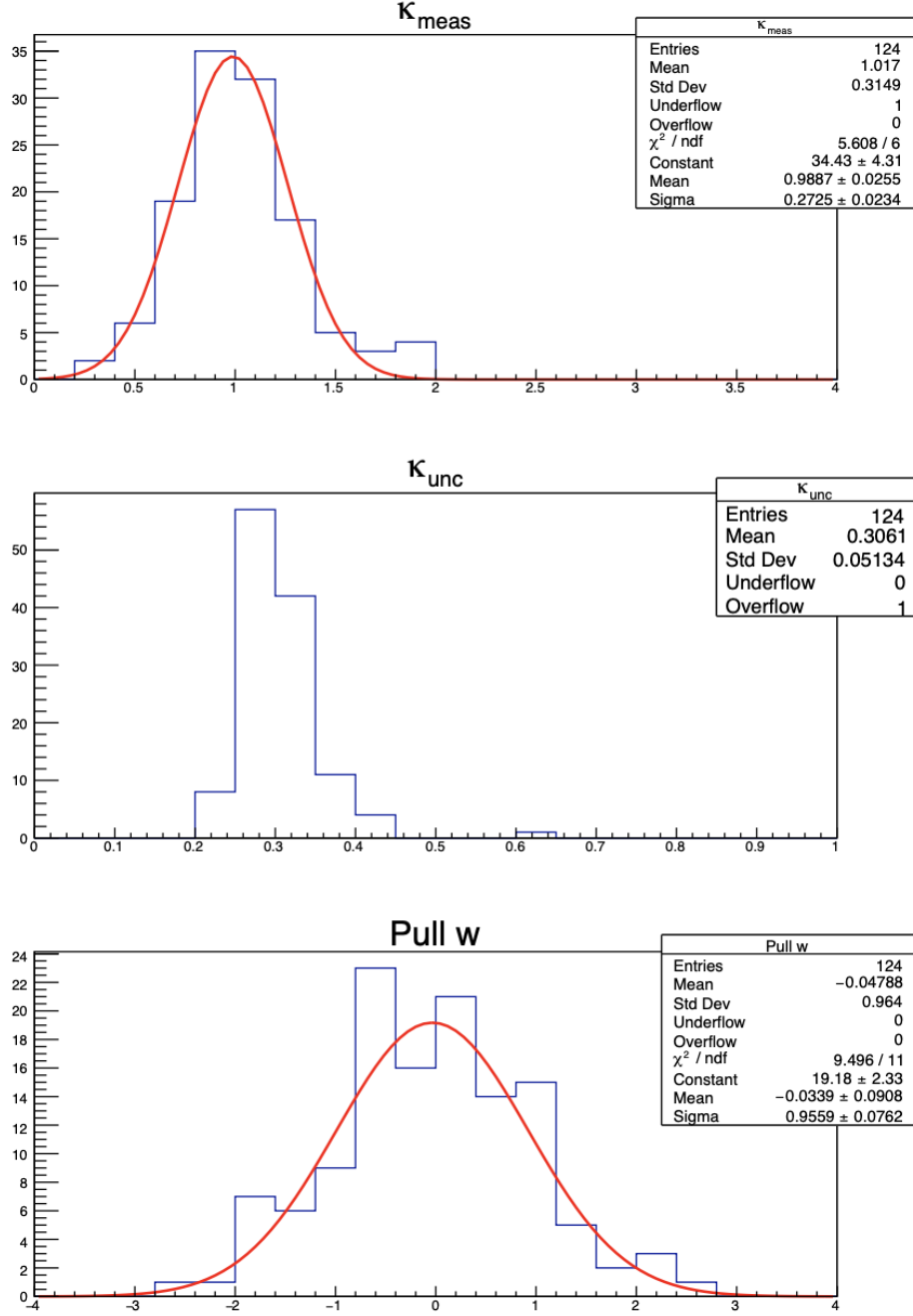


Figure 11.4: Histograms of the measured value of (κ_{meas} , top), of the corresponding statistical uncertainty (κ_{unc} , middle) and of the pull value (ω , bottom) for signal events only. Taken from Ref. [89].

This outcome demonstrates that the analysis successfully passed the validation test. Datasets including background process (here qcd non-resonant $b\bar{b}\gamma\gamma$ background) have been studied to produce likelihood scans (*cf.* Figure 11.5).

The minimum of the extended NLL is still clearly peaked around the $\kappa_\lambda = 1.00$.

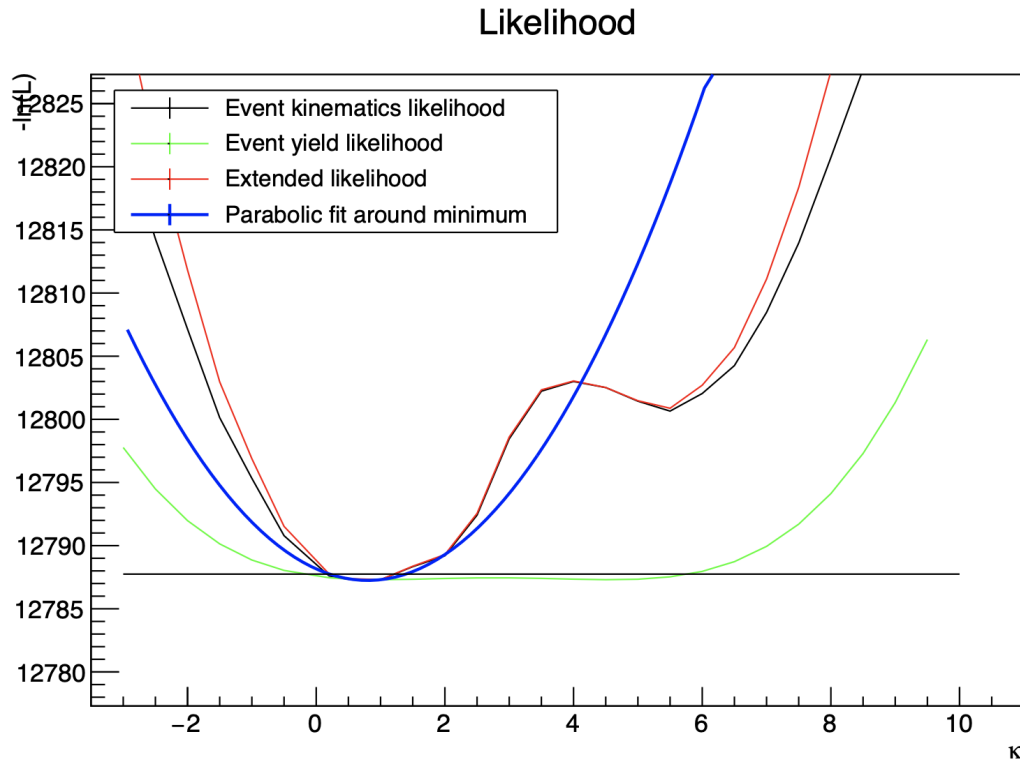


Figure 11.5: Negative logarithm of the event kinematics likelihood (black), the event yield likelihood (green) and the extended likelihood (red) as a function of κ_λ for a sample of 16 ggF signal events (generated at $\kappa_\lambda = 1$), and 290 non-resonant $b\bar{b}\gamma\gamma$ background events.

The (blue) curve is a parabolic fit around the minimum of the extended likelihood (red), same as in Figure 8.3. Taken from Ref. [89].

Due to CPU-limitations (on time and resources) and the consequent expected number of background events needed for each likelihood scan, it was not possible for the authors to produce the distributions for the best-fitted κ_λ from the resulting likelihood scan histogram.

11.5.3 Treatment of Zero-Likelihood Events

An important technical observation was made when processing background $t\bar{t}H$ events: a non-trivial amount of them returned with zero likelihood under the signal hypothesis.

While this is physically plausible due to the large difference between the kinematics of signal and background, a small number of events also produced a zero likelihood value under their own correct hypothesis. The authors addressed this by identifying

and removing such events from the statistical ensemble.

An other issue observed by the authors was non-negligible number of events producing ill-defined likelihood scans.

In these cases, the integral failed to converge smoothly, leading to noise or abrupt kinks in the $\log \mathcal{L}(\kappa)$ curve.

The solution adopted was to identify such pathological events using pre-fits and replace them with equivalent non-problematic events from the same dataset.

11.6 Summary and Outlook Toward NLO Extensions

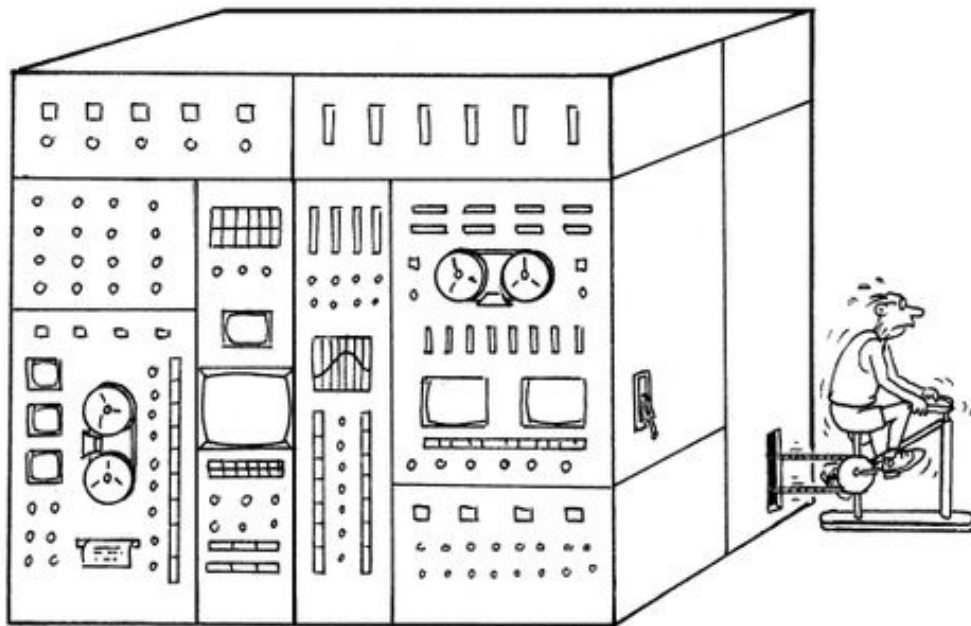
The study conducted in Ref. [89] constitutes the first dedicated implementation of the Matrix Element Method for the process $gg \rightarrow HH \rightarrow b\bar{b}\gamma\gamma$ at Leading Order.

Facing a channel of exceptionally low signal yield and overwhelming irreducible backgrounds, they developed and validated a complete MEM analysis pipeline.

They successfully demonstrated that the MEM could provide a meaningful sensitivity to the Higgs boson self-coupling. The use of extended likelihood techniques and the switch to a modular and numerically robust framework like MOMEMTA allowed them to stabilize integrations, manage convergence pathologies, and extract κ_λ using all available information.

Part IV

Developing a Matrix Element Method at NLO



The Matrix Element Method has established itself as a powerful analysis technique in particle physics, particularly valuable for extracting fundamental parameters and enhancing signal discrimination in processes with limited statistics.

However, as experimental precision increases (especially at the LHC), a persistent limitation has become evident: the MEM has predominantly been applied using theoretical predictions at Leading Order accuracy.

While LO computations offer a tractable implementation framework and are sufficient for qualitative insights, they neglect the impact of higher-order QCD corrections, which can significantly affect both the total cross-sections and differential distributions, e.g in Higgs boson production at the LHC.

Chapter 12 motivates the extension of extending the Matrix Element Method to Next-to-Leading Order, outlining the main obstacles that arise beyond Leading Order.

Chapter 13 surveys the key theoretical and phenomenological studies that have addressed these challenges with NLO MEM formulations for different analysis.

And **Chapter 14** presents the framework developed in this thesis: a new MEM@NLO implementation within MOMEMTA applied to the extraction of κ_λ in the $b\bar{b}\gamma\gamma$ final state.

Content

12 Problem Statement and Motivation	147
12.1 Order of the Monte Carlo generated events and order of the MEM . . .	148
12.2 Using NLO generated samples on MEM@LO	149
12.3 Problem statement	150
13 Theoretical considerations on the MEM at NLO	153
13.1 Existing Foundations of the NLO Formalism	153
13.2 Incorporating Initial-State Radiation to the Leading Order formalism	154
13.2.1 Boost Correction Method	154
13.2.2 Sudakov Reweighting	155
13.3 Extending the Matrix Element Method to Next-to-Leading Order . .	155
13.4 Variants of the Matrix Element Method at Next-to-Leading Order . .	157
13.5 Challenges Identified in the Literature	157
13.6 Conclusions	158
14 Our Contribution: A New MEM Formalism at NLO	159
14.1 Access to the Matrix Elements at NLO	159
14.2 Modifying POWHEG-BOX-V2	160
14.2.1 ggHH repository	160
14.2.2 $t\bar{t}H$ repository	161
14.3 Validation of the interface with matrix element comparison	161
14.3.1 Matrix element for $gg \rightarrow HH \rightarrow b\bar{b}\gamma\gamma$ at LO	161
14.3.2 Matrix Elements for $gg \rightarrow HH \rightarrow b\bar{b}\gamma\gamma$ at NLO	164

14.3.3	Matrix Elements for $t\bar{t}H$ at LO	165
14.3.4	Matrix Elements for $t\bar{t}H$ at NLO	166
14.4	Use of MADGRAPH5 for our MEM@NLO	167
14.5	Modifying MOMEMTA	168
14.5.1	Block N: Main Ideas	168
14.5.2	ExtraRadiation_3DOF: Main idea	173
14.5.3	Determination of the Infrared (IR) and Ultraviolet (UV) Limits	174
14.5.4	Updating Lua Steering Files	175
14.6	Summary of our Choice of MEM Integration Variables	177
14.7	Improving the Transfer Function for ATLAS fully simulated events .	178
14.8	Validation and Conclusion	180

Chapter 12

Problem Statement and Motivation

Historically, the MEM has been applied predominantly at LO, where the scattering amplitude includes tree-level Feynman diagrams only.

This approximation has been more than enough for the many applications we have already discussed in Chapter 10. The sensitivity to loops and other higher order corrections depends on the analysis. The impact of loop amplitudes and other higher-order corrections is highly process-dependent.

At the Tevatron for example, top-quark pair production ($q\bar{q} \rightarrow t\bar{t}$) was described almost entirely by tree-level diagrams and occurred close to the collider's kinematic threshold.

By contrast, Higgs pair boson production at the LHC is dominated by the loop-induced gluon-fusion mechanism, and the much higher centre-of-mass energy can produce Higgs bosons with large transverse momentum, making higher-order effects particularly significant.

Excluding these corrections leads to biased parameter extractions, undermining the method's statistical [121]. Incorporating Next-to-Leading Order corrections into the MEM is therefore imperative for consistency with the precision frontier in experimental measurements.

The extension of the Matrix Element Method to NLO represents a non-trivial theoretical and computational advancement. While the strategy described in Chapter 8 is well-defined at Leading Order, its extension to higher orders in perturbation theory faces several conceptual and technical challenges.

12.1 Order of the Monte Carlo generated events and order of the MEM

Before diving into the development of the Matrix Element Method at Next-to-Leading Order, let's clarify the terms to avoid any confusion: Leading Order and Next-Leading Order are used to define the order of the perturbative expansion for a given *matrix element*.

Order of the Monte Carlo generated events Matrix elements are the engine of the MC event generators, and the perturbative order at which they are evaluated sets the physical reality of the resulting generated events. Consequently, one distinguishes between *leading-order* and *next-to-leading-order* MC samples.

Order of the Matrix Element Methods Matrix elements are key elements for the Matrix Element Method, as they are used within the multi-dimensional integral (*cf.* Eq. (8.5)).

The perturbative order of the matrix element (LO, NLO,...) defines the theoretical order of the MEM analysis itself.

Throughout this manuscript we attach small graphical icons to each MEM configuration so that the reader can immediately recognize its perturbative order. The legend for these icons is shown in Fig. 12.1.

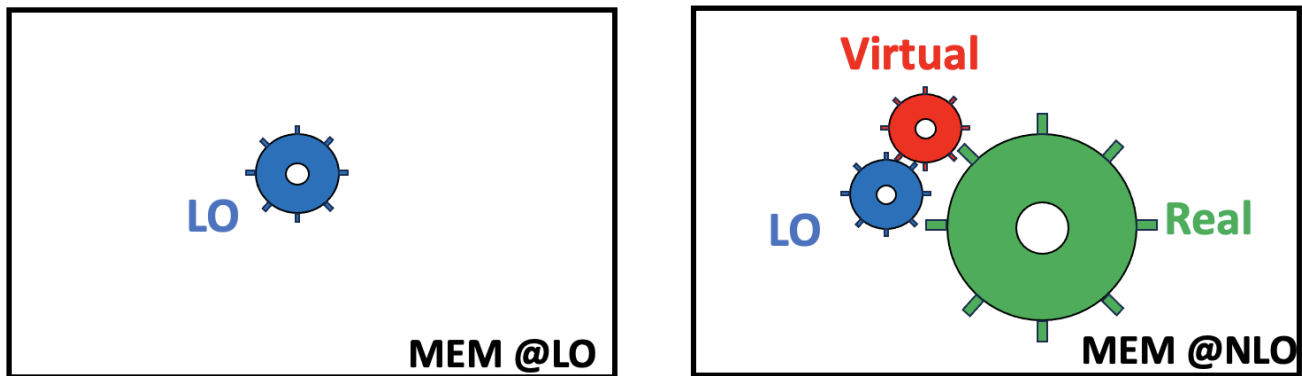


Figure 12.1: Indicators used in the following of this manuscript to avoid any confusion about the order of the Matrix Element Method analysis. (Left) indicator for Leading Order MEM ; (Right) indicator for Next-to-Leading Order MEM.

MEM analysis can be performed by mixing and matching the perturbative order of the Monte Carlo sample (LO or NLO) with any of the MEM's (LO or NLO). Possible pairings are illustrated in Fig. 12.2.

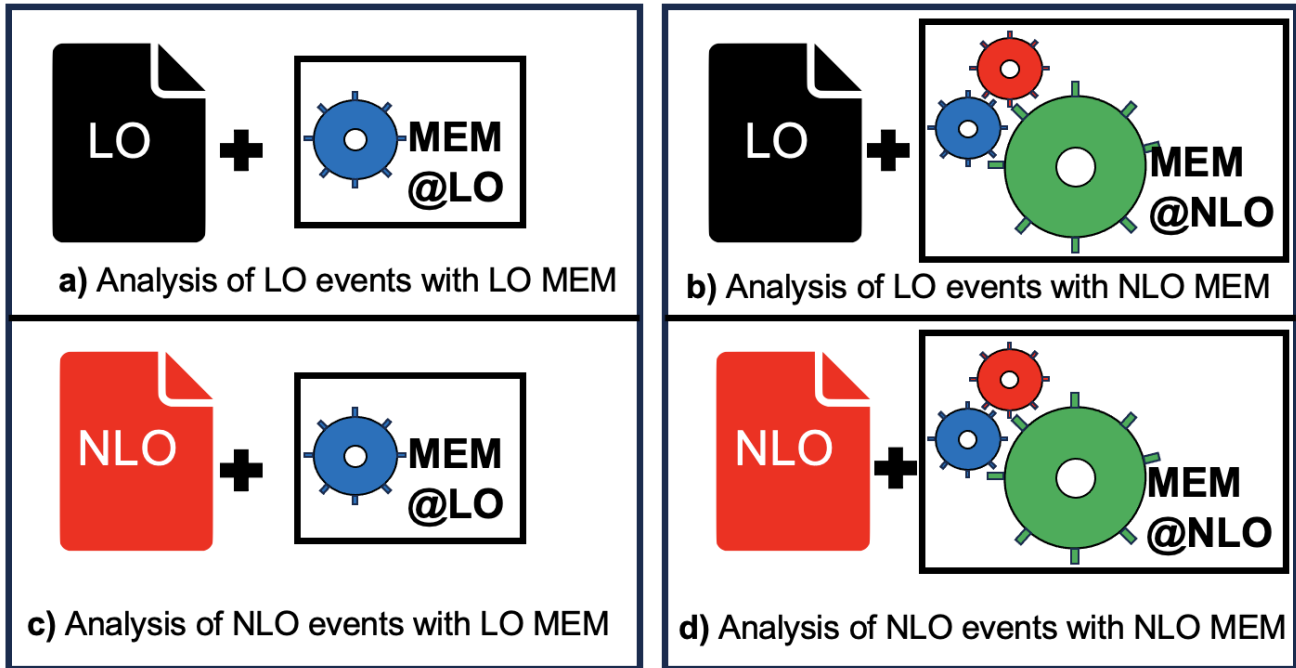


Figure 12.2: Representation of all the different possible combination when LO and NLO MC generated events are studied under LO and NLO Matrix Element Methods.

(a) LO MC events with LO MEM ; (b) LO MC events with NLO MEM ; (c) NLO MC events with LO MEM ; (d) NLO MC events with NLO MEM.

12.2 Using NLO generated samples on MEM@LO

The legacy analysis, presented in Chapter 11, was dedicated to validating the method using only LO MC generated events.

To build upon this foundation, we aimed to both fully understand and reproduce the MEM@LO framework. The entire analysis was reconstructed from the ground up, following the same logic and methodology, while ensuring complete independence from the legacy implementation.

This effort served several purposes: to gain a detailed understanding of the original choices and assumptions; to verify that the newly developed plotting macros and analysis tools could independently and correctly reproduce the main results; and to establish a robust and well-controlled framework suitable for the next natural step: testing the MEM@LO on NLO MC generated datasets.

We successfully reproduced the excellent performance of MEM@LO on LO generated events, and extended the study by applying NLO generated events (using the POWHEG-BOX-V2 software, as described in subsection 15.1.2), assessing for the first time the response of this LO-based framework to higher-order event kinematics. The resulting ROC curves, obtained for both LO and NLO event samples, are shown in Fig. 12.3. A detailed discussion and interpretation of these results are presented

in Section 16.1, and in particular in Fig. 16.2.

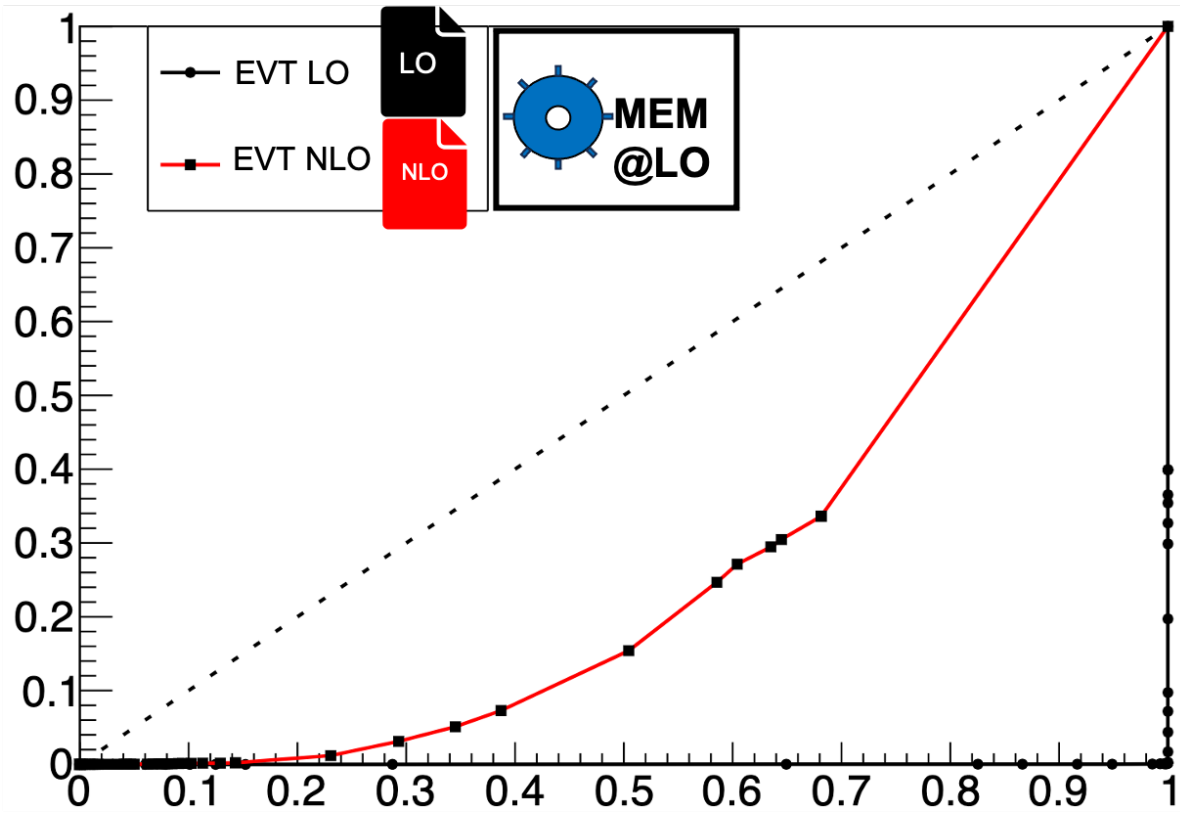


Figure 12.3: ROC curve of Leading-Order (LO, in black) and Next-to-Leading-Order (NLO, in red) MC generated events, using a LO Matrix Element Method (MEM@LO).

This graph motivates the need for a MEM@NLO, and the results presented here will be discussed with a greater level of detail in Section 16.1 (*cf.* Figure 16.2).

The very good discrimination of LO events (in black) with our MEM@LO in Fig. 12.3 serves as baseline validation, confirming the results found by the legacy analysis. The most striking feature is that the curve corresponding to the NLO events (in red) shows a noticeably weaker discriminating power, indicating that the MEM@LO is less effective when applied to events generated at higher order.

This result is hardly surprising: a Leading Order MEM does not have the tools to account for the extra radiation and kinematic shifts present in NLO events. More realistic events are therefore intrinsically harder to study, raising the question of whether the discrimination power lost in Fig. 12.3 can be recovered by upgrading the analysis to a MEM@NLO framework.

12.3 Problem statement

Going from Leading to Next-to-Leading Order requires adding two extra ingredients to the matrix element in the cross-section calculation: *virtual* loop corrections and

real emission contributions, which are both theoretically challenging to express.

$$\sigma^{\text{NLO}} = \underbrace{\int_n d\Phi_n [B(\Phi_n) + V(\Phi_n)]}_{\text{Born+Virtual}} + \underbrace{\int_{n+1} d\Phi_{n+1} R(\Phi_{n+1})}_{\text{Real}}. \quad (12.1)$$

where Φ_n and Φ_{n+1} denote the complete phase-space variables for n - and $(n+1)$ -particle final states, respectively.

Recall that the inclusive cross-section for Higgs production via gluon–gluon fusion grows significantly when higher orders are included: going from LO to NLO (and again to NNLO, *cf.* Table 3.1). This strong sensitivity underscores the indispensable role of radiative corrections in precision physics.

Chapter 13

Theoretical considerations on the MEM at NLO

This chapter provides a qualitative roadmap of how the particle physics community incorporated real and virtual NLO corrections, extending the Matrix Element Method beyond Leading Order.

13.1 Existing Foundations of the NLO Formalism

Including Next-to-Leading Order corrections (with both virtual loops and real emissions, *cf.* Eq. (12.1)) is mandatory if theoretical predictions are to match the experimental precision of the LHC and future colliders.

Each NLO contribution is divergent when considered individually. Real-emission terms develop infrared (IR) singularities when the emitted parton becomes soft or collinear, whereas virtual corrections contain both ultraviolet (UV) and infrared divergences.

Renormalisation (a standard technique used to absorb UV divergences into redefined parameters of the theory) removes the UV poles, while the IR divergences cancel only after combining the virtual and real contributions.

In fixed-order calculations, the cancellation can be handled analytically or with subtraction methods. The Matrix Element Method, however, works event by event: it needs a fully exclusive, point-wise differential cross-section for each measured kinematic configuration, not an integrated rate.

Ensuring IR finiteness in this context is far from trivial. The weight must be built from IR-safe observables, usually jet four-momenta defined by an infrared and collinear-safe algorithm. Bringing NLO accuracy into the MEM requires more than just adding loop and real diagrams: it requires a fully differential, IR-finite reformulation of the NLO machinery that meshes with the MEM likelihood.

This need has driven the development of specialised jet-clustering prescriptions and phase-space parametrisations, which we review in the following sections.

13.2 Incorporating Initial-State Radiation to the Leading Order formalism

Remember that in its standard Leading Order implementation, the MEM assumes that the final state perfectly matches the partonic configuration described by the matrix element. This assumption becomes problematic at hadron colliders like the LHC, where additional QCD radiation, particularly initial-state radiation (ISR), is abundant.



Figure 13.1: Schematic depiction of the event topology for pair production of heavy particles X, together with initial-state radiation (ISR).
Taken from Ref. [122].

ISR refers to the extra gluon emissions from the incoming partons **before** the hard scattering (*cf.* Figure 13.1). They alter the kinematic structure of the event by boosting the system transverse to the beam direction and by introducing extra jets that are not accounted for in the LO matrix element.

Since MEM likelihoods rely on an accurate modeling of the full event kinematics, unaccounted ISR leads to important biases in parameter extraction and degraded statistical power.

To mitigate these effects without resorting to full higher-order calculations, several strategies have been developed to approximately include ISR effects within the LO MEM framework [122–124].

13.2.1 Boost Correction Method

Assuming additional invisible QCD radiation in the process, the simplest method, consists of correcting the event kinematics by applying a transverse boost that compensates for the net ISR momentum within the MEM integral (*cf.* Ref. [122]).

The mappings from $(n+1)$ to n parton configurations must preserve phase space volume, and Jacobians arising from this transformation should be included in the likelihood calculation.

Since the longitudinal components of the incoming partons are already integrated over in the MEM, only the transverse momentum coordinates needs to be boosted. The idea is to shift the momenta of the incoming partons in the matrix element by the total transverse momentum carried by ISR jets, such that the reconstructed final state has zero net transverse momentum (*cf.* Figure 13.2).

This boost is a very simple approximation, and preserves the Lorentz invariance of the matrix element. It should be noted, however, that such a boost modifies the different energies and therefore does not exactly correspond to the original hard-scattering configuration.

Even if this method does not explicitly describe the effects of the particular QCD

vertices and internal propagators, it has the great advantage of not increasing the dimensionality of the phase space integration. As a result, the overall computational cost stays comparable to that of a standard MEM@LO (an essential advantage when wall-clock time and computing resources are limited).

13.2.2 Sudakov Reweighting

While the boost correction accounts for kinematic shifts, it does not model the probability of ISR emissions. To include this, *Sudakov reweighting* can be employed.

The Sudakov form factor, $\Delta(Q^2, q^2)$, gives the probability of no emissions occurring between two transverse momentum scales $Q^2 < q^2$. Its inclusion effectively reweights each boosted event by the probability that no additional emissions beyond those observed took place.

In the backward evolution formalism suitable for ISR, the Sudakov factor is expressed as an integral over splitting functions and parton distribution functions (PDFs):

$$\Delta_{\text{ISR}}(Q^2, q^2) = \exp \left[- \int_{q^2}^{Q^2} \frac{dk^2}{k^2} \frac{\alpha_s(k^2)}{2\pi} \sum_j \int dz P_{j \rightarrow i}(z) \frac{f_j(x/z, k^2)}{f_i(x, k^2)} \right], \quad (13.1)$$

where $P_{j \rightarrow i}(z)$ are the Altarelli-Parisi splitting functions, for two different scales $q^2 < Q^2$.

It has been found in Ref. [122] that when both the boost correction and Sudakov reweighting are used, the MEM is able to approximately recover the correct event likelihoods in the presence of moderate ISR. This results in a better mass peak reconstruction, and more accurate parameter estimation.

13.3 Extending the Matrix Element Method to Next-to-Leading Order

The limitations of Leading Order Matrix Element Methods become particularly severe in precision measurements where additional QCD radiation plays a non-negligible role.

To enhance the theoretical robustness and extend the applicability of the MEM to a wider class of observables and kinematic regions, it is crucial to develop formulations that incorporate Next-to-Leading Order QCD corrections.

At this point the reader should be well aware about the fact that two new classes of contributions arise at NLO: virtual corrections, involving one-loop diagrams with the same external partons as at LO, and real emissions, corresponding to tree-level diagrams with one additional parton. These contributions live in different phase spaces (*cf.* Eq.12.1) and are separately infrared divergent and only their sum is finite. This poses a challenge for defining a meaningful likelihood on an event-by-event basis.

Use of Boosts and Forward branching phase space generator (FBPS)

This issue was addressed in the method proposed by Campbell, Giele, and Williams [125] and further extended in Baumeister and Weinzierl [124].

A central element is the construction of weights that include both virtual and real terms. For each reconstructed event, a mapping to a Born-level configuration is defined by undoing the effects of extra radiation via a boost (*cf.* Figure 13.2). This is similar to what has already been discussed in Section 13.2.1, with the addition that the remaining longitudinal and energy components from the resulting imbalance (X , in blue) has been re-absorbed into the colliding partons (instead of the transverse contribution only).

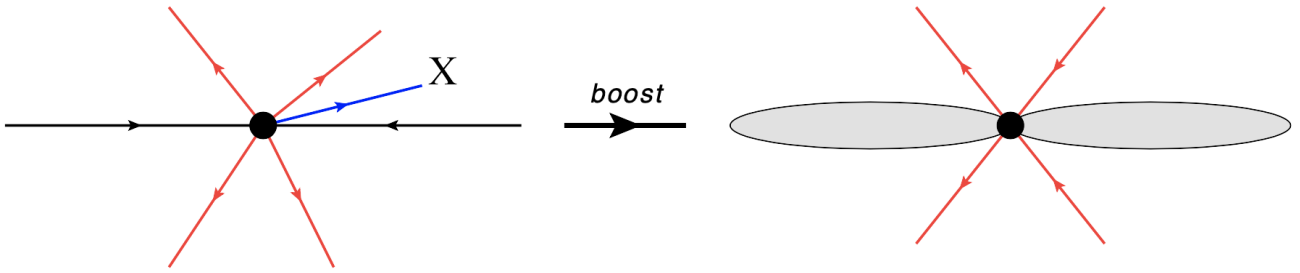


Figure 13.2: Boost correction method used in Matrix Element Methods at Leading-Order.

The left hand side depicts a collision that results in the production of four leptons (in red) that do not balance in the transverse plane.

The resulting imbalance (X , in blue) represents the remaining event which is not modelled in the Born matrix element. A boost is applied to the event such that X has no components in the transverse plane, with the remaining longitudinal and energy components absorbed into the colliding partons.

Taken from Ref. [125].

An other difference with the ISR boost is the addition of the real contributions treatment.

The associated phase-space is also defined and integrated over using a so-called forward branching phase space generator [126].

Starting from the Born phase space point,

$$\hat{p}_a + \hat{p}_b \rightarrow Q,$$

the FBPS generates the real radiation by branching one of the initial state momenta to produce the real phase space point

$$p_a + p_b \rightarrow Q + p_r.$$

Following conventions from Ref. [125], the hatted notation indicate a Born phase space point while the un-hatted momenta represent the real phase space point.

The phase space generator needs to integrate out all initial state radiation within the constraints of fixed momenta of the identified final state particles. The author have shown that this can be achieved using a FBPS generator defined by,

$$d\Phi(p_a + p_b \rightarrow Q + p_r) = d\Phi(\hat{p}_a + \hat{p}_b \rightarrow Q) \times d\Phi_{\text{FBPS}}(p_a, p_b, p_r) \times \theta_{\text{veto}}, \quad (13.2)$$

where θ_{veto} (optionally) vetoes events that generate an additional jet. At NLO the jet veto cut is simply defined with a cut on the transverse momemta of the extra radiation p_r .

In this framework, the differential cross-section is the sum of both contributions:

$$L(\mathbf{x}|\mathbf{h}) = \frac{1}{\sigma_{\mathbf{h}}^{\text{NLO}}} [V_{\mathbf{h}}(\mathbf{x}) + R_{\mathbf{h}}(\mathbf{x})], \quad (13.3)$$

where $V_{\mathbf{h}}(x)$ contains both the Born and virtual terms, and $R_{\mathbf{h}}(x)$ the real-emission contribution integrated for a given reconstructed event \mathbf{x} under the hypothesis \mathbf{h} .

13.4 Variants of the Matrix Element Method at Next-to-Leading Order

With the theoretical groundwork for a Next-to-Leading Order Matrix Element Method now established, several practical implementations have emerged (each tailored to specific physics cases and computational constraints).

They differ mainly in how they combine real and virtual corrections, how jets are defined and recombined, and how detector effects are encoded through transfer functions.

Sub-Jet Resolution Variant

One variant that is worth mentioning is the *sub-jet-based* variant, presented in Ref. [124].

It explicitly resolves one additional emission within a jet, using a resolution parameter p_T^{min} .

If an event can contain a sub-jet structure above this threshold, the real-emission matrix element is used; otherwise, the virtual correction dominates. This method smoothly interpolates between n - and $(n+1)$ -jet descriptions:

$$\mathcal{L}_{\text{sub-jet}}(\vec{x}|\mathbf{h}) = \begin{cases} \frac{1}{\sigma_{\text{NLO}}} [\text{LO} + \text{Virtual}], & \text{if no resolved sub-jets,} \\ \frac{1}{\sigma_{\text{NLO}}} [\text{Real}], & \text{if resolved sub-jets present.} \end{cases} \quad (13.4)$$

13.5 Challenges Identified in the Literature

In this section, we review the key challenges identified in previous studies on the implementation of the Matrix Element Method at NLO.

Infrared Divergences and Phase Space Slicing The authors of Ref. [123, 124] warn that the handling of the infrared divergences cancellations necessitates a careful implementation of phase space slicing.

In the phase space slicing method, the cross-section at NLO accuracy $d\sigma_{NLO}$ is formed of two main contributions: $d\sigma_{Hard}$ constructed from the matrix element for the real corrections evaluated for phase space points where all partons are resolved (i.e the additional parton is neither collinear to the incoming partons nor soft), and a Born-like part is comprised of three terms $d\sigma_{LO}$, $d\sigma_{Virtual}$ as well as the so-called soft and collinear parts $d\sigma_{soft/coll}$ (with “soft” referring to emissions of vanishing energy and “collinear” to emissions that are parallel to an initial or final state parton).

The separation of the phase space for the real corrections into resolved and unresolved regions is mediated in Ref. [123] by the slicing parameter x_{min} which acts as a scale to separate the two.

$$d\sigma_{NLO} = d\sigma_{Hard} + d\sigma_{LO} + d\sigma_{Virtual} + d\sigma_{soft/coll} + \mathcal{O}(x_{min}) \quad (13.5)$$

The different matrix element contributions and choices should be consistent altogether so that the divergences cancel properly with each other.

Computational Complexity and Integration Issues The evaluation of multi-dimensional integrals over phase space at NLO, imposes significant computational demands. Optimised sampling and adaptive integration techniques are required.

Matching Jet Definitions Across Theory and Experiment Ensuring that the jet definitions used in theoretical predictions match those in experimental analyses is non-trivial, particularly when introducing non-standard clustering prescriptions. This challenge is very specific regarding the user flexibility in the choice of spectator partons.

13.6 Conclusions

The extension of the Matrix Element Method to NLO accuracy represents a significant advancement in the field of collider phenomenology.

It addresses a major limitation of the traditional MEM by incorporating theoretically consistent, fully differential predictions that match the precision of modern experiments.

While critical technical and computational challenges persist, the methodology is validated and proven to be robust for a variety of processes studied by the authors in the articles we introduced in this chapter.

Chapter 14

Our Contribution: A New MEM Formalism at NLO

After reviewing the various Next-to-Leading-Order Matrix Element Method strategies in Chapter 13, we now introduce the key steps in the constructions of our new formalism, and describe how it has been implemented within the existing MO-MEMTA framework.

To promote full transparency and ensure the reproducibility of the work carried out for this new MEM framework at NLO, a public GITLAB repository containing the code developed during this thesis has been made publicly available at https://gitlab.com/mtartarin/phd_share_public.

The repository includes all essential files, along with a list of explicit software dependencies, to run the new MEM@NLO framework (and to reproduce the main results that will be presented in Part V).

14.1 Access to the Matrix Elements at NLO

Among the many challenges involved in developing a new MEM formalism, reliable access to the appropriate matrix elements is at the top of the list.

At Leading Order, we had access to the necessary amplitudes using the MADGRAPH5 software.

When advancing to NLO, however, the calculation becomes far more complicated for this version of the MADGRAPH5 software.

To construct a MEM at fixed order, one must supply all NLO contributions (Born+Virtual, and Real) for arbitrary phase-space points.

Deriving these amplitudes from first principles would constitute a separate work on its own, and is not the goal of this thesis.

Over the past years, the particle physics community has devoted substantial effort to releasing publicly available codes for next-to-leading-order (NLO) cross-section calculations and event generation.

Our goal has been to interface (any of) them into the MOMEMTA framework, allowing every NLO contribution to be evaluated point-by-point for the MEM integration.

We explored several possibilities: First, we revisited MADGRAPH5. But because LO matrix element generation had already required significant manual intervention, a full NLO implementation proved impractical.

Second, we investigated general purpose NLO codes such as MCFM, but without any success in directly accessing the matrix element of interest.

Finally we turned to POWHEG-BOX-V2, in which the sub-repository **ggHH** developed by Heinrich *et al.* [127, 128] provided the NLO matrix elements for $gg \rightarrow HH$, including optional modifications of the self-coupling parameter κ_λ and top-mass schemes.

While the POWHEG-BOX-V2 software excels at event generation, it is **not** designed to return amplitudes for arbitrary kinematic points. The development of a dedicated interface was therefore essential to enable its use within any MEM framework. The main design principles of the interface we created are summarized in section 14.2.

Building such an interface required a significant investment of time and effort. We began with a detailed study of the POWHEG-BOX-V2 framework, including an in-depth review of its documentation, analysis of its program architecture, and inspection of its data flow, in order to determine which components were relevant for the MEM evaluation.

The initial objective was to first establish a *functional* bridge, capable of querying the Born, Virtual, and Real amplitudes directly from the POWHEG-BOX-V2 software.

Through this process, our work ultimately went beyond the initial goal and resulted in a lean interface to MOMEMTA, with minimal modifications to the native POWHEG-BOX-V2 code base while exposing all quantities required by the MEM integration software.

14.2 Modifying POWHEG-BOX-V2

14.2.1 ggHH repository

The original code in POWHEG-BOX-V2 is mainly written in Fortran 77, whereas MOMEMTA is C++/Python which constitutes the first issue to surpass. Our strategy involved seven main steps:

- (1) Exhaustive study of the complex structure of POWHEG-BOX-V2 through its manual [96] and code;
- (2) Extensive diagnostic runs;
- (3) Minimal, well-documented edits to the source;
- (5) Selective calls to the subroutines that instantiate the appropriate dynamical

scales and couplings;

- (6) Extraction of the required amplitudes without invoking the full event generator;
- (7) Rigorous validation against LO results from MADGRAPH5 (*cf.* Section 14.3).

No bookkeeping of the time spent on the modification to POWHEG-BOX-V2 or its interface to MoMEMTA has been made, but the investment to this task was important.

This allowed us to achieve the point-wise evaluation of the Born, Virtual, and Real matrix elements for any $gg \rightarrow HH$ kinematics.

Despite our efforts to minimize the source code modifications, the POWHEG-BOX-V2 code base has been modified to such an extent that it can no longer perform the task for which it was originally designed.

We used two copies of the softwares: One for the interface, and a ‘clean’ one for event generation.

14.2.2 $t\bar{t}H$ repository

The POWHEG-BOX-V2 software offers many other different subrepositories, such as $t\bar{t}H$, which is one of our main background process.

All of the work done in understanding the code structure for $ggHH$ helped us interface the $t\bar{t}H$ repository to MoMEMta in a matter of several days only (compared to the multiple months previously needed).

14.3 Validation of the interface with matrix element comparison

Matrix element for $gg \rightarrow HH$: The global code modifications are described in 14.2.

After implementing the interface, we validated the LO amplitudes by direct comparison between POWHEG-BOX-V2 and MADGRAPH5 both at LO. Figure 14.1 shows the relative difference:

$$\frac{\text{ME}_{\text{POWHEG}} - \text{ME}_{\text{MG}}}{\text{ME}_{\text{POWHEG}}}$$

with and without a consistent choice for the strong coupling value $\alpha_s = 0.1184$ (*i.e.* MADGRAPH5 value).

When the strong coupling α_s choice was consistent between the two, the agreement became almost perfect, demonstrating that this interface worked as expected and preserved the normalization of the (Born) matrix element.

14.3.1 Matrix element for $gg \rightarrow HH \rightarrow b\bar{b}\gamma\gamma$ at LO

We have discussed the matrix element for $gg \rightarrow HH$, which is not our full signal process. Our final state particles are $b\bar{b}\gamma\gamma$, and are obtained through Higgs decay.

In POWHEG–BOX–V2 this decay is done at the level of event generation, which means that the matrix element accessible from this software stops at the Higgs production. To bypass this difficulty, we exploited the fact that the Higgs boson is a colour-neutral scalar and invoked the QCD factorisation theorem, which allows the matrix element to be factorised into a hard-scattering part multiplied by the Higgs boson decays.

In practice, we used MADGRAPH5 software to generate the Higgs boson decays. To do so, we produced several LO matrix elements ($gg \rightarrow HH \rightarrow b\bar{b}\gamma\gamma$, $gg \rightarrow HH$, $H \rightarrow b\bar{b}$, and $H \rightarrow \gamma\gamma$) in order to isolate precisely the sections of code responsible for the Higgs decays.

These decay routines were then incorporated into the $gg \rightarrow HH$ matrix element obtained from the POWHEG–BOX–V2 software, providing a complete description of the $gg \rightarrow HH \rightarrow b\bar{b}\gamma\gamma$ process at NLO.

We also anticipated that the $H \rightarrow b\bar{b}$ and $H \rightarrow \gamma\gamma$ codes automatically generated by MADGRAPH5 would require minor modifications before merging with the POWHEG–BOX–V2 output.

In particular, we identified and isolated the specific sections responsible for the Higgs wavefunctions. Our inspection confirmed that the Higgs wavefunctions used in the full $gg \rightarrow HH \rightarrow b\bar{b}\gamma\gamma$ process differed from those appearing in the isolated decay blocks ($H \rightarrow b\bar{b}$ and $H \rightarrow \gamma\gamma$).

In the full process, the Higgs bosons were treated as off-shell propagators, whereas in the isolated decay codes they appeared as on-shell external particles. To ensure consistency, we replaced the default on-shell vertex functions `VVS3_0` (for $H \rightarrow \gamma\gamma$) and `FFS1_0` (for $H \rightarrow b\bar{b}$) by their off-shell counterparts `VVS3_3` and `FFS1_3`, respectively.

Note on the `VVS3_0/VVS3_3` and `FFS1_0/FFS1_3` functions. In the MADGRAPH5 framework, helicity amplitudes are computed using routines derived from the HELAS (HELicity Amplitude Subroutines) library [129]. These routines implement all fundamental interaction vertices and wavefunction constructions required to evaluate matrix elements numerically. Among them, the `VVS` and `FFS` routines handle vector–vector–scalar and fermion–fermion–scalar interactions, respectively. The functions labeled with a suffix `_0` (e.g. `VVS3_0`, `FFS1_0`) evaluate amplitudes assuming that the scalar particle is on-shell, as is the case when the scalar appears as an external state. Conversely, the routines ending in `_3` (e.g. `VVS3_3`, `FFS1_3`) construct the corresponding wavefunctions for an off-shell scalar propagating internally in a diagram.

We see in Figure 14.2 that we achieve an excellent approximation by adding the $H \rightarrow b\bar{b}$ and $H \rightarrow \gamma\gamma$ decay contributions by hand from MADGRAPH5 codes to the output matrix element from POWHEG–BOX–V2.

Validation plots

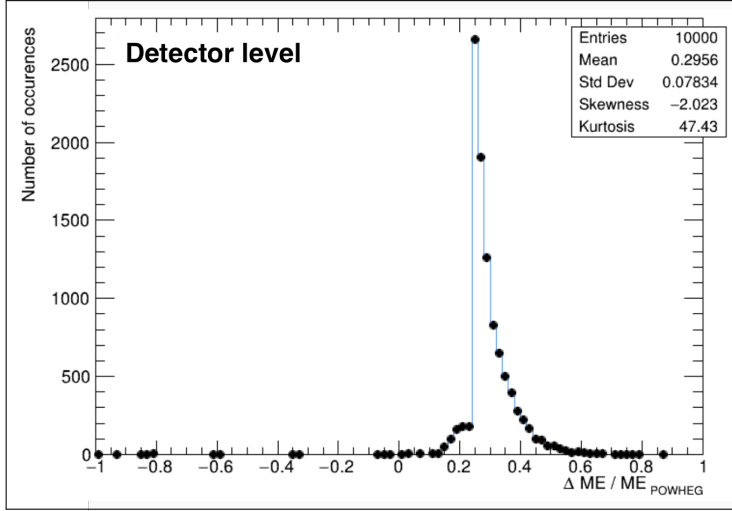
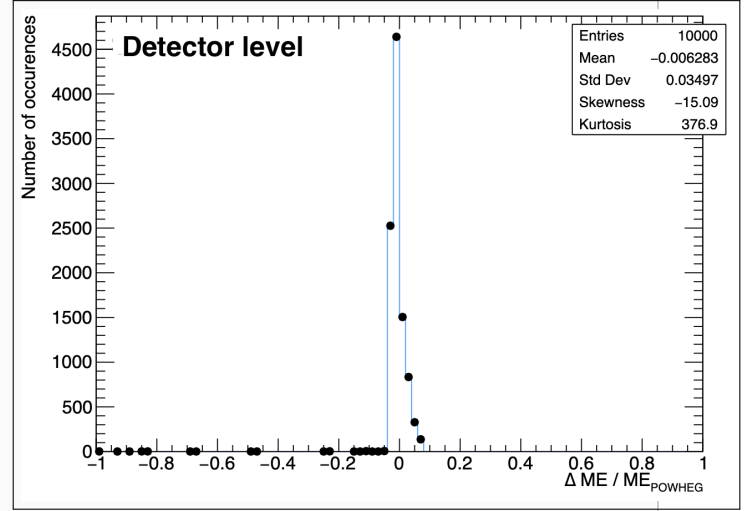
(a) Without modification of α_s (b) With the same $\alpha_s = 0.1184$

Figure 14.1: Histograms of the direct comparison between LO matrix elements for the process $gg \rightarrow HH$ from POWHEG-BOX-V2 and MadGraph@NLO for 10 000 different evaluations. Both x-axis correspond to the quantity $ME_{POWHEG} - ME_{MG}$ normalized by the ME_{POWHEG} value, and the y-axis correspond to the number of occurrences per bin.

Validation plot

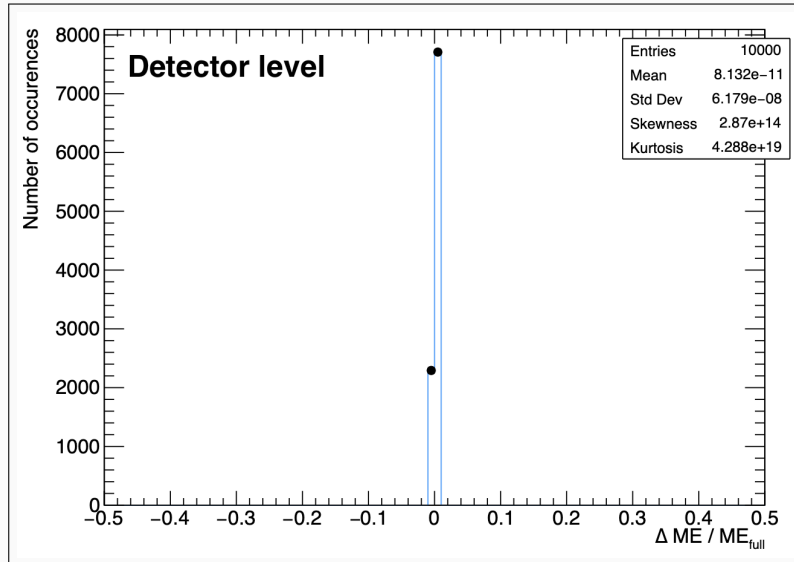


Figure 14.2: Histogram of the direct comparison between LO matrix elements for the process $gg \rightarrow HH$ [from Magraph@NLO] with the addition of $H \rightarrow b\bar{b}$ and $H \rightarrow \gamma\gamma$ by hand [from Magraph@NLO], to the full $gg \rightarrow HH \rightarrow b\bar{b}\gamma\gamma$ [from Madgraph@NLO] for 10 000 different evaluations (with a fixed value of $\alpha_s = 0.1184$).

14.3.2 Matrix Elements for $gg \rightarrow HH \rightarrow b\bar{b}\gamma\gamma$ at NLO

For the NLO amplitudes, we identified the different parts in POWHEG–BOX–V2 that would be necessary in the initialization and extraction of the Virtual and Real contributions separately.

Virtual contribution

A subtle issue arose in the virtual contributions. For Higgs mass values different from $m_H = 125 \text{ GeV}$ the internal variable `coshtheta` can become ill-defined, corrupting the amplitude by returning MEM weights of -1 .

We traced this issue back to an implicit on-shell condition in the code (which assumed the mass of the Higgs was exactly $m_H = 125 \text{ GeV}$ for the definition of the Mandelstam variable u , expressed as a function of s , t and m_H), and implemented a local safeguard: the virtual term is evaluated only when m_H lies within a narrow tolerance of its physical value.

By doing so, we ensure that the virtual contribution is consistent with its design within the POWHEG–BOX–V2 software.

Real contribution

For the real amplitude an additional factor of $(2\pi)/\alpha_s$ is introduced at a later stage in the native POWHEG-BOX-V2 workflow. And because we bypass this stage is our interface, the factor must be removed manually. Other minor edits ensure the right initialisation for this contribution, and a self-consistent treatment of collinear limits and phase-space cuts.

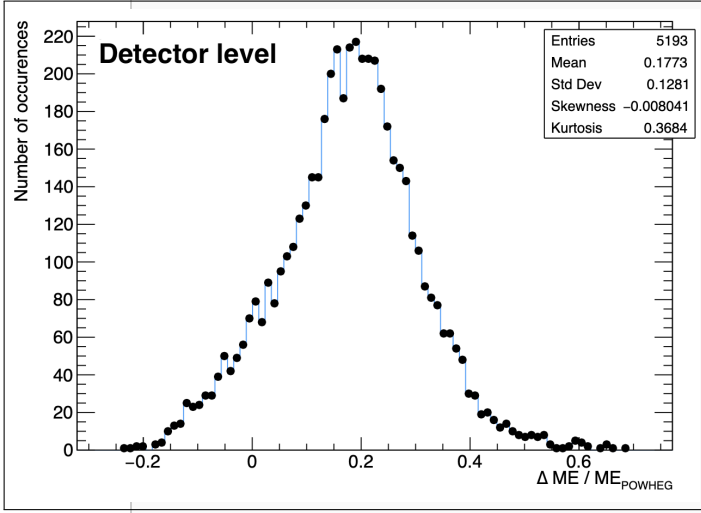
Adding Higgs decay

Considering the success of adding Higgs decay by hand at LO, we reconducted the same idea for both the virtual and real outputs to account for the Higgs decay.

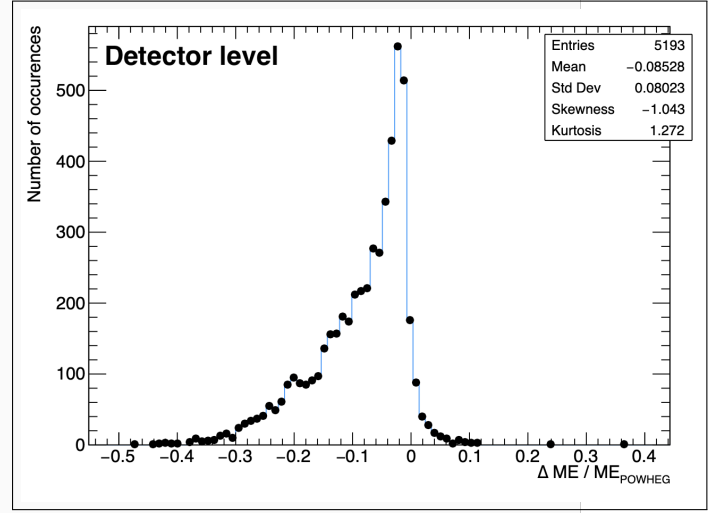
14.3.3 Matrix Elements for $t\bar{t}H$ at LO

Following the same reasoning, we validated our new interface of $t\bar{t}H$ by comparing outputs from LO contributions between POWHEG-BOX-V2 and MADGRAPH5 $t\bar{t}H$ process (i.e as final state particles).

Grouped plot: Matrix Element Validation



(a) Without modification of α_s



(b) With the same $\alpha_s = 0.1184$

Figure 14.3: Histograms of the direct comparison between LO matrix elements for the process $t\bar{t}H$ from POWHEG-BOX-V2 and Madgraph@NLO for 5193 different evaluations. Both x-axis correspond to the quantity $ME_{POWHEG} - ME_{MG}$ normalized by the ME_{POWHEG} value, and the y-axis correspond to the number of occurrences within each bins.

As we can see in Figure 14.3, the interface was successful as the matrix elements at LO were once again in very good agreement.

14.3.4 Matrix Elements for $t\bar{t}H$ at NLO

For the background process $t\bar{t}H$, we also used MADGRAPH5 to estimate the real-emission contribution by explicitly adding an extra parton q in the final state: $(t\bar{t}Hq)$. Due to the known limitations of the available UFO models we used, however, MADGRAPH5 could not compute the virtual contributions in any processes involving Higgs bosons. As a result, our NLO matrix element for the $t\bar{t}H$ process was limited to the Born and real-emission terms only.

Access to the real-emission contribution through MADGRAPH5 enabled a direct comparison with the corresponding results obtained from POWHEG-BOX-V2, shown in Figure 14.4.

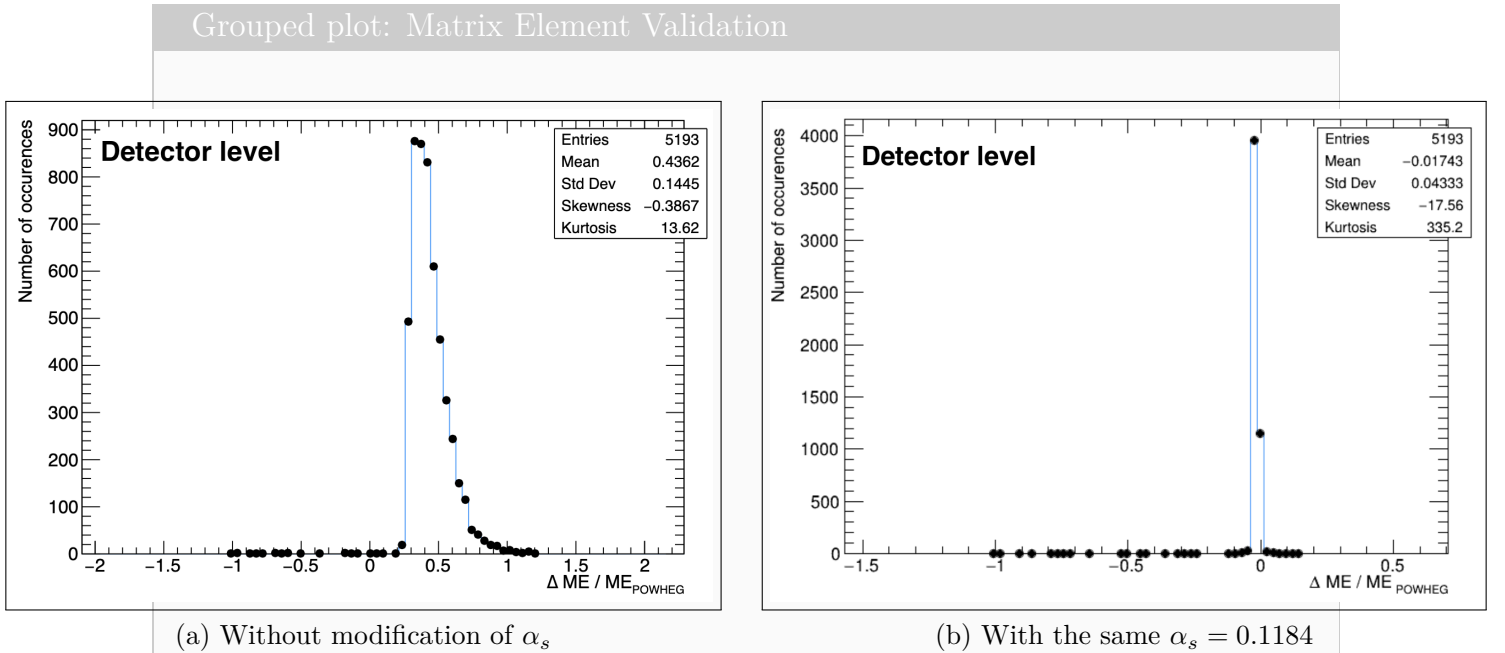


Figure 14.4: Histograms of the direct comparison between Real Matrix Elements for the process $t\bar{t}Hq$ from POWHEG-BOX-V2 and Madgraph@NLO for 5193 different evaluations. Both x-axis correspond to the quantity $ME_{POWHEG} - ME_{MG}$ normalized by the ME_{POWHEG} value, and the y-axis correspond to the number of occurrences within each bins.

This comparison between the real matrix elements of POWHEG-BOX-V2 and MAGRAPH@NLO for the $t\bar{t}Hq$ process holds very well as we can see in Figure 14.4. We therefore have the confirmation that the interface also works for the real contribution.

Issue for $t\bar{t}H$ with decay addition In contrast to the ggF signal process, incorporating the top-quark decays (into W bosons and b-quark) by hand proved to be considerably more complex.

Integrating these parts of the MADGRAPH5 output into the POWHEG-BOX-V2

framework proved particularly challenging, as it would have required careful treatment of additional constraints such as charge conservation, spin correlations, and particle polarizations.

Given that implementing these decays manually within POWHEG-BOX-V2 would have required a substantial additional effort, and considering the excellent agreement already observed in Figure 14.3 and Figure 14.4, we concluded that using MADGRAPH5 alone for the complete $t\bar{t}H \rightarrow b\bar{b}\gamma\gamma$ matrix element computation at NLO was sufficient.

Indeed, relying solely on MADGRAPH5 would ensure a self-consistent framework in which the decay implementation would naturally be connected to the hard-scattering part, ensuring a coherent description of the full process.

14.4 Use of MadGraph5 for our MEM@NLO

The MADGRAPH5 software remained an invaluable tool throughout this project. At LO it supplied benchmark amplitudes for $gg \rightarrow HH$, $t\bar{t}H$, and qcd background $b\bar{b}\gamma\gamma$; its decay chains were essential for constructing the $gg \rightarrow HH$ matrix element with on-shell Higgs bosons (and to attempt the same for $t\bar{t}H$).

The MoMEMta-MagMEE plug-in allowed us to export C++ code directly from the automatically generated fortran code, though **several critical patches** were required to match the coding conventions of MOMEMTA for the needs of our analysis.

14.5 Modifying MoMEMta

Although inherently modular, the public release of MoMEMTA is aimed at LO applications. None of the existing examples integrate over an undetected NLO radiation.

To accommodate configurations with additional (undetected) NLO radiations, we made two main additions to MoMEMta to account for such NLO descriptions.

(i) New Main Blocks. After carefully examining the mathematical and coding structure of the existing main blocks (both in the original MADWEIGHT paper [93] and within the MoMEMTA framework), we found that none of the available implementations could remove the degrees of freedom of an additional invisible NLO radiation.

This motivated the development of two alternative approaches. We started with Block M, which was an attempt to remove the extra radiation three extra degrees of freedom in one step, but proved numerically unstable (*cf.* Appendix B.2). The second attempt, Block N, which will be described shortly after, offers a more general and robust solution.

(ii) A Dedicated Module for Extra Degrees of Freedom. For processes that already involve invisible particles at LO (*e.g.* $t\bar{t}H$) and therefore cannot accommodate the removal of additional degrees of freedom through conservation laws, we developed the `ExtraRadiation_3DOF` module, which introduces three independent integration dimensions that span the volume of phase space of interest for the extra radiation.

14.5.1 Block N: Main Ideas

As discussed in Section 9.3.3, (Main) Blocks are used to reduce the dimensionality of the integral in Eq. 8.5 by introducing well-chosen changes of variables. This reduction exploits the conservation equations that appear in the form of the $\delta\left(a_1 + a_2 - \sum_{j=1}^n y_j\right)$ contribution.

In preparation for our work, we carried out a detailed study of all existing main and secondary blocks implemented in MoMEMTA. For each block, we derived the corresponding change of variables and manually computed the determinant of the associated Jacobian.

These calculations were cross-checked using both the MATHEMATICA software [130] and the analytical results provided in the MADWEIGHT documentation [93]. Only after this thorough validation did we proceed to extend the existing formalism.

Building on this work, we developed a new main block, named BLOCK N, specifically designed to handle configurations with an additional invisible NLO radiation. Using the four conservation equations, this block simultaneously eliminates the two Bjorken fractions (q_1 and q_2) and the transverse components of the additional radiation momentum (p_x^{rad} and p_y^{rad}), while keeping its longitudinal component (p_z^{rad}) as

a free integration variable.

The choice of p_z^{rad} as the integration variable, rather than p_x^{rad} or p_y^{rad} , is physically motivated: The longitudinal momentum, aligned with the beam axis, cannot be disentangled from the unknown partonic boost along the same direction and is therefore a natural choice of integration variable.

The resulting BLOCK N is illustrated in Figure 14.5, following the graphical conventions used for main blocks in MADWEIGHT.

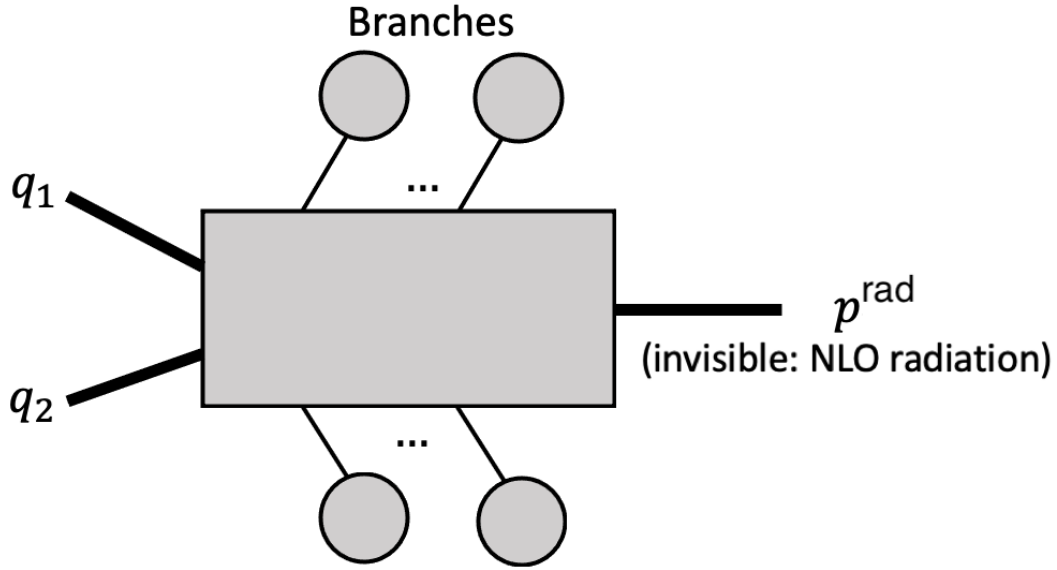


Figure 14.5: Schematic representation of Block N, following the conventions used by MOMEMTA.

The corresponding Jacobian associated to the Block N is derived from the system:

$$\begin{cases} p_x^{\text{rad}} = -P_x, \\ p_y^{\text{rad}} = -P_y, \\ q_{1,E} - q_{2,E} = P_z, \\ q_{1,E} + q_{2,E} - \sqrt{(p_x^{\text{rad}})^2 + (p_y^{\text{rad}})^2 + (p_z^{\text{rad}})^2} = E_T, \end{cases}$$

where P_x , P_y , P_z and E_T are the sums of the corresponding contributions over final-state $b\bar{b}\gamma\gamma$, p^{rad} denotes the unresolved real-radiation, and $q'_i = \frac{1}{\sqrt{2}}q_i\sqrt{s}$ is the corresponding energy and longitudinal momentum of gluon i .

From this system of equations, we can compute the Jacobian associated with the change of variables (or more precisely the norm of the inverse Jacobian J^{-1} of the transformation that will be actually needed):

$$J^{-1} = \begin{pmatrix} \frac{\partial P_x}{\partial p_x^{\text{rad}}} & \frac{\partial P_x}{\partial p_y^{\text{rad}}} & \frac{\partial P_x}{\partial q_{1,E}} & \frac{\partial P_x}{\partial q_{2,E}} \\ \frac{\partial P_y}{\partial p_x^{\text{rad}}} & \frac{\partial P_y}{\partial p_y^{\text{rad}}} & \frac{\partial P_y}{\partial q_{1,E}} & \frac{\partial P_y}{\partial q_{2,E}} \\ \frac{\partial P_z}{\partial p_x^{\text{rad}}} & \frac{\partial P_z}{\partial p_y^{\text{rad}}} & \frac{\partial P_z}{\partial q_{1,E}} & \frac{\partial P_z}{\partial q_{2,E}} \\ \frac{\partial E_T}{\partial p_x^{\text{rad}}} & \frac{\partial E_T}{\partial p_y^{\text{rad}}} & \frac{\partial E_T}{\partial q_{1,E}} & \frac{\partial E_T}{\partial q_{2,E}} \end{pmatrix} = \begin{pmatrix} -1 & 0 & 0 & 0 \\ 0 & -1 & 0 & 0 \\ 0 & 0 & 1 & -1 \\ -\frac{p_x^{\text{rad}}}{E^{\text{rad}}} & -\frac{p_y^{\text{rad}}}{E^{\text{rad}}} & 1 & 1 \end{pmatrix} \quad (14.1)$$

The (norm of the) determinant of the inverse Jacobian matrix J^{-1} reads:

$$|\det(J^{-1})| = |(-1)(-1) \cdot \det \begin{pmatrix} 1 & -1 \\ 1 & 1 \end{pmatrix}| = \left| \det \begin{pmatrix} 1 & -1 \\ 1 & 1 \end{pmatrix} \right| = |2| = 2 \quad (14.2)$$

The correct determinant of the Jacobian of interest for our study is $\det(J)$, which can be directly related to $\det(J^{-1})$ by:

$$|\det(J)| = \frac{1}{|\det(J^{-1})|} = \frac{1}{2} \quad (14.3)$$

Validation of Block N

The novelty of this formalism limited the range of available validation strategies. We therefore adopted the following approach: Comparing the physical distribution of the additional radiation p_z^{rad} to the (average) value of the MEM integrand (at the corresponding p_z^{rad} values inside each bins of the histograms), for 10 000 NLO generated signal events (using POWHEG-BOX-V2).

Discussion of Figure 14.6: Each pair of figures (top pair, middle pair and bottom pair) should be interpreted together: the left panel always shows the distribution on a linear vertical scale, while the right panel uses a logarithmic vertical scale.

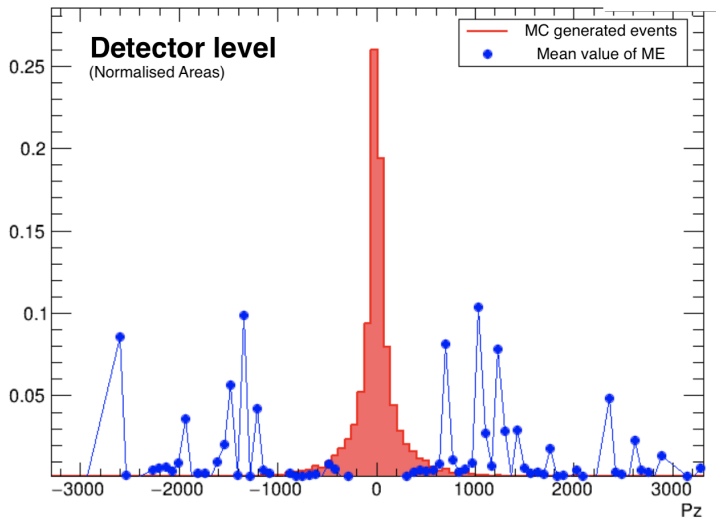
Each plot displays two overlaid contributions:

- **in red:** The distribution of the p_z^{rad} component of the real radiation parton, in ggF events generated at NLO using POWHEG-BOX-V2.
- **in blue:** The mean value of the real matrix element evaluated for each event, within the corresponding p_z^{rad} bin.

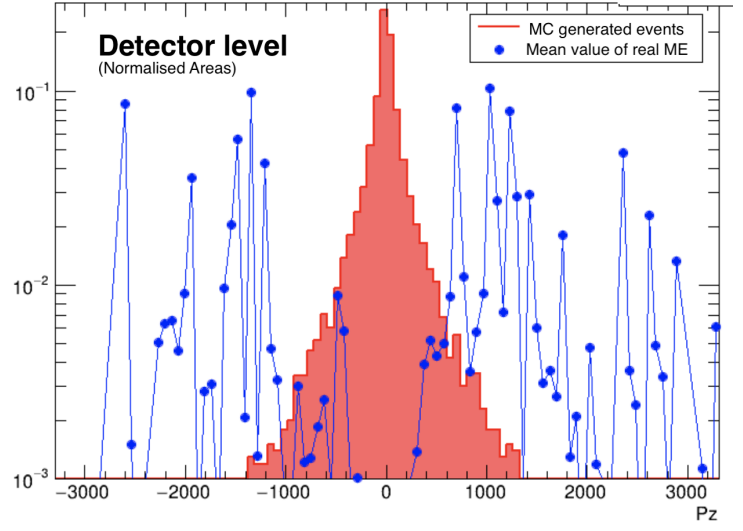
All areas are normalized to unity in order to facilitate the comparison of the shapes of the distributions.

This work is performed on 3 different levels of increasing complexity (top, middle and bottom) to understand how the Block N formalism as a whole allows the reconstruction of the physical distribution:

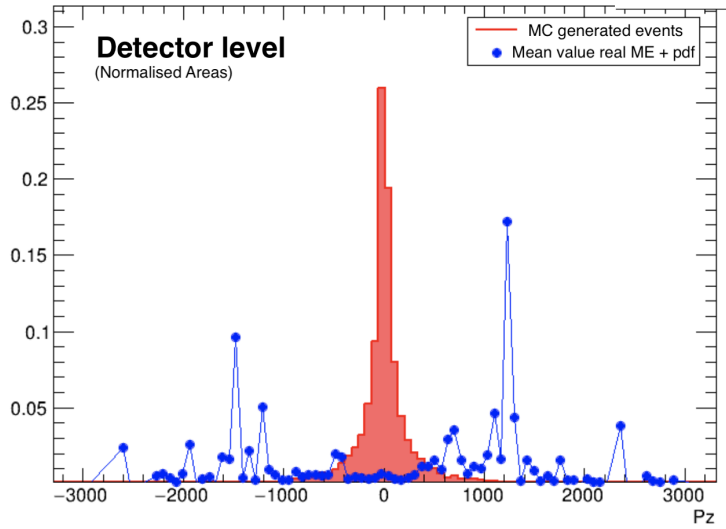
- **(14.6a), (14.6b): Real Matrix Element only**
These plots show the contribution from the squared real matrix element, without any parton distribution functions (PDFs) or phase-space weighting.



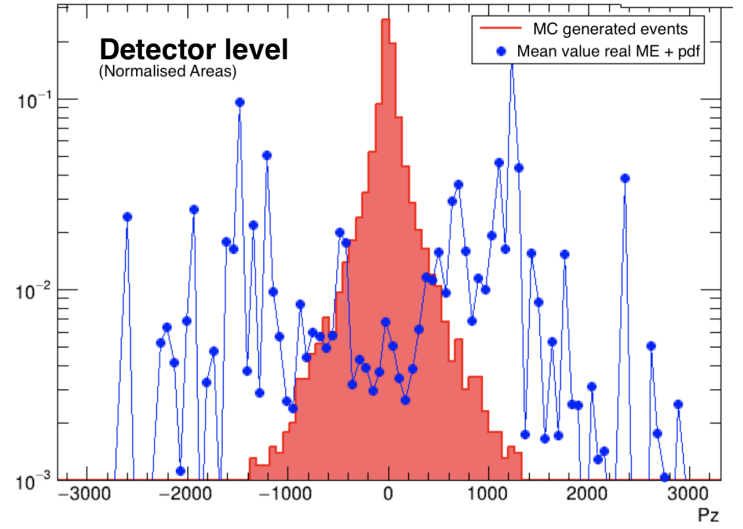
(a) Real matrix element only



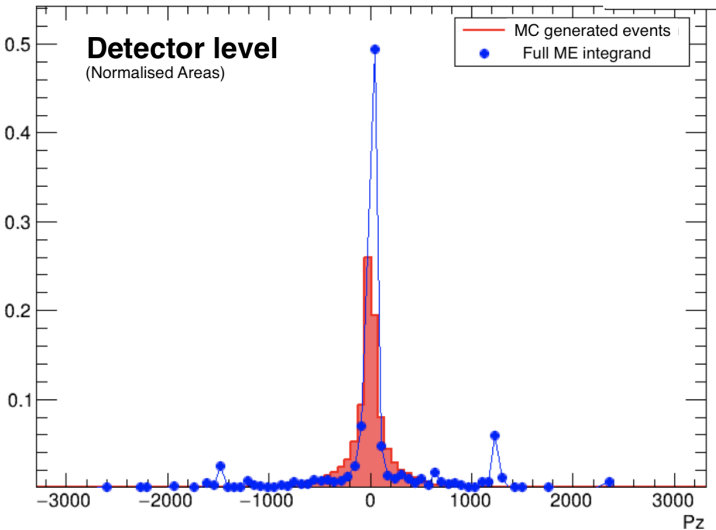
(b) with vertical axis on logarithmic scale



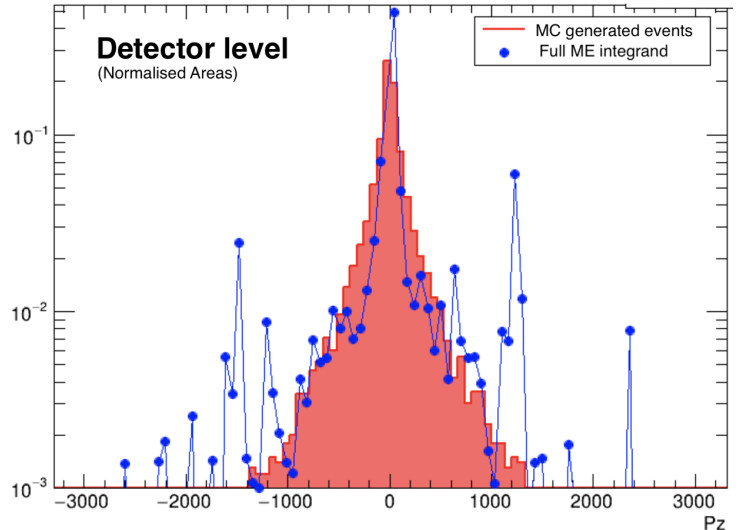
(c) Real matrix element weighted by PDFs



(d) with vertical axis on logarithmic scale



(e) Full MEM Real Integrand



(f) with vertical axis on logarithmic scale

Figure 14.6: All curves area are normalized to unity in order to facilitate comparison.

A discussion of these plots can be found in section 14.5.1

- **(14.6c), (14.6d): Real Matrix Element multiplied by PDFs**

The real matrix element is weighted by the initial-state parton flux via the PDFs, reflecting the parton-level composition of the proton beams.

- **(14.6e), (14.6f): Full MEM Integrand**

These plots show the complete Matrix Element Method integrand, including the real matrix element, the PDFs, and the phase-space Jacobian determinant relevant for the integration.

If we only consider the contribution from the real matrix elements (*cf.* Figures 14.6a and 14.6b), it does not properly account for the distribution of the additional radiation P_z . This is an issue for any integration algorithm that explore the phase-space, which will focus important resources on unphysical areas of the p_z^{rad} variable.

The addition of the Bjorken parton distribution functions $f(q_1)$ and $f(q_2)$ to the real matrix element (*cf.* Figures 14.6c and 14.6d) do not solve the issue. We can still see an improvement in the central region around $p_z^{\text{rad}} = 0$ which became more physical, but this is not sufficient enough.

Finally, we can see an excellent agreement **after** successive inclusion of the real matrix element, the parton density functions, **and** the *full* Jacobian altogether (*cf.* Figures 14.6e and 14.6f). Here the *full* Jacobian refers to the product of the phase-space and the Main Block N jacobians, which should be merged as one single entity within MOMEMTA.

Collinear and Soft Radiation Treatment

Proper treatment of collinear and soft limits of the additional real emission is essential in any Matrix Element Method implementation at Next-to-Leading Order (MEM@NLO), due to the singular behavior of the (real) matrix element in these regions of phase space.

If not handled carefully, these singularities can lead to instabilities in the likelihood evaluation and numerical divergences in the integration.

In the context of NLO QCD, these problematic configurations correspond to *unresolved* radiation, *i.e.* real partons that are either collinear to a final-state particle or carry very low transverse momentum (soft).

To regulate these infrared (IR) divergences, we adopt a simple yet effective cut-based strategy. We developed a new dedicated MOMEMTA module that we called **CollinearTreatment**, that identifies whether the additional radiation generated during the MEM integration (either via `Block_N` or `ExtraRadiation_3DOF`) lies in the vicinity of any reconstructed final-state particle.

The module computes angular distances ΔR between the extra radiation and all final-state objects (*e.g.* photons γ and b -jets) and applies thresholds to determine whether the configuration is unresolved (*cf.* Section 15.3.1).

If the radiation is collinear to a **photon**, we discard the entire phase-space point from the integration, as such a configuration would realistically lead to mis-reconstructed energy deposits in the electromagnetic calorimeter. This is implemented by returning a zero value for the MEM integrand at that point.

If the radiation is collinear to a **b -jet**, we perform a kinematic adjustment by rescaling the energy of the corresponding jet to account for the unresolved splitting. This reflects the physical interpretation that partons inside jets are clustered by the detector reconstruction algorithms.

In addition to collinear divergences, soft divergences also require regulation. We apply a lower cut on the transverse momentum of the extra radiation, p_T^{\min} , which effectively excludes configurations where the emitted parton becomes unresolved due to vanishing energy (*cf.* Table 14.1).

This soft cut ensures integrability of the real-emission term and is consistent with the phase-space behavior observed in NLO event generators (*cf.* Section 14.5.3). The precise value of p_T^{\min} is process-dependent and was optimized using the distributions of the extra radiation in samples generated with POWHEG-BOX-V2 and MADGRAPH5.

Together, these collinear and soft protections ensure that the MEM likelihood remains numerically stable and physically meaningful in all regions of the integration domain.

14.5.2 ExtraRadiation_3DOF: Main idea

The module `ExtraRadiation_3DOF` introduces three additional independent integration dimensions, which can be parameterized either in Cartesian coordinates (p_x, p_y, p_z) or in cylindrical phase space (p_T, ϕ, E) depending on the user needs. As we introduced earlier, this extension is designed for processes where the presence of invisible particles at LO (*e.g.* $t\bar{t}H$) already force the choice of main (and secondary) blocks.

Because the δ -functions in the integral (of Eq. (8.5)) can eliminate at most four degrees of freedom, any process involving further invisible particles requires a generalized treatment to properly account for the remaining unconstrained variables.

This new module `ExtraRadiation_3DOF` operates in complement of the already existing modules and blocks, and is to be treated independently of them. One of the key point was to understand exactly how the integration variables were defined and used in MOMEMTA (i.e in the range $[0, 1]$), and to modify them accordingly to construct our variables of interest in the appropriate range.

The implementation of this new module within MOMEMTA proved to be far from straightforward, and the concise description presented in this subsection does not fully reflect the complexity of the challenges involved.

14.5.3 Determination of the Infrared (IR) and Ultraviolet (UV) Limits

Integration limits for the extra radiation variables have been explicitly implemented within the phase-space generation modules `Block_N` and `ExtraRadiation_3D0F`.

To regulate the infrared and ultraviolet behavior of the integrand, we apply both soft and hard cuts on the transverse momentum p_T of the extra radiation.

While the infrared cut is essential to control the divergence of the integrand in the soft and collinear limits, the ultraviolet cut is introduced for numerical stability and to confine the integration to the physically relevant phase-space region. Indeed, although the integrand remains finite at large p_T , the event probability in this region is extremely small, and extending the integration beyond a reasonable p_T range would only increase numerical noise without affecting the physical result.

The specific values of the integration limits were determined through a detailed analysis of the kinematic properties of the additional radiation in NLO generated events. These distributions were obtained using POWHEG-BOX-V2 for most processes (or MADGRAPH5 in cases where POWHEG-BOX-V2 samples were unavailable).

An example of such a study is shown in Figure 14.7, which displays the transverse momentum p_T spectrum of the real emission for the $gg \rightarrow HH$ process at NLO. The final cut values were chosen to balance physical realism, numerical stability, and computational efficiency.

A summary of all of the choices of cuts used for this analysis is given in the Table 14.1 for all of the different processes.

Process	p_T^{\min}	p_T^{\max}	E^{\min}	E^{\max}	$ p_z ^{\min}$	$ p_z ^{\max}$
$gg \rightarrow HH$ (ggF)	15	300	15	1550	2	$\sqrt{E_{\max}^2 - p_{T,\min}^2}$
$t\bar{t}H$	12	500	20	1875	1	$\sqrt{E_{\max}^2 - p_{T,\min}^2}$
QCD background	10	330	15	1800	0.05	$\sqrt{E_{\max}^2 - p_{T,\min}^2}$
singleHiggs	20	182	20	1620	2	$\sqrt{E_{\max}^2 - p_{T,\min}^2}$

Table 14.1: Choice of integration limits for the kinematic variables of interest for the additional real radiation in the MEM phase-space.

The impact of the infrared (IR) cut on the transverse momentum p_T of the additional radiation on the MEM outcome will be evaluated through the resulting ROC curves in Section 17.1.4.

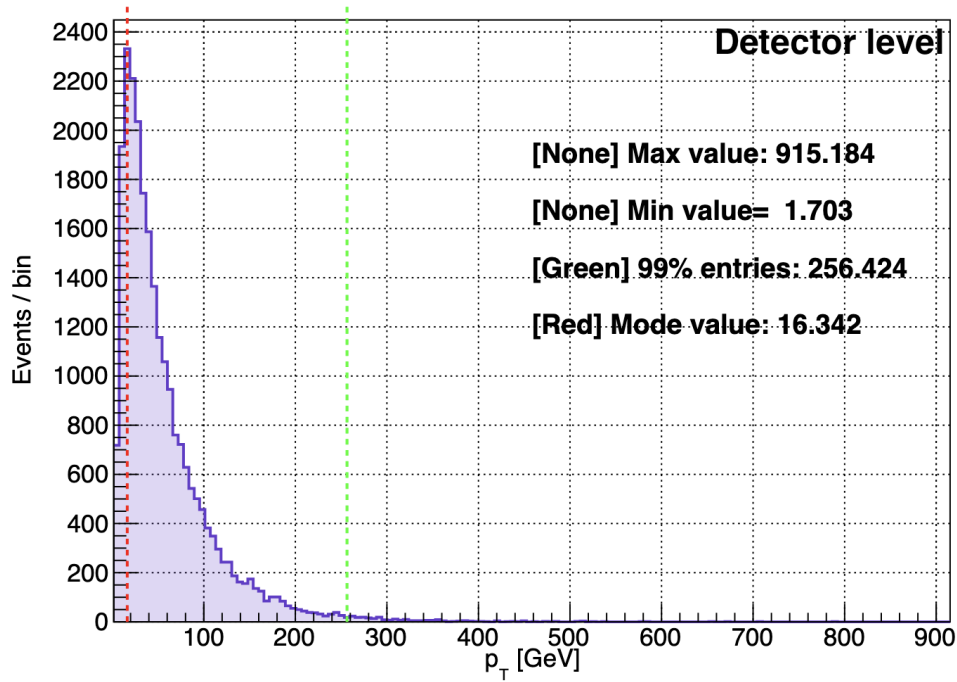


Figure 14.7: Distribution of the extra (real) radiation transverse momentum p_T for $gg \rightarrow HH$ NLO events generated with using the POWHEG-BOX-V2 software.

The **red** dashed line indicates the mode (*i.e.* the most populated bin in the histogram) of the spectrum ($p_T^{\text{mode}} \simeq 16$ GeV), while the **green** dashed line marks the value below which 99 % of the entries lie ($p_T^{99\%} \simeq 2.6 \times 10^2$ GeV).

These two points are used to define the lower and upper integration choices of $(p_T^{\text{min}}, p_T^{\text{max}})$ adopted for the MEM cuts in phase-space generation.

14.5.4 Updating Lua Steering Files

Remember that in the MOMEMTA framework, Lua steering files serve as configuration scripts that control the structure and logic of the integration setup (*cf.* Figure 15.8). These files define the sequence of modules (such as Main Blocks, Secondary Blocks, and Transfer Functions), specify the phase-space mappings, and manage the input-output flow between components without modifying the core C++ code.

For Leading Order processes, we were able to adapt existing Lua templates from the legacy analysis, with only minimal modifications.

The treatment of virtual corrections at NLO reuses the same integration logic and structure as LO computations, so no major changes were necessary in that case.

However, for the Real NLO contributions, new steering files had to be developed from scratch, due to the fundamental change in phase-space topology introduced by the additional radiation.

For instance, in the $gg \rightarrow HH$ and $b\bar{b}\gamma\gamma$ channels, one of the many change was the replacement of the `Block_A` with our custom `Block_N`, while for the $t\bar{t}H$ process,

we kept `Block_F` and supplemented it with the `ExtraRadiation_3DOF` module to account for the additional integration degrees of freedom.

The development of these new Lua steering files was not straightforward. The Lua structure has its own logic, and documentation or examples (at LO) applications are rare. Many aspects of the configuration (such as the order of module declarations, the correct reuse of intermediate objects, or the handling of invisible particles) had to be deduced through extensive *trial and error*.

Building these Real NLO Lua steering files required substantial debugging and iterative refinement.

We ultimately arrived to develop configurations that were both valid within the MoMEMta architecture and accurate from a physics standpoint.

14.6 Summary of our Choice of MEM Integration Variables

Table 14.2 summarizes the possible choice of integration variables used in our MEM calculation for each process considered in this analysis (as the choices shown are not unique).

Process	Dimension of integration	Variables of integration (<i>not mandatory choice</i>)
ggF Di-Higgs @LO	2 ($\rightarrow 0$)	(H width); $\gamma_{1,E}$
$t\bar{t}H$ @LO	9 ($\rightarrow 6$)	(H width, top_1 width, top_2 width); permutation of (b_3, b_4); $\gamma_{1,E}$; $b_{3,E}$; $b_{4,E}$; q_1 ; q_2
QCD @LO	2	$\gamma_{1,E}$; $\gamma_{2,E}$
singleHiggs @LO	2	(H width); $\gamma_{1,E}$
ggF Di-Higgs @NLO Real	5 (\rightarrow 3)	(H_1 width; H_2 width); $\gamma_{1,E}$; $b_{3,E}$; p_z^{rad}
$t\bar{t}H$ @NLO Real	12 (\rightarrow 9)	[LO] variables + p_T^{rad} ; ϕ^{rad} ; E^{rad}
QCD @NLO Real	5	$\gamma_{1,E}$; $\gamma_{2,E}$; $b_{3,E}$; $b_{4,E}$; p_z^{rad}
singleHiggs @NLO Real	5	(H width); $\gamma_{1,E}$; $b_{3,E}$; $b_{4,E}$; p_z^{rad}

Table 14.2: Summary of integration dimensions and variable choices across Leading and Next-to-Leading Order processes.

Values in parentheses indicate possible dimensionality reduction after constraining the width of off-shell particles (*e.g.* the Higgs boson).

Different parametrizations are possible depending on the structure of the final state and the adopted optimization strategy.

Variables shown in parentheses correspond to intermediate Breit–Wigner resonances whose contribution can be integrated out analytically if the narrow width approximation is applied (which leads to a reduction in the dimensionality of the integral, indicated by an arrow ‘ \rightarrow ’).

Variables listed in Table 14.2 include the reconstructed energies of the final-state objects, particularly the Higgs decay products: the photons ($\gamma_{1,E}$, $\gamma_{2,E}$) and the b -jets ($b_{3,E}$, $b_{4,E}$).

More detail about how to derive the dimension of the MEM Likelihood likelihood is available in Appendix A

In the case of NLO real-emission processes, additional degrees of freedom associated with the unresolved radiation are introduced. These are denoted using the index **rad** (*e.g.* p_T^{rad} for the extra radiation transverse momentum), which represents the momentum components of the extra parton integrated over in the MEM likelihood.

14.7 Improving the Transfer Function for ATLAS fully simulated events

Recall that the transfer function $W(\mathbf{y}, \mathbf{x}^i)$, introduced in Eq. (8.5), describes the probability of reconstructing the measured kinematics \mathbf{x}^i from an underlying partonic configuration \mathbf{y} .

In simple terms, W encodes *how* the detector smears or distorts the true kinematics and it also tells us *how likely* it would be for a particle \mathbf{y} to be observed as \mathbf{x}^i . The quality of the transfer function is crucial. It directly affects the accuracy of the likelihood computation. In the baseline version of this analysis, we used a simplified model where the energy smearing is Gaussian. The relative resolution was fixed to:

$$\frac{\sigma}{E} \approx 1\% \quad \text{for photons}, \quad \frac{\sigma}{E} \approx 10\% \quad \text{for } b\text{-jets}. \quad (14.4)$$

This is the only transfer function currently implemented in MOMEMTA. To improve realism, we developed a more refined transfer function using ATLAS simulated n-tuples. Figures 14.8 and 14.9 show the outcome of this effort for photons and b -jets.

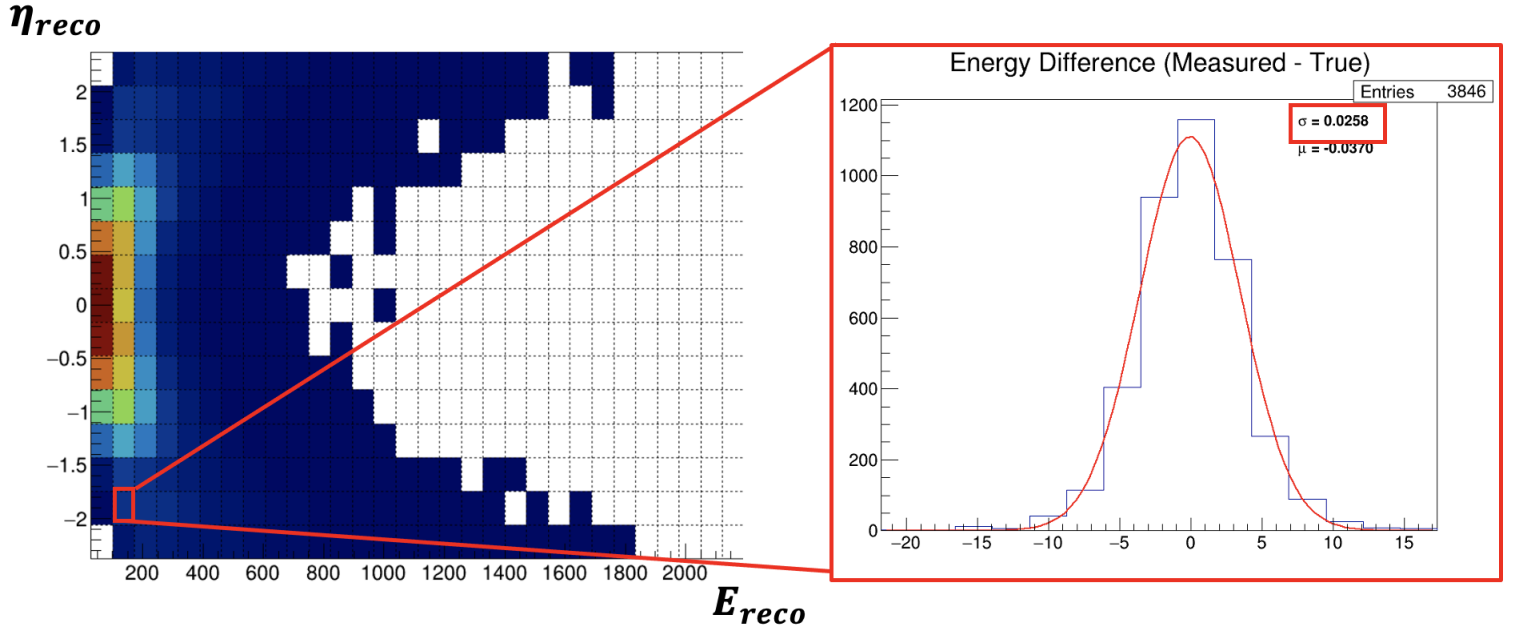


Figure 14.8: 2D grid in $(E_{\text{reco}}, \eta_{\text{reco}})$ plane for ATLAS simulated n-tuples events, for the case of photons here. The procedure is the same for the b -jets.

This procedure applies to any of reconstructed object:

It uses the relation between truth-level and reconstructed kinematics from the n-tuple. For each particle, we take its reconstructed energy E_{reco} and pseudorapidity η_{reco} .

We then match it to its generator-level counterpart and record E_{true} .

We build a 2D grid in the $(E_{\text{reco}}, \eta_{\text{reco}})$ plane. Each bin collects the values of the

difference $E_{\text{reco}} - E_{\text{true}}$ across events. For every bin, we store these values inside an histogram that we fit using a Gaussian distribution.

The fitted width σ gives us the resolution in that bin (*cf.* Figure 14.8).

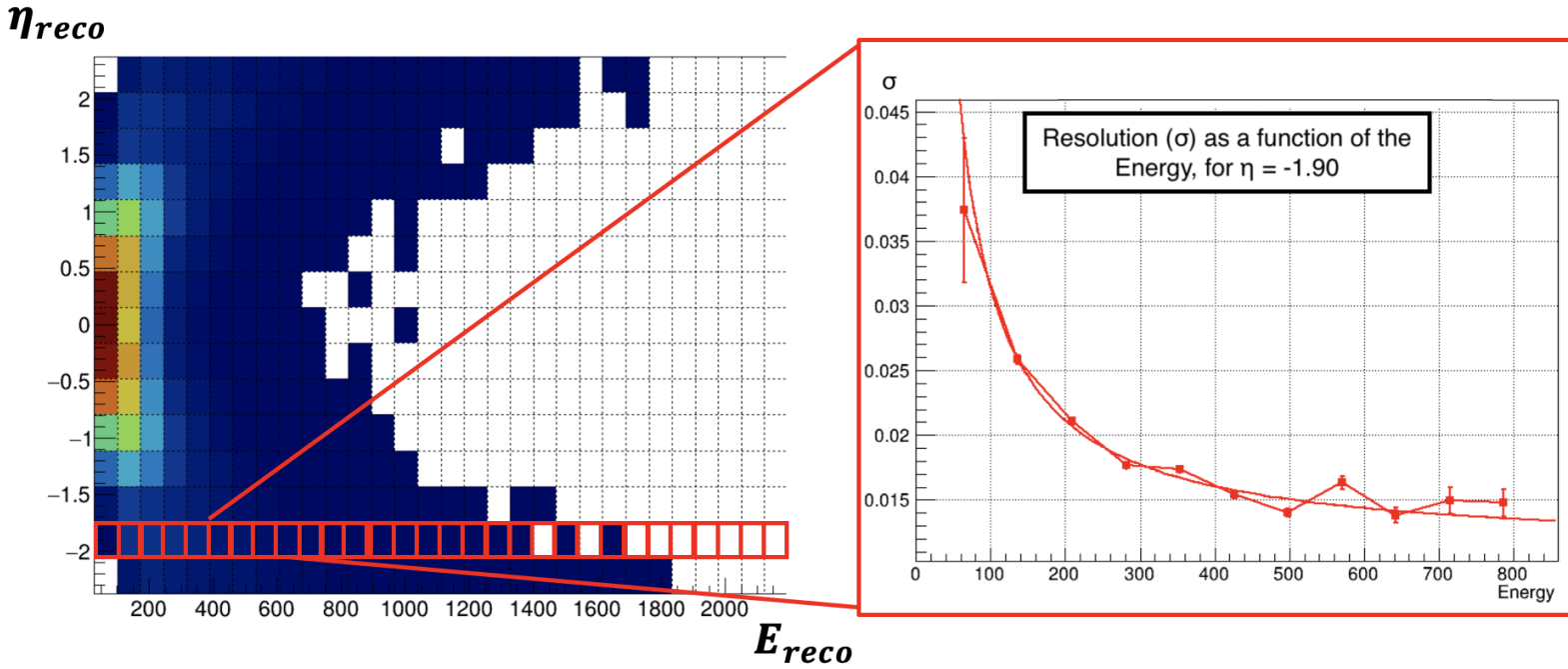


Figure 14.9: Schematic overview on how the relative resolution σ/E_{reco} is obtained from the 2D Grid.

After extracting σ in each bin, we study the relative resolution σ/E_{reco} as a function of energy. This is done at fixed η_{reco} (*cf.* Figure 14.9).

The dependence is modeled with the standard ATLAS resolution formula:

$$\frac{\sigma}{E} = \sqrt{\left(\frac{S}{\sqrt{E}}\right)^2 + C^2 + \left(\frac{N}{E}\right)^2} \quad (14.5)$$

Here, S is the stochastic term, C the constant term, and N the noise term. These parameters are fitted for each slice in η .

This results in a smooth, continuous description of detector smearing, as a function of both energy and pseudorapidity.

For bins that are poorly populated in the n-tuples, we use the fit to interpolate resolution values across phase space.

This refined model should give us a more realistic, data-driven transfer function and reflect the actual behavior of the ATLAS detector. The impact of this improved $W(\mathbf{y}, \mathbf{x}^i)$ on the MEM is evaluated in Appendix B.3.

14.8 Validation and Conclusion

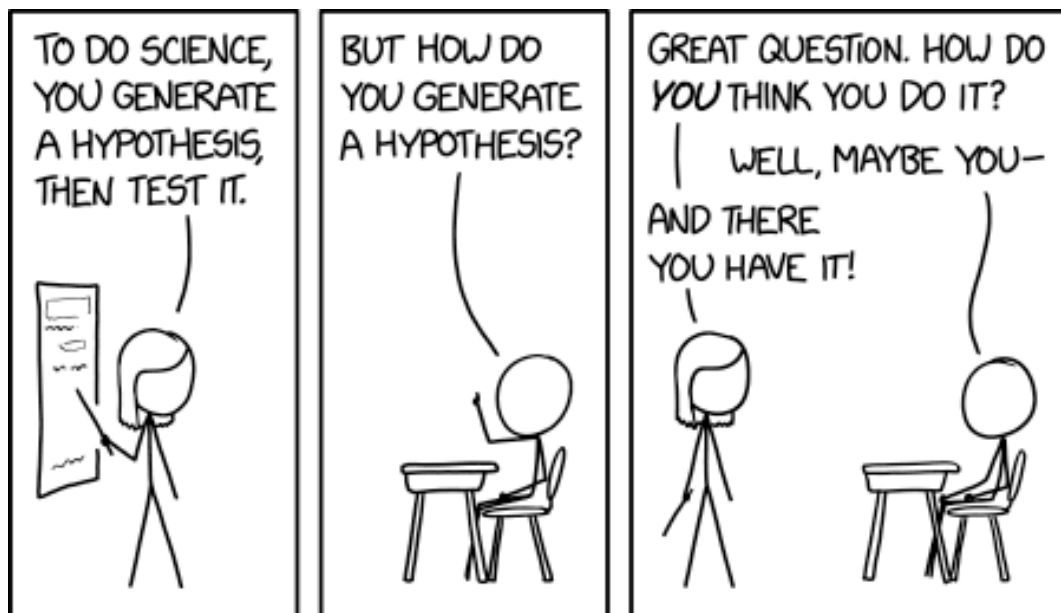
The development of this new NLO MEM formalism required an in-depth understanding on both POWHEG-BOX-V2 and MOMEMTA softwares.

The inherent limitations from a Leading Order treatment, such as the poor modeling of radiation, is directly addressed by our new formalism.

Its validation is performed in the forthcoming chapters (*cf.* Chapters 16 and 17), in the presentation of our results of the measurement of the κ_λ coupling modifier in the $b\bar{b}\gamma\gamma$ final state.

Part V

Results



In this final part of the manuscript, we present the main results obtained with our newly developed MEM@NLO framework. As already mentioned in Chapter 14, and in the spirit of transparency and reproducibility, the code developed during this thesis has been made publicly available at https://gitlab.com/mtartarin/phd_save_public. The repository provides all necessary files, together with a list of explicit software dependencies, to run the new MEM@NLO framework and reproduce the main results presented in the following chapters.

In this part of the manuscript, we will finally address an important question that has been raised in the previous chapters: can the value of the Higgs self-coupling λ_{3H} , parametrised by κ_λ , be recovered from data with the precision promised by this new MEM formalism at NLO?

This part is organised in three chapters:

Chapter 15 details the analysis pipeline: event generation, object reconstruction and smearing, and weight computation.

For each plot, table, or figure we strive to document the exact settings that lead from raw Monte-Carlo events to final likelihood weights, enabling independent verification.

Chapter 16 revisits the work with the MEM at Leading Order, extending and refining the studies reported in chapter 11 using our own analysis pipeline.

Chapter 17 presents our most compelling findings (obtained with the full MEM@NLO formalism) and compares them with existing results.

Content

15 Analysis Framework and Methodology	185
15.1 Monte Carlo Events Generated for this Analysis	185
15.1.1 Using the MADGRAPH5 software	185
15.1.2 Using the POWHEG-BOX-V2 software	188
15.2 Using official ATLAS fully simulated events	193
15.3 Pre-selection cuts and smearing	195
15.3.1 Pre-selection and cuts	195
15.3.2 Event smearing	195
15.4 Automated framework for MEM weight production	196
15.4.1 Motivation and file multiplicity	196
15.4.2 Computing time considerations	198
15.4.3 Schematic overview of the automated framework	200
15.5 Interpreting the results from the MEM: ROC Curves and Likelihoods	203
15.5.1 ROC Curves	203
15.5.2 Likelihood scans (as a function of κ_λ)	204
16 Results: With Our LO Matrix Element Method	211
16.1 ROC Curves using MEM@LO	212
16.1.1 $t\bar{t}H$ background	212

16.1.2	QCD di-photon background	215
16.1.3	Single-Higgs background	216
16.2	Likelihood Scans using LO generated samples	218
16.2.1	[LO] Signal-only	218
16.2.2	[LO] including $t\bar{t}H$ background	221
16.2.3	[LO] including QCD background	223
16.2.4	[LO] including singleHiggs background	225
16.2.5	[LO] including all three main backgrounds	227
16.3	Summary for the MEM@LO	230
17	Results: With Our New NLO Matrix Element Method	233
17.1	ROC Curves using MEM@NLO	234
17.1.1	$t\bar{t}H$ background	234
17.1.2	QCD di-photon background	236
17.1.3	Single-Higgs background	238
17.1.4	Impact of the radiation transverse momentum (p_T^{rad}) IR cut on the ROC	239
17.2	Likelihood Scan Performance: using NLO ISR generated samples . . .	242
17.2.1	[NLO ISR] Signal-only pseudo-data	242
17.2.2	[NLO ISR] including $t\bar{t}H$ background	245
17.2.3	[NLO ISR] including QCD background	247
17.2.4	[NLO ISR] including single-Higgs background	249
17.2.5	[NLO ISR] including all three main backgrounds	251
17.3	Likelihood Scan Performance: using ATLAS fully simulated events . .	254
17.3.1	[ATLAS fullsim] Signal-only pseudo-data	254
17.3.2	[ATLAS fullsim] including $t\bar{t}H$ background	257
17.3.3	[ATLAS fullsim] including QCD background	259
17.3.4	[ATLAS fullsim] including single-Higgs background	261
17.3.5	[ATLAS fullsim] including all three main backgrounds	263
17.4	Summary and Interpretation for the MEM@NLO	266
17.4.1	For the Monte Carlo NLO ISR generated events	266
17.4.2	For the ATLAS fully simulated events	268
	Conclusion	271

Chapter 15

Analysis Framework and Methodology

Readers who are primarily interested in the performance of the MEM@NLO framework may prefer to jump directly to Chapter 16 for Leading Order and Chapter 17 for the Next-to-Leading Order. But to get more context on how the ROC curves and profile-likelihood plots were produced, Section 15.5 from this chapter describes the custom scripts that convert raw MEM outputs into the graphical summaries used throughout this work.

Readers who wish to reproduce the analysis (or simply understand the full workflow) will find a step-by-step guide in this chapter.

Sections 15.1 and 15.2 describe how the Monte-Carlo samples are produced; Section 15.3 explains how those samples are made detector-like through smearing and pre-selection; and Section 15.4 details the automated ‘MEM factory’ that converts events into MEM weights with minimal user interaction.

15.1 Monte Carlo Events Generated for this Analysis

The particle physics community uses many software packages to generate Monte-Carlo (MC) samples for model testing or comparison to data, some of which were introduced earlier.

We focus here on the two generators used to produce the datasets employed for this work (apart from the official ATLAS fully simulated datasets, which will be discussed shortly after): MADGRAPH5_AMC@NLO and POWHEG-BOX-V2.

15.1.1 Using the MadGraph5 software

The MADGRAPH5 software has already been presented in Chapter 11. We discussed there already that the generation of signal gluon fusion (ggF) at LO required a new UFO model (`SM_EFT_FF_bt_haa_kappa`), which we reproduced on our own and compared to the original for validation.

Version and extra software

Several MADGRAPH5 versions were tested during development. The version `v3.1.1` was selected and mainly used because the UFO model for ggF has been validated against this release. The full list of software dependencies and setup used in this work environment is available in Appendix C.

Generating the signal: $gg \rightarrow HH$ at LO

After re-deriving the `SM_EFT_FF_bt_haa_kappa` UFO model, we generated the signal sample with the following commands:

```
./bin/mg5_aMC
import model SM_EFT_FF_bt_haa_kappa
generate g g > h h , h > b b~ , h > a a
output fortran_signal --hel_recycling=False
launch
```

The flag `--hel_recycling=False` prevents MADGRAPH5 from requesting unused Fortran helpers.

Generating the background: $t\bar{t}H$ at LO

```
import model SM_EFT_FF_bt_haa_kappa
define p = g u c d s b u~ c~ d~ s~ b~
generate p p > h t t~ , h > a a ,
      (t > w+ b, w+ > e+ ve),
      (t~ > w- b~, w- > e- ve~)
output fortran_ttH
launch
```

We intentionally force leptonic decays $W \rightarrow e\nu$ to reproduce the generation of events indicated in Ref. [89]. This does not impact the generation of events, only the value of the total cross-section returned by MADGRAPH5.

An experimental analysis could veto events with identified electrons or muons, but in this study we keep the background as signal-like as possible to test MEM discrimination power.

Generating the QCD di-photon background (LO and Real-only NLO)

LO sample.

```
./bin/mg5_aMC
import model SM_EFT_FF_bt_haa_kappa
define p = g u c d s b u~ c~ d~ s~ b~
define x = b b~
generate p p > x x a a
output fortran_QCD_LO
launch
```

NLO (real + virtual): An attempt

```
import model SM_NLO
define p = g u c d s b u~ c~ d~ s~ b~
define x = b b~
generate p p > x x a a [QCD]
output fortran_QCD_NLO_full
launch
```

MADGRAPH5 reports the generation of 3576 real, 190 born and 4510 virtual diagrams.

However, the MoMEMta–MaGMEE interface fails to translate the matrix element files generated by MADGRAPH5 and the process terminates with the error message: No integration channels found.

It is therefore not possible to either produce QCD di-photon background events at full NLO order with this implementation, or to access the corresponding matrix elements for the MEM implementation using the MoMEMta–MagMEE plugin.

NLO sample used (Real-only).

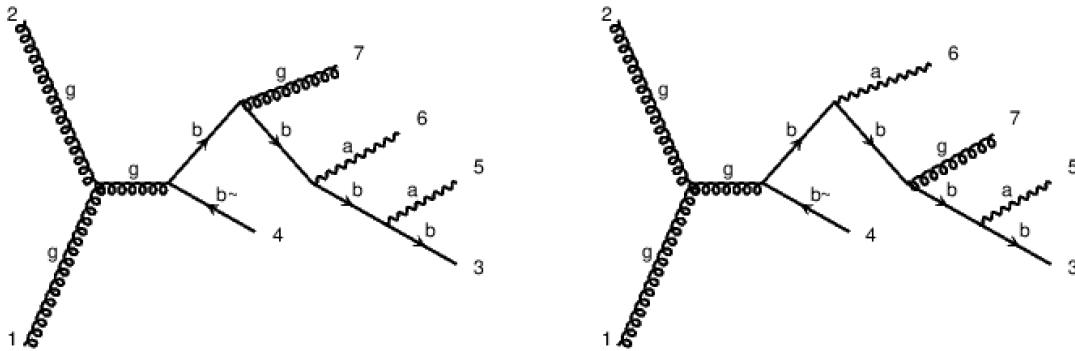


Figure 15.1: Feynman diagram for real QCD background, automatically generated by the MADGRAPH@NLO software.

```
import model SM_NLO
define p = g u c d s b u~ c~ d~ s~ b~
define x = b b~
generate p p > x x a a g
output fortran_QCD_NLO_Real
launch
```

This Real-only sample is successfully converted by MoMEMta–MagMEE, and allows the generation of events. Some of the corresponding Feynman diagrams at NLO (real contribution) are given in Figure 15.1

Unfortunately, the minimal pre-selection cuts used for analysis (*cf.* Section 15.3.1) are too strong on these NLO QCD generated events. The pre-selection efficiency of passing these cuts was found to be extremely low (around 0.0028; see Table 15.1 for details), meaning that only a small fraction of unweighted events survive them.

In practice, generating 20 000 uncut events required about more than six days. At this efficiency, this yields only about 57 events per week.

Reaching the target of 10 000 cut QCD events would therefore require an estimated 175 weeks of continuous generation (i.e 3 years and 4 months), which is not an option given our time and resource.

For now, QCD events generated at Leading Order have been used in our analysis as a practical substitute for their Next-to-Leading Order counterparts. In future studies, more stringent generator-level cuts (that are still weak enough not to impact the sample) should be used.

Generating the single-Higgs background (LO and real-only NLO)

LO sample.

```
import model SM_EFT_FF_bt_haa_kappa
define p = g u c d s b u~ c~ d~ s~ b~
generate p p > h b b~, h > a a
output fortran_singleHiggs_LO
launch
```

NLO sample (real only).

```
import model SM_NLO
define p = g u c d s b u~ c~ d~ s~ b~
generate p p > h b b~ g, h > a a
output fortran_singleHiggs_Real
launch
```

Because the process contains a Higgs decay, the [QCD] flag is not supported and only real diagrams are generated.

15.1.2 Using the POWHEG-BOX-V2 software

The POWHEG-BOX-V2 software has been used for the NLO event generation of the signal and the $t\bar{t}H$ background.

Version and extra softwares needed

For the event generation, small and non-intrusive modifications have been made to ensure the appropriate linking to external softwares and the expected software compiled executable `pwg_main`.

Generating the signal: $gg \rightarrow HH$ NLO

Gluon–fusion Higgs-pair events are produced with the `ggHH` sub-repository of POWHEG-BOX-V2 (Heinrich *et al.* [127]).

The process can be generated in four ‘modes’ (0–3), each adding more complexity and top-mass dependence.

Although we have successfully produced samples in all modes, this study relies exclusively on mode 3 (“full theory”).

All generator settings (including the mode flag and the Higgs self-coupling modifier κ_λ) are controlled via the `powheg.input-save` card.

By varying κ_λ we produced dedicated Monte-Carlo samples for each hypothesis used in the MEM analysis.

Each run writes its hard-scattering events to one or more `pwgevents.lhe` files.

Every record contains the two incoming partons and three outgoing particles: two Higgs bosons and, when applicable, an extra recoil parton from real emission.

Higgs decays and parton showering are handled by a customised version of the supplied *main-PYTHIA8-lhef* executable. The modifications ensure consistent treatment of κ_λ throughout the decay chain and have a significant impact on the final-state kinematics used later by the MEM.

Ambiguous definition of ‘NLO’ generated events

The generation of ‘NLO’ MC events is ambiguous, as we can define 3 different level of complexities (visually represented in Figure 15.2):

- ‘**ISR**’ (Initial State Radiation, in **red**) will be used in this manuscript to describe NLO-generated samples without parton shower (this notion has already been introduced in Section 13.2).
This will be our main reference for NLO generated files throughout this manuscript, unless stated otherwise.
- ‘**FSRdr**’ (Final State Radiation + ΔR , in **green**) will be used in this manuscript to describe NLO-generated samples with parton shower, and where the extra partons (gluons here) from the showering within a cone of size ΔR around the ISR- b partons are added back (in energy) to the latter.
- ‘**FSRend**’ (Final State Radiation, ‘end of the chain’, in **orange**) will be used to describe NLO-generated samples with parton shower, and where the extra partons from the showering are never added back to the b partons. We only look at the ‘end of the chain’ particles.

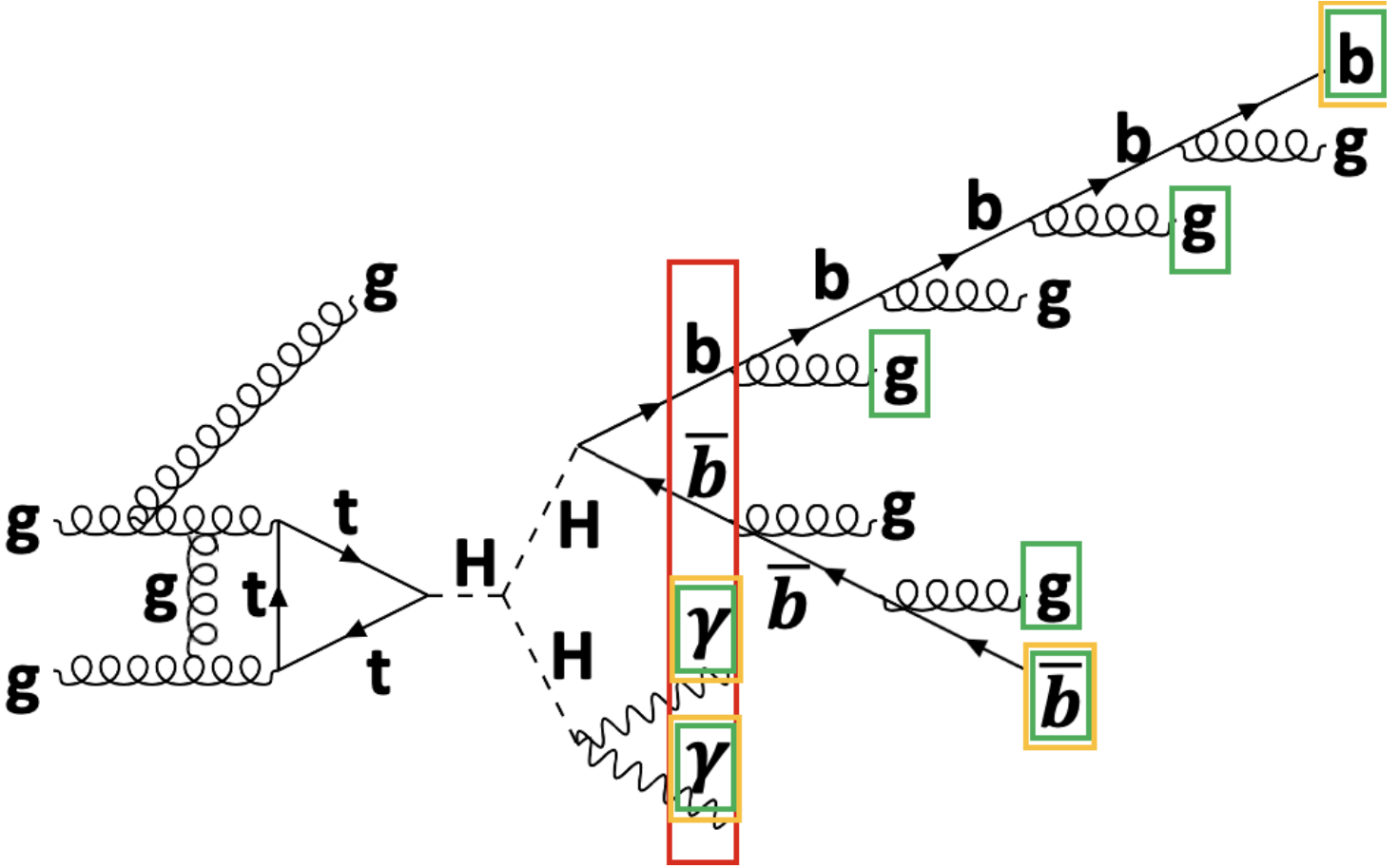


Figure 15.2: Multiple definition of ‘NLO’ generated events, depending on the choices of the $b\bar{b}\gamma\gamma$ final state particles and how they are defined kinematically. We decided to name the different choices: ‘ISR’ (in red); ‘FSRdr’ (in green); and ‘FSRend’ (in orange).

The original *main-PYTHIA8-lhef* output did not allow to directly access or easily distinguish between these three possibilities. We modified this part of the code inside the Fortran *main-PYTHIA8.f* file so that 4 additional output files were generated for each run:

- ‘ALL.txt’, which outputs the whole process each time. With all of the steps and particles involved. It can be used for debugging purposes.
- ‘ISR.txt’, where we get as output the 2 initial partons, the 2 Higgs bosons **right before decay**, their respective direct daughters, and the extra radiation parton.
- ‘FSRdr.txt’, where the output structure is the same as for ‘ISR’ but the logic is very different. We added a piece of code that identified and stored the ‘end-chain’ b -jets (from the Higgs daughters candidates showering). For each additional radiation produced through parton showering, it computes the ΔR quantity relative to these end-chains b partons to assert if any merging is necessary. In the need of merging, we sum the energies of the corresponding ‘end-chain’

b -jet with the energy from the corresponding extra-radiation while keeping the ‘end-chain’ b -jet angles to their original values. We therefore only needed to rescale the three-momentum $|\vec{p}|$ norm value by fixing b -jet the mass to 4.7 GeV (consistent with MADGRAPH5 parameter cards value).

- ‘FSRend.txt’, where the output structure is the same as for ‘ISR’ but the logic is very different. We used the same new code from ‘FSRdr’ to identify the ‘end-chain’ b -jets created from the the ‘ISR’ Higgs daughter b -jets candidates, without doing any radiation energy summation this time.

The photons are not impacted by the parton shower in this POWHEG-BOX-V2 sub-repository. So this work has been mainly focusing on the b -jets (though it is possible for any extra-radiation coming from the b -jet to impact the signature of any photon nearby). We take all of these possibilities into account in our Next-to-Leading Order MEM.

An other important modification concerns the file *main31.cmd*, which controls the parton showers and decays. We forced the Higgs decay channels to be 50% $H \rightarrow b\bar{b}$ and 50% $H \rightarrow \gamma\gamma$. Consequently, roughly 50% of produced events have the desired $b\bar{b}\gamma\gamma$ final state. Another 25% of them have $b\bar{b}b\bar{b}$, and the remaining 25% consists of $\gamma\gamma\gamma\gamma$ final state.

We ensured that all our modifications to the existing POWHEG-BOX-V2 base code were as **minimal** and **localized** as possible in order to avoid introducing unintended or undetected behavior that could bias our analysis.

Validation of the Higgs decay from our modified POWHEG-BOX-V2

As a cross-check of the many changes implemented in the POWHEG-BOX-V2 interface with PYTHIA, it was important that we reproduce the Higgs decay with an independent routine that we developed from scratch.

Each Higgs boson is treated separately in its rest frame (*cf.* Figure 15.3).

The reference distributions obtained with the standard POWHEG+PYTHIA chain are displayed in Figure 15.4.

We model Higgs boson decay as follow:

In the Higgs center-of-mass (c.o.m) frame the two identical daughter particles should obey the following relations:

$$p_{1x} = -p_{2x}, \quad p_{1y} = -p_{2y}, \quad p_{1z} = -p_{2z}, \quad E_1 = E_2 = \frac{1}{2} E^*, \quad (15.1)$$

with E^* the Higgs energy in the c.o.m frame.

Generation of the four-momenta proceeds as follow:

1. **Polar angle** θ^* : drawn from the following distribution

$$f(\theta^*) = \frac{1}{2} \sin \theta^*,$$

This leads to a flat distribution in $\cos(\theta^*)$ (*cf.* Appendix B).

2. **Azimuthal angle** φ^* : draw from a uniform distribution in the interval $[0, 2\pi)$.

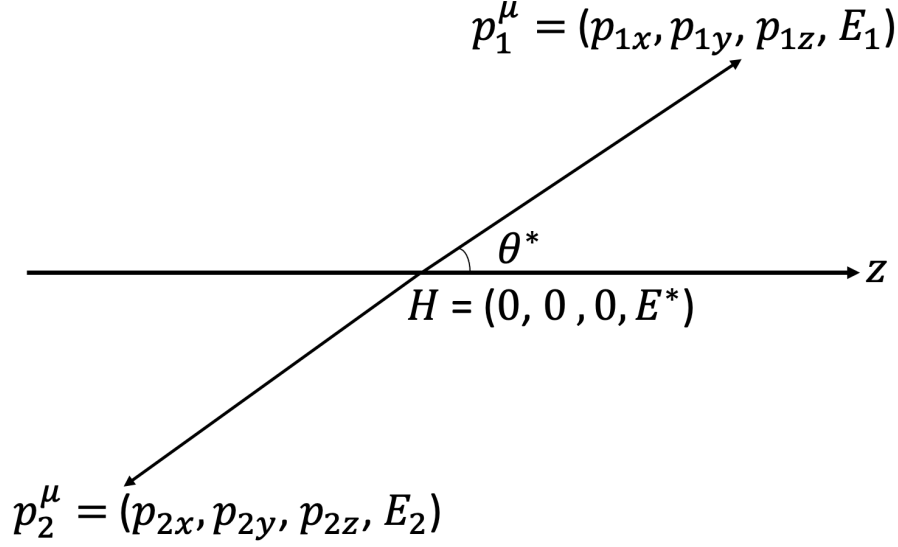


Figure 15.3: Representation of the Higgs boson H decay into two particles of same nature p_1 and p_2 , within the Higgs rest frame.

3. Momentum magnitude:

$$|\vec{p}_1| = |\vec{p}_2| = \frac{1}{2}\sqrt{E^{*2} - 4m^2},$$

obtained from the on-mass-shell condition and the equality $m_1 = m_2 \equiv m$, with m the mass of the Higgs decay daughters.

The Eqs. (15.1), together with the three items above, fully determine the four-vectors of the Higgs decay products. A boost back to the laboratory frame successfully generates the event kinematic of interest.

Excellent agreement is observed in Figure 15.5 for the pseudo-rapidity η (defined from the θ variable) distributions for the remaining kinematic variables of interest are shown in Appendix B.

Generating the background: $t\bar{t}H$ NLO

We used the POWHEG-BOX-V2 $t\bar{t}H$ sub-repository to generate MC events at NLO accuracy for the $t\bar{t}H$ background. The generation of the `pwgevents.lhe` file with $t\bar{t}H$ final state particles was successful, but the decay into $b\bar{b}\gamma\gamma$ final state using the existing interface with PYTHIA failed.

To correct this issue, we carefully adapted the existing and working interface from the `ggHH` sub-repository for the $t\bar{t}H$ decay and parton showering, and forced the Higgs decay $H \rightarrow \gamma\gamma$ at 100% within `main31.cmd`.

The same terminologies for NLO generated samples ('ISR', 'FSRdr' and 'FSRend') can be used here too.

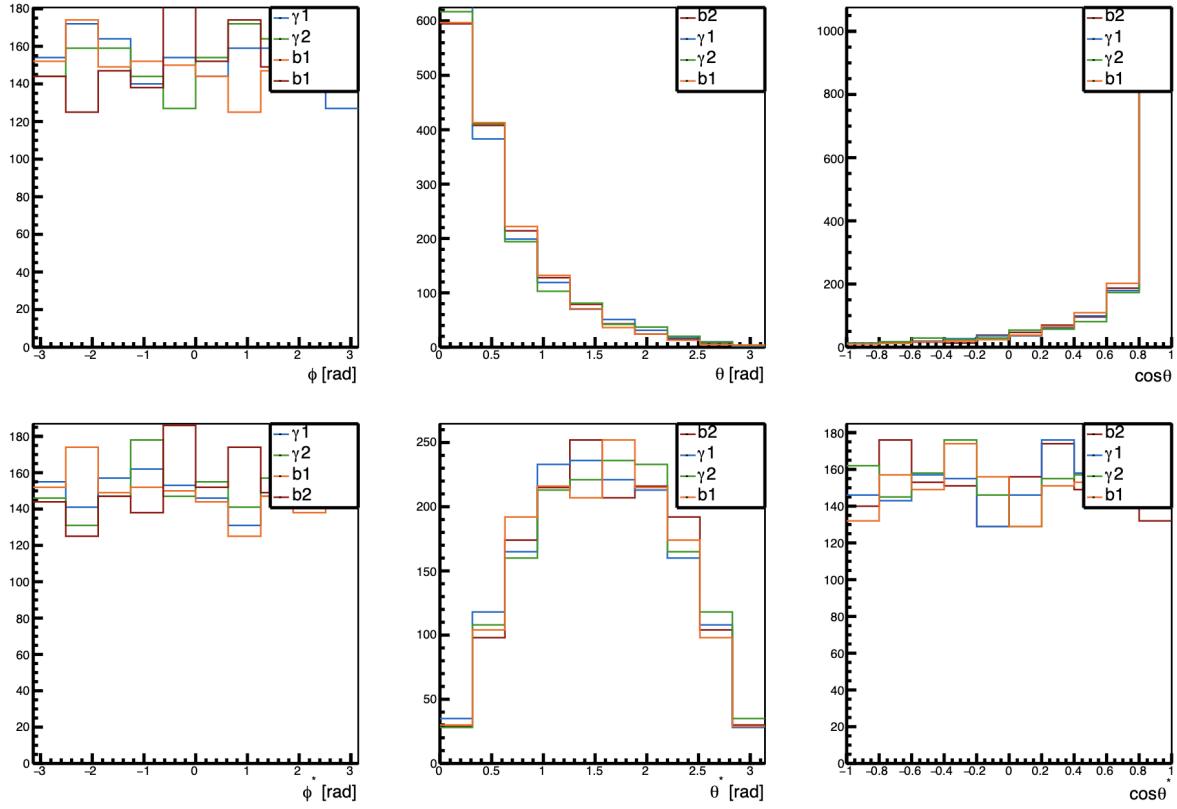


Figure 15.4: Angular distributions of the Higgs boson decay daughters (named γ_1 , γ_2 , b_1 , b_2).

Top row: laboratory frame observables: azimuthal angle ϕ , polar angle θ , and $\cos(\theta)$.

Bottom row: the same observables evaluated in the respective Higgs rest frames (denoted with a superscript star: ϕ^* , θ^* , $\cos(\theta^*)$).

The four colored histograms are overlaid in each panel, with the legend displayed in the upper-right corner.

15.2 Using official ATLAS fully simulated events

In addition to the Monte Carlo samples that we generated ourselves for the signal and background processes, we also made use of ATLAS fully simulated n-tuples used for the non-resonant $HH \rightarrow b\bar{b}\gamma\gamma$ analysis, (introduced earlier in Table. 6.1).

These datasets offer a more realistic modeling of the detector response, following the standard simulation workflows of the ATLAS collaboration.

Employing these ATLAS fully simulated events in the MEM analysis is essential for validation, because it allows us to deliberately remain agnostic about the underlying event-generation details (*e.g.* matrix element generator, parton shower model, underlying event tune), thus avoiding any potential bias in the extraction of the κ_λ parameter that could arise from tuning or over-fitting to a known configuration.

The use of these official samples and the official ATLAS analysis framework represents a significant step towards a future analysis of ATLAS data.

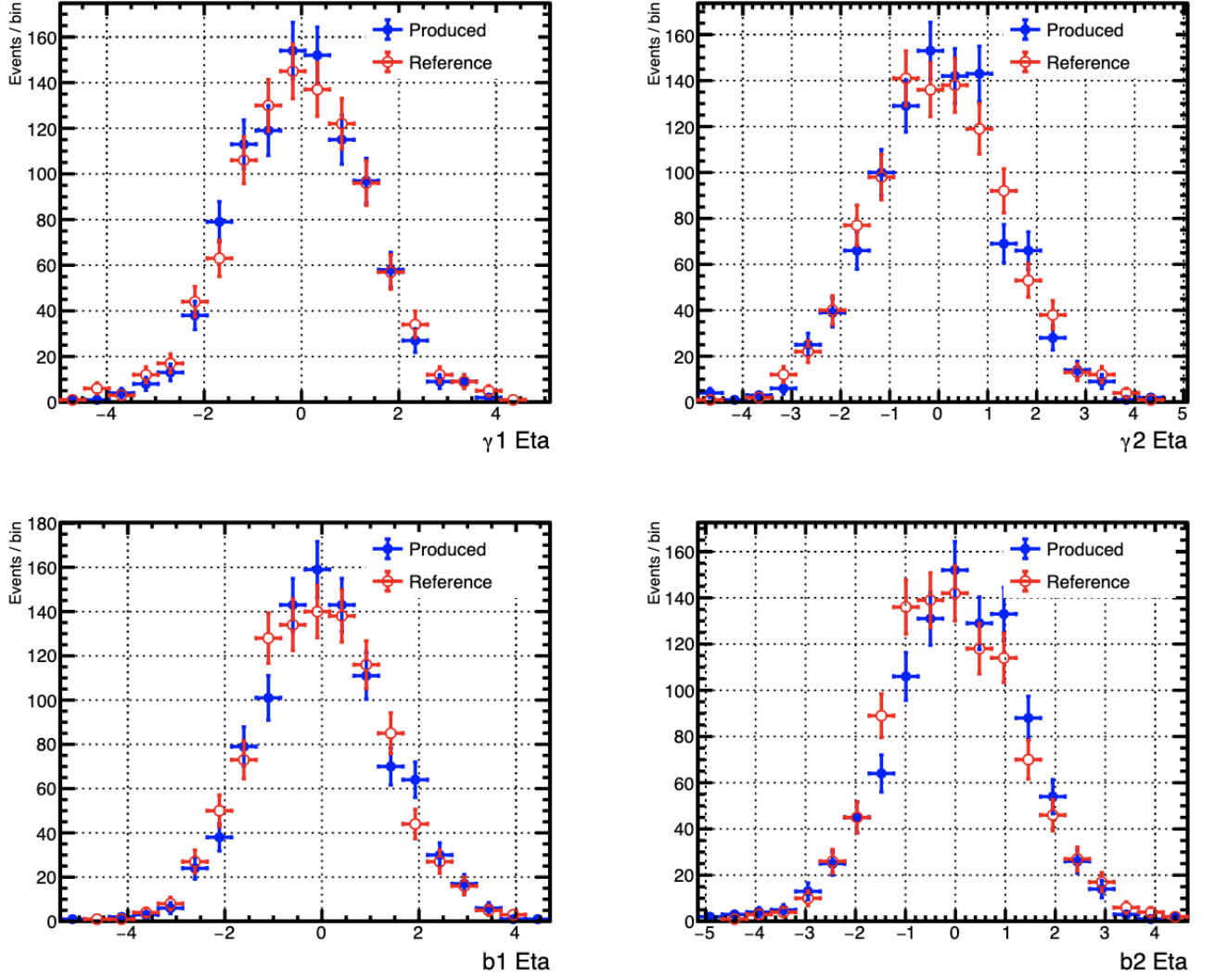


Figure 15.5: Comparison of the pseudo-rapidity (η) distributions for the four decay products of the Higgs boson in the $b\bar{b}\gamma\gamma$ final state. Blue markers represent events produced with the modified implementation, while red markers denote the reference sample from POWHEG-BOX-V2.

We developed dedicated scripts to extract the reconstructed kinematic information relevant for all processes under study (*i.e.* the gluon-fusion signal ggF , the $t\bar{t}H$ background, QCD continuum background, and single Higgs production) and to translate this information into a readable format for our MEM.

Our scripts also support the retrieval of generator-level (truth) information through a one-to-one matching procedure between reconstructed and truth-level particles. This feature was crucial for validating each event and studying transfer function behavior.

15.3 Pre-selection cuts and smearing

15.3.1 Pre-selection and cuts

We will rely on the Matrix Element Method for signal/background discrimination. We therefore adopt a **minimal** pre-selection (close to the ATLAS trigger thresholds).

The following selection criteria are applied to the two photons γ and the two b -jets:

Kinematic and angular selection criteria

- **Photon kinematic cuts**
 - $p_T^{\gamma_{\text{lead}}} > 35 \text{ GeV}, p_T^{\gamma_{\text{sub}}} > 25 \text{ GeV}$
 - $|\eta_\gamma| < 1.37$ or $1.52 < |\eta_\gamma| < 2.37$
 - $120 \text{ GeV} < m_{\gamma\gamma} < 130 \text{ GeV}$
 - $p_T^{\gamma_{\text{lead}}} > 0.35 m_{\gamma\gamma}, p_T^{\gamma_{\text{sub}}} > 0.25 m_{\gamma\gamma}$
- **b -jet kinematic cuts**
 - $p_T^b > 25 \text{ GeV}$
 - $|\eta_b| < 2.5$
- **Angular separations**
 - $\Delta R(\gamma, \gamma) > 0.2$
 - $\Delta R(\gamma, b) > 0.2$
 - $\Delta R(b, b) > 0.4$
 - $\Delta R(\text{rad}, \gamma) > 0.2$

where p_T refers to the transverse momentum, η is the pseudorapidity, ΔR denotes the angular separation between objects, and *rad* denotes the extra NLO radiation parton. Subscripts such as *lead* and *sub* refer to the ordering in transverse momentum, *lead* being the highest.

In contrast to the broader mass window of $105 < m_{\gamma\gamma} < 160 \text{ GeV}$ used to model the background from data sidebands (*cf.* Section 6.2), our MEM analysis is applied only to events within the tighter signal window $120 < m_{\gamma\gamma} < 130 \text{ GeV}$.

The strategy was to target the subset of background events that most closely resemble the signal, thereby enhancing the MEM great sensitivity to the subtle differences between Higgs boson decays and the irreducible background.

15.3.2 Event smearing

In order to evaluate the performance of the MEM under conditions that mimic those encountered by the ATLAS detector, a simple parametrized model of detector response is applied through *object smearing*.

This procedure introduces a controlled degradation of the parton-level kinematic quantities, providing a bridge between generator-level studies and fully reconstructed data.

The smearing is implemented by modifying the energies of each of the final-state objects $b\bar{b}\gamma\gamma$. For each reconstructed photon, the true (generator-level) energy E_γ^{true} is replaced by a smeared value

$$E_\gamma^{\text{smeared}} = \mathcal{N}(E_\gamma^{\text{true}}, 0.01 E_\gamma^{\text{true}}), \quad (15.2)$$

where $\mathcal{N}(\mu, \sigma)$ denotes a Normal distribution with mean μ and standard deviation σ . The choice of a 1% relative width reflects the excellent intrinsic energy resolution of the ATLAS electromagnetic calorimeter in the barrel region (as already discussed in Eq. (14.4)).

The energies of the b -jets are smeared with a broader distribution:

$$E_{b\text{-jet}}^{\text{smeared}} = \mathcal{N}(E_{b\text{-jet}}^{\text{true}}, 0.10 E_{b\text{-jet}}^{\text{true}}), \quad (15.3)$$

corresponding to a 10% relative width. This parameterisation encapsulates the more modest energy resolution attainable in the ATLAS hadronic calorimeter.

The angular variables (namely the pseudorapidity η and azimuthal angle ϕ) of the photons and jets are left unchanged in this study, as they are considered measured with high precision.

15.4 Automated framework for MEM weight production

With 10000 events per dataset, 36 κ_λ hypotheses, and both BV and Real contributions at NLO, **manual** job configuration, validation and bookkeeping is out of the question.

This section documents the *MEM factory* that keeps the bookkeeping clear and the CPUs busy.

15.4.1 Motivation and file multiplicity

An analysis based on the Matrix Element Method demands a very large number of event weights for each event in the selected Monte Carlo datasets.

For a given event, weights are computed for all relevant processes (signal and backgrounds) and, when using MEM@NLO, for both perturbative contributions: Born+Virtual (BV) and Real.

In addition, for the channel $gg \rightarrow HH \rightarrow b\bar{b}\gamma\gamma$, the MEM evaluation must be performed for a wide range of Higgs self-coupling values.

For this analysis we cover $\kappa_\lambda \in [-3.50, 10.00]$, using $N_{\kappa_\lambda} = 36$ distinct values. The full set of the 36 κ_λ hypotheses considered is

$$\begin{aligned} &\{-3.50 \quad -3.00 \quad -2.50 \quad -2.00 \quad -1.80 \quad -1.50 \quad -1.20 \quad -1.00 \quad -0.80 \\ &\quad -0.50 \quad -0.20 \quad 0.00 \quad 0.20 \quad 0.50 \quad 0.80 \quad \mathbf{1.00} \quad 1.20 \quad 1.50 \\ &\quad 1.80 \quad 2.00 \quad 2.50 \quad 3.00 \quad 3.50 \quad 4.00 \quad 4.50 \quad 5.00 \quad 5.50 \\ &\quad 6.00 \quad 6.50 \quad 7.00 \quad 7.50 \quad 8.00 \quad 8.50 \quad 9.00 \quad 9.50 \quad 10.00\}. \end{aligned}$$

When MEM@NLO is employed, each hypothesis is evaluated twice (BV and Real), and the two contributions are summed to obtain the full NLO weight. For MEM@LO only the Born contribution is required.

Including all N_{proc} background processes of the ATLAS di-Higgs analysis, the total number of weights grows extremely fast and cannot be managed reliably without an automated workflow.

File multiplicity

Each of our Monte Carlo datasets (defined by the generator settings, perturbative order, ...etc), have been generated with $N_{\text{evt}} = 10^4$ unweighted events.

For MEM@NLO, it is necessary to compute two weights (BV and Real) per event, giving

$$N_{\text{files}} = 2 N_{\kappa_\lambda} N_{\text{proc}} + 2 N_{\text{proc}} (N_{\text{proc}} - 1), \quad (15.4)$$

where $N_{\text{proc}} = N_{\text{sig}} + N_{\text{bkg}}$ and N_{sig} denotes the number of signal datasets studied (generated with different κ_λ value).

For a minimal example with one signal dataset (i.e κ_λ generating value, $N_{\text{sig}} = 1$) and one background ($N_{\text{bkg}} = 1$), Eq. (15.4) yields $N_{\text{files}} = 2 \times 36 \times 2 + 2 \times 2 \times 1 = 148$ weight files.

The corresponding number of individual weight evaluations is

$$N_{\text{wgt}} = N_{\text{evt}} \times N_{\text{files}} = 1.48 \times 10^6. \quad (15.5)$$

Grouping the events in sets of $N_{\text{evt}}^{\text{run}} = 20$ events (where one batch job will be submitted per set of events), leads to

$$N_{\text{runs}} = \left\lceil \frac{N_{\text{wgt}}}{N_{\text{evt}}^{\text{run}}} \right\rceil = 7.4 \times 10^4 \quad (15.6)$$

batch jobs submitted.

A realistic ATLAS background model with $N_{\text{bkg}} \simeq 4$ increases each of these numbers accordingly, making a fully automated workflow indispensable for serious NLO MEM analyses.

15.4.2 Computing time considerations

The dominant cost of a single NLO weight evaluation stems from the multi-dimensional integration performed using the CUBA library within MOMEMTA.

Figure 15.6 displays the wall-clock time distribution for a NLO signal sample evaluated under its corresponding NLO hypothesis. The mode execution time (*i.e.* the pic in the histogram) is $\langle t_{\text{evt}} \rangle \approx 13$ min per event, with rare phase-space points taking up to $t_{\text{evt}} \approx 14$ h (*i.e.* 837 min).

To drastically improve the time of the computation, a parallelization strategy has been implemented.

Theoretically the built-in implementation of CUBA within MOMEMTA allows to use parallel run on a chosen number of cores (through the variable CUBACORES), but its initialization was not straightforward. We still managed to implement and have full control over this parameter eventually.

Extensive tests validates this new implementation and the efficiency of parallel runs on multiple cores, without changing the MEM weight output.

Figure 15.7 demonstrate the resulting speed-up, considerably reducing the time needed for the most time-consuming events in the right tail of the distribution from around 837 min to 294 min for NLO generated signal events.

This figure also reveals an unexpected outcome: the parallelization strategy introduces a slight increase of the mode wall-time per event (by only a few minutes, which is a small sacrifice for the gain on the tail of the distribution).

Interpretation and beyond

Enabling CUBACORES does **not** change the number of integrand evaluations, it merely distributes them across several CPU cores. In other words, the maximum wall-clock time drops significantly but the total CPU time (and thus the computing budget) remains unchanged.

The parallel option should therefore be viewed as a shortcut that delivers the same physics results much faster, not as a fundamental solution to the high-dimensional integration cost.

We note that machine learning (ML) surrogates (*i.e.* neural-network models trained to reproduce the output of the numerical integration) for MEM weights have been proposed in the literature and promise further speed-ups with a smaller resource footprint. However, as demonstrating a fully operational MEM@NLO was the primary goal of this thesis, the development of a ML acceleration layer is left for future implementations.

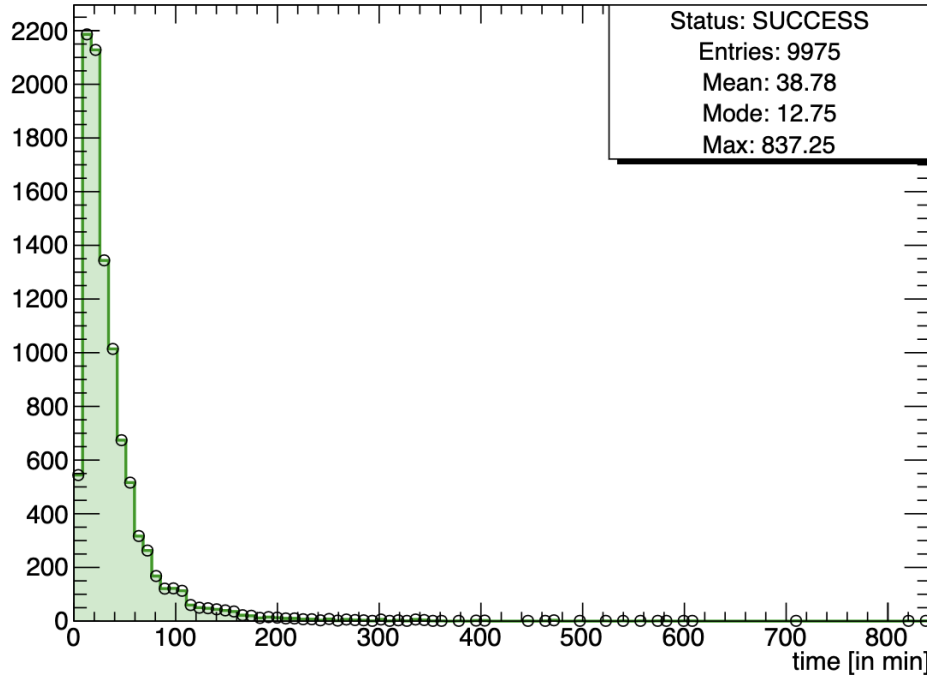


Figure 15.6: Wall-clock Time (in minutes) per event for a NLO signal sample evaluated under the corresponding NLO hypothesis **before** parallelisation. The mean, mode and maximum values of the distributions are indicated.

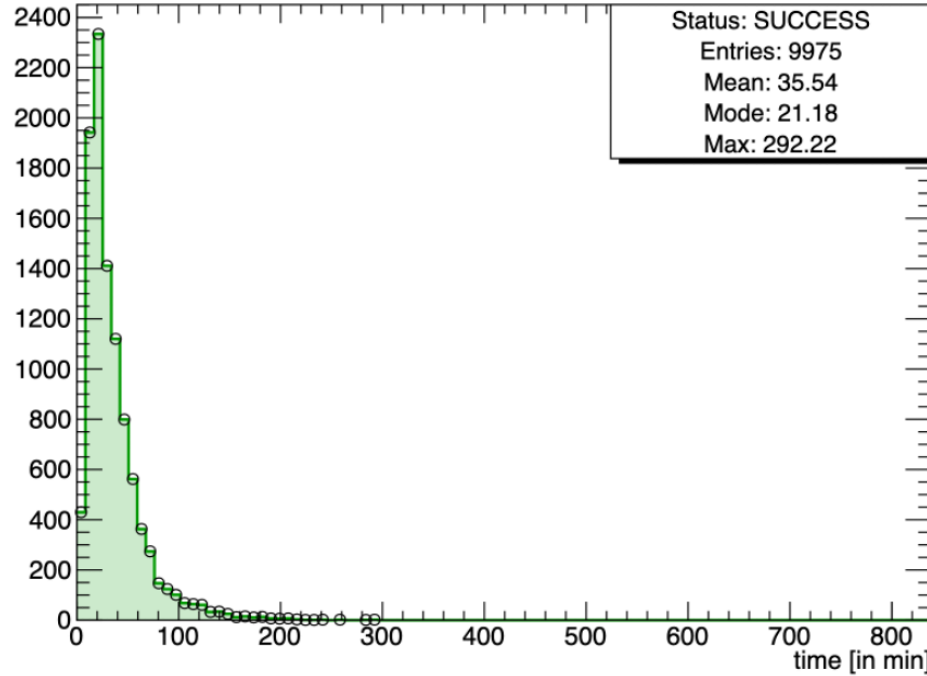


Figure 15.7: Wall-clock Time (in minutes) per event for a NLO signal sample evaluated under the corresponding NLO hypothesis **after** enabling CUBACORES parallelisation in MoMEMTA. The mean, mode and maximum values of the distributions are indicated.

15.4.3 Schematic overview of the automated framework

Automated framework for the MEM outputs Now that the need for an automated framework in large scale MEM production has been established, we introduce our automated framework through the schematic shown in Fig. 15.8.

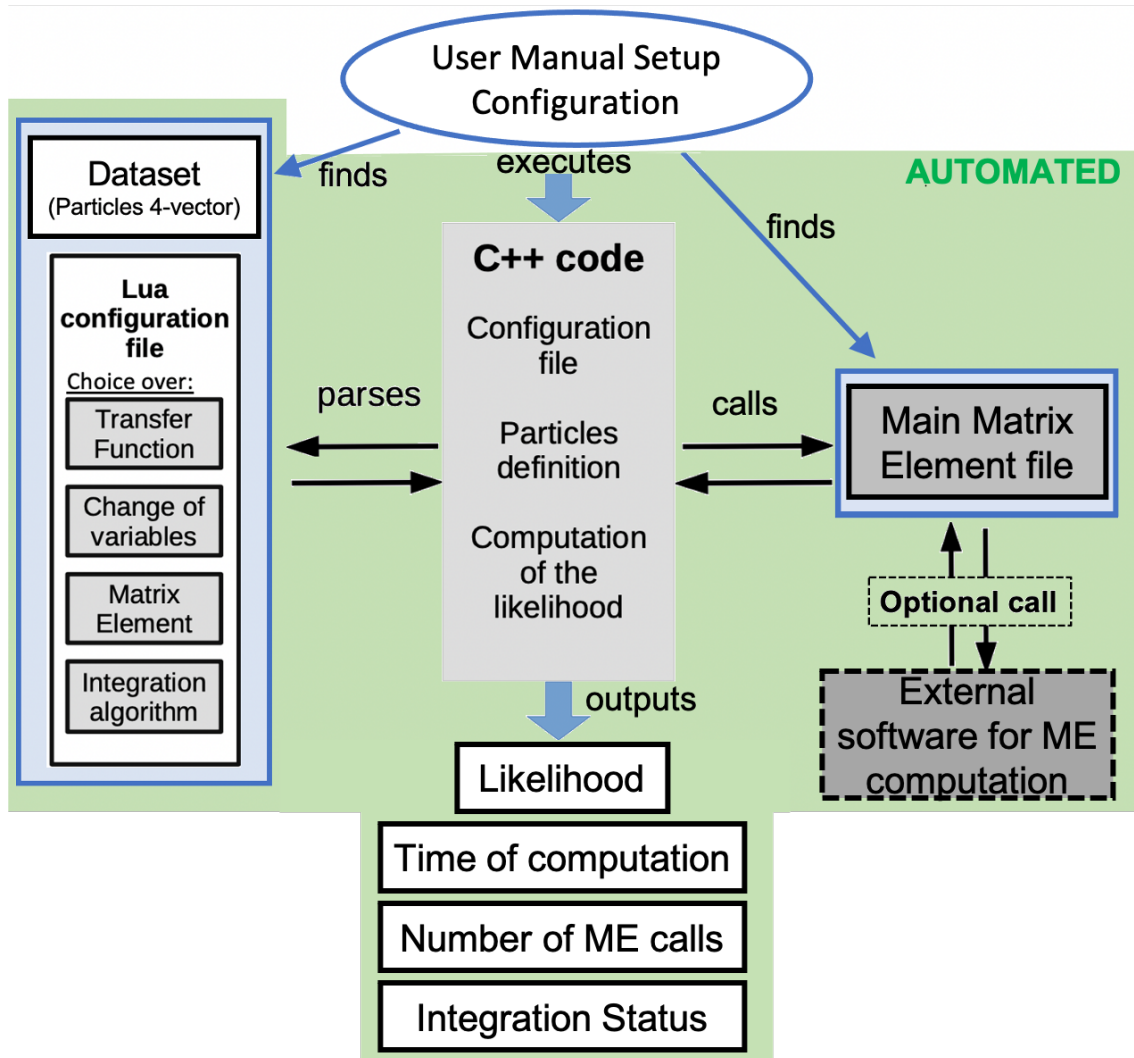


Figure 15.8: Schematic overview of the automated MEM factory, organized and automated for result efficiency and clarity. We reproduced the idea behind Figure 11.2: the lighter the color, the clearer the computation for the user. With the addition of the green area which represents the workflow that is managed automatically.

The green region encloses the part of the workflow that is executed entirely by the automation layer, from dataset ingestion to the production and validation of weight files.

Lighter color tones identify stages where the user has more explicit control, while darker shades indicate the few steps that require limited manual intervention (*e.g.* the inspection of particle-level four-vectors stored in the input datasets).

A dedicated block in the left highlights an important part of our work which is

the interface to external matrix element providers (POWHEG-BOX-V2 in the present study), shaded in darker tone as any additional modifications to this interface should be avoided as much as possible.

Modifications to this component by new users should be made only after a thorough review of the software and this new interface with MOMEMTA.

A single *control-panel* file lets the user specify every key run parameter (chosen dataset, κ_λ hypothesis, whether to recompile the workflow scripts, number of events per job, and so on...). The following part of the MEM is fully automated.

With strict tagging conventions and files management, the automated framework guarantees a one-to-one correspondence between the generator record and the final collection of weights, irrespective of the order in which the batch system computes the individual jobs or each weights MEM hypothesis.

We have modified the MEM output format to record more than the final integration result (*i.e.* the ‘Likelihood’, or weight) alone. For every event we now also store the time of the computation, the status flag returned by the chosen integration algorithm, and the total number of calls to the matrix element.

Because we require a strict one-to-one correspondence between input events, physics hypotheses and output records, post-processing these diagnostics must be performed with particular care.

Treatment of the MEM output uncertainties It is important to note that each weight (or Likelihood) returned by the MEM is accompanied by an estimate of its numerical uncertainty.

In practice, we noticed that this integration error is typically two orders of magnitude smaller than the weight itself. When it was not the case, it was a great indicator of cases where the numerical integration had difficulty converging. This information was valuable in guiding improvements to the MEM implementation itself.

For the purpose of developing the first and successful version of the MEM@NLO, we therefore did not properly include these error estimations in the computation of the AUC values or in the likelihood scans.

Given their small relative size, we expect them to have no visible impact on the central values of the fitted κ_λ . They could, however, slightly modify the uncertainties related to them.

All error estimates are stored and remain very easily accessible in the macros, so their inclusion in future projects or more refined analyses can be done without difficulty.

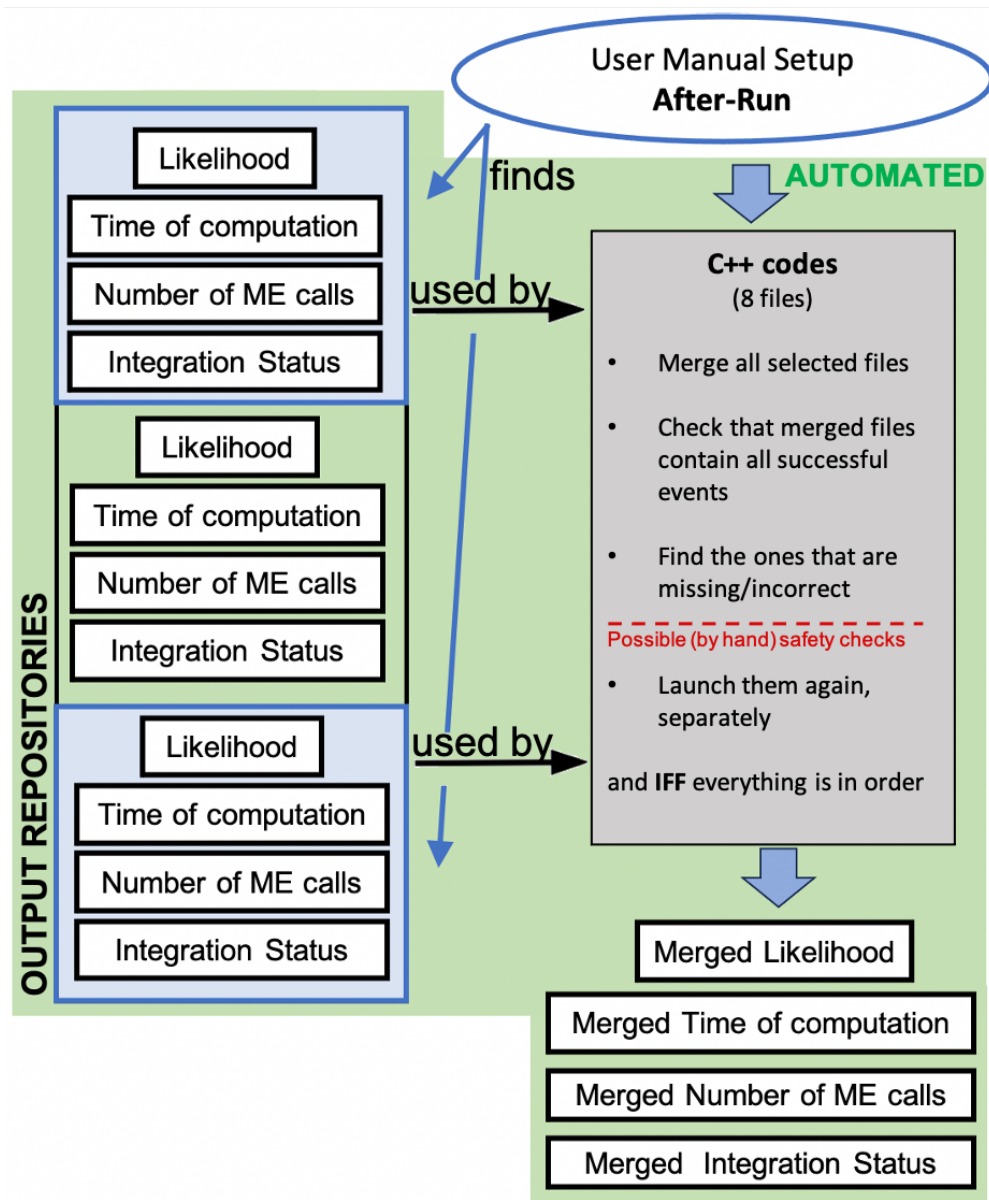


Figure 15.9: Schematic overview of the automated workflow **needed** after MEM result production. We reproduced the idea behind the Figure 11.2: the lighter the color, the clearer the computation for the user. With the addition of the **green** area which represents the workflow that is managed automatically.

The **green** region encloses the part of the workflow that is executed entirely by the automation layer.

Automated framework after the production of MEM outputs Manual book-keeping quickly becomes impractical once the workload grows beyond reasonable bounds, so a dedicated automated workflow after the MEM runs has been implemented. Its structure is illustrated in Fig. 15.9.

Some jobs inevitably terminate prematurely (for example because of time limits, insufficient memory or unexpected core dumps).

We have organized this framework to identify events whose computations failed and

run them again separately with the appropriate parameters, thereby preserving the one-to-one mapping across all datasets and hypotheses.

Four validation scripts enforce the safety-guard needed to ensure that no incomplete or corrupted output passes through the post-processing chain.

The automation layers (*cf.* Figures. 15.8 and 15.9) have at least two benefits:

First, we could have not produced the many event weights required for this analysis without it: the probability of confusing data sets, process hypotheses or event numbers would have been non-trivial.

Second, the platform enabled rapid iteration; every corrupted file, batch timeout or metadata mismatch was detected, logged and resubmitted automatically, allowing issues to be corrected on the fly. The time invested in building this almost-fully automated framework from the ground up has therefore proven to be exceptionally well spent.

15.5 Interpreting the results from the MEM: ROC Curves and Likelihoods

To interpret the outputs of the Matrix Element Method, we developed two main key analysis scripts.

These tools automate the generation of the main performance plots used throughout this study: the ROC curves and the likelihood scans.

Both scripts are designed to be modular, adaptable to all of the different hypotheses, and optimized for handling large event samples.

15.5.1 ROC Curves

The ROC evaluation script quantifies the discriminating power of the Matrix Element Method by analyzing the likelihood ratio between signal and background events, as described in Section 8.2.

The script supports a wide range of configurations, allowing the user to explore various signal and background hypotheses. It is typically launched via a *control-panel* file, where run parameters and plotting options can be easily set. This offers high flexibility for performing systematic studies and visualizing results.

Events for which both the signal and background weights are zero are excluded from the analysis. These situations correspond to cases where the numerical integration fails to converge to a meaningful value for **either** hypothesis. Ideally, with sufficient time and computing resources, a dedicated study would have been carried out to

understand these rare events in detail and identify possible improvements: whether related to the choice of integration algorithm, the regions of the phase space and kinematics, or even the distortions introduced by the smearing procedure on these specific events.

For each ROC curve presented in this manuscript, we explicitly quantify the fraction of events removed under this condition to maintain transparency in the statistical interpretation.

Given that the fraction of such events is relatively small, and that their likelihood ratios would be undefined, we chose to proceed by excluding them from the present analysis. In future analyses on real ATLAS data, improved integration techniques (or hybrid approaches combining multiple algorithms or techniques) could be developed to ensure that no events remain without any valid weights.

Each ROC curve is constructed by scanning over 40 predefined threshold values (*i.e.* the ‘cuts’) for the likelihood ratio. These thresholds span a broad range, effectively covering likelihood ratios from 0 to $+\infty$. Additional care was taken to correctly handle extreme and undefined values in the comparison logic, in particular for the treatment of the asymptotic behaviors near zero and infinity.

The area under the ROC curve (AUC), an important quantity for qualitative assessment of the ROC, is computed numerically using a piecewise linear (polygonal) approximation for integration. Since the ROC curve is derived from a discrete set of threshold values, the AUC is itself an approximation of the ideal continuous integral. For each ROC curve shown in this manuscript, we indicate the AUC associated to each curve.

It is important to keep in mind that the final MEM analysis will **not** include any cut on the likelihood ratio to select signal-like events.

Remember from Eq. (8.11) that the extended Likelihood is defined using all events (after pre-selection), under all of the processes hypotheses involving no cut or ratio. Cuts on the likelihood ratio are only used to produce ROC curves to quantitatively show the MEM discrimination power.

15.5.2 Likelihood scans (as a function of κ_λ)

The likelihood scan (and ensemble-test) serves as our main tool for the measurement of the κ_λ hypothesis from pseudo-datasets using our Matrix Element Methods (at LO or NLO).

It evaluates the NNLO expressions of the different likelihoods (kinematic, yield and extended) for given values of κ_λ , and produces 2D scans that reveal the analysis sensitivity to the coupling modifier κ_λ .

A quadratic fit around the extended curve $\mathcal{L}_{\text{ext}}(\kappa)$, returns the best estimate $\hat{\kappa}_\lambda$ and its 1σ uncertainty via Wilks’ theorem.

Event pre-selection Events whose weight is zero for their own production hypothesis are dropped, because they are considered ill-defined. For transparency, every likelihood figure quotes this fraction of ‘ill-defined’ events that were removed.

Weight smoothing For a small fraction of events, weights can slightly ‘fluctuate’ as one can see in Figure 15.10, likely due to phase-space integration fluctuations.

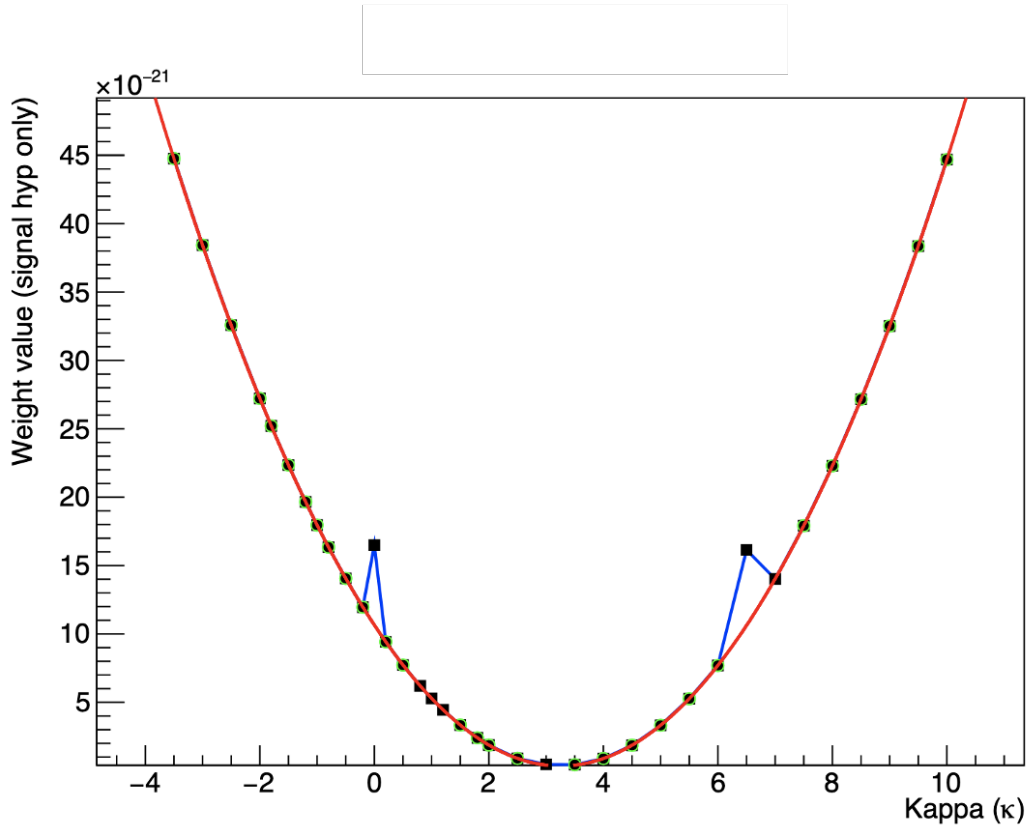


Figure 15.10: Automatic fitting procedure on Matrix Element Method outcomes under the signal hypothesis to avoid ‘fluctuations’ for a small subset of κ_λ hypotheses caused by issues in the numerical integrator, and stabilize the likelihood scans.

We have constructed our script so that the user can optionally fit each weight output as a function of κ_λ with the (expected) quadratic form (cf Figure 15.10), and use the fitted value in the likelihood calculation instead. This option stabilizes the future scans of likelihoods.

User interface All options (grid points, hypotheses to compare, smoothing, run range, and plotting style) are configured using a *control-panel* file. No manual editing of the C++ source is required, which makes the tool easy to deploy and gives a lot of freedom to the user.

Cross-sections and efficiencies We summarize in Table 15.1 the computed values of the product $\sigma \cdot \varepsilon$, where σ denotes the cross-section (including all relevant

branching ratios) and ε represents the pre-selection efficiency after detector-level cuts. These combined values are a key input to our analysis.

It is **very important** to note that the values inside Table 15.1 *do not yet account* for Higgs (or top) decays, to add transparency on the values derived from either POWHEG-BOX-V2 or MADGRAPH5.

The QCD factorization theorem allows us to add the corresponding branching ratios (*cf.* Table 15.2) by hand when we need to compute the total cross-section σ_p^{obs} for the process of interest p , which will serve as the full normalization factor for the MEM weights (*cf.* Eq. (8.5) in Chapter 8).

It also directly determines the expected event yield for each process at a given integrated luminosity, and therefore plays a critical role in shaping the yield likelihood, and the generation of likelihood scans used for the κ_λ parameter extraction.

Process	LO			NLO		
	σ [pb]	ε	$\sigma \cdot \varepsilon$ [pb]	σ [pb]	ε	$\sigma \cdot \varepsilon$ [pb]
signal ggF ($\kappa_\lambda = 1.00$)	0.01983	0.3982	0.00789	0.03874	0.423669	0.01641
$t\bar{t}H$	0.349	0.436148	0.1524	0.603	0.120844	0.0729
QCD $b\bar{b}\gamma\gamma$ background	0.05969449	0.00667	0.000398	0	0.00283182	0.001557
Single-Higgs	0.1038	0.12056	0.01252	0.553	0.15868	0.0878

Table 15.1: Summary of cross-sections σ [in pb], pre-selection efficiencies ε , and their product $\sigma \cdot \varepsilon$ [in pb] computed and used for all processes under study (at both LO and NLO).

The signal process is shown here for $\kappa_\lambda = 1.00$ as an example.

Note: The specific branching ratios (BR) have not been included in the cross-sections σ values, for transparency purposes.

Decay mode	Branching ratio (BR)	
	Value	Source
$H \rightarrow b\bar{b}$	0.5796	HPAIR
$H \rightarrow \gamma\gamma$	2.276×10^{-3}	HPAIR
$t \rightarrow Wb$	0.988	PDG

Table 15.2: Branching ratios (BR) used in this analysis. The values for the Higgs decays are taken mainly from the HPAIR software and compared to the literature. The top-quark branching ratio is close to unity and plays a minor role here, but is included for completeness.

The cross-sections σ values used in this study were obtained from the same generator used to produce the corresponding event samples whenever it was possible (*i.e.* either POWHEG-BOX-V2 or MADGRAPH5).

For the gluon-fusion signal process (ggF), we relied instead on theoretical predictions from HPAIR, which also provides accurate NLO calculations including the full κ_λ dependence.

And the single Higgs background, the NLO cross-section extracted from MADGRAPH5 proved unreliable, as it included only the real emission component and was strongly dependent on the generation cuts used in the `param_card`. To ensure a consistent and physically meaningful normalization, we instead used the official prediction from the Higgs Cross-Section Working Group (Handbook 4, *cf.* Ref. [132]).

As for the QCD background, we note that, as discussed in Section 15.1.1, generating a sufficient number of NLO events proved unfeasible due to extremely low selection efficiency after cuts. So the limitations of MADGRAPH5 in providing a complete or reliable NLO cross-section are not a major concern here, given that this NLO contribution is instead effectively modeled using Leading Order samples.

This is why a placeholder value of zero is shown in **red** for the corresponding NLO QCD entry in the Table. 15.1, to indicate that no reliable cross-section has been used in this analysis.

Importance of the Yield Likelihood

The signal cross-section for non-resonant Higgs boson pair production in gluon fusion has a strong and non-linear dependence on the self-coupling parameter $\kappa_\lambda = \lambda_{HHH}/\lambda_{HHH}^{\text{SM}}$.

This behavior is exploited by many traditional analysis strategies, such as *event-counting methods*, where the expected number of signal events is directly proportional to the cross-section for a given κ_λ .

In our MEM-based approach, this information is incorporated through the *Yield likelihood*, denoted as $\mathcal{L}_{\text{yield}}(\kappa_\lambda)$.

Figure 15.11 illustrates an example of this yield likelihood, evaluated for an integrated luminosity of 300 fb^{-1} .

The left panel shows the theoretical cross-section curve (at NLO, using HPAIR, multiplied by the selection efficiency) as a function of κ_λ . The quadratic shape arises from the interference between the triangle and box diagrams and leads to an important feature of the curve: **a mirror solution for each given cross-section value**.

This symmetry implies that for a given cross-section (and therefore expected yield), there may exist two different values of κ_λ that are equally compatible with the observation.

In the example shown, the Standard Model value $\kappa_\lambda = 1.0$ has a symmetric counterpart near $\kappa_\lambda = 4.0$. This is clearly visible in the bottom-panel, where the yield likelihood shows a second local minimum near that value.

Such mirror solutions are a known limitation of event-counting methods and contribute significantly to the large upper uncertainties observed in existing measure-

ments of κ_λ (*cf.* Chapter 6 which reviews the most recent combined Higgs self-coupling limits from ATLAS and CMS, and Section 6.2 which presents the most recent results of ATLAS non-resonant $HH \rightarrow b\bar{b}\gamma\gamma$ analysis).

We will see that the MEM offers a complementary advantage by including both the shape (via $\mathcal{L}_{\text{kinematic}}$) and the yield information (via $\mathcal{L}_{\text{yield}}$). It becomes possible to reduce the impact of the mirror solution by resolving degeneracies using full event kinematics.

Graphical Representation of Likelihoods

Unlike ROC curves which depend only on relative ranking between signal and background hypotheses, the absolute values of the likelihoods are critical for the extraction of physical parameters like κ_λ .

Recall that the product of both the kinematic and yield likelihoods creates the extended likelihood, and because these likelihoods differ in their numerical scale it would be misleading to display them on the same graph without any **graphical** modifications.

To ensure a meaningful visual representation, we choose to center all likelihood plots around the extended likelihood, which is shown using its unaltered numerical values.

For illustrative purposes only, we apply vertical shifts to the individual kinematic and yield likelihoods so that the minima of all three curves align on the same y-axis position.

This alignment preserves the relative shapes of the curves while making it easier to compare their individual curvature and sensitivity to κ_λ (*cf.* Figure 16.5 for an illustrated application).

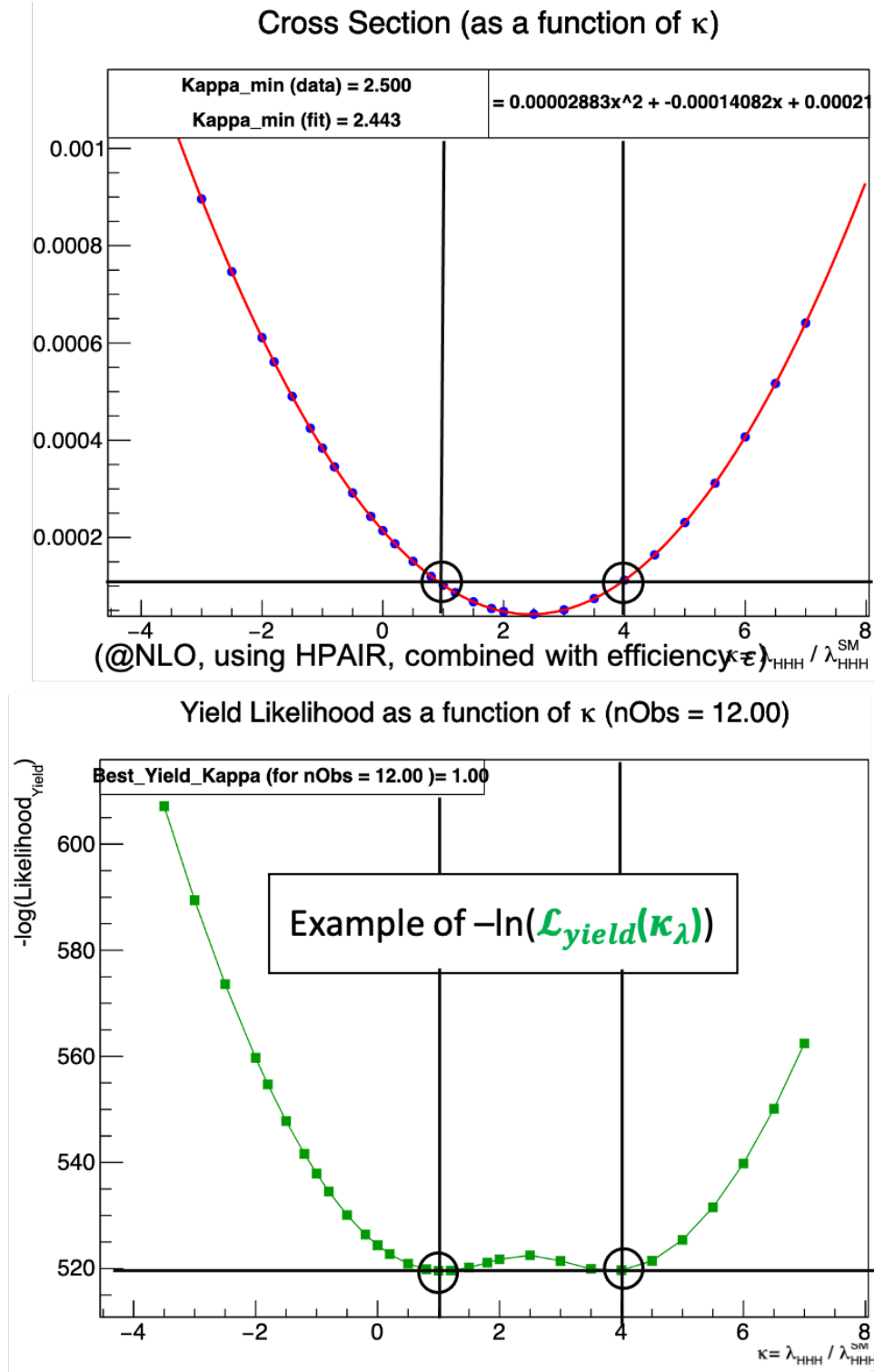


Figure 15.11: Illustration of the theoretical cross-section as a function of κ_{λ} (top), compared to the (negative log) Yield likelihood $-\log \mathcal{L}_{\text{yield}}(\kappa_{\lambda})$ at 300 fb^{-1} (bottom).

Both curves exhibit the well-known mirror symmetry between $\kappa_{\lambda} = 1.0$ and $\kappa_{\lambda} = 4.0$, highlighting a major challenge in extracting precise constraints on the Higgs self-coupling.

Chapter 16

Results: With Our LO Matrix Element Method

This chapter defines the reference point against which every higher-order (*i.e.* NLO here) development will be measured.

Our implementation restarts from zero, using only publicly available codes (event generators and MoMEMta).

We reconstructed (and when necessary modernised) the original approach without reusing any of the code from the initial study at Leading-Order, originally developed by Eble and Stark (*cf.* Ref. [89], already discussed in Chapter 11).

To provide a solid foundation for the developments presented in this thesis, the entirety of the MEM framework at LO has been carefully validated against previous results. This includes reproducing all critical results and confirming internal consistency between the matrix-element models, the event-simulation pipeline, the likelihood-scan behavior and the statistical discrimination power. This reproduction also ensures that all improvements introduced in the next stage are evaluated with respect to a rigorously understood and technically up-to-date baseline.

It also gave us the opportunity to extend the work of the Leading Order Matrix Element Method by producing for the first time results with additional backgrounds either separated or combined **together**.

First results obtained with the Leading-Order implementation of the Matrix Element Method were presented to the community at several meetings: the COMETA Workshop on EFT in di-Higgs and VBS (Paris, March 2025) [133], the Higgs Pairs Workshop (Isola d'Elba, May 2025) [134], the ATLAS Physique ATLAS France (PAF) meeting in Annecy (May 2025) [135], and the EPS-HEP 2025 conference in Marseille (July 2025) [136].

These LO results were presented at the beginning of our presentations as motivation for our results with our newly developed Matrix-Element Method at NLO (*cf.* Chapter 17).

16.1 ROC Curves using MEM@LO

Each of the following subsections will present ROC curves for one given background channel: $t\bar{t}H$, QCD and singleHiggs.

The signal hypothesis events used for the discrimination are gluon fusion (ggF) with $\kappa_\lambda = 1.00$.

16.1.1 $t\bar{t}H$ background

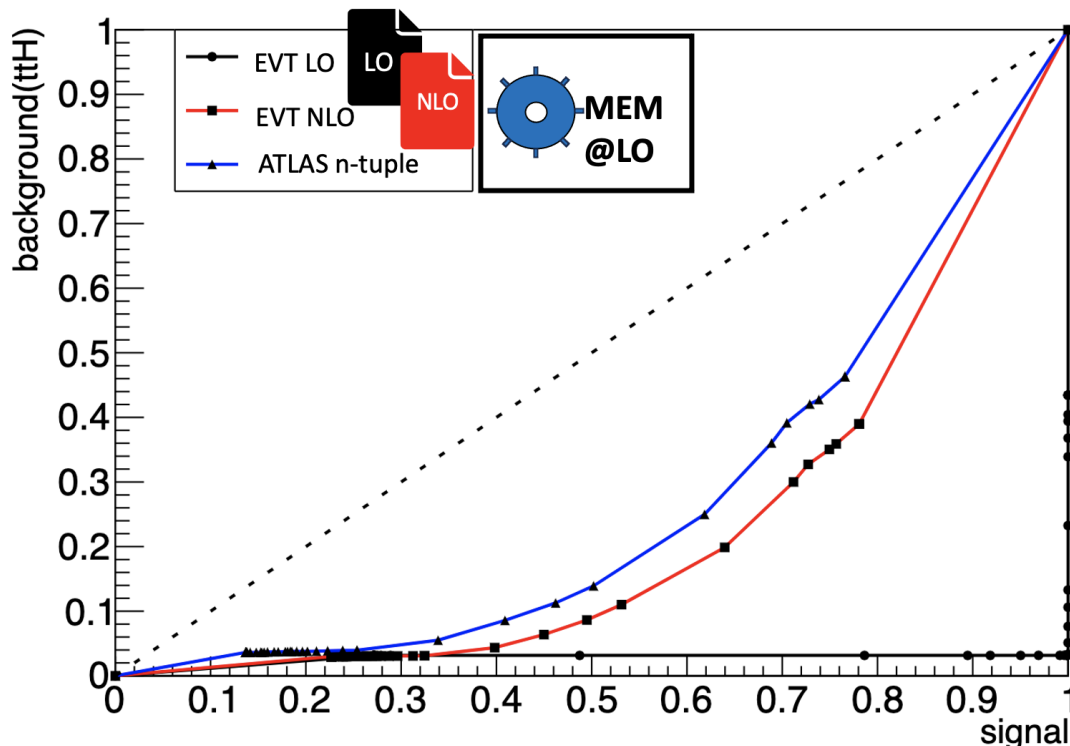


Figure 16.1: ROC curve obtained with MEM@LO when the dominant background is $t\bar{t}H$ (using the DIVONNE algorithm for both hypotheses).

The dashed line indicates the expectation from a random classifier

Results in Table 16.1 quantitatively demonstrate that the discriminating power of MEM@LO against the $t\bar{t}H$ background is sensitive to the order of the generated event.

Figure 16.1 on the other hand, shows that using the DIVONNE algorithm for both hypotheses produces an almost ideal ROC shape for LO generated events, but with a slight inflate near the x -axis indicating that some $t\bar{t}H$ events have vanishing weights under the $t\bar{t}H$ hypothesis while having non-vanishing weights for the signal hypothesis.

Changing the integration algorithm for the $t\bar{t}H$ background from DIVONNE to VEGAS fixed the convergence problem for the LO samples, but it increased the AUC value for the more realistic NLO ISR events and ATLAS simulation n-tuples (*cf.* Figure 16.2).

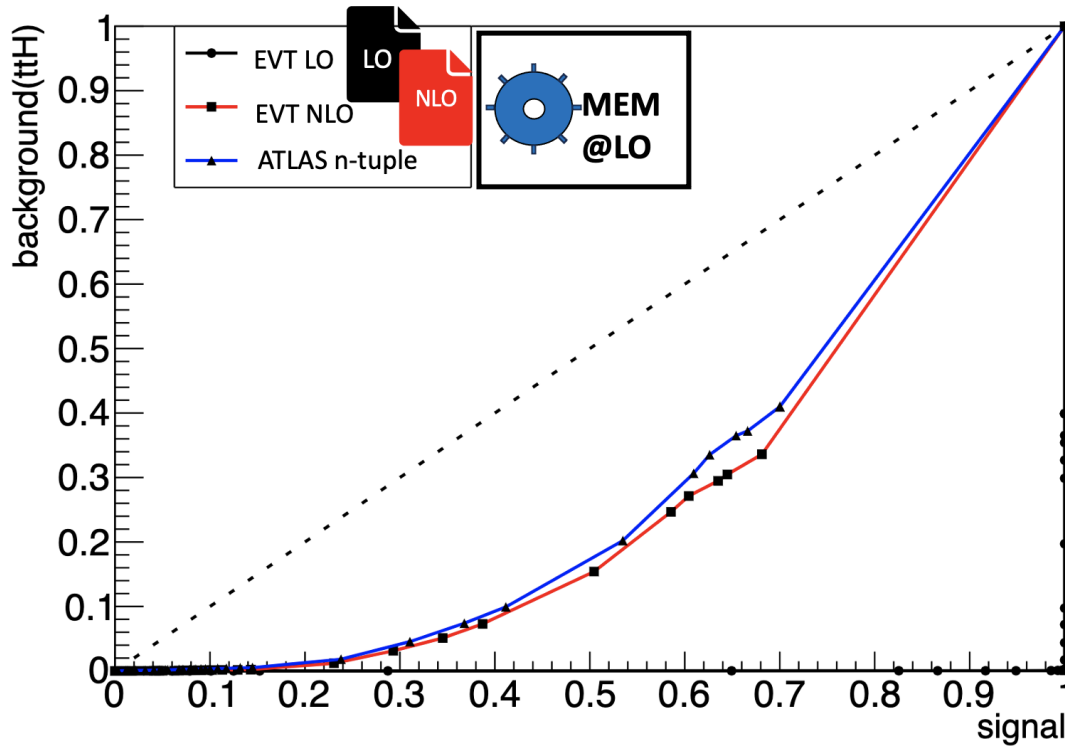


Figure 16.2: ROC curve obtained with MEM@LO when the dominant background is $t\bar{t}H$ using the VEGAS integration algorithm for the background hypothesis.

The dashed line indicates the expectation from a random classifier

$[t\bar{t}H \text{ Background}]$	AUC (%)	signal rejected (%)	% background rejected (%)
LO	2.73	0	8.13
LO (VEGAS)	0.02	0	0
NLO ISR	22.98	12.78	13.77
NLO ISR (VEGAS)	27.75	0.03	0.01
ATLAS n-tuples	27.36	8.58	11.47
ATLAS n-tuples (VEGAS)	29.28	0.01	0.02

Table 16.1: Table for the values of interest hidden in Figure 16.1 and 16.2. The MEM integration algorithm is (DIVONNE) unless stated otherwise.

Are indicated in this table: the area under the curve (AUC) (in %); the number of signal events that have zero weights values for **both** hypothesis at the same time (in %); and the number of background events that have zero weights values for **both** hypothesis at the same time (in %).

A more thorough assessment of the dependence on the integration algorithm should be performed. Whereas DIVONNE may yield a weight zero value for some events, VEGAS more produces a non-zero output but with the status flag `ACCURACY_NOT_REACHED`, and statistical uncertainties of the same order as the central value. This indicates for the latter that the result is **unreliable**, though non-zero, and should be re-evaluated with tighter integration settings, an alternative algorithm, or a combination.

These events should not be discarded, but treated more carefully.

The most important result from Figure 16.1 is that the MEM@LO offers little separation between the gluon-fusion signal and the $t\bar{t}H$ background when more realistic events are used (either by including initial-state radiation (ISR) corrections at NLO (NLO ISR) or by relying on the ATLAS simulated n-tuples).

The percentage of signal and background events to remain weightless for both hypothesis increased consequently, and the AUC increases up to 27.36%.

This highlight once again the intrinsic limitations of a MEM@LO treatment for the study of more realistic dataset samples, that we have already discussed earlier in Section 12.2.

16.1.2 QCD di-photon background

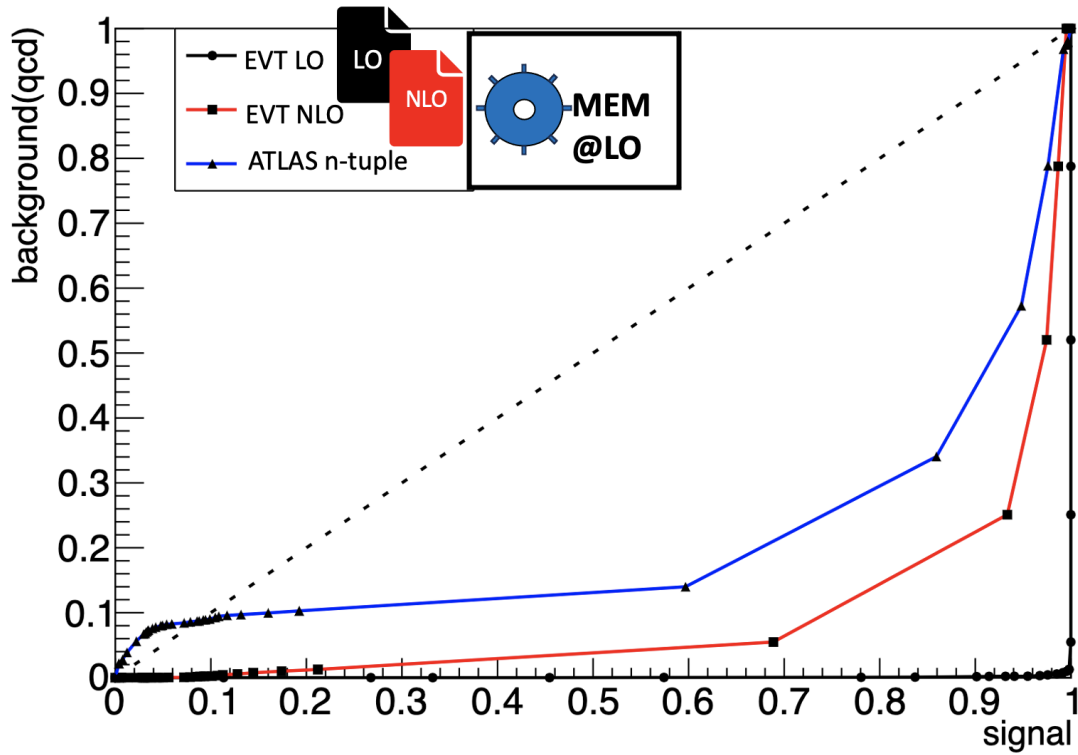


Figure 16.3: ROC curve obtained with MEM@LO for the $b\bar{b}\gamma\gamma$ QCD background. The dashed line indicates the expectation from a random classifier

[QCD Background]	AUC (%)	signal rejected (%)	% background rejected (%)
LO	0.06	0	0
NLO ISR	9.05	31.73	0
ATLAS n-tuples	20.96	29.76	54.45

Table 16.2: Table for the values of interest hidden in Figure 16.3. The MEM integration algorithm is (DIVONNE) unless stated otherwise.

Are indicated in this table: the area under the curve (AUC) (in %); the number of signal events that have zero weights values for **both** hypothesis at the same time (in %); and the number of background events that have zero weights values for **both** hypothesis at the same time (in %).

The results in Figure 16.3 are produced using the DIVONNE algorithm for the multi-dimensional integration for both signal and QCD $b\bar{b}\gamma\gamma$ background.

Figure 16.3 and the first line of Table 16.2 show that the MEM@LO achieves excellent discrimination against the QCD background: an AUC of just 0.06% and no events with simultaneously vanishing signal and background weights.

When initial-state radiation is injected in the generated events (NLO ISR), the separation degrades significantly ($AUC = 9.05\%$) and roughly one third of the signal events become weightless for both hypothesis.

The ATLAS simulation n-tuples further challenge the MEM@LO: the AUC rises to 20.96% and more than half of the background events receive zero weights for both hypotheses.

16.1.3 Single-Higgs background

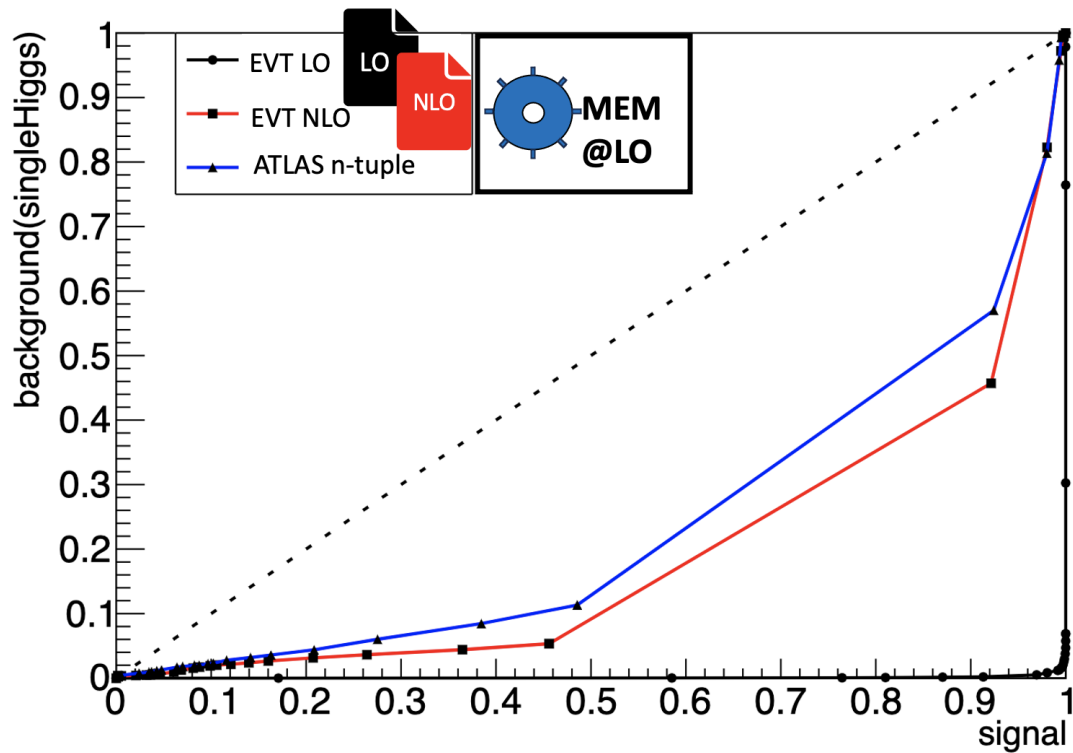


Figure 16.4: ROC curve obtained with MEM@LO against the single Higgs background.

The dashed line indicates the expectation from a random classifier.

[single-Higgs Background]	AUC (%)	signal rejected (%)	% background rejected (%)
LO	0.08	0	0
NLO ISR	18.87	31.77	36.02
ATLAS n-tuples	23.33	29.81	44.36

Table 16.3: Table for the values of interest hidden in Figure 16.4. The MEM integration algorithm is (DIVONNE) unless stated otherwise.

Are indicated in this table: the area under the curve (AUC) (in %); the number of signal events that have zero weights values for **both** hypothesis at the same time (in %); and the number of background events that have zero weights values for **both** hypothesis at the same time (in %).

The results produced in Figure 16.3 are produced using the DIVONNE algorithm for the multi-dimensional integration for both signal and the singleHiggs background.

On LO generated events. the MEM@LO achieves an AUC of only 0.08% (first row of Table 16.3), signalling excellent separation power. The DIVONNE integrator converges strongly.

The situation changes when initial-state radiation is introduced at the generator level (NLO ISR) here again.

The AUC rises to 18.87%, and roughly one third of both signal (31.77%) and background (36.02%) events become weightless.

A further test with the ATLAS simulated n-tuples confirms this behavior: The AUC rises to 23.3%, but most importantly, a little less than half of the background (44%) events become weightless.

Conclusion

Overall the pattern is the same for all backgrounds: the MEM@LO excels when no extra radiation is present (i.e for LO generated events), but loses discriminating power rapidly once more realistic events are considered.

The performance loss observed is consistent with expectations, as additional hard and soft radiation opens regions of phase space that the LO matrix elements cannot describe, leaving the integrator to extrapolate.

It is important to note that the ROC probes only the ratio of the likelihoods, returned by the MEM. The curves are therefore insensitive to the overall deterioration one can observe for the individual weights of more realistic events. The absolute weight values can drop by multiple orders of magnitude (up to $\mathcal{O}(10^{-100})$) if not to a zero value. Although this global scale factor does not alter the ROC curve, it *does* matter for analyses that use the weights directly, such as extended likelihood scans.

Considering this, all likelihood scans studies presented in the next section are based exclusively on the LO MC generated samples.

16.2 Likelihood Scans using LO generated samples

Each Likelihood scan follows the prescriptions detailed in Section 15.5.2. For each background sample we indicate in a table the percentage of events that are removed from the likelihood analysis because the weight computed under the *true* process hypothesis is exactly zero.

16.2.1 [LO] Signal-only

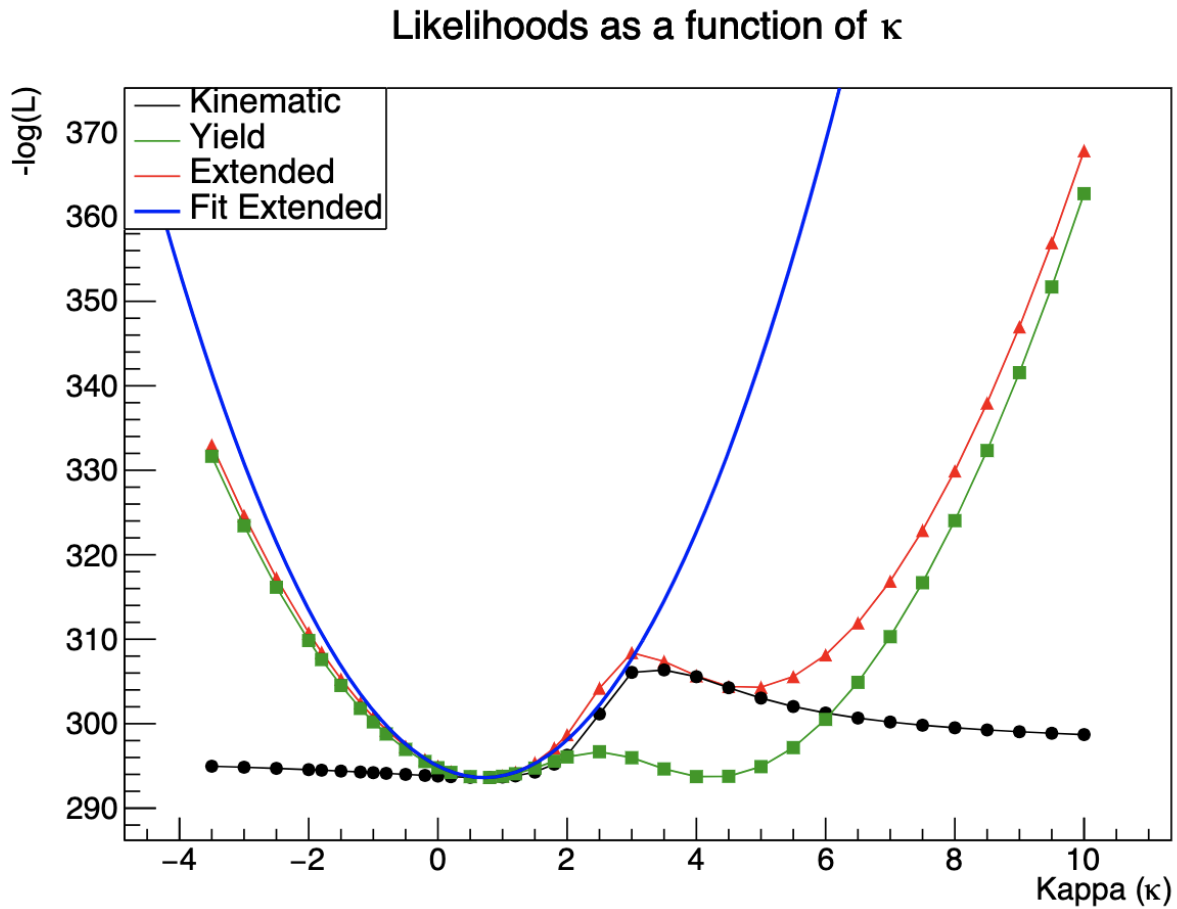


Figure 16.5: Example likelihood scan for one pseudo-dataset consisting of signal events ($\kappa_\lambda = 1.00$) analysed under MEM@LO.

The graph shows $-\log \mathcal{L}$ as a function of the coupling modifier κ_λ for multiple likelihoods:

Black: kinematic component only (\mathcal{L}_{Kin}). **Green:** yield term ($\mathcal{L}_{\text{yield}}$). **Red:** extended likelihood (\mathcal{L}_{ext}). **Blue:** quadratic fit to $-\log \mathcal{L}_{\text{ext}}$ used to extract the best-fit value and its statistical uncertainty.

Figure 16.5 disentangles the relative importance of the kinematic and yield information for a representative pseudo-experiment. The extended likelihood (red) combines both ingredients.

A quadratic fit to $-\log \mathcal{L}_{\text{ext}}$ (in blue) allows the recovery of $\hat{\kappa}_\lambda$ at around 1.00 as well as the uncertainty values.

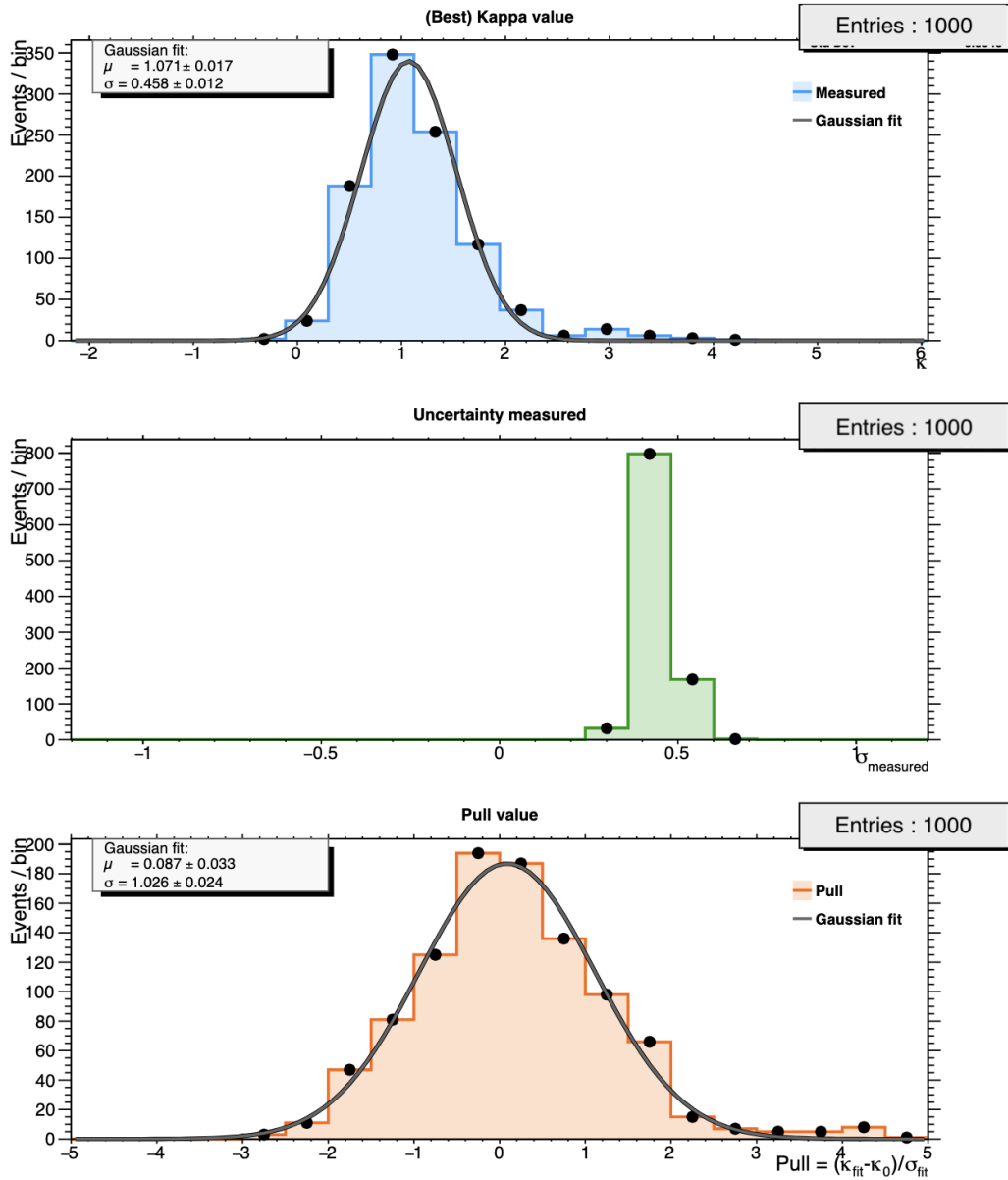


Figure 16.6: Likelihood scan for a pure signal MC generated dataset.

Process	Number events flagged as <i>ill</i> (%)
signal ggF ($\kappa_\lambda = 1.00$)	0

Table 16.4: Fraction of ‘ill’ events (zero weight for their own hypothesis) removed before the likelihood scan of Figure 16.6.

Figure 16.6 summarises the outcome of 1000 pseudo-experiments in which pure signal events (with $\kappa_\lambda = 1.00$) generated at LO are analysed with a MEM@LO likelihood fit.

The upper panel shows the distribution of the fitted coupling $\hat{\kappa}_\lambda$ for each profile likelihood scans.

A Gaussian fit of the histogram of the best fit returns $\kappa_{\text{mean}} = 1.071 \pm 0.017$ and $\sigma_\kappa = 0.458 \pm 0.012$.

The middle panel displays the fitted uncertainty σ_{fit} obtained from the extended likelihood. Its distribution is sharply peaked at ~ 0.44 , confirming that the likelihood curvature provides a stable error estimate across toys.

And finally the lower panel tests the coverage by plotting the pull $\omega = (\hat{\kappa}_\lambda - \kappa_{\text{test}})/\sigma_{\text{fit}}$. The fitted pull mean is 0.087 ± 0.033 and the width 1.026 ± 0.024 , both statistically consistent with the ideal values $(0, 1)$.

Hence the pure signal ensemble generated at LO fitted using MEM@LO is shown to be unbiased and its quoted uncertainties are well calibrated.

In summary the profile likelihood machinery recovers the injected coupling with excellent coverage in this very simple case, validating the MEM@LO implementation in the absence of background or higher order radiation.

16.2.2 [LO] including $t\bar{t}H$ background

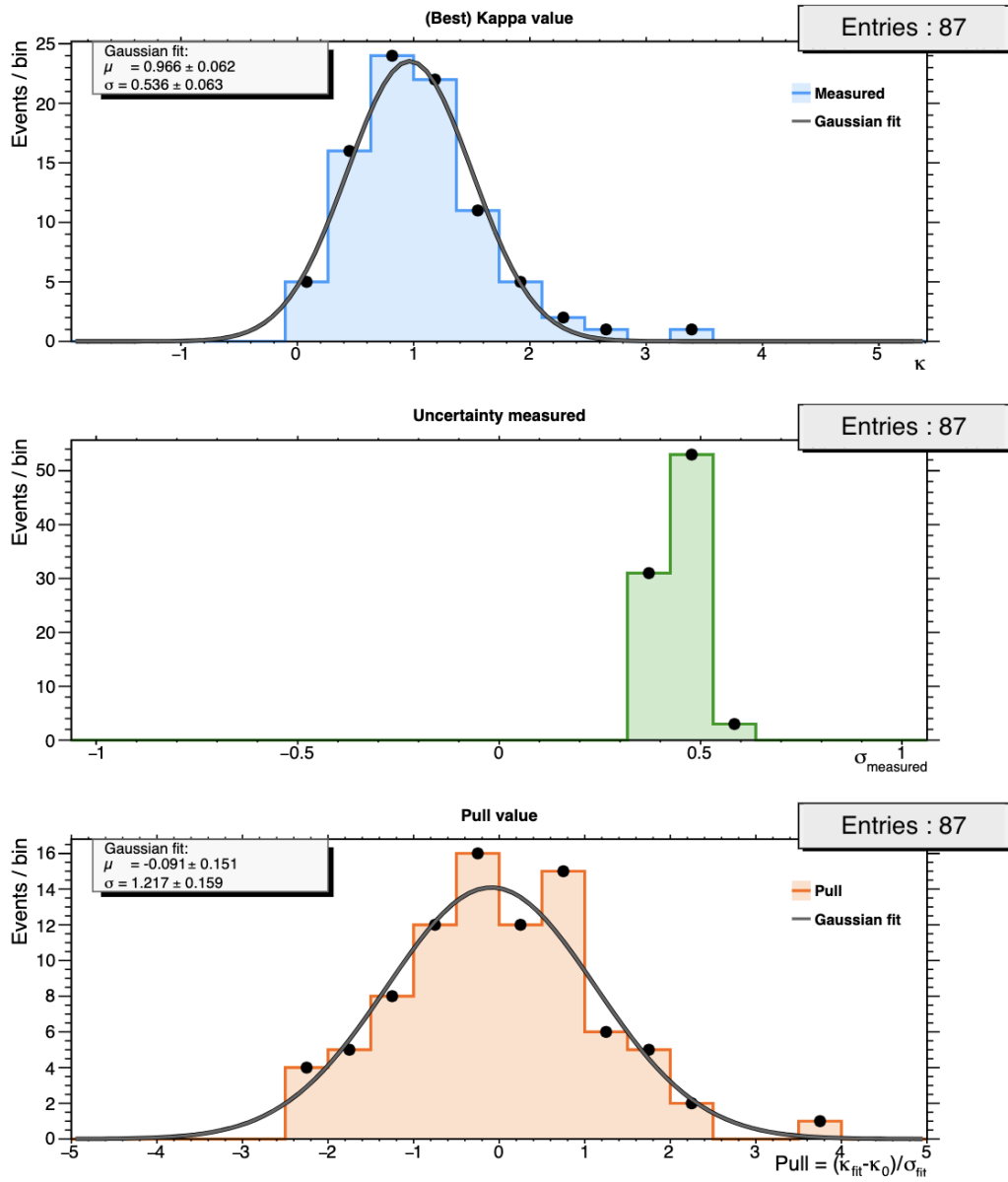


Figure 16.7: Likelihood scan for MC generated dataset of both signal and $t\bar{t}H$ background.

Processes	Number events flagged as <i>ill</i> (%)
signal ggF ($\kappa_\lambda = 1.00$)	0
$t\bar{t}H$	11.03

Table 16.5: Fraction of ‘ill’ events (zero weight for their own hypothesis) removed before the likelihood scan of Figure 16.7.

Figure 16.7 shows the outcome of the likelihood scans performance when the $t\bar{t}H$ background is included. Only 87 pseudo-datasets were produced due to the large number of events needed for each likelihood scans.

Best-fit estimator: The upper panel displays the distribution of the fitted coupling $\hat{\kappa}_\lambda$, with a Gaussian fit giving $\kappa_{\text{mean}} = 0.966 \pm 0.062$ and $\sigma_\kappa = 0.536 \pm 0.063$. The width has increased by about 17% relative to the pure-signal study (an expected consequence of the additional of background).

Estimated uncertainty: The middle panel shows the fitted error distribution, peaking at $\sigma_{\text{fit}} \simeq 0.44$, essentially unchanged with respect to the signal-only case.

Pull distribution: The pull mean is -0.091 ± 0.151 (consistent with zero), but the width $\sigma_{\text{pull}} = 1.217 \pm 0.159$ exceeds the ideal value 1 by about 20%.

16.2.3 [LO] including QCD background

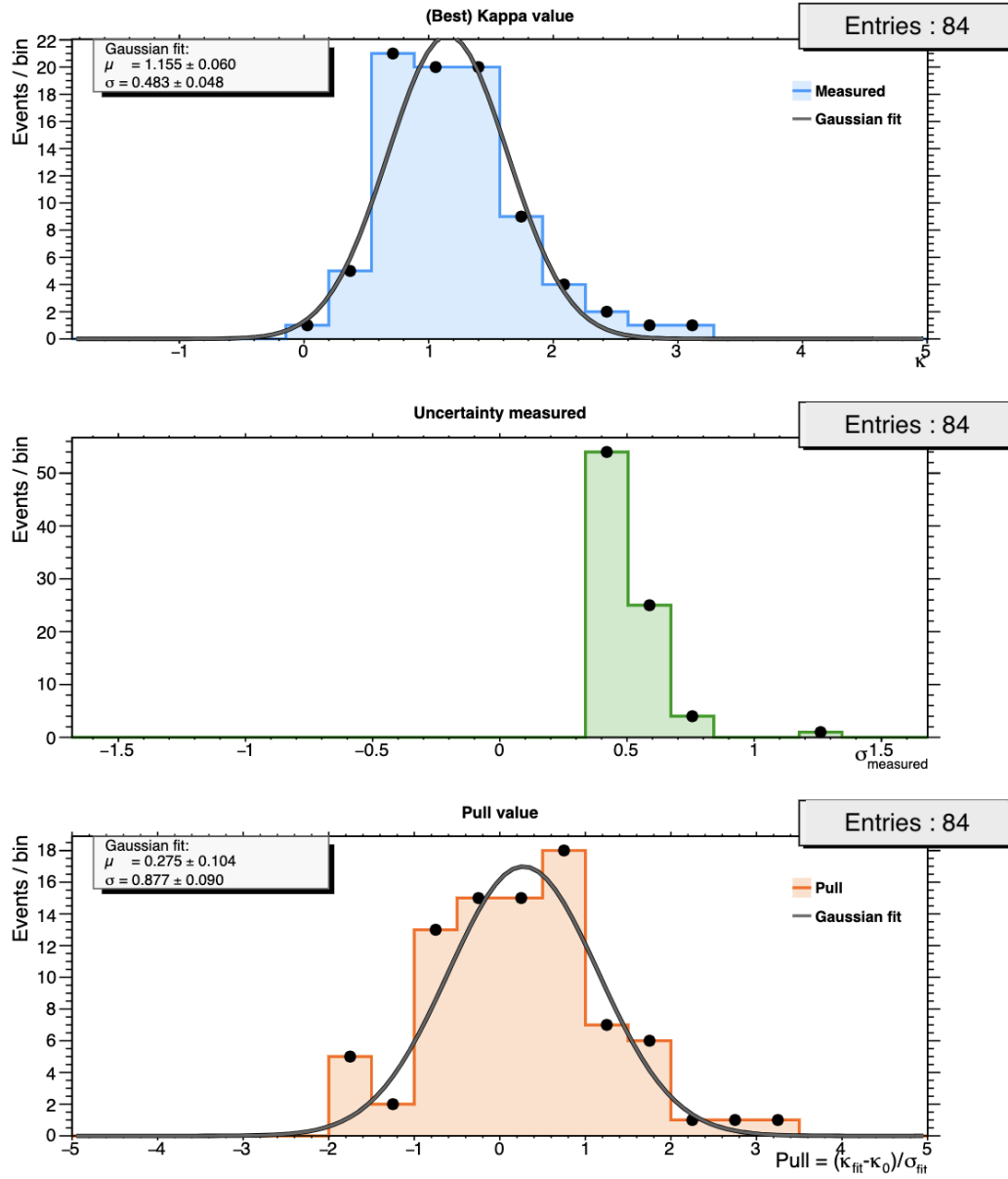


Figure 16.8: Likelihood scan for MC generated dataset of both signal and QCD background.

Processes	Number events flagged as <i>ill</i> (%)
signal ggF ($\kappa_\lambda = 1.00$)	0
QCD background	0

Table 16.6: Fraction of ‘ill’ events (zero weight for their own hypothesis) removed before the likelihood scan of Figure 16.8.

Figure 16.8 summarises the performance of the likelihood scans produced in the presence of the QCD background. Only 84 pseudo-datasets were produced due to the large number of events needed for each likelihood scans.

Best-fit estimator: The upper panel displays the distribution of the fitted coupling $\hat{\kappa}_\lambda$. A Gaussian fit yields $\kappa_{\text{mean}} = 1.155 \pm 0.060$ and $\sigma_\kappa = 0.483 \pm 0.048$. The central value is shifted upward by about +0.15 compared with the injected parameter. Although still within one-third of the statistical resolution, the bias is noticeably larger than in the $t\bar{t}H$ study, reflecting the stronger degeneracy between signal and QCD at LO.

Estimated uncertainty: The middle panel shows the fitted error distribution, centred at $\sigma_{\text{fit}} \simeq 0.52$.

Pull distribution: The lower panel gives the pull $\omega = (\hat{\kappa}_\lambda - \kappa_{\text{test}})/\sigma_{\text{fit}}$. A Gaussian fit returns a mean of $\omega_{\text{pull}} = 0.275 \pm 0.104$ and a width $\sigma_{\text{pull}} = 0.9916$ which is consistent with the ideal value of 1.0

16.2.4 [LO] including singleHiggs background

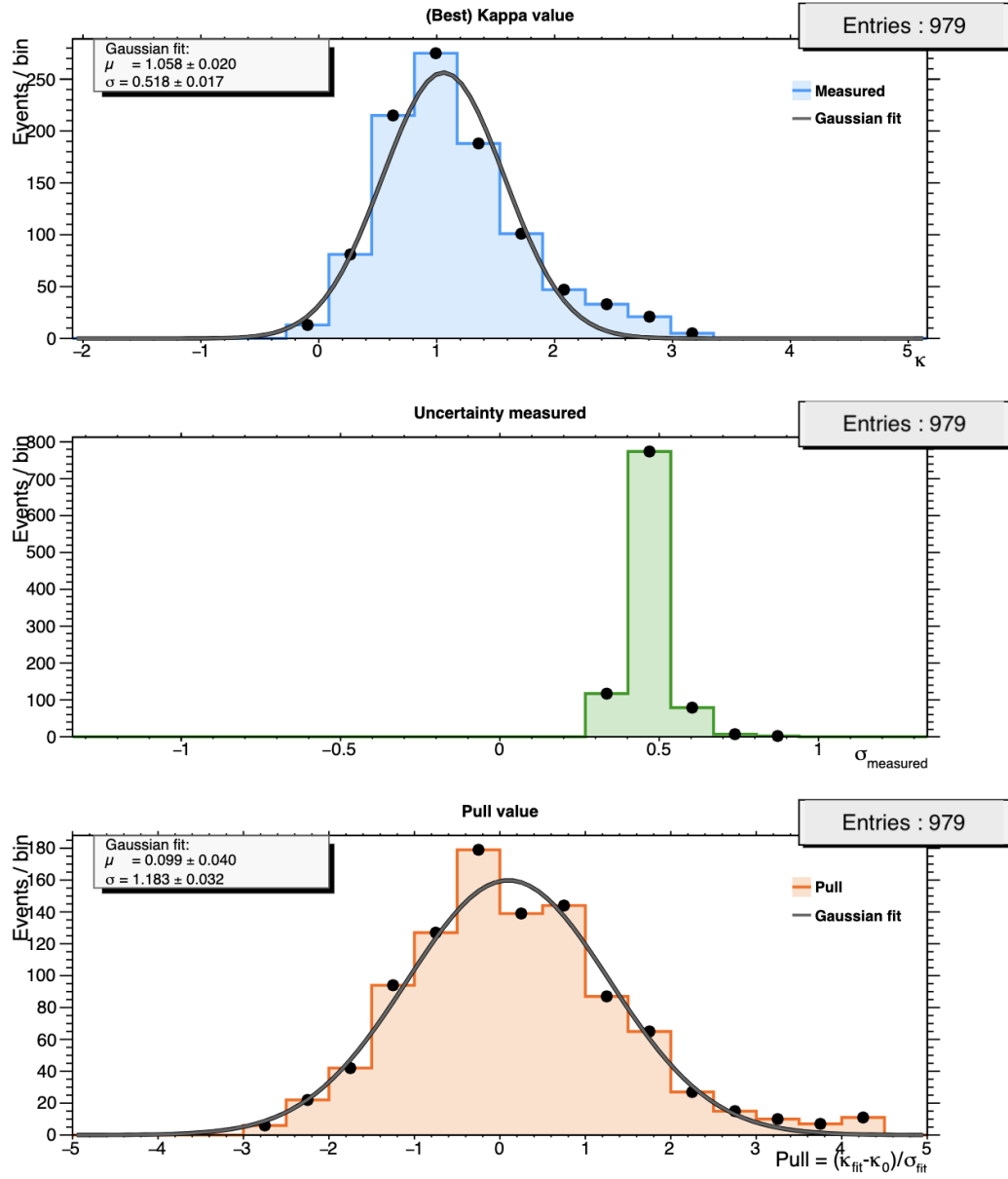


Figure 16.9: Likelihood scan for MC generated dataset of both signal and singleHiggs background

Processes	Number events flagged as <i>ill</i> (%)
signal ggF ($\kappa_\lambda = 1.00$)	0
singleHiggs	0

Table 16.7: Fraction of ‘ill’ events (zero weight for their own hypothesis) removed before the likelihood scan of Figure 16.9.

Figure 16.9 presents the MEM@LO profile likelihood performance in the presence of the single-Higgs background. A total of 979 pseudo-experiments have been produced.

Best-fit estimator: The upper panel shows the distribution of the fitted coupling $\hat{\kappa}_\lambda$. A Gaussian fit returns $\kappa_{\text{mean}} = 1.058 \pm 0.020$ and $\sigma_\kappa = 0.518 \pm 0.017$.

Estimated uncertainty: The middle panel displays the fitted error distribution, sharply peaked at $\sigma_{\text{fit}} \simeq 0.46$, only slightly larger than in the signal-only case.

Pull distribution: The lower panel gives the pull $\omega = (\hat{\kappa}_\lambda - \kappa_{\text{test}})/\sigma_{\text{fit}}$. A Gaussian fit yields $\omega_{\text{pull}} = 0.099 \pm 0.040$ and $\sigma_{\text{pull}} = 1.183 \pm 0.032$. The mean is compatible with zero, but the width exceeds the ideal value of unity by roughly 18%.

16.2.5 [LO] including all three main backgrounds

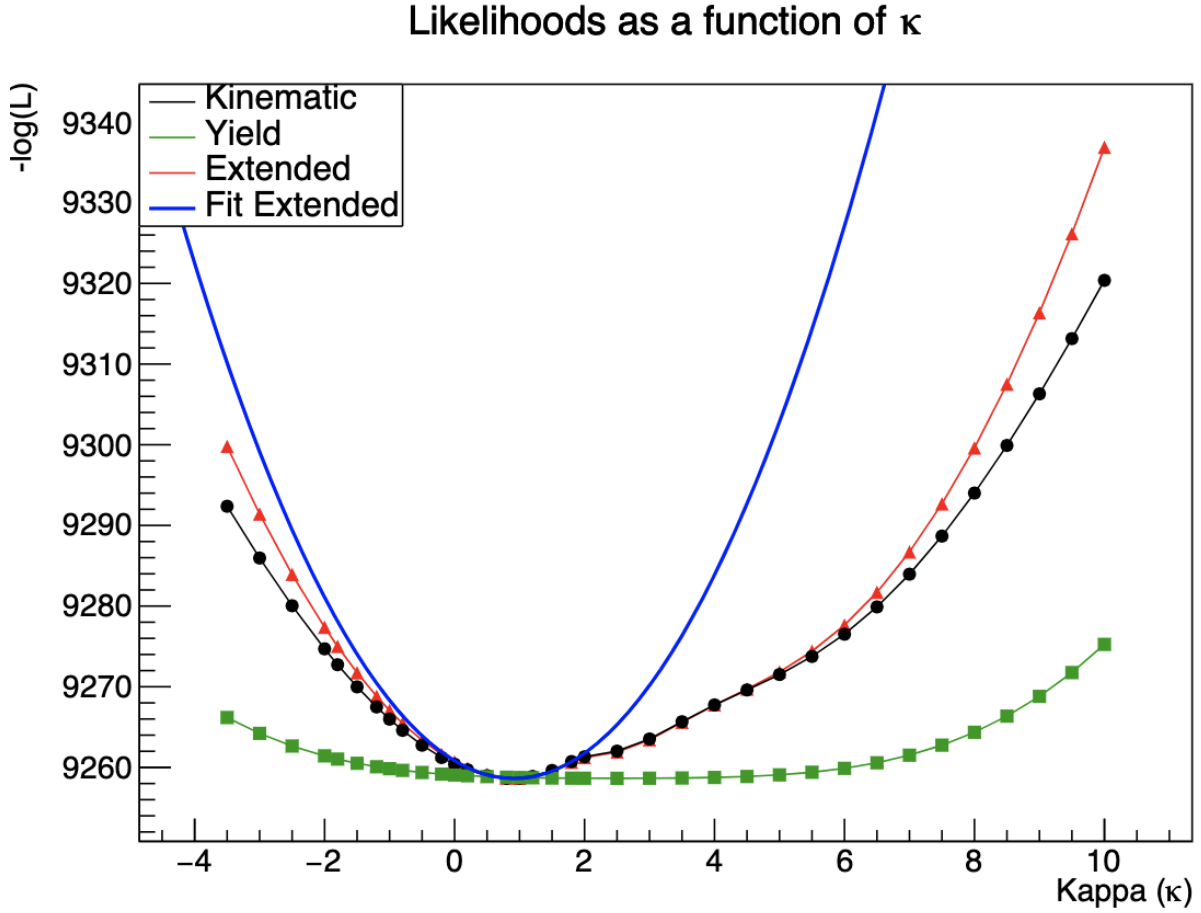


Figure 16.10: Example likelihood scan for one pseudo-dataset consisting of a mix of all processes (including signal ggF generated for $\kappa_\lambda = 1.00$), analysed under MEM@LO.

The graph shows $-\log \mathcal{L}$ as a function of the coupling modifier κ_λ for multiple likelihoods:

Black: kinematic component only (\mathcal{L}_{Kin}). **Green:** yield term ($\mathcal{L}_{\text{yield}}$). **Red:** extended likelihood (\mathcal{L}_{ext}). **Blue:** quadratic fit to $-\log \mathcal{L}_{\text{ext}}$ used to extract the best-fit value and its statistical uncertainty.

An other interesting addition to the study of the Matrix Element Method at Leading Order in the $b\bar{b}\gamma\gamma$ channel that we have produced is the performance of likelihood scans using pseudo-datasets in the presence of **all three** backgrounds: $t\bar{t}H$, single-Higgs and the QCD background (*cf.* Figure 16.10).

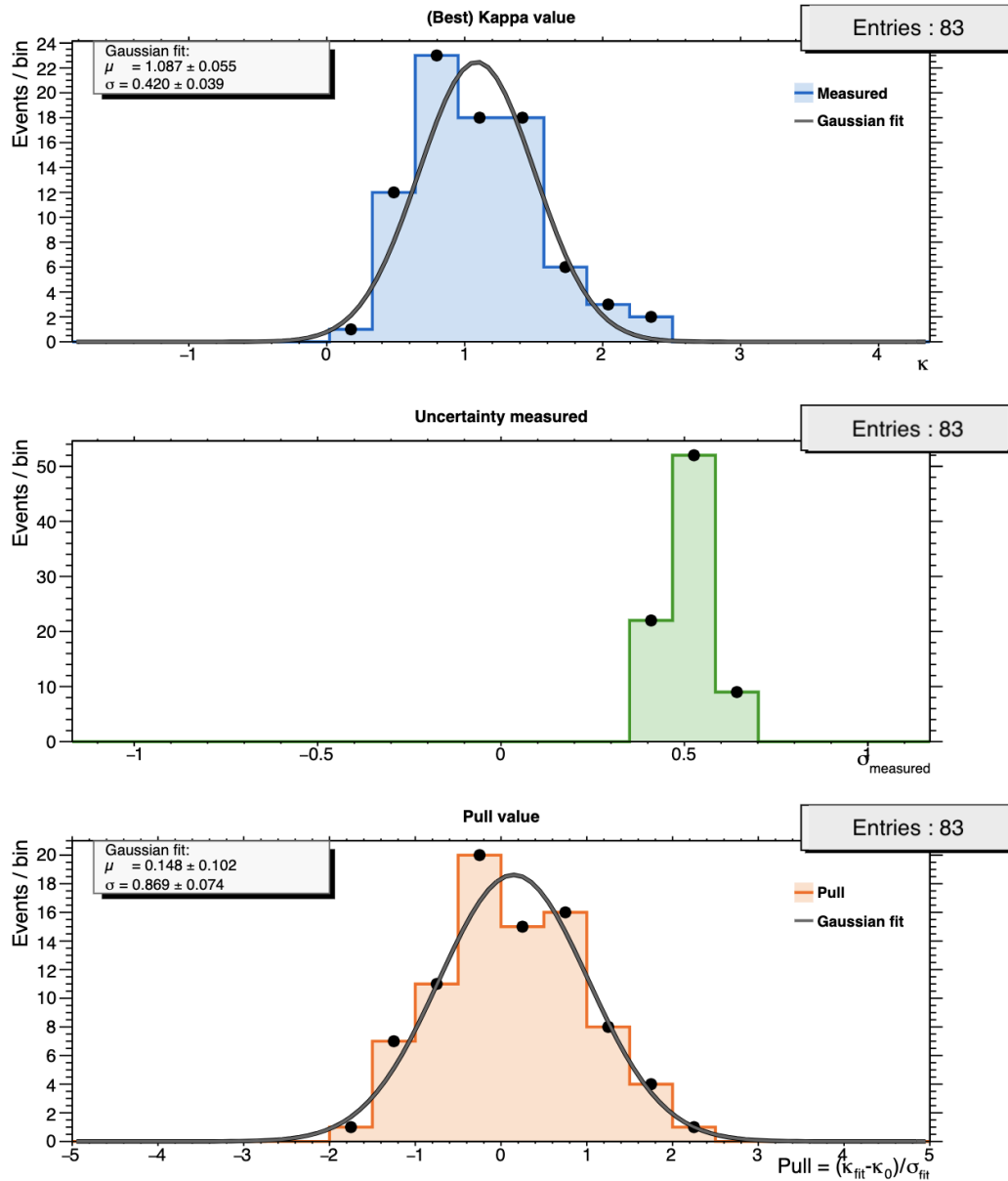


Figure 16.11: Likelihood scan for MC generated dataset of signal and all of the back-grounds, altogether.

Processes	Number events flagged as <i>ill</i> (%)
signal ggF ($\kappa_\lambda = 1.00$)	0
$t\bar{t}H$	11.03
QCD background	0
singleHiggs	0

Table 16.8: Fraction of ‘ill’ events (zero weight for their own hypothesis) removed before the likelihood scan of Figure 16.11.

Figure 16.11 summarises the performance of all the likelihood scans produced in this combination of processes. Only 84 pseudo-datasets were retained due to the large

number of events needed in each likelihood scans.

Best-fit estimator. The upper panel shows the distribution of the fitted self-coupling $\hat{\kappa}_\lambda$. A Gaussian fit gives $\kappa_{\text{mean}} = 1.087 \pm 0.055$ and $\sigma_\kappa = 0.420 \pm 0.039$. The central value sits only $+0.09$ above the injected parameter ($\kappa_\lambda = 1.00$), about one-fifth of the statistical width, so the overall bias is small.

Estimated uncertainty. The middle panel shows the spread of the fitted errors with an average $\sigma_{\text{fit}} \approx 0.51$, close to (yet slightly larger than) the width of the best-fit distribution.

Pull distribution. The lower panel plots $\omega = (\hat{\kappa}_\lambda - \kappa_{\text{test}})/\sigma_{\text{fit}}$. The mean pull is 0.15 ± 0.10 , consistent with the small positive bias, while the width is $\sigma_{\text{pull}} = 0.87 \pm 0.07$. The width below unity confirms that the quoted errors are slightly conservative but still give a reliable measure of the fit quality.

16.3 Summary for the MEM@LO

Likelihood Scan Performance

MEM@LO, $\sqrt{s}=14$ TeV, $b\bar{b}\gamma\gamma$ final state, with 300 fb^{-1}

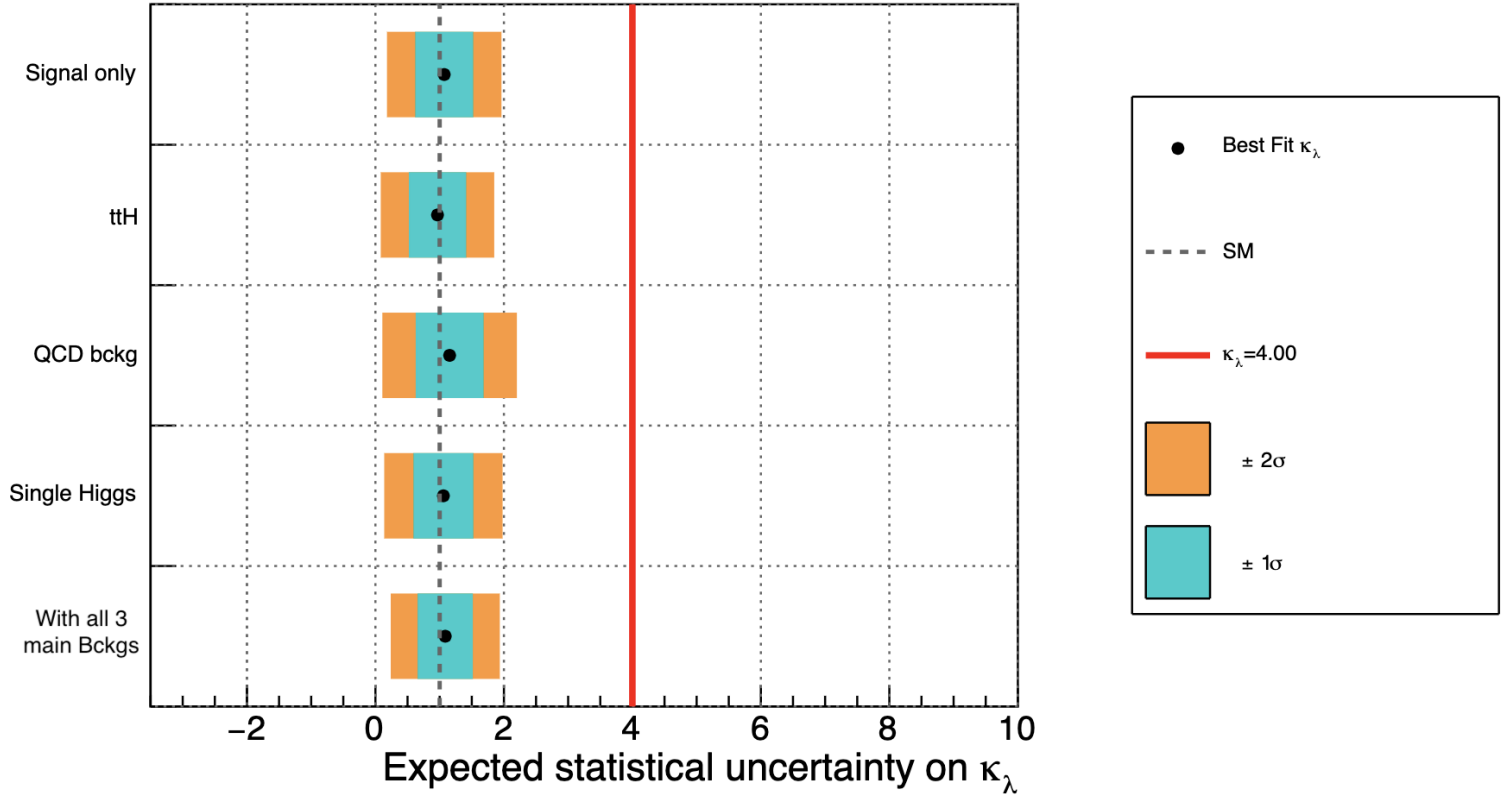


Figure 16.12: Summary of the MEM@LO profile likelihood performance for the $b\bar{b}\gamma\gamma$ final state at $\sqrt{s} = 14$ TeV, for an integrated luminosity of 300 fb^{-1} . For each pseudo-datasets ensemble the black dot marks the measured Higgs self-coupling modifier κ_λ , while the dashed grey line indicates the SM value ($\kappa_\lambda = 1.00$). The turquoise (orange) regions give the $\pm 1\sigma$ ($\pm 2\sigma$) expected bands obtained from toy fluctuations.

Figure 16.12 and Table 16.9 condense the performance of the MEM@LO profile likelihood fits for all datasets considered.

The black markers in the figure reproduce the best-fit values $\hat{\kappa}_\lambda$ quoted in the second column of the table, while the turquoise and orange bands help visualize the $\pm 1\sigma$ and $\pm 2\sigma$ intervals obtained from the toy ensembles.

For the signal-only sample the estimator is essentially unbiased ($\kappa_{\text{mean}} = 1.07 \pm 0.02$) and the pull distribution is perfectly calibrated ($\sigma_{\text{pull}} \simeq 1.03$). The most important deviation to the SM κ_λ value comes from the QCD background addition with ($\kappa_{\text{mean}} = 1.155 \pm 0.060$) and ($\sigma_\kappa = 0.483 \pm 0.048$). Even so, this slight shift corresponds to fewer than 3σ deviation: the result remains statistically consistent with the Standard Model value.

Even with all three backgrounds **used together**, the MEM@LO fit keeps good sensitivity. It measures $\kappa_{\text{mean}} = \mathbf{1.087 \pm 0.055}$ with a pull width of $\omega_{\text{mean}} = \mathbf{0.87}$. This shows that the method remains precise and statistically reliable in the full LO background mixture considered.

Process	Best fit		Measured uncertainty	Pull distribution	
	κ_{mean}	σ_{κ}		ω_{mean}	σ_{pull}
Signal only	1.071 ± 0.017	0.458 ± 0.012	0.441 ± 0.047	0.087 ± 0.033	1.026 ± 0.024
$t\bar{t}H$	0.966 ± 0.062	0.536 ± 0.063	0.437 ± 0.048	-0.091 ± 0.151	1.217 ± 0.159
QCD ($b\bar{b}\gamma\gamma$)	1.155 ± 0.060	0.483 ± 0.048	0.519 ± 0.105	0.275 ± 0.104	0.877 ± 0.090
Single Higgs	1.058 ± 0.020	0.518 ± 0.017	0.456 ± 0.059	0.099 ± 0.040	1.183 ± 0.032
Together	1.087 ± 0.055	0.420 ± 0.039	0.509 ± 0.056	0.148 ± 0.102	0.869 ± 0.074

Table 16.9: Summary of likelihood-scan performance for each process (MEM@LO).

The “best-fit” column quotes the Gaussian mean from the top histogram of each figure (κ_{mean}), and σ_{κ} is the corresponding width. The measured uncertainty is the mean of the green histogram, and the pull parameters come from the Gaussian fit to the bottom histogram (ω_{mean}).

Chapter 17

Results: With Our New NLO Matrix Element Method

Having validated the legacy Leading Order framework in Chapter 16, we now introduce the hallmark contribution of this thesis: the outputs of the new Matrix Element Method formalism at Next-to-Leading Order (MEM@NLO) and its impact on the measurement of the Higgs boson self-coupling modifier κ_λ .

The chapter follows the same logic as the previous one so that each improvement can be inspected and compared to the previous baseline.

Preliminary results obtained with the new Next-to-Leading Order Matrix Element Method have already been presented at several venues: the COMETA Workshop on EFT in di-Higgs and VBS (Paris, March 2025) [133], the Higgs Pairs Workshop (Isola d'Elba, May 2025) [134], the Physique ATLAS France (PAF) meeting in Annecy (May 2025) [135], and the EPS-HEP 2025 conference in Marseille (July 2025) [136].

The positive feedback received during the presentation of our results confirmed the novelty and relevance of the MEM@NLO strategy and guided the final refinements described in this chapter.

17.1 ROC Curves using MEM@NLO

Here again, each subsection will present our result for a given background channel: $t\bar{t}H$, QCD background and singleHiggs. The signal hypothesis events used for the discrimination are SM di-Higgs pair production using gluon fusion (ggF) with $\kappa_\lambda = 1.00$ (i.e no deviation from the SM).

All ROC curves are produced using the code previously described in 15.5.1.

17.1.1 $t\bar{t}H$ background

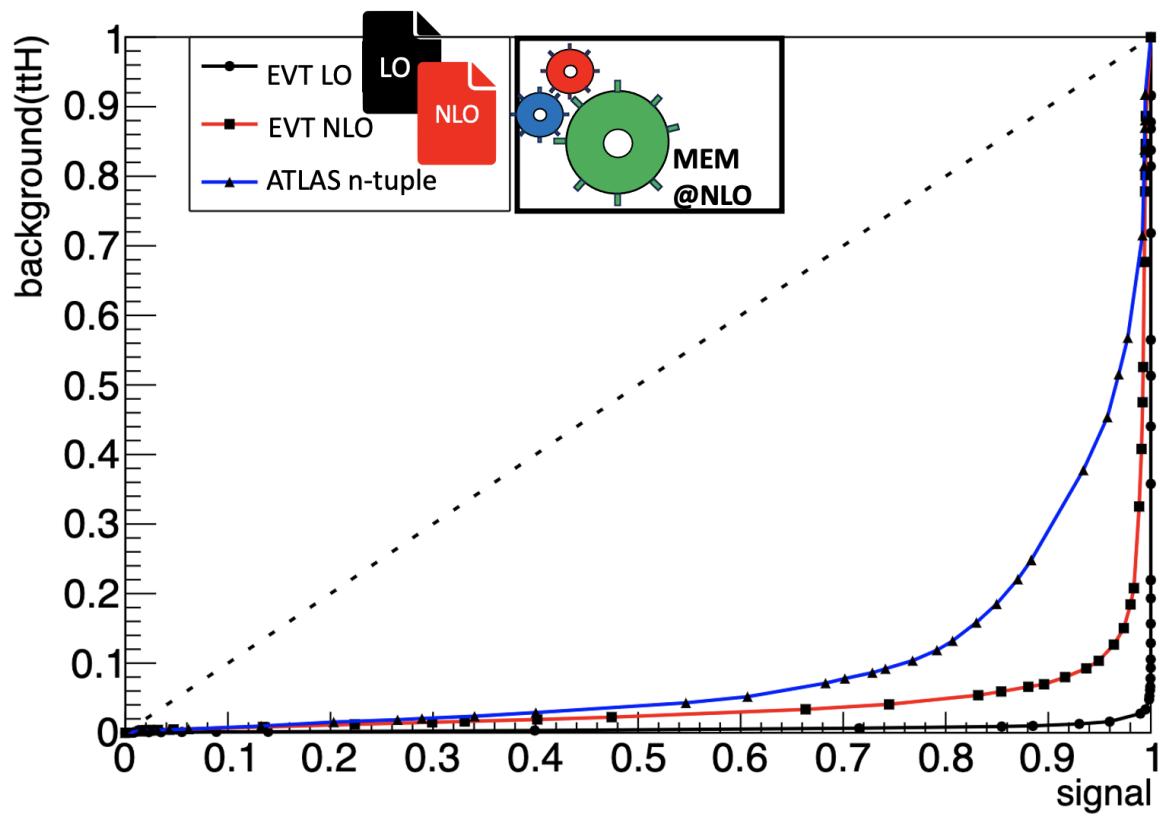
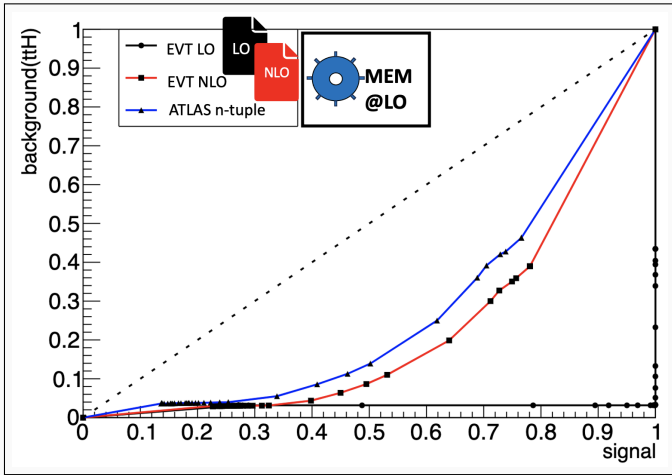


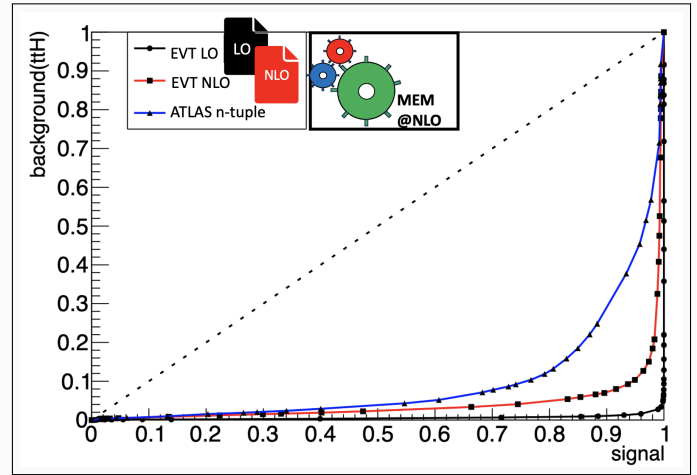
Figure 17.1: ROC curve obtained with MEM@NLO when the dominant background is $t\bar{t}H$ (using the DIVONNE algorithm for both hypotheses). The dashed line indicates the expectation from a random classifier.

The ROC curve in Figure 17.1 shows a sensible improvement in the discrimination of more realistic datasets when using our new formalism of the Matrix Element Method at NLO.

It is also interesting to notice going into NLO solves the issue on the choice of the DIVONNE integration algorithm for the $t\bar{t}H$ hypothesis simply by adding the real contributions for better separation on the events.

Comparison of LO and NLO ROC for $t\bar{t}H$ background (using DIVONNE algorithm)

(a) MEM@LO



(b) MEM@NLO

$[t\bar{t}H \text{ Background}]$	AUC (%)	signal rejected (%)	% background rejected (%)
LO	0.56	0	0.01
NLO ISR	4.09	0.48	0.55
ATLAS n-tuples	9.69	0.31	0.37

Table 17.1: Table for the values of interest hidden in Figure 17.1. The MEM integration algorithm is (DIVONNE) unless stated otherwise. Are indicated in this table: the area under the curve (AUC) (in %); the number of signal events that have zero weights values for **both** hypothesis at the same time (in %); and the number of background events that have zero weights values for **both** hypothesis at the same time (in %).

Table 17.1 shows that the MEM@NLO greatly improves (or keeps) the discrimination power with $t\bar{t}H$ background events, in particular for the NLO ISR generated events where the gains over MEM@LO is clearly visible.

Another key point, not visible in the figure, is that a fewer number of events now receive a zero weight for either hypothesis.

Together, these results show that using the newly developed Matrix Element Method at NLO gives significant improvement in the discrimination performance.

17.1.2 QCD di-photon background

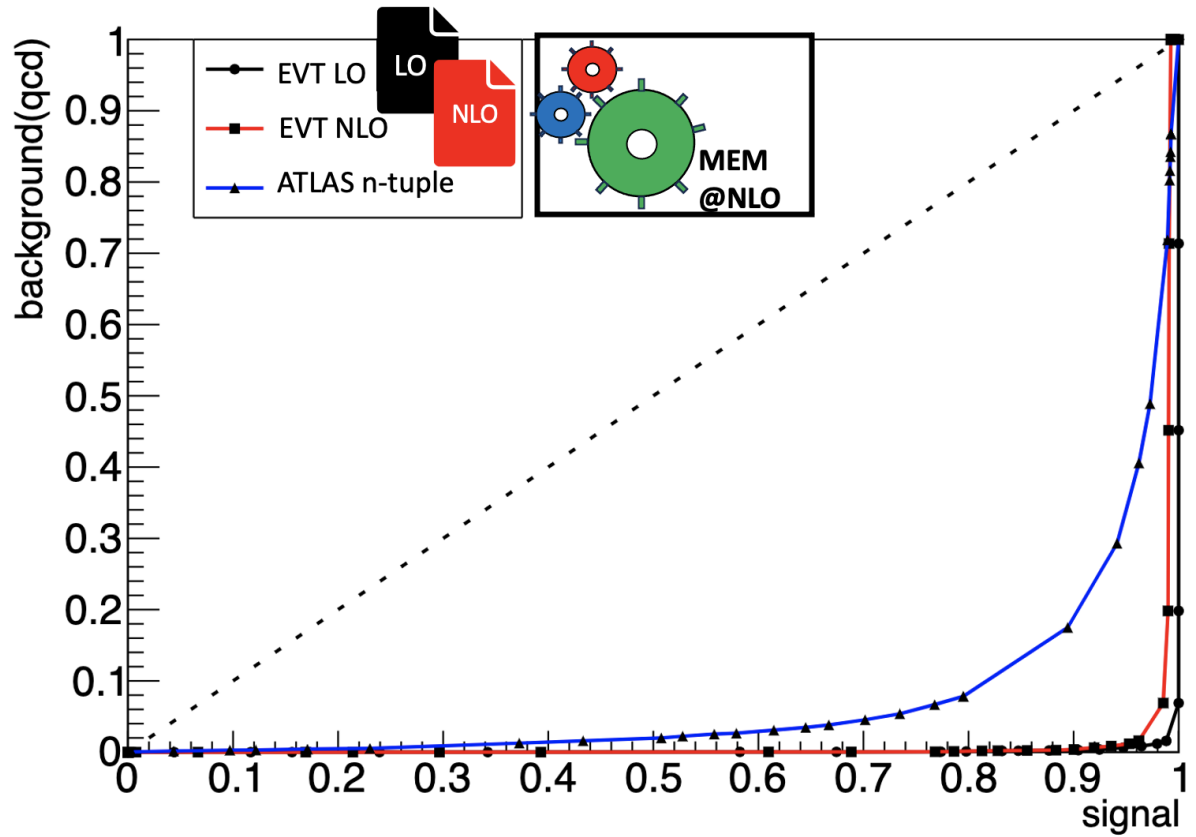
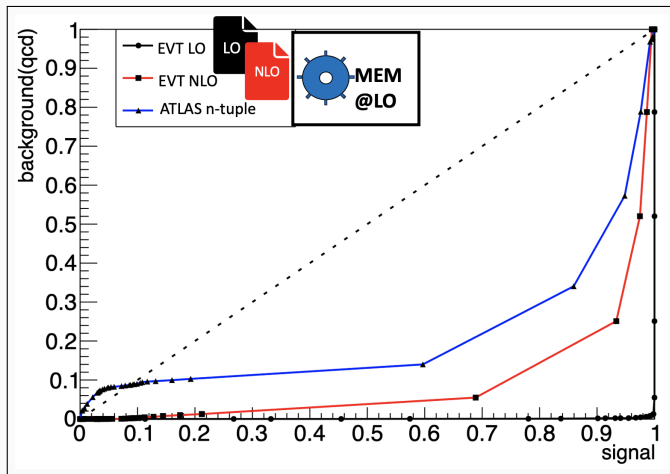
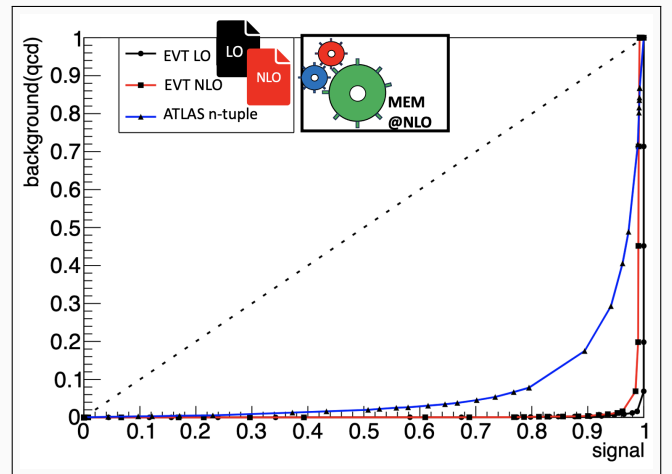


Figure 17.2: ROC curve obtained with MEM@NLO for the $b\bar{b}\gamma\gamma$ QCD background. The dashed line indicates the expectation from a random classifier

Comparison of LO and NLO ROC for QCD background



(a) MEM@LO



(b) MEM@NLO

[QCD Background]	AUC (%)	signal rejected (%)	% background rejected (%)
LO	0.14	0	0
NLO ISR	1.18	0.29	0
ATLAS n-tuples	7.08	0.11	0.10

Table 17.2: Table for the values of interest hidden in Figure 17.2. The MEM integration algorithm is (DIVONNE) unless stated otherwise. Are indicated in this table: the area under the curve (AUC) (in %); the number of signal events that have zero weights values for **both** hypothesis at the same time (in %); and the number of background events that have zero weights values for **both** hypothesis at the same time (in %).

The results in Figure 17.2 are produced using the DIVONNE algorithm for the multi-dimensional integration for both signal and QCD di-photon background.

Here again, Table 17.2 shows that the MEM@NLO greatly improves (or keeps) the discrimination power with QCD di-photon background events, in particular for the NLO ISR generated events where gains over MEM@LO are clearly visible in the comparison panel. And a fewer number of events now receive a zero weight for either hypothesis.

These results validate once again this new MEM@NLO formalism.

17.1.3 Single-Higgs background

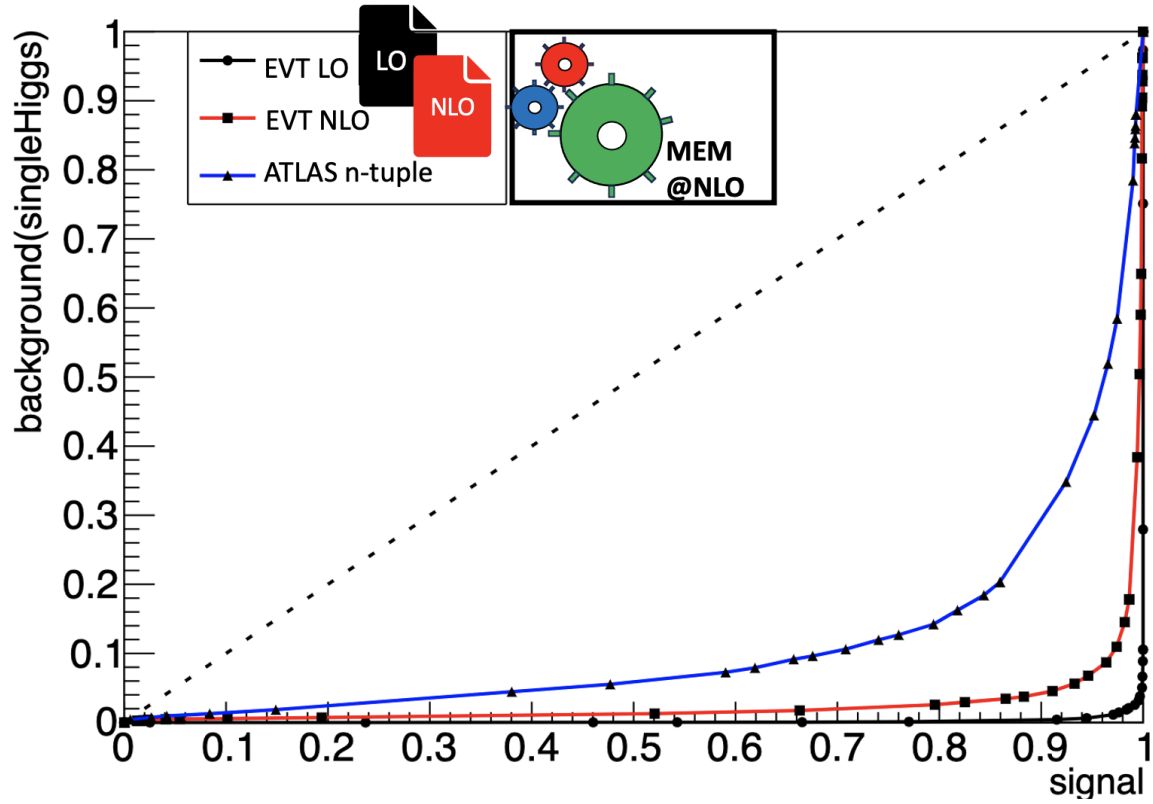
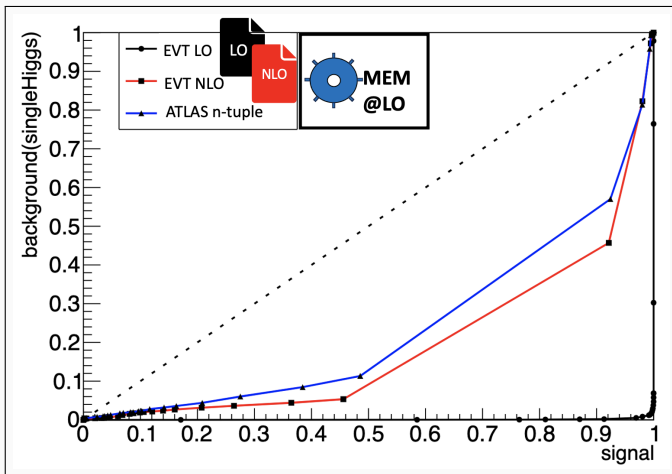
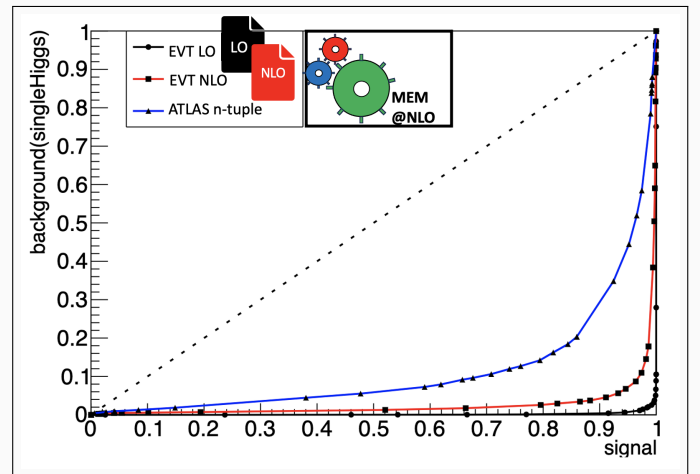


Figure 17.3: ROC curve obtained with MEM@NLO when the dominant background is singleHiggs. The dashed line indicates the expectation from a random classifier

Comparison of LO and NLO ROC for singleHiggs background



(a) MEM@LO



(b) MEM@NLO

[single-Higgs Background]	AUC (%)	signal rejected (%)	% background rejected (%)
LO	0.24	0	0
NLO ISR	3.12	0.51	0.14
ATLAS n-tuples	11.33	0.15	0.59

Table 17.3: Table for the values of interest hidden in Figure 17.3. The MEM integration algorithm is (DIVONNE) unless stated otherwise. Are indicated in this table: the area under the curve (AUC) (in %); the number of signal events that have zero weights values for **both** hypothesis at the same time (in %); and the number of background events that have zero weights values for **both** hypothesis at the same time (in %).

The results produced in Figure 17.3 are produced using the DIVONNE algorithm for the multi-dimensional integration for both signal and the singleHiggs background. Once again, Table 17.3 shows that the MEM@NLO greatly improves (or keeps) the discrimination power with singleHiggs background events, in particular for the NLO ISR generated events where gains over MEM@LO are clearly visible in the comparison panel. And a fewer number of events now receive a zero weight for either hypothesis.

These results validate once again this new MEM@NLO formalism.

17.1.4 Impact of the radiation transverse momentum (p_T^{rad}) IR cut on the ROC

To assess the influence of the p_T cut applied to the real NLO radiation in the MEM phase-space integration (in the case of the gluon-fusion process ggF), we conducted a systematic scan over several values of the cut threshold.

We computed the ROC curve for several choices of p_T value, and extracted the corresponding area under the curve (AUC). The results are shown in Figures 17.4 and 17.5.

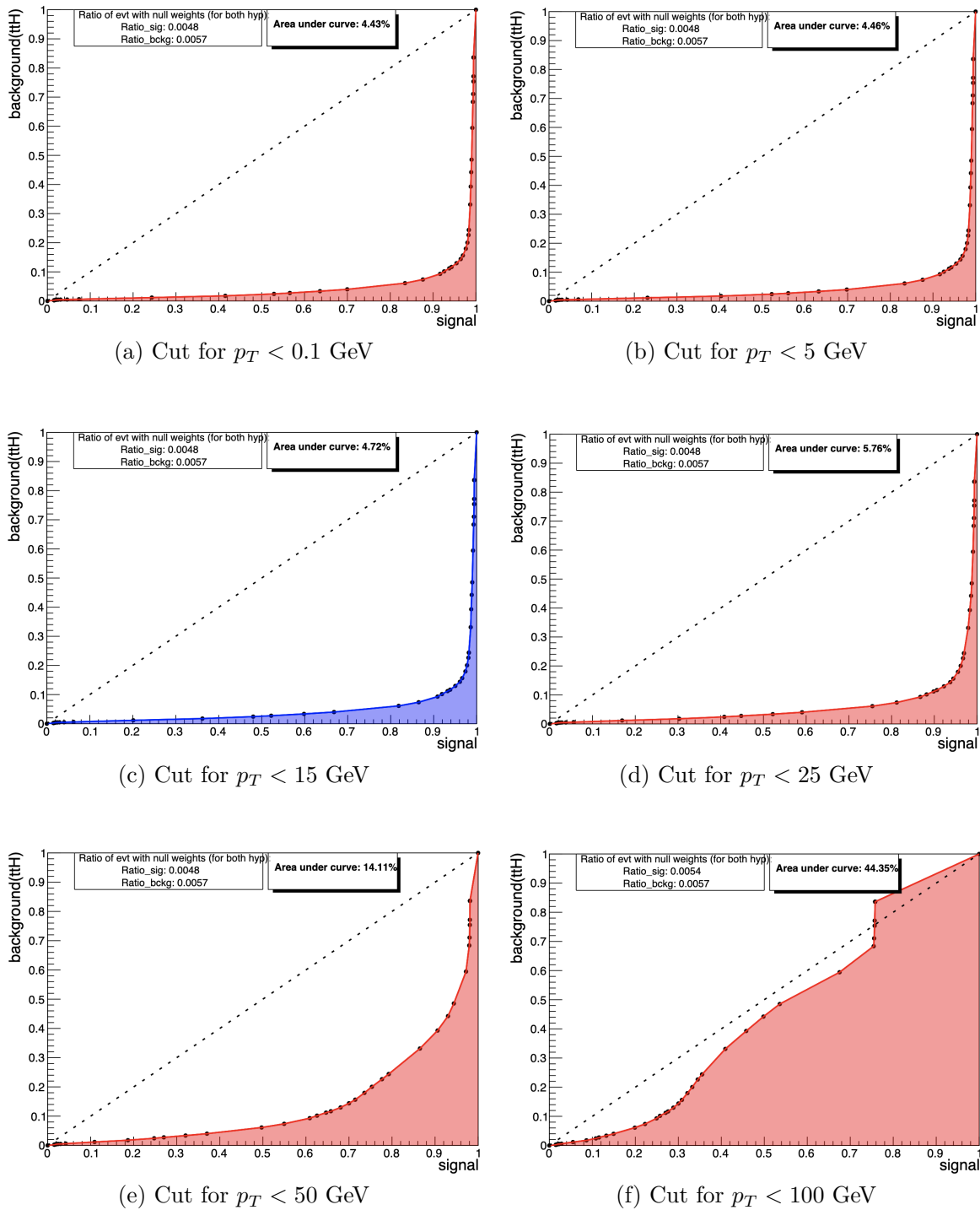


Figure 17.4: Comparison of different ROC curves for different choices of cuts on the transverse momentum p_T for the generation of the phase-space of the signal ggF extra radiation.

No change has been made on the ttH background MEM to keep consistency between plots and only study the impact of this change on the signal.

The ROC curve in Figure 17.4.c corresponds to our reference choice of cut.

We observe that for values of the p_T cut up to and including 15 GeV, the AUC remains remarkably stable, with only minimal variations.

Beyond this threshold, however, the AUC degrades sharply.

This behavior is expected: increasing the infrared cut on the transverse momentum restricts the phase-space region over which the MEM integration is performed, forcing the algorithm to sample over configurations with harder radiation. As a result, the integration becomes less representative of the true kinematics of the events, and the computed weights lose their discriminating power. In this regime, the overlap between the signal and background hypotheses grows, leading to a noticeable reduction in the separation performance.

The reference value $p_T = 15$ GeV (used throughout this work) was initially motivated by the physical spectrum study of the signal real radiation presented in Section 14.7. The present ROC-based validation confirms that this value is both statistically and physically optimal.

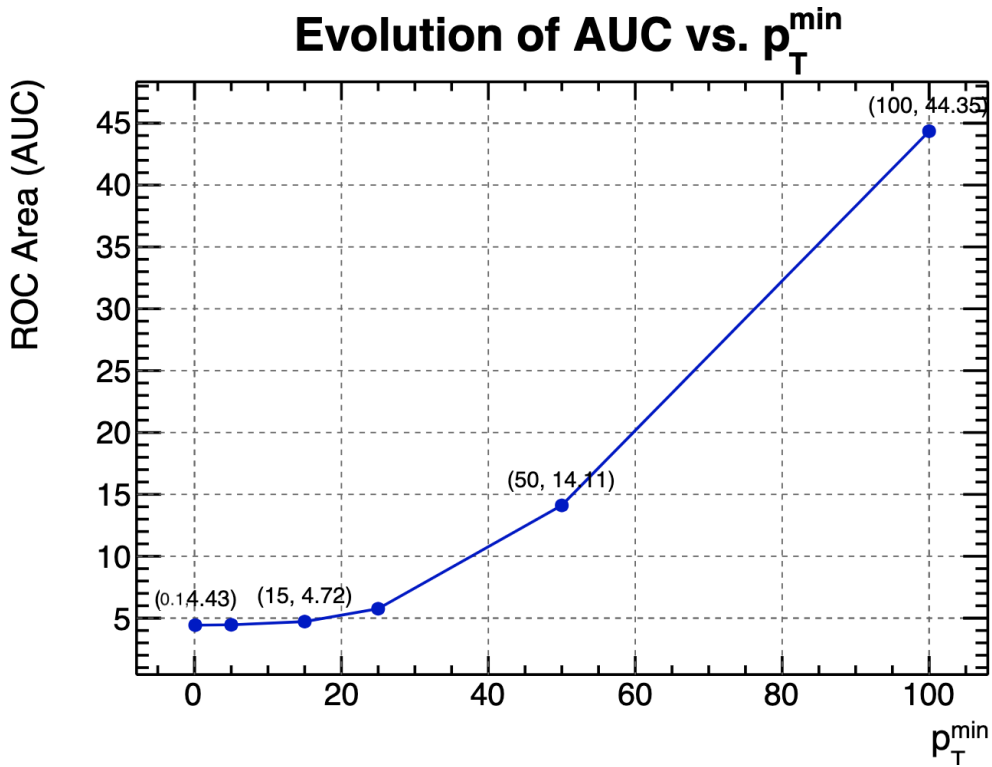


Figure 17.5: Evolution of the AUC value depending on the choice of p_T cut (for the signal ggF extra radiation), using values from Figure 17.4

Choosing a more aggressive cut (*i.e.* lower than 15 GeV) does not improve the AUC further, because our MEM configuration already excludes the soft and collinear regions via internal safeguards.

17.2 Likelihood Scan Performance: using NLO ISR generated samples

Each Likelihood scan follows the prescriptions detailed in Section 15.5.2. For each background sample we indicate in a table the percentage of events that are removed from the likelihood analysis because the weight computed under the *true* process hypothesis is exactly zero.

17.2.1 [NLO ISR] Signal-only pseudo-data

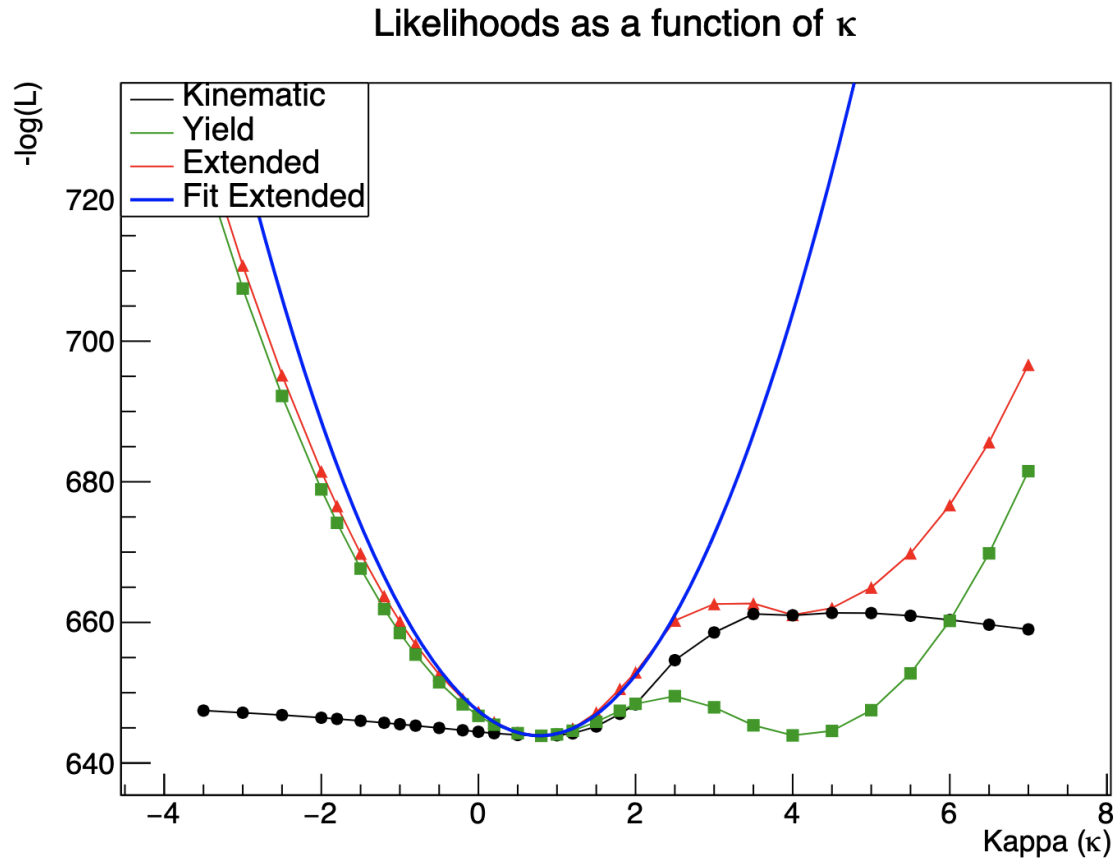


Figure 17.6: Example likelihood scan for one pseudo-dataset consisting of NLO ISR signal events ($\kappa_\lambda = 1.00$) analysed under MEM@NLO.

The graph shows $-\log \mathcal{L}$ as a function of the coupling modifier κ_λ for multiple likelihoods:

Black: kinematic component only (\mathcal{L}_{Kin}). **Green:** yield term ($\mathcal{L}_{\text{yield}}$). **Red:** extended likelihood (\mathcal{L}_{ext}). **Blue:** quadratic fit to $-\log \mathcal{L}_{\text{ext}}$ used to extract the best-fit value and its statistical uncertainty.

An example of a pure signal generated at NLO ISR, using MEM@NLO for the production of a likelihood scan profile is provided in Figure 17.6.

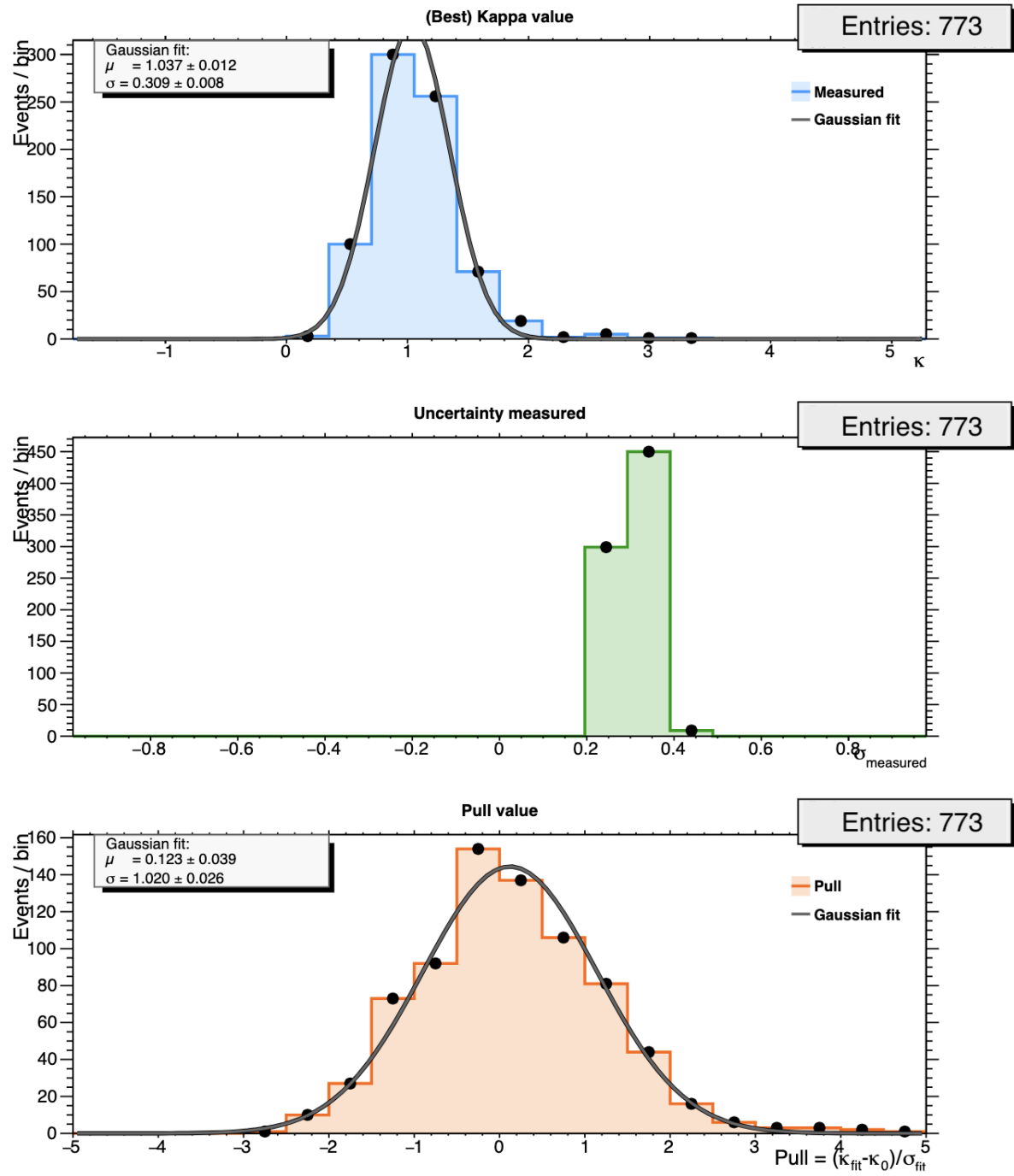


Figure 17.7: Likelihood scan for a pure signal sample using MEM@NLO weights.

Process	Number events flagged as <i>ill</i> (%)
signal ggF ($\kappa_\lambda = 1.00$)	1.85

Table 17.4: Fraction of ‘ill’ events (zero weight for their own hypothesis) removed before the likelihood scan of Figure 17.7.

For the special case of signal files, if the weight is zero for any of the κ_λ hypothesis it is removed from the list completely.

Figure 17.7 summarizes the outcome of 773 pseudo-experiments in which pure signal events (with $\kappa_\lambda = 1.00$) generated at NLO ISR are analysed with a MEM@NLO.

The upper panel shows the distribution of the fitted coupling $\hat{\kappa}_\lambda$ for each profile likelihood scans.

A Gaussian fit of the histogram of the best fit returns $\kappa_{\text{mean}} = 1.037 \pm 0.012$ and $\sigma_\kappa = 0.309 \pm 0.08$.

The middle panel displays the fitted uncertainty σ_{fit} obtained from the extended likelihood. Its distribution is sharply peaked at ~ 0.309 , confirming that the likelihood curvature provides a stable error estimate across toys here again.

And finally the lower panel tests the coverage by plotting the pull $\omega = (\hat{\kappa}_\lambda - \kappa_{\text{test}})/\sigma_{\text{fit}}$. The fitted pull mean is 0.123 ± 0.039 and the width 1.020 ± 0.026 , both statistically consistent with the ideal values $(0, 1)$.

In summary the profile likelihood machinery recovers the injected coupling with excellent coverage in this very simple case, validating the MEM@NLO implementation in the absence of background.

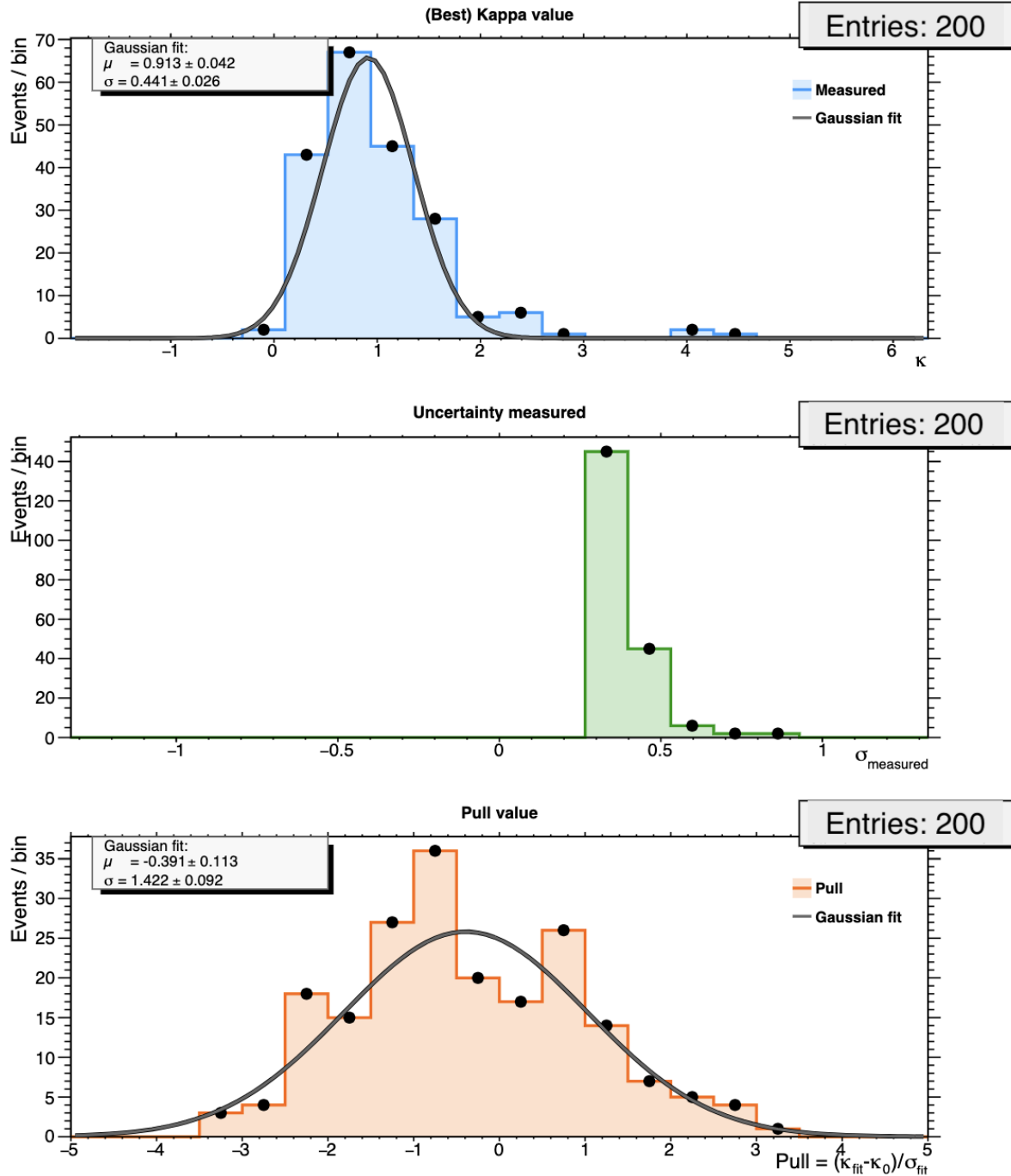
17.2.2 [NLO ISR] including $t\bar{t}H$ background

Figure 17.8: Histograms of the performance of the likelihood scans with $t\bar{t}H$ background included.

Top: distribution of the best-fit coupling parameter $\hat{\kappa}_{\lambda}$, with Gaussian fit overlaid. **Middle:** distribution of the estimated uncertainty σ_{measured} . **Bottom:** distribution of the pull values, defined as $(\hat{\kappa}_{\lambda} - \kappa_{\text{true}}) / \sigma_{\text{measured}}$.

Processes	Number events flagged as <i>ill</i> (%)
signal ggF ($\kappa_\lambda = 1.00$)	1.85
$t\bar{t}H$	3.65

Table 17.5: Fraction of ‘ill’ events (zero weight for their own hypothesis) removed before the likelihood scan of Figure 17.8.

Figure 17.8 summarizes the likelihood–scan performance when the $t\bar{t}H$ background is included and the analysis is carried out with MEM@NLO. Only 200 pseudo-datasets were produced due to the large number of events needed for each likelihood scans.

Best–fit estimator. The upper panel shows the distribution of the fitted coupling $\hat{\kappa}_\lambda$. A Gaussian fit yields $\kappa_{\text{mean}} = 0.913 \pm 0.042$ with a width of $\sigma_\kappa = 0.441 \pm 0.026$. The spread is about 18% narrower than in the corresponding MEM@LO study, reflecting the gain from the NLO treatment.

Estimated uncertainty. The middle panel gives the fitted error distribution, which peaks at $\sigma_{\text{fit}} \simeq 0.44$, in line with the width extracted above.

Pull distribution. The pull mean is -0.039 ± 0.113 , consistent with zero, but the width $\sigma_{\text{pull}} = 1.422 \pm 0.092$ exceeds the ideal value of 1 by roughly 40%, indicating that the quoted uncertainties are still somewhat underestimated.

17.2.3 [NLO ISR] including QCD background

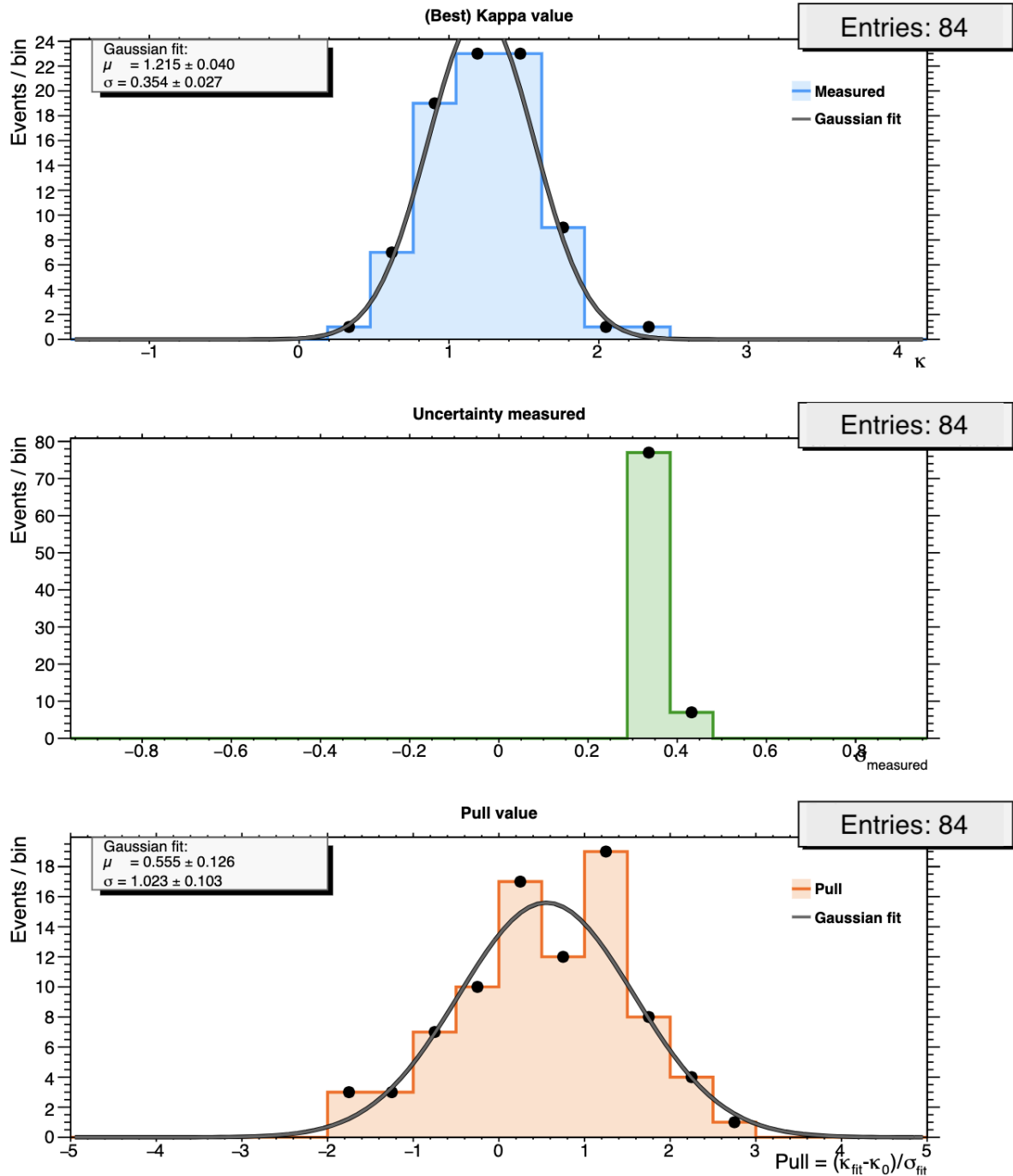


Figure 17.9: Histograms of the performance of the likelihood scans with QCD background included.

Top: distribution of the best-fit coupling parameter $\hat{\kappa}_\lambda$, with Gaussian fit overlaid. **Middle:** distribution of the estimated uncertainty σ_{measured} . **Bottom:** distribution of the pull values, defined as $(\hat{\kappa}_\lambda - \kappa_{\text{true}}) / \sigma_{\text{measured}}$.

Processes	Number events flagged as <i>ill</i> (%)
signal ggF ($\kappa_\lambda = 1.00$)	1.85
QCD background	0

Table 17.6: Fraction of ‘ill’ events (zero weight for their own hypothesis) removed before the likelihood scan of Figure 17.9.

Figure 17.9 shows the likelihood-scan performance when a QCD continuum background is included and the analysis is performed with MEM@NLO. A total of 84 pseudo-datasets were analysed.

Best-fit estimator. The top panel displays the distribution of the fitted coupling $\hat{\kappa}_\lambda$. A Gaussian fit gives $\kappa_{\text{mean}} = 1.215 \pm 0.502$ and a width of $\sigma_\kappa = 0.354 \pm 0.027$. The narrower spread, compared with the $t\bar{t}H$ study, reflects the smaller statistical impact of the QCD background in this channel.

One also need to keep in mind that we are using Leading Order generated QCD events here, in substitution for their NLO counterparts (*cf.* Section 15.1.1).

Estimated uncertainty. The central panel shows the fitted error distribution, which peaks at $\sigma_{\text{fit}} \simeq 0.35$, fully consistent with the width obtained above.

Pull distribution. The pull mean is 0.055 ± 0.126 , statistically compatible with zero, while the width $\sigma_{\text{pull}} = 1.023 \pm 0.103$ is very close to the ideal value of 1. This indicates that, with the QCD background included, the MEM@NLO delivers an unbiased estimate of both the central value and its uncertainty.

17.2.4 [NLO ISR] including single-Higgs background

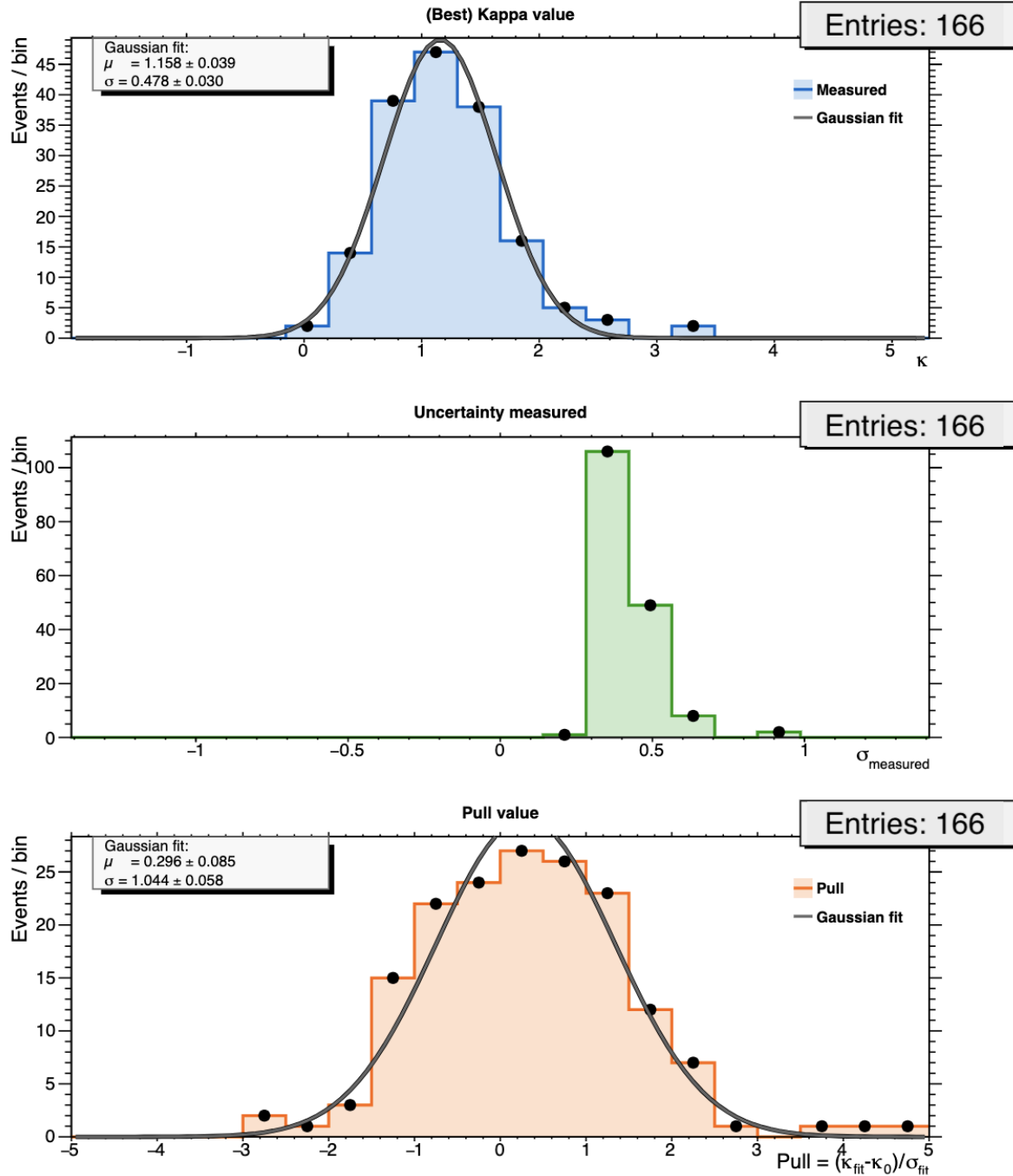


Figure 17.10: Histograms of the performance of the likelihood scans with single-Higgs background included.

Top: distribution of the best-fit coupling parameter $\hat{\kappa}_\lambda$, with Gaussian fit overlaid. **Middle:** distribution of the estimated uncertainty σ_{measured} . **Bottom:** distribution of the pull values, defined as $(\hat{\kappa}_\lambda - \kappa_{\text{true}}) / \sigma_{\text{measured}}$.

Processes	Number events flagged as <i>ill</i> (%)
signal ggF ($\kappa_\lambda = 1.00$)	1.85
singleHiggs	0.14

Table 17.7: Fraction of ‘ill’ events (zero weight for their own hypothesis) removed before the likelihood scan of Figure 17.10.

Figure 17.10 displays the MEM@NLO likelihood–scan results when a single-Higgs background (generated with NLO + ISR accuracy) is included. A total of 166 pseudo-datasets were analysed.

Best-fit estimator. The upper panel shows the fitted coupling $\hat{\kappa}_\lambda$. A Gaussian fit gives $\kappa_{\text{mean}} = 1.158 \pm 0.039$ with a width of $\sigma_\kappa = 0.478 \pm 0.030$.

Estimated uncertainty. The middle panel shows the distribution of the fitted errors; it peaks at $\sigma_{\text{fit}} \simeq 0.48$, matching the width quoted above.

Pull distribution. The pull mean is 0.296 ± 0.085 , consistent with zero within 4σ . The width $\sigma_{\text{pull}} = 1.044 \pm 0.058$ is close to the ideal value of 1, indicating that the quoted uncertainties are well calibrated for this background configuration.

17.2.5 [NLO ISR] including all three main backgrounds

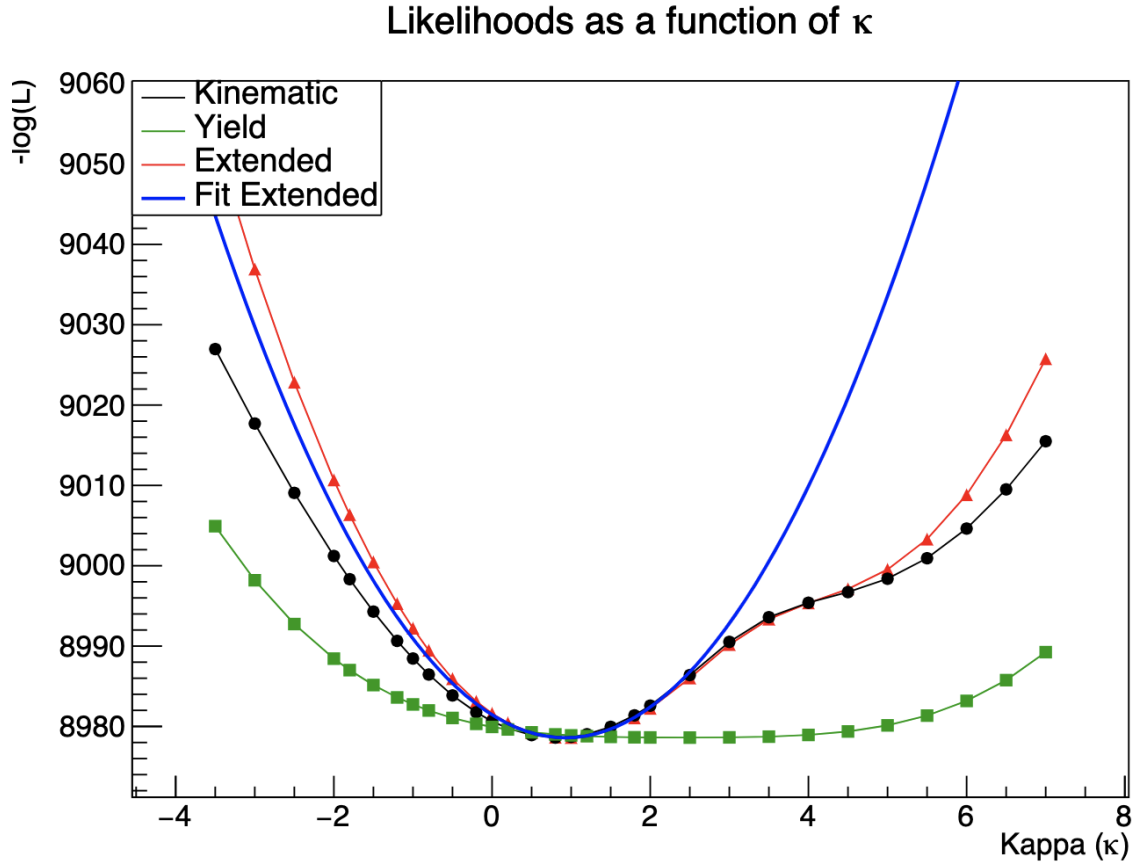


Figure 17.11: Example likelihood scan for one pseudo-dataset consisting of a combination of NLO ISR signal events ($\kappa_\lambda = 1.00$) and backgrounds, analysed under MEM@NLO.

The graph shows $-\log \mathcal{L}$ as a function of the coupling modifier κ_λ for multiple likelihoods:

Black: kinematic component only (\mathcal{L}_{Kin}). **Green:** yield term ($\mathcal{L}_{\text{yield}}$). **Red:** extended likelihood (\mathcal{L}_{ext}). **Blue:** quadratic fit to $-\log \mathcal{L}_{\text{ext}}$ used to extract the best-fit value and its statistical uncertainty.

An example of a likelihood scan profile for a sample of all processes combined together (at NLO ISR), using MEM@NLO is provided in Figure 17.11.

Processes	Number events flagged as <i>ill</i> (%)
signal ggF ($\kappa_\lambda = 1.00$)	1.85
$t\bar{t}H$	3.65
QCD background	0
singleHiggs	0.14

Table 17.8: Fraction of ‘ill’ events (zero weight for their own hypothesis) removed before the likelihood scan of Figure 17.12.

Figure 17.12 presents the MEM@NLO likelihood-scan results obtained with the

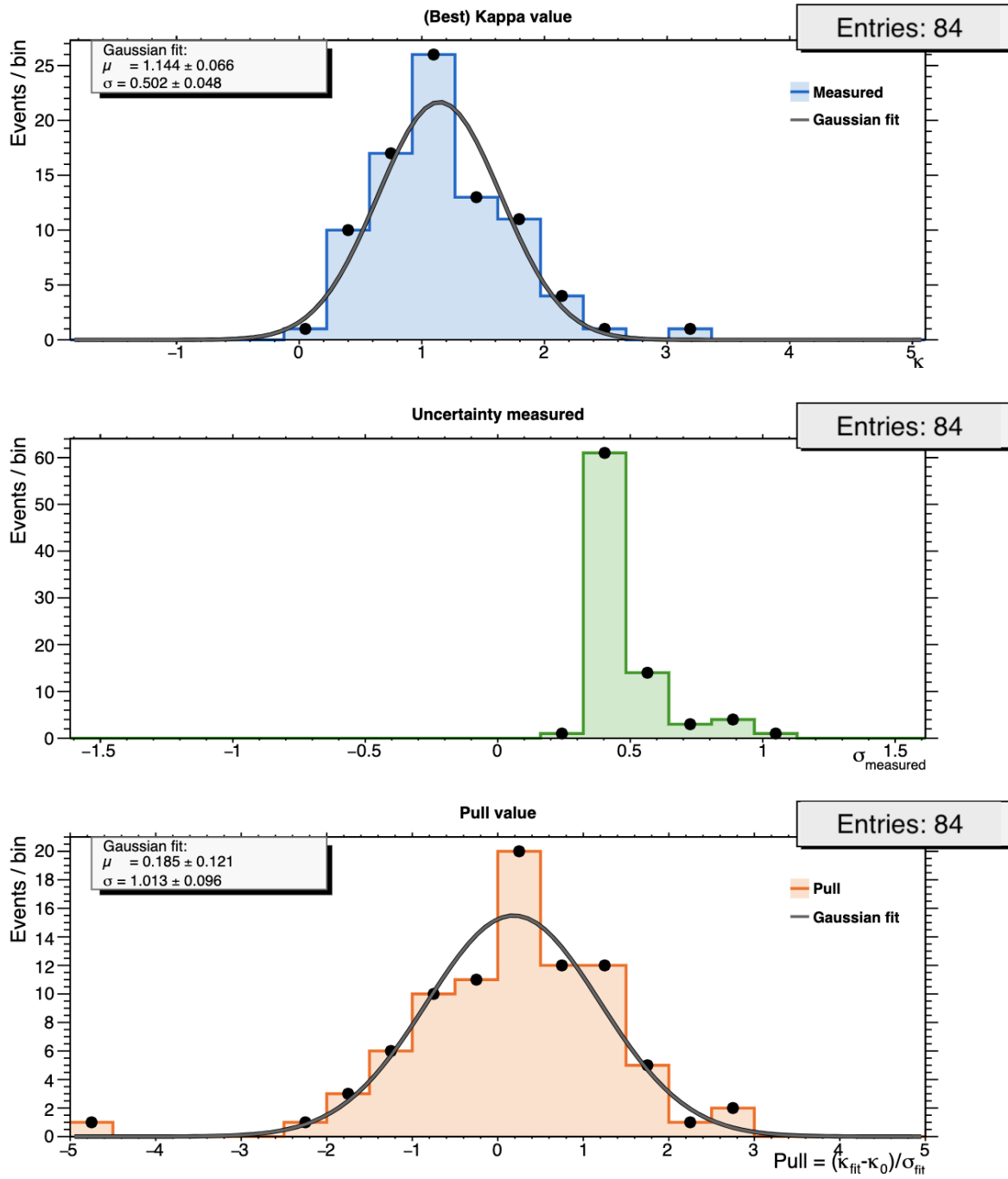


Figure 17.12: Histograms of the performance of the likelihood scans with all background included.

Top: distribution of the best-fit coupling parameter $\hat{\kappa}_\lambda$, with Gaussian fit overlaid. **Middle:** distribution of the estimated uncertainty σ_{measured} . **Bottom:** distribution of the pull values, defined as $(\hat{\kappa}_\lambda - \kappa_{\text{true}}) / \sigma_{\text{measured}}$.

addition of all three main background samples (*i.e.* $t\bar{t}H$, single-Higgs, and QCD di-Photon backgrounds), each generated at NLO ISR. A total of 84 pseudo-datasets were analysed.

Best-fit estimator. The upper panel shows the distribution of the fitted coupling $\hat{\kappa}_\lambda$. A Gaussian fit yields $\kappa_{\text{mean}} = 1.144 \pm 0.066$ with a width of $\sigma_\kappa = 0.502 \pm 0.048$.
Estimated uncertainty. The middle panel displays the fitted error distribution, peaking at $\sigma_{\text{fit}} \simeq 0.50$, in excellent agreement with the observed spread.
Pull distribution. The pull mean is -0.185 ± 0.121 , statistically compatible with zero, and the width $\sigma_{\text{pull}} = 1.013 \pm 0.096$ is essentially ideal.

These metrics confirm that, even with all major backgrounds included at NLO, the MEM@NLO framework still delivers an unbiased estimate of κ_λ with well-calibrated uncertainties.

17.3 Likelihood Scan Performance: using ATLAS fully simulated events

Each Likelihood scan follows the prescriptions detailed in Section 15.5.2.

For each background sample we indicate in a table the percentage of events that are removed from the likelihood analysis because the weight computed under the *true* process hypothesis is exactly zero.

17.3.1 [ATLAS fullsim] Signal-only pseudo-data

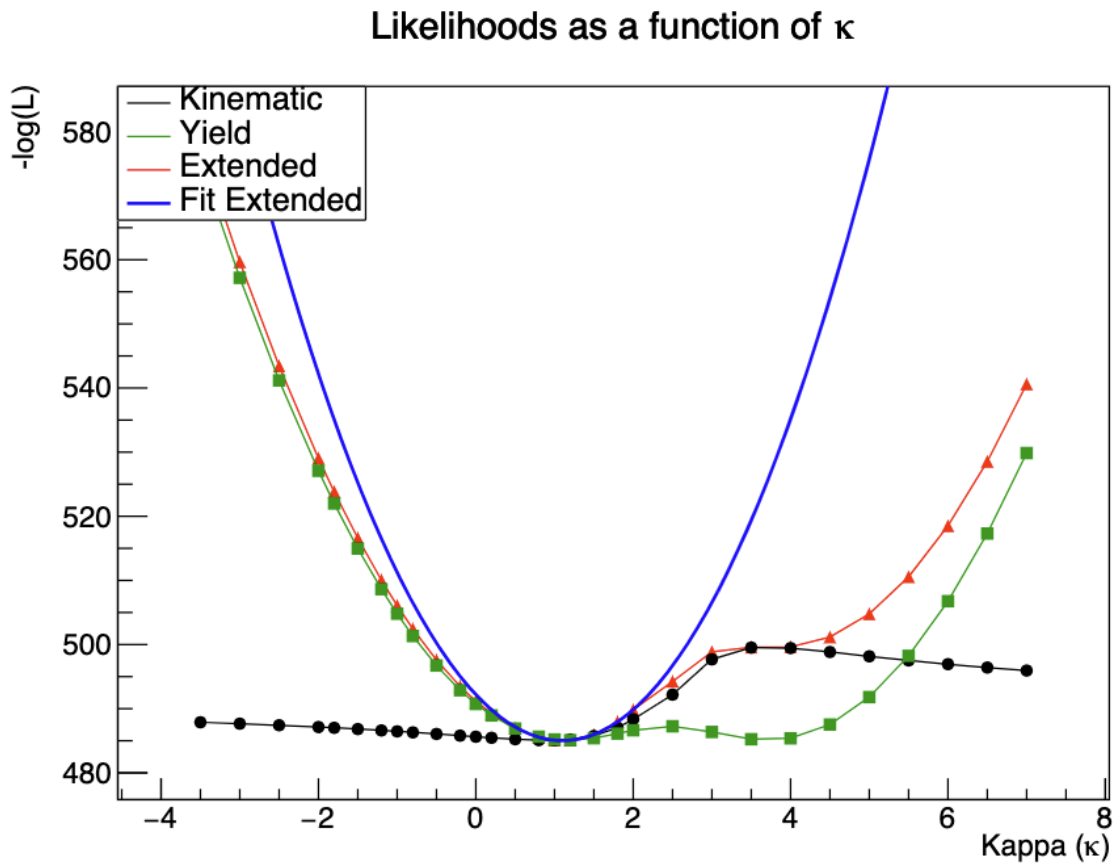


Figure 17.13: Example likelihood scan for one pseudo-dataset consisting of ATLAS simulated n-tuples signal events ($\kappa_\lambda = 1.00$) analysed under MEM@NLO.

The graph shows $-\log \mathcal{L}$ as a function of the coupling modifier κ_λ for multiple likelihoods:

Black: kinematic component only (\mathcal{L}_{Kin}). **Green:** yield term ($\mathcal{L}_{\text{yield}}$). **Red:** extended likelihood (\mathcal{L}_{ext}). **Blue:** quadratic fit to $-\log \mathcal{L}_{\text{ext}}$ used to extract the best-fit value and its statistical uncertainty.

An example of a pure signal n-tuples generated by the ATLAS collaboration, using MEM@NLO for the production of a likelihood scan profile is provided in Figure 17.13.

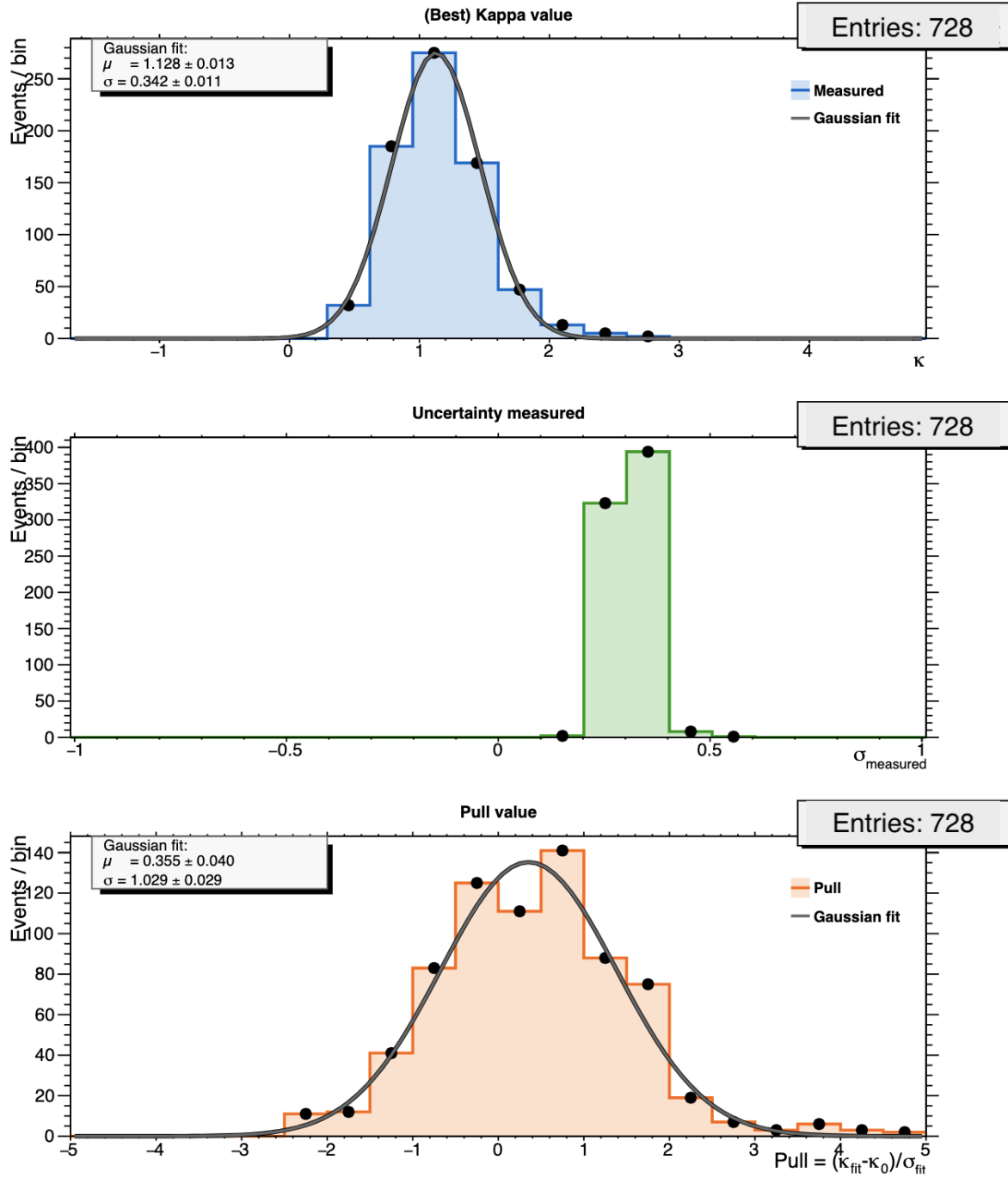


Figure 17.14: Likelihood scan for a pure signal sample of ATLAS simulated n-tuples using MEM@NLO weights.

Process	Number events flagged as <i>ill</i> (%)
signal ggF ($\kappa_\lambda = 1.00$)	6.72

Table 17.9: Fraction of ‘ill’ events (zero weight for their own hypothesis) removed before the likelihood scan of Figure 17.14.

Figure 17.14 presents the MEM@NLO likelihood-scan results for the *signal-only* sample obtained with full ATLAS simulation. A total of 728 pseudo-datasets were

analysed.

Best-fit estimator. The upper panel shows the distribution of the fitted coupling $\hat{\kappa}_\lambda$. A Gaussian fit yields $\kappa_{\text{mean}} = 1.128 \pm 0.013$ with a width of $\sigma_\kappa = 0.342 \pm 0.011$.

Estimated uncertainty. The middle panel displays the fitted error distribution, peaking at $\sigma_{\text{fit}} \simeq 0.35$, in excellent agreement with the observed spread.

Pull distribution. The pull mean is 0.355 ± 0.040 , statistically compatible with zero, and the width $\sigma_{\text{pull}} = 1.029 \pm 0.029$ is essentially ideal.

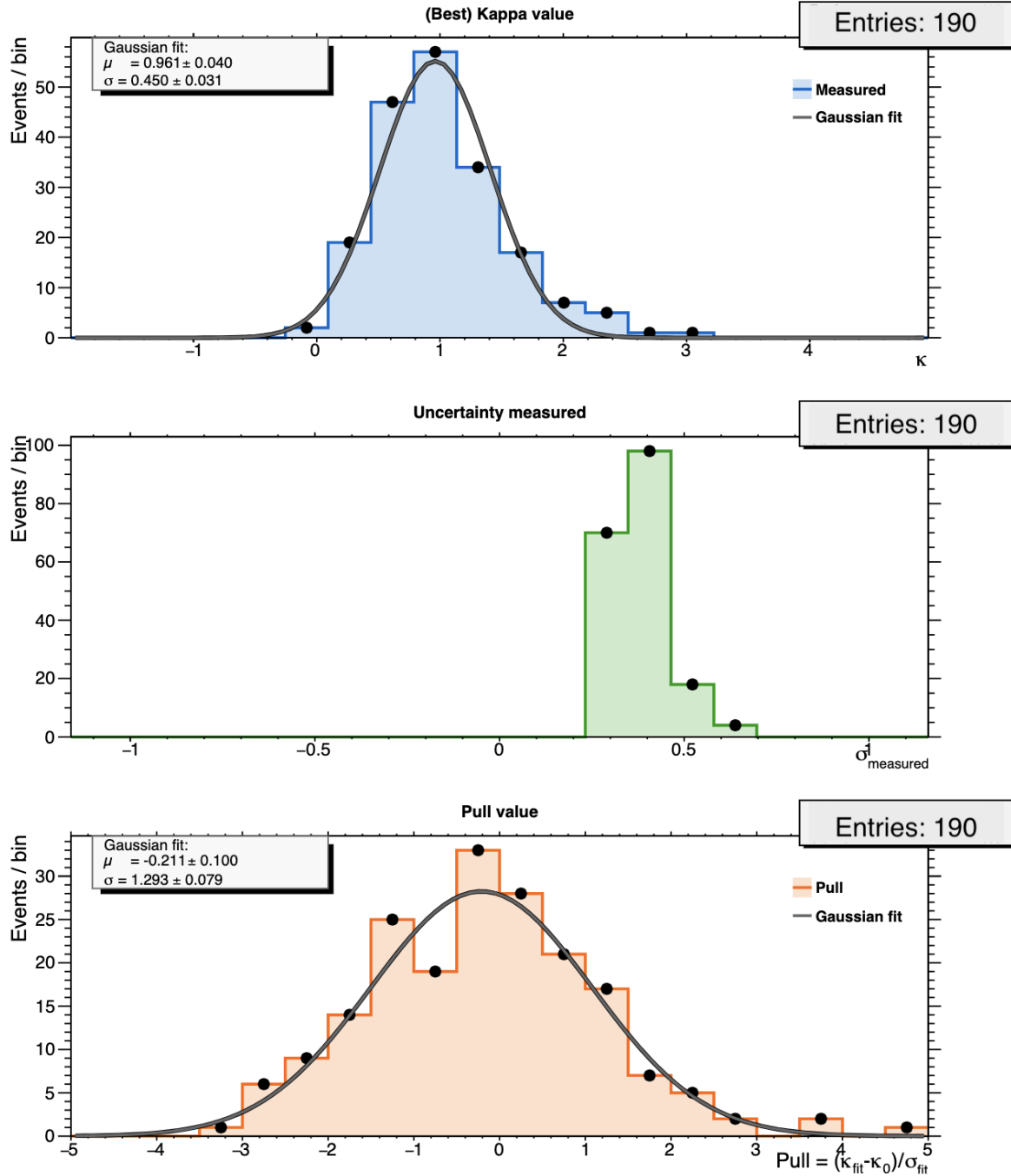
17.3.2 [ATLAS fullsim] including $t\bar{t}H$ background

Figure 17.15: Histograms of the performance of the likelihood scans with $t\bar{t}H$ background included.

Top: distribution of the best-fit coupling parameter $\hat{\kappa}_\lambda$, with Gaussian fit overlaid. **Middle:** distribution of the estimated uncertainty σ_{measured} . **Bottom:** distribution of the pull values, defined as $(\hat{\kappa}_\lambda - \kappa_{\text{true}}) / \sigma_{\text{measured}}$.

Processes	Number events flagged as <i>ill</i> (%)
signal ggF ($\kappa_\lambda = 1.00$)	6.72
$t\bar{t}H$	2.42

Table 17.10: Fraction of ‘ill’ events (zero weight for their own hypothesis) removed before the likelihood scan of Figure 17.16.

Figure 17.15 shows the likelihood-scan results when a $t\bar{t}H$ background is added. A total of 190 pseudo-datasets were analysed.

Best-fit estimator. A Gaussian fit gives $\kappa_{\text{mean}} = 0.961 \pm 0.040$ and $\sigma_\kappa = 0.450 \pm 0.031$.

Estimated uncertainty. The error distribution peaks at $\sigma_{\text{fit}} \simeq 0.46$, matching the measured width.

Pull distribution. The pull mean is -0.211 ± 0.100 , and the width $\sigma_{\text{pull}} = 1.293 \pm 0.079$ indicates a slight under-estimate of the quoted errors.

17.3.3 [ATLAS fullsim] including QCD background

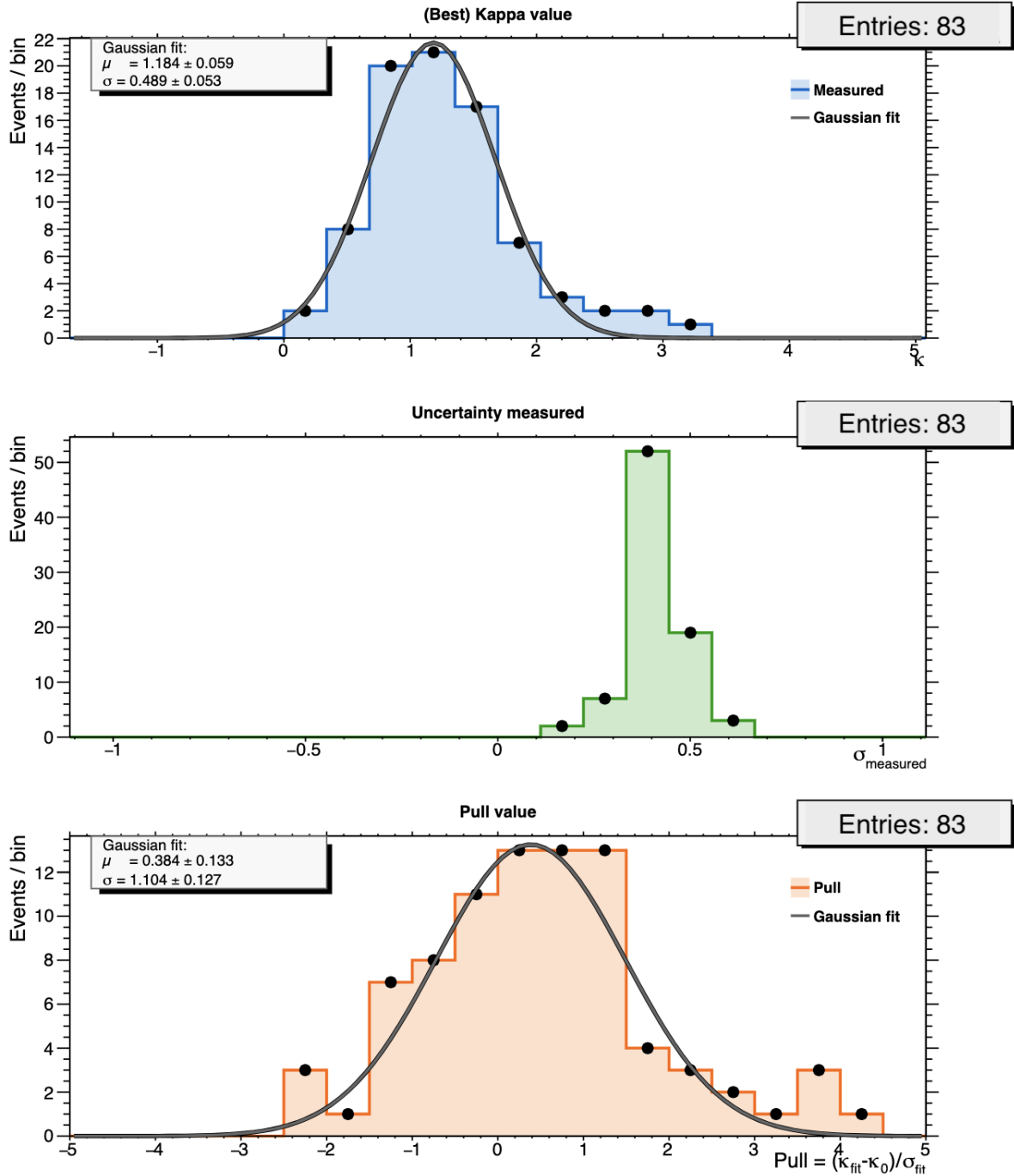


Figure 17.16: Histograms of the performance of the likelihood scans with QCD background included.

Top: distribution of the best-fit coupling parameter $\hat{\kappa}_\lambda$, with Gaussian fit overlaid. **Middle:** distribution of the estimated uncertainty σ_{measured} . **Bottom:** distribution of the pull values, defined as $(\hat{\kappa}_\lambda - \kappa_{\text{true}}) / \sigma_{\text{measured}}$.

Processes	Number events flagged as <i>ill</i> (%)
signal ggF ($\kappa_\lambda = 1.00$)	6.72
QCD background	0.011

Table 17.11: Fraction of ‘ill’ events (zero weight for their own hypothesis) removed before the likelihood scan of Figure 17.16.

Figure 17.16 reports the scan that includes a *QCD continuum* background. Eighty-three pseudo-datasets were analysed.

Best-fit estimator. The fitted distribution yields $\kappa_{\text{mean}} = 1.118 \pm 0.034$ with $\sigma_\kappa = 0.371 \pm 0.030$.

Estimated uncertainty. The corresponding error peak at $\sigma_{\text{fit}} \simeq 0.37$ closely follows the observed width.

Pull distribution. The pull mean is 0.303 ± 0.076 and the width $\sigma_{\text{pull}} = 0.905 \pm 0.060$, suggesting slightly conservative uncertainties.

17.3.4 [ATLAS fullsim] including single-Higgs background

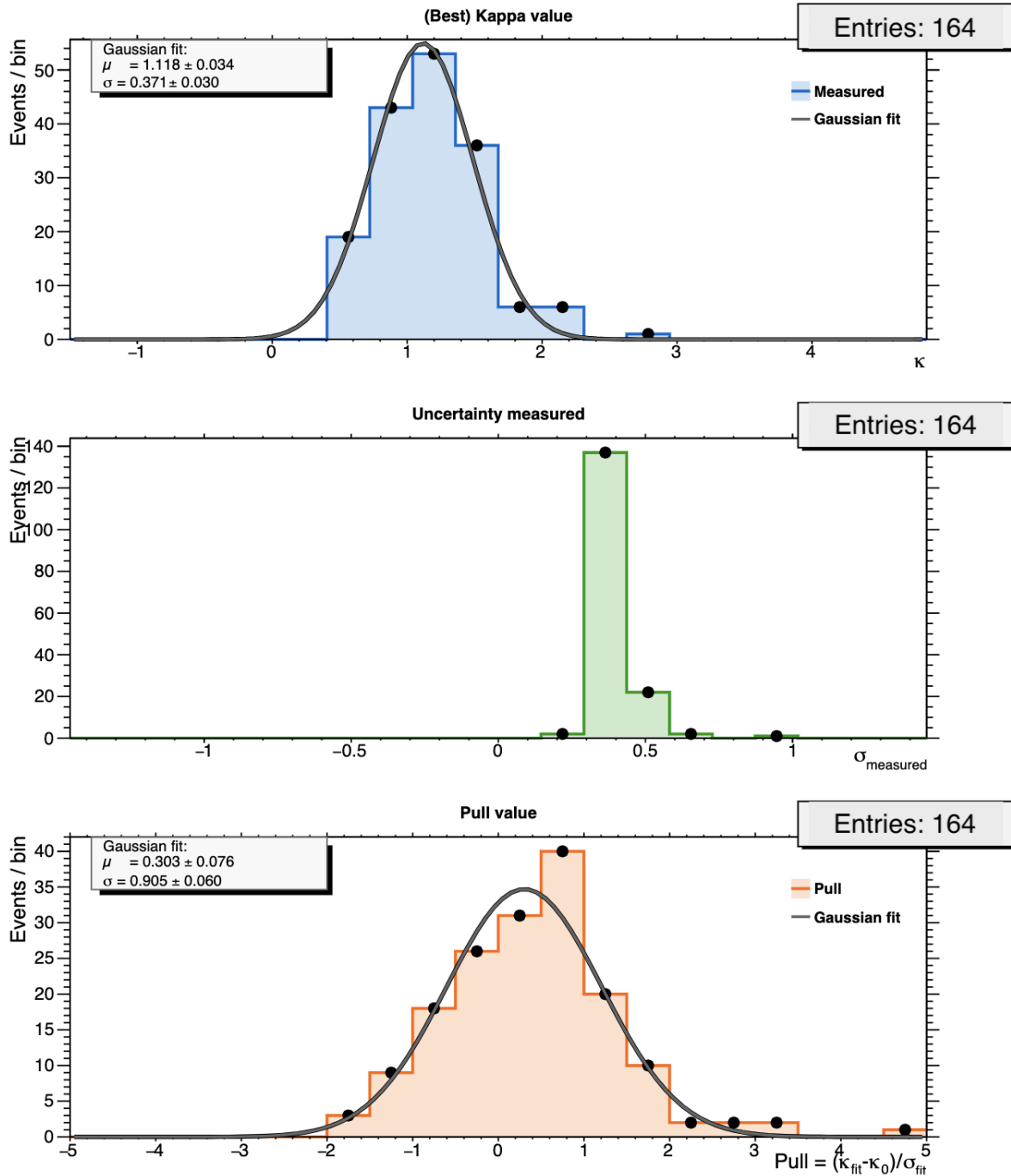


Figure 17.17: Histograms of the performance of the likelihood scans with single-Higgs background included.

Top: distribution of the best-fit coupling parameter $\hat{\kappa}_\lambda$, with Gaussian fit overlaid. **Middle:** distribution of the estimated uncertainty σ_{measured} . **Bottom:** distribution of the pull values, defined as $(\hat{\kappa}_\lambda - \kappa_{\text{true}}) / \sigma_{\text{measured}}$.

Processes	Number events flagged as <i>ill</i> (%)
signal ggF ($\kappa_\lambda = 1.00$)	6.72
singleHiggs	0.066

Table 17.12: Fraction of ‘ill’ events (zero weight for their own hypothesis) removed before the likelihood scan of Figure 17.17.

Figure 17.17 displays the results with a *single-Higgs* background included. A total of 164 pseudo-datasets were analysed.

Best-fit estimator. The Gaussian fit gives $\kappa_{\text{mean}} = 1.184 \pm 0.059$ and $\sigma_\kappa = 0.489 \pm 0.053$.

Estimated uncertainty. The error distribution peaks at $\sigma_{\text{fit}} \simeq 0.49$, consistent with the fitted width.

Pull distribution. The pull mean is 0.384 ± 0.133 and the width $\sigma_{\text{pull}} = 1.104 \pm 0.127$, indicating well-calibrated uncertainties.

17.3.5 [ATLAS fullsim] including all three main backgrounds

An example of a likelihood scan profile for a sample of all processes combined together (for ATLAS simulated n-tuples), using MEM@NLO is provided in Figure 17.18.

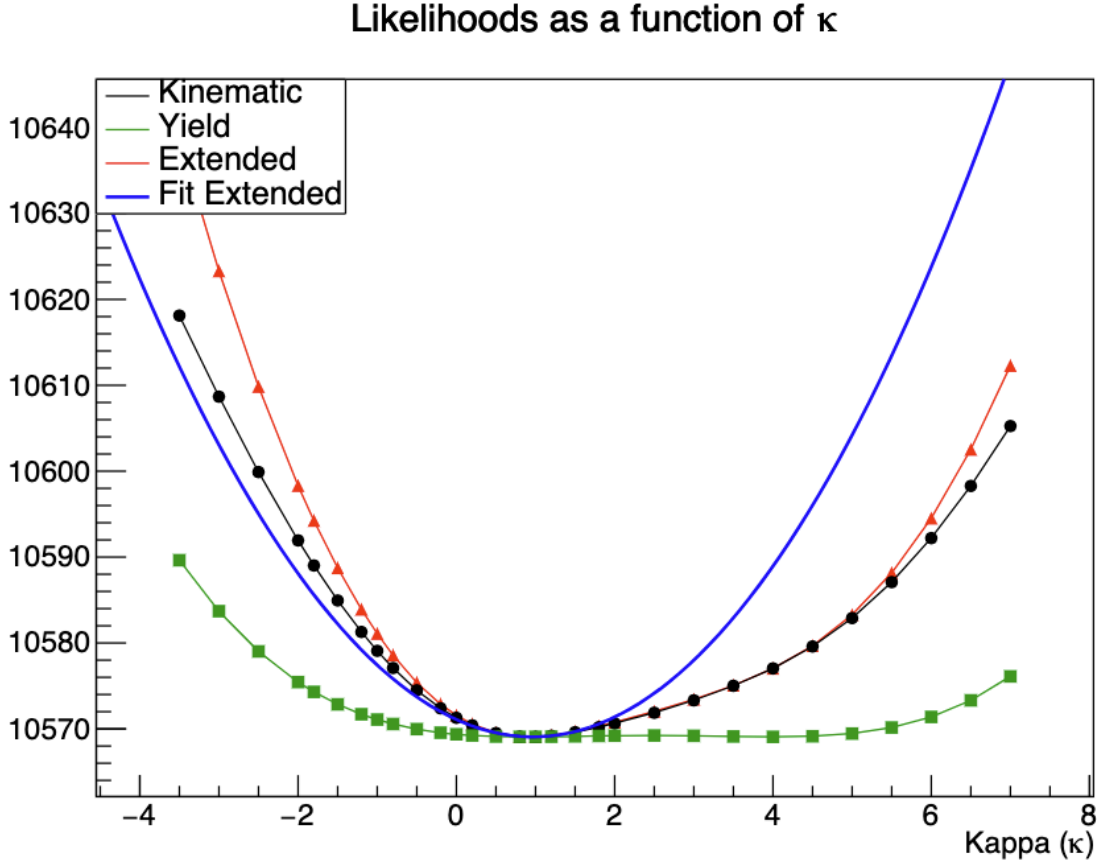


Figure 17.18: Example likelihood scan for one pseudo-dataset consisting of a combination of ATLAS simulated n-tuples signal events ($\kappa_\lambda = 1.00$) and backgrounds, analysed under MEM@NLO.

The graph shows $-\log \mathcal{L}$ as a function of the coupling modifier κ_λ for multiple likelihoods:

Black: kinematic component only (\mathcal{L}_{Kin}). **Green:** yield term ($\mathcal{L}_{\text{yield}}$). **Red:** extended likelihood (\mathcal{L}_{ext}). **Blue:** quadratic fit to $-\log \mathcal{L}_{\text{ext}}$ used to extract the best-fit value and its statistical uncertainty.

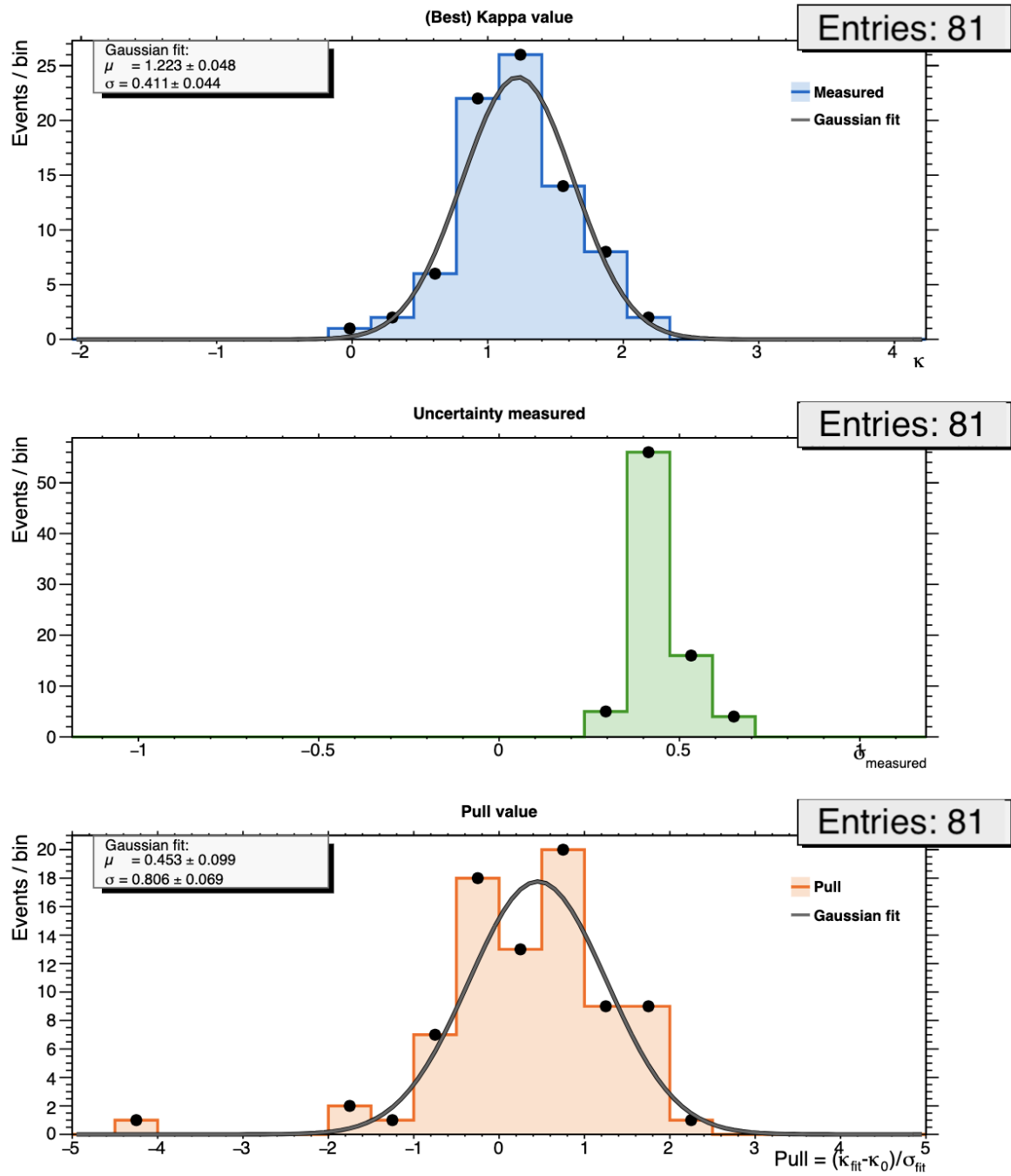


Figure 17.19: Histograms of the performance of the likelihood scans for all background sample combined together (with the signal).

Top: distribution of the best-fit coupling parameter $\hat{\kappa}_\lambda$, with Gaussian fit overlaid. **Middle:** distribution of the estimated uncertainty σ_{measured} . **Bottom:** distribution of the pull values, defined as $(\hat{\kappa}_\lambda - \kappa_{\text{true}}) / \sigma_{\text{measured}}$.

Processes	Number events flagged as <i>ill</i> (%)
signal ggF ($\kappa_\lambda = 1.00$)	6.72
$t\bar{t}H$	2.42
QCD background	0.011
singleHiggs	0.066

Table 17.13: Fraction of ‘ill’ events (zero weight for their own hypothesis) removed before the likelihood scan of Figure 17.19.

Figure 17.19 presents the MEM@NLO likelihood-scan results for the *combined* ATLAS background sample, which merges the $t\bar{t}H$, single-Higgs, and QCD contributions. A total of 83 pseudo-datasets were analysed.

Best-fit estimator. The upper panel shows the distribution of $\hat{\kappa}_\lambda$; a Gaussian fit yields $\kappa_{\text{mean}} = 1.102 \pm 0.047$ with $\sigma_\kappa = 0.372 \pm 0.059$.

Estimated uncertainty. The middle panel peaks at $\sigma_{\text{fit}} \simeq 0.45$, in good agreement with the fitted width.

Pull distribution. The pull mean is 0.206 ± 0.097 , consistent with zero, and the width $\sigma_{\text{pull}} = 0.827 \pm 0.083$ suggests the uncertainties are slightly conservative but well under control.

17.4 Summary and Interpretation for the MEM@NLO

In this section, we present and interpret the final results obtained with the MEM@NLO formalism we developed during this thesis, both for the NLO-ISR Monte Carlo samples we produced, and for the official ATLAS full-simulation n -tuples.

17.4.1 For the Monte Carlo NLO ISR generated events

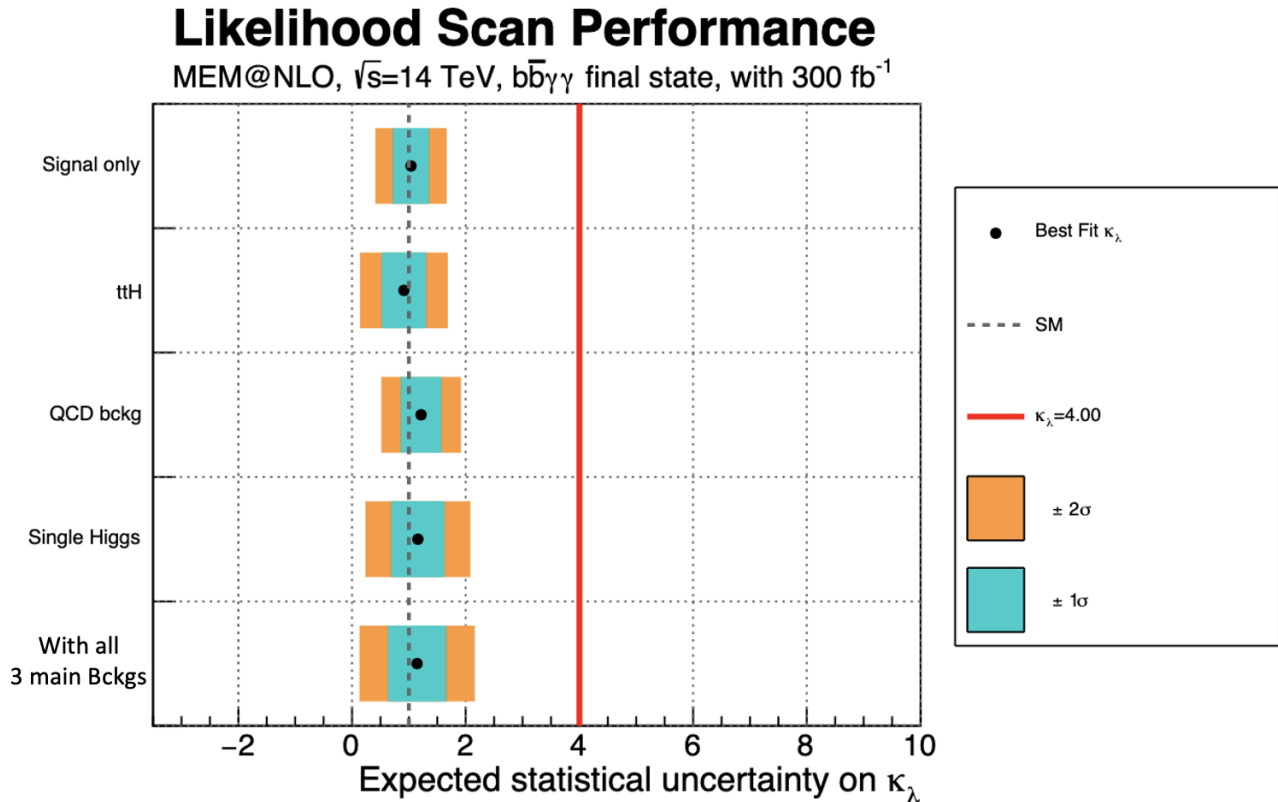


Figure 17.20: Summary of the MEM@NLO profile likelihood performance for the $b\bar{b}\gamma\gamma$ final state at $\sqrt{s} = 14\text{ TeV}$ for an integrated luminosity of 300 fb^{-1} .

For each pseudo-datasets ensemble the black dot marks the measured Higgs self-coupling modifier κ_λ , while the dashed grey line indicates the SM value ($\kappa_\lambda = 1.00$). The turquoise (orange) regions give the $\pm 1\sigma$ ($\pm 2\sigma$) expected bands obtained from toy fluctuations.

Figure 17.20 and Table 17.14 show how the new MEM@NLO performs on NLO ISR Monte Carlo generated events.

For the sample that contains only signal events the method returns $\kappa_{\text{mean}} = 1.04 \pm 0.01$ with a pull width essentially equal to one, confirming that the statistical error is correct.

When each background is added individually, the fit becomes less precise (as expected), but remains well-behaved: the bias on κ_{mean} stays below 0.4 and the pull width never drifts far from the ideal value, even for the challenging $t\bar{t}H$ background.

The key result of this analysis is the one which **combines all** of the three main backgrounds simultaneously. The MEM@NLO finds:

$$\kappa_{\text{mean}} = 1.14 \pm 0.07 \quad \text{with a pull width of } \omega_{\text{mean}} = 1.01.$$

The pull width is consistent with unity, and the fit recovers the injected value $\kappa_\lambda = 1.00$ with high precision. Taken together, these results show that the MEM@NLO retains its high accuracy and provides well-calibrated uncertainties even in the presence of the full, realistic (but still ISR) background mixture.

Finally, these results show no overlay with the *mirror* solution $\kappa_\lambda = 4.00$, associated to $\kappa_\lambda = 1.00$ (as discussed in Section 15.5.2).

Our Matrix Element Method at NLO **effectively removes this mirror pair ambiguity** by using the full kinematic information available, and delivers a single, well-defined value for the Higgs self-coupling (or rather κ_λ , defined as the ratio of its measurement over the SM prediction).

Process	Best fit		Measured uncertainty	Pull distribution	
	κ_{mean}	σ_κ		ω_{mean}	σ_{pull}
Signal only	1.037 ± 0.012	0.309 ± 0.008	0.302 ± 0.030	0.123 ± 0.039	1.020 ± 0.026
$t\bar{t}H$	0.913 ± 0.042	0.441 ± 0.026	0.381 ± 0.087	-0.391 ± 0.113	1.422 ± 0.092
QCD ($b\bar{b}\gamma\gamma$)	1.215 ± 0.040	0.354 ± 0.027	0.345 ± 0.030	0.555 ± 0.126	1.023 ± 0.103
Single Higgs	1.158 ± 0.039	0.478 ± 0.030	0.418 ± 0.088	0.296 ± 0.085	1.044 ± 0.058
All bckg	1.144 ± 0.066	0.502 ± 0.048	0.485 ± 0.142	-0.185 ± 0.121	1.013 ± 0.096

Table 17.14: Summary of likelihood-scan performance for each process for NLO ISR generated events analysed using MEM@NLO.

The best-fit entries list the Gaussian mean (κ_{mean}) and width (σ_κ) of the blue histogram at the top. The measured uncertainty is the mean of the green histogram in the middle panel, while the pull parameters are taken from the Gaussian fit to the bottom panel.

17.4.2 For the ATLAS fully simulated events

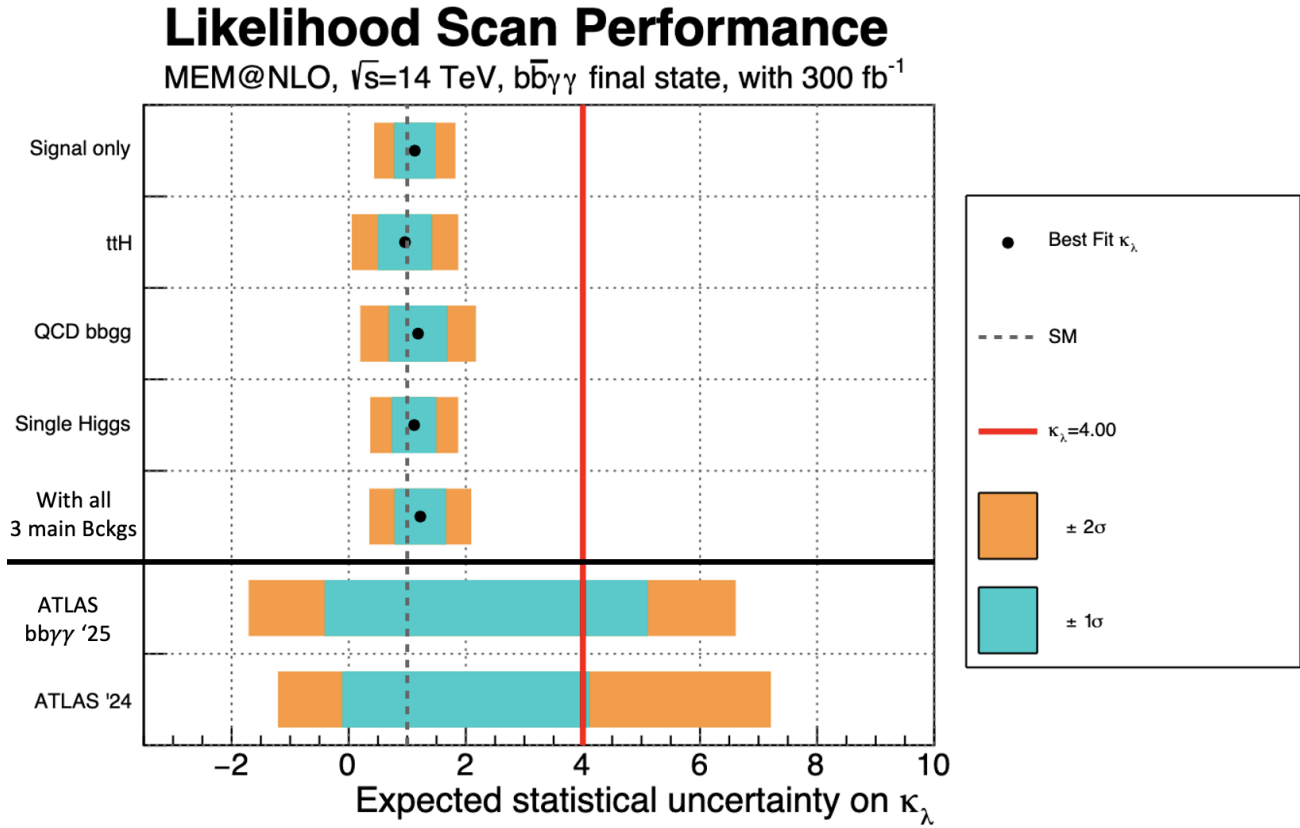


Figure 17.21: Summary of the MEM@NLO profile likelihood performance for the $b\bar{b}\gamma\gamma$ final state at $\sqrt{s} = 14$ TeV for an integrated luminosity of 300 fb $^{-1}$. We use the same convention as from Figure 17.20.

Public ATLAS limits are shown for indication context only, where ‘ATLAS bbyy ’25’ refers to Ref. [66] and ‘ATLAS ’24’ refers to Ref. [64].

Figure 17.21 and Table 17.15 give an overview of the results obtained using the official ATLAS fully simulated $b\bar{b}\gamma\gamma$ n-tuples. Apart from knowing the name of the different files (and the κ_λ value used at generation for the signal sample), no extra information has been required to perform this analysis with our MEM@NLO implementation.

Even in this blind setting, the MEM@NLO recovers the injected coupling with striking accuracy.

For the signal-only file the fit returns $\kappa_{\text{mean}} = 1.13 \pm 0.01$ and a pull width of 1.03, proof that the statistical error is correctly estimated and validating our implementation here again.

When each background is added one at a time, the bias stays below ~ 0.2 and the pull width remains within 30 % of the ideal value. This shows that the method is robust against realistic jet activity and detector effects. Another important result is that none of the scans shows a secondary minimum at $\kappa_\lambda = 4.0$: the detailed kinematic information in the MEM eliminates the **mirror** solution.

The most relevant result is the global fit including the signal **combined together with all** main background using ATLAS fully simulated events. Yet even with this very realistic environment, the MEM@NLO finds:

$$\kappa_{\text{mean}} = \mathbf{1.223 \pm 0.411} \quad \text{with a width of } \omega = \mathbf{0.806}.$$

The fit recovers the injected value $\kappa_\lambda = 1.00$ to well within its statistical uncertainty, demonstrating great accuracy in a fully realistic setting.

Such precision, achieved with a single final state and without any information about the events, highlights the strength of our new MEM@NLO formalism for extracting the Higgs self-coupling value in fully simulated ATLAS data.

Further studies should be carried out with a larger event samples to boost statistical precision and tighten the uncertainties on these parameters. Also, the inclusion and proper propagation of systematic uncertainties should be investigated to assess their impact on the final measurement.

The official ATLAS analysis results on κ_λ have been included in Figure 17.21 solely to provide context on the results we obtained on ATLAS full-simulation samples using our MEM@NLO framework. They are shown only as a reference to the current experimental state of the art, not as a point of comparison, since the official analyses are based on real data and include a full treatment of systematic uncertainties.

When placed alongside the most recent inclusive and channel-specific results from ATLAS and CMS Run-2 combination, which currently constrain κ_λ to approximately $-1.2 < \kappa_\lambda < 7.2$ and $-1.4 < \kappa_\lambda < 7.0$ (at 95 % CL, *cf.* Section 6.1), our method achieves a level of precision that is highly competitive with the state of the art.

It is also relatively tighter than the ATLAS Collaboration latest result specific to the $HH \rightarrow b\bar{b}\gamma\gamma$ channel, which constrains κ_λ within the range $[-1.4, 6.8]$ (at 95 % CL, *cf.* Section 6.2).

Process	Best fit		Measured uncertainty	Pull distribution	
	κ_{mean}	σ_κ		ω_{mean}	σ_{pull}
Signal only	1.128 ± 0.013	0.342 ± 0.011	0.307 ± 0.031	0.355 ± 0.040	1.029 ± 0.029
$t\bar{t}H$	0.961 ± 0.040	0.450 ± 0.031	0.383 ± 0.068	-0.211 ± 0.100	1.293 ± 0.079
QCD ($b\bar{b}\gamma\gamma$)	1.184 ± 0.059	0.489 ± 0.053	0.401 ± 0.076	0.384 ± 0.133	1.104 ± 0.127
Single Higgs	1.118 ± 0.034	0.371 ± 0.030	0.386 ± 0.071	0.303 ± 0.076	0.905 ± 0.060
All bckg	1.223 ± 0.048	0.411 ± 0.044	0.443 ± 0.068	0.453 ± 0.099	0.806 ± 0.069

Table 17.15: Summary of likelihood-scan performance for ATLAS simulated $b\bar{b}\gamma\gamma$ samples analysed with MEM@NLO. We use the same convention as from Table 17.20.

Conclusion

The measurement of the Higgs boson trilinear self-coupling λ_{3H} remains one of the most powerful tests of electroweak symmetry breaking.

In this thesis, we tightened the (still) wide limits on the scale factor κ_λ using the first Next-to-Leading Order Matrix Element Method (MEM@NLO), newly developed in the context of the $gg \rightarrow HH \rightarrow b\bar{b}\gamma\gamma$ channel.

The new framework incorporates an analytic NLO matrix element with full top-mass dependence, an IR-safe real emission treatment, and an automated "MEM factory" designed to produce MEM output in high quantity and quality.

Interfaced with a modified version of the MOMEMTA software, the method was validated against NLO Monte-Carlo samples and ATLAS $b\bar{b}\gamma\gamma$ fullsim n -tuples. The MEM@NLO delivers:

- $\kappa_\lambda = 1.14$ with an associated uncertainty $\sigma_\kappa = 0.50$ on NLO ISR samples;
- $\kappa_\lambda = 1.22$ with an associated uncertainty $\sigma_\kappa = 0.41$ on fully simulated ATLAS events.

Another major achievement of this method is the **removal of the mirror solution** near $\kappa_\lambda = 4.0$.

This long-standing degeneracy, often unresolved by the traditional approaches used in official analysis, is effectively lifted by the use of the full kinematic information available within the MEM@NLO.

The resulting **sharp and unambiguous likelihoods** obtained in this work demonstrate the strong capability of the method to constrain the Higgs self-coupling with high precision.

These results establish the MEM@NLO as a competitive strategy for a more precise determination of the Higgs self-coupling λ_{3H} .

Although this work has focused on simulated data, the developed framework is fully operational for Run-3 conditions and could be readily integrated into the ATLAS di-Higgs combination analyses.

Looking ahead, the new MEM@NLO formalism has been designed with sufficient generality to be naturally extended to other final states (*e.g.* $b\bar{b}\tau^+\tau^-$ or $b\bar{b}b\bar{b}$) and to SMEFT interpretations performed at full NLO accuracy.

Thanks to its modular and general design, this new implementation presented in this thesis can serve as a template for rare-process studies, paving the way toward precision Higgs measurements at the LHC and into the HL-LHC era.

Part VI

Appendices

A Dimension of the Matrix Element Method Likelihood Integral

A.1 General setting

In this Appendix, we will derive the formula to count the degrees of freedom, depending on which process is used by the Matrix Element Method.

It corresponds to the dimension of integral in Eq. 8.5 for a hadron-hadron collision, producing a final state with N on-shell particles $\{p_i\}_{i=1}^N$, and two incoming partons carrying the pair of Bjorken momentum fractions (x_1, x_2) .

Before imposing any constraint, the phase-space therefore contains $4N + 2$ *degrees of freedom* (as the Bjorken variables only contribute to one each).

Delta functions δ The exact partonic phase space includes delta functions enforcing energy-momentum conservation. Schematically, the N -body phase space reads

$$d\Phi_N = \delta^{(4)}\left(x_1 P_1 + x_2 P_2 - \sum_{i=1}^N p_i\right) dx_1 dx_2 \prod_{i=1}^N d^4 p_i, \quad (.1)$$

The $\delta^{(4)}$ functions removes *four* degrees of freedom,

Mass conservation Fixing the mass of the particles also allow us to reduce the dimension by N .

Transfer functions W The MEM also uses *transfer functions* W (TFs), that encode the probability to observe a reconstructed object given a parton-level four-vector. When a TF is set as a Dirac delta, the corresponding variable is *not integrated* and

the overall dimensionality is reduced by one. It is common to use Dirac delta TF for the angular variables θ (or η) and ϕ for the **visible particles**.

Permutations Depeding on the process, permutations can be needed for the final state partons. They artificially increases the number of degree of freedom inside the main integral by one for each. We will denote the number of permutations as N_{perm} . As an example, one can think of the $t\bar{t}H$ process in the $b\bar{b}\gamma\gamma$ channel, for which we need to add a permutation on the b-jets.

Invisible particles and additional constraints Invisible particles (e.g. neutrinos, or gluons) contribute with *three* extra degrees of freedom each (by counting out the one on-shell constraint).

If none of their kinematic components is constrained by external information, they remain part of the integration.

Extra radiation from Next-to-Leading Order contributions inside the MEM are considered invisible particles.

Additionally, any other constraint like narrow-width approximations (NWA) applied to intermediate resonances, or mass-shell constraints on composite systems, reduces the dimensionality by one.

A.2 Step-by-step illustration

For pedagogical clarity, the counting can be summarized step by step in Figure 22. Starting from all four-momenta of the N final-state particles and Bjorken momentum fractions (x_1, x_2) .

We will decompose $N = N_{\text{vis}} + N_{\text{inv}}$, to distinguish between visible and invisible final state particles.

Following the procedure illustrated in Figure 22, the remaining number of degrees of freedom in the MEM integral can be expressed as:

$$\text{DoF} = 3N - 2N_{\text{vis}} + N_{\text{perm}} - 2 \quad \text{or equivalently} \quad \text{DoF} = 3N_{\text{inv}} + N_{\text{vis}} + N_{\text{perm}} - 2, \quad (.2)$$

A.3 Remarks on practical parameterizations

The choice of integration variables is not unique (cf. Table 14.2 for ours). It is often advantageous to parameterize the remaining degrees of freedom in variables with weak correlations and smooth transfer functions, e.g. using either Cartesian (p_x, p_y, p_z) or “detector-friendly” (p_T, ϕ, E) coordinates for the unconstrained three-momenta.

$$\begin{array}{l}
 4N + 2 \\
 \downarrow -4 \text{ from } \delta \text{ functions} \\
 4N - 2 \\
 \downarrow -N \text{ from the known mass values} \\
 3N - 2 \\
 \downarrow -N_{\text{vis}} \text{ from the TF on } \Theta_{\text{vis}} \\
 3N - N_{\text{vis}} - 2 \\
 \downarrow -N_{\text{vis}} \text{ from the TF on } \varphi_{\text{vis}} \\
 3N - 2N_{\text{vis}} - 2 \\
 \downarrow + N_{\text{perm}} \text{ from additional permutations} \\
 \left\{ \begin{array}{l} 3N - 2N_{\text{vis}} + N_{\text{perm}} - 2 \\ \text{or} \\ 3N_{\text{inv}} + N_{\text{vis}} + N_{\text{perm}} - 2 \end{array} \right.
 \end{array}$$

Figure 22: Step-by-step illustration for the counting of the dimension of the MEM Likelihood integral, written by hand.

B Follow-up on the validation of the Higgs decay

This Appendix provides more validation plots for the Section 15.1.2.

Deriving the parton level polar angle θ^* density Let $\theta^* \in [0, \pi]$ be a random variable and $f(\theta^*)$ its probability-density function (pdf):

$$\int_0^\pi f(\theta^*) d\theta^* = 1.$$

Introduce the change of variable

$$u = \cos \theta^*, \quad u \in [-1, 1],$$

and denote by $g(u)$ the pdf of u . By definition,

$$\int_{-1}^1 g(u) du = 1,$$

and, at the infinitesimal level,

$$f(\theta^*) d\theta^* = g(u) du.$$

Let's assume that u is *uniformly distributed* on $[-1, 1]$ by looking at Figure 15.4, at first approximation:

$$g(u) = c, \quad c = \frac{1}{2},$$

and note that $|du| = \sin \theta^* d\theta^*$. Hence

$$f(\theta^*) = g(u) \frac{|du|}{d\theta^*} = \frac{1}{2} \sin \theta^*.$$

The factor $1/2$ guarantees normalisation, $\int_0^\pi \frac{1}{2} \sin \theta^* d\theta^* = 1$.

Figure. 23 provides a visual confirmation about the choice of distribution of the θ^* variable using a (normalized) sine function.

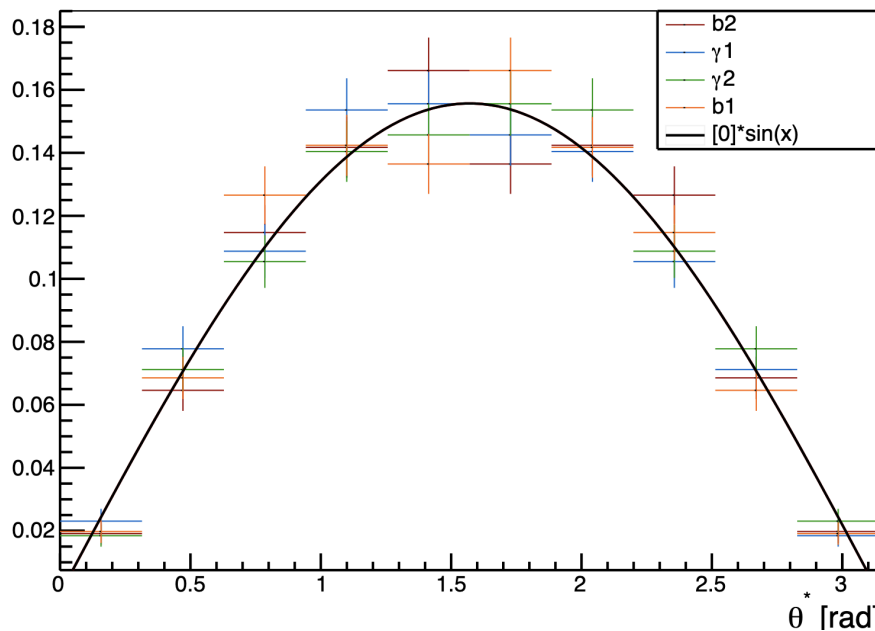


Figure 23: Validity of the θ^* distribution using a sine function fit.

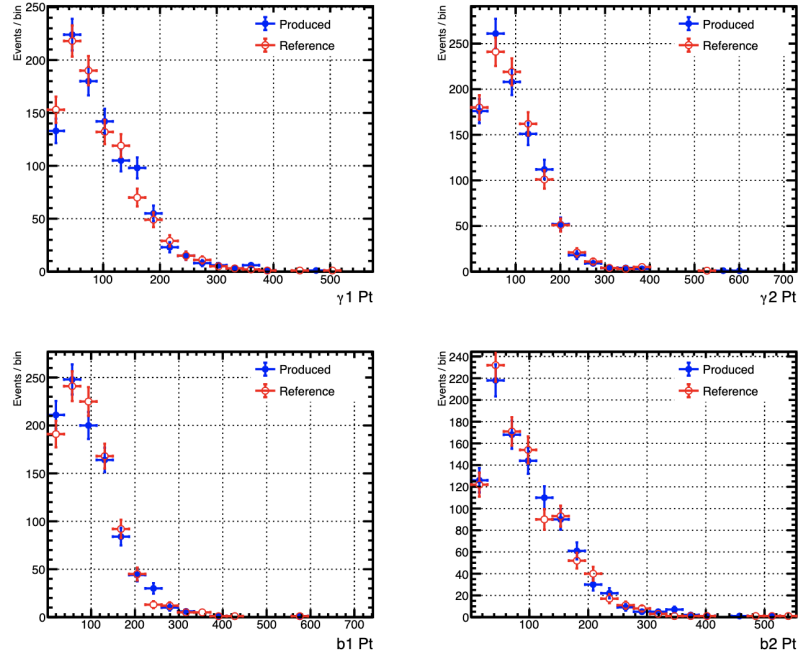


Figure 24: Comparison of the transverse momentum p_T distributions for the four decay products of the Higgs boson in the $b\bar{b}\gamma\gamma$ final state. Blue markers represent events produced with the modified POWHEG-BOX-V2 implementation, while red markers denote the reference sample.

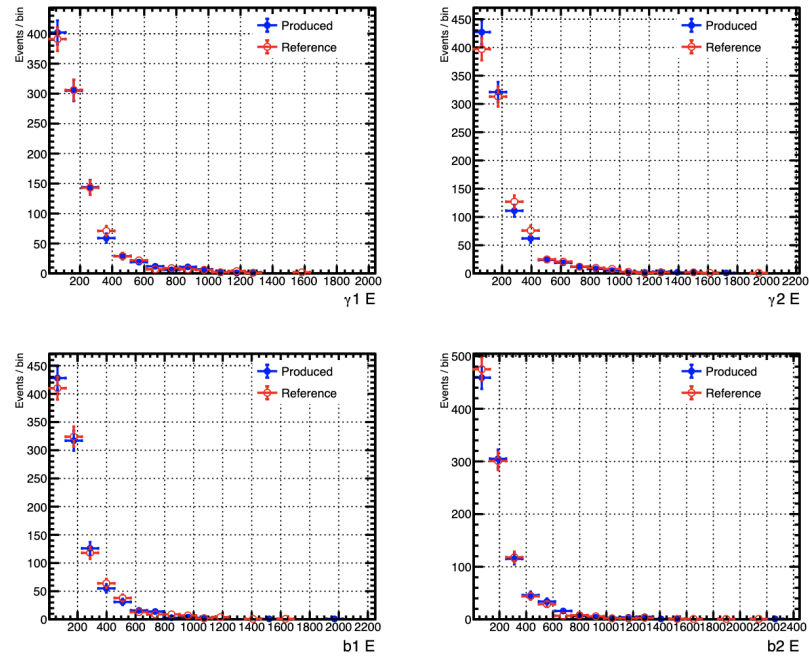


Figure 25: Comparison of the energy E distributions for the four decay products of the Higgs boson in the $b\bar{b}\gamma\gamma$ final state. Same conventions as Figure 24

In addition to the Figure. 15.5 already presented in Section 15.1.2, we add in this Appendix the Figures. 24 and 25 for the comparison for the variables p_T and E respectively.

B.1 Boosted samples

A complementary study is performed by producing *boosted* Monte Carlo samples in order to probe the robustness of the MEM formalism and to test the impact of boosting the kinematic of the reconstructed events (inspired by Ref. [122,125]). The boosting procedure is applied at parton level, and the same smearing and cut prescriptions are used as detailed in Section 15.3.2.

Two distinct strategies have been used, reflecting the intrinsic kinematic properties of the Leading-Order (LO) and Next-to-Leading-Order (NLO).

LO boosted dataset production The $b\bar{b}\gamma\gamma$ system at LO is by construction produced strictly at rest in the transverse plane $\vec{p}_T^{H\bar{H}} = 0$.

We can boost the $b\bar{b}\gamma\gamma$ final state particles, to emulate the recoil expected from QCD radiation. The boost rapidities are defined through the velocity components β_x and β_y , drawn independently from a uniform distribution in the range $[-0.08, 0.08]$.

NLO boosted dataset production The NLO additional real radiation induces a genuine recoil in the transverse plane, leading to a non-vanishing \vec{p}_T for the $b\bar{b}\gamma\gamma$ system.

In this case, a transverse boost is performed as a correction to the recoil so that the resulting $b\bar{b}\gamma\gamma$ system is *exactly* at rest in the p_T plane.

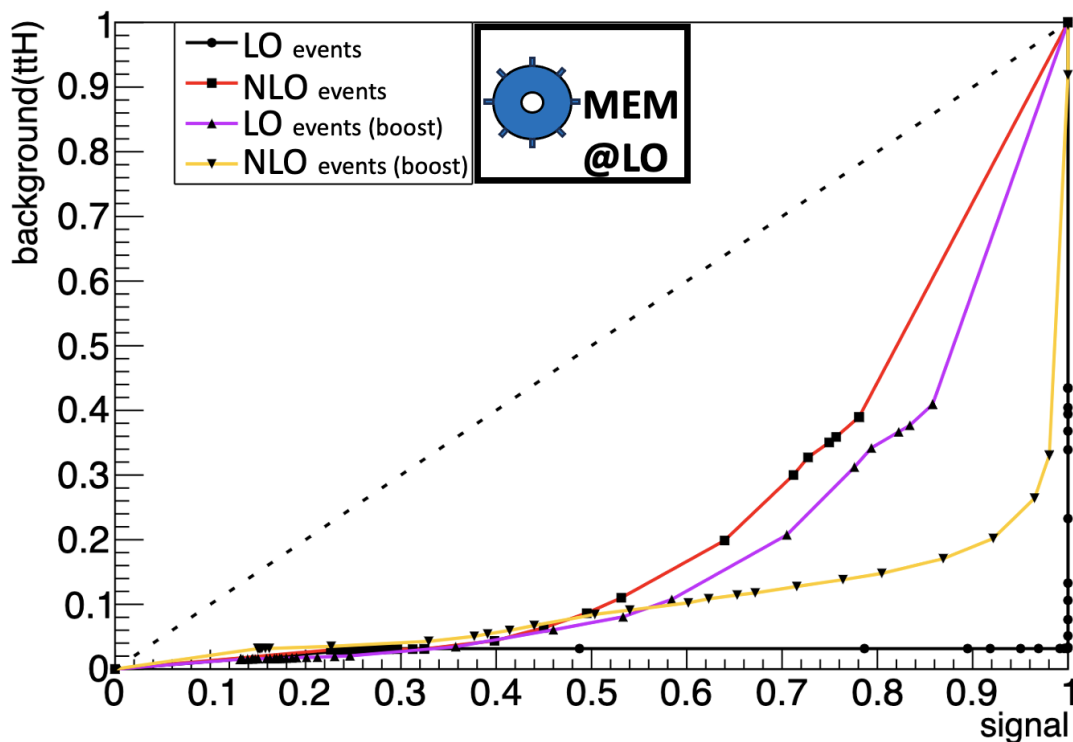


Figure 26: ROC curve obtained with MEM@LO against the ttH background to see the impact of boosted kinematic events.

[$t\bar{t}H$ Background]	AUC (%)	signal rejected (%)	% background rejected (%)
LO classic (black)	2.73	0	8.13
LO Boosted (purple)	18.82	3.39	4.73
NLO_ISR classic (red)	22.98	12.78	13.77
NLO_ISR Boosted (yellow)	10.12	0	0

Table 16: Table for the values of interest hidden in Fig. 26. The MEM integration algorithm is (DIVONNE).

Are indicated in this table: the area under the curve (AUC) (in %); the number of signal events that have zero weights values for **both** hypothesis at the same time (in %); and the number of background events that have zero weights values for **both** hypothesis at the same time (in %).

ROC curve of boosted NLO events with MEM@LO We observe in Figure 26 that boosting the NLO generated files (orange curve) in the $b\bar{b}\gamma\gamma$ system transverse momenta rest frame artificially increase the discrimination power from the MEM output **ratios** (by decreasing the AUC).

We also see that boosting the LO generated files **out of** the $b\bar{b}\gamma\gamma$ system rest frame (in yellow) completely *washes out* the kinematic information that was accessible before the boost. Their discriminated by the MEM@LO is very similar of those of the regular NLO generated events (in red).

Likelihood scans of boosted NLO events with MEM@LO The study of likelihood scans in Figure 28 and Figure 27 indicate that the boosted NLO files do not allow the measurement of κ_λ using a MEM@LO analysis.

This can seem counter-intuitive, as we have observed a small improvement in the ROC curves. But remember that the ROC curves are defined from **ratios** of MEM outputs, and likelihood scans use the MEM output values as it.

Processes	Number events flagged as ill (%)
signal ggF ($\kappa_\lambda = 1.00$)	0
$t\bar{t}H$ background	327

Table 17: Fraction of "ill" events (zero weight for their own hypothesis) removed before the likelihood scan of Fig. 28.

We can conclude that the measurement of κ_λ from NLO generated events is **not possible** using the MEM@LO, even when boosting into a Leading-Order friendly frame.

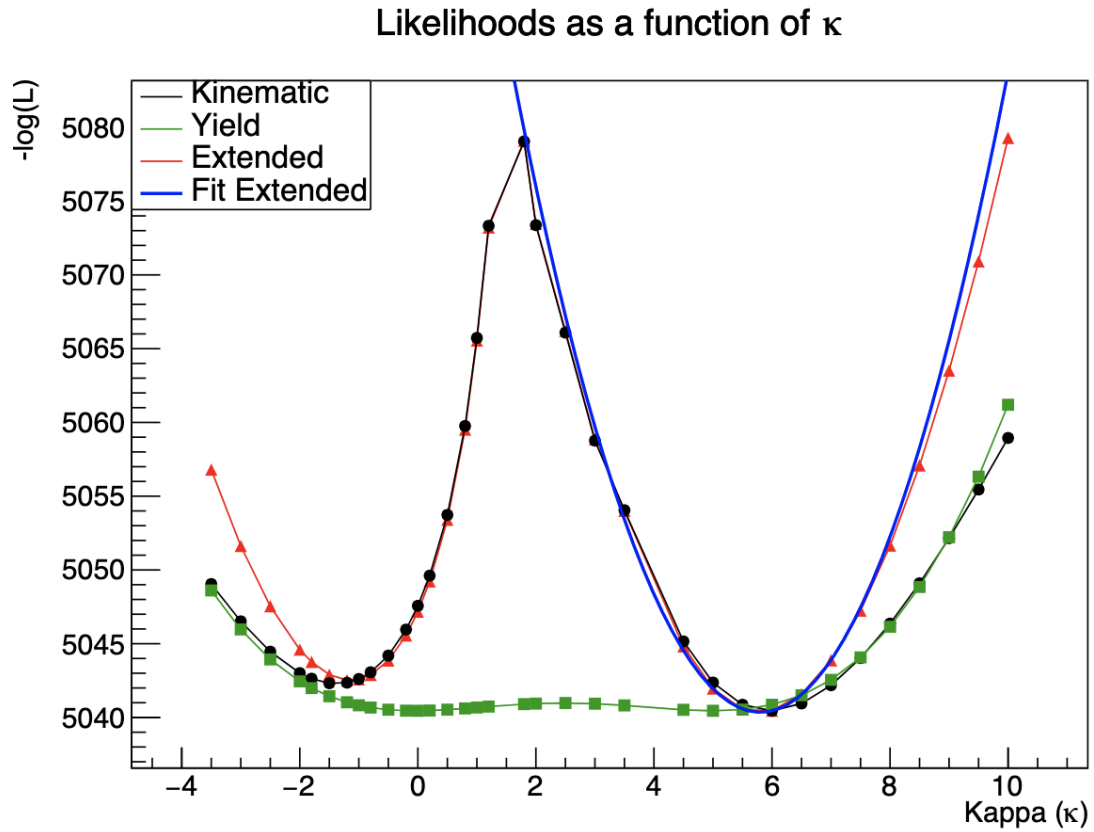


Figure 27: Example likelihood scan for one pseudo-dataset consisting of boosted NLO events ($\kappa_\lambda = 1.00$) analysed under MEM@LO with $t\bar{t}H$ background. The graph shows $-\log \mathcal{L}$ as a function of the coupling modifier κ_λ for multiple likelihoods:

Black: kinematic component only (\mathcal{L}_{Kin}). **Green:** yield term ($\mathcal{L}_{\text{yield}}$). **Red:** extended likelihood (\mathcal{L}_{ext}). **Blue:** quadratic fit to $-\log \mathcal{L}_{\text{ext}}$ used to extract the best-fit value and its statistical uncertainty.

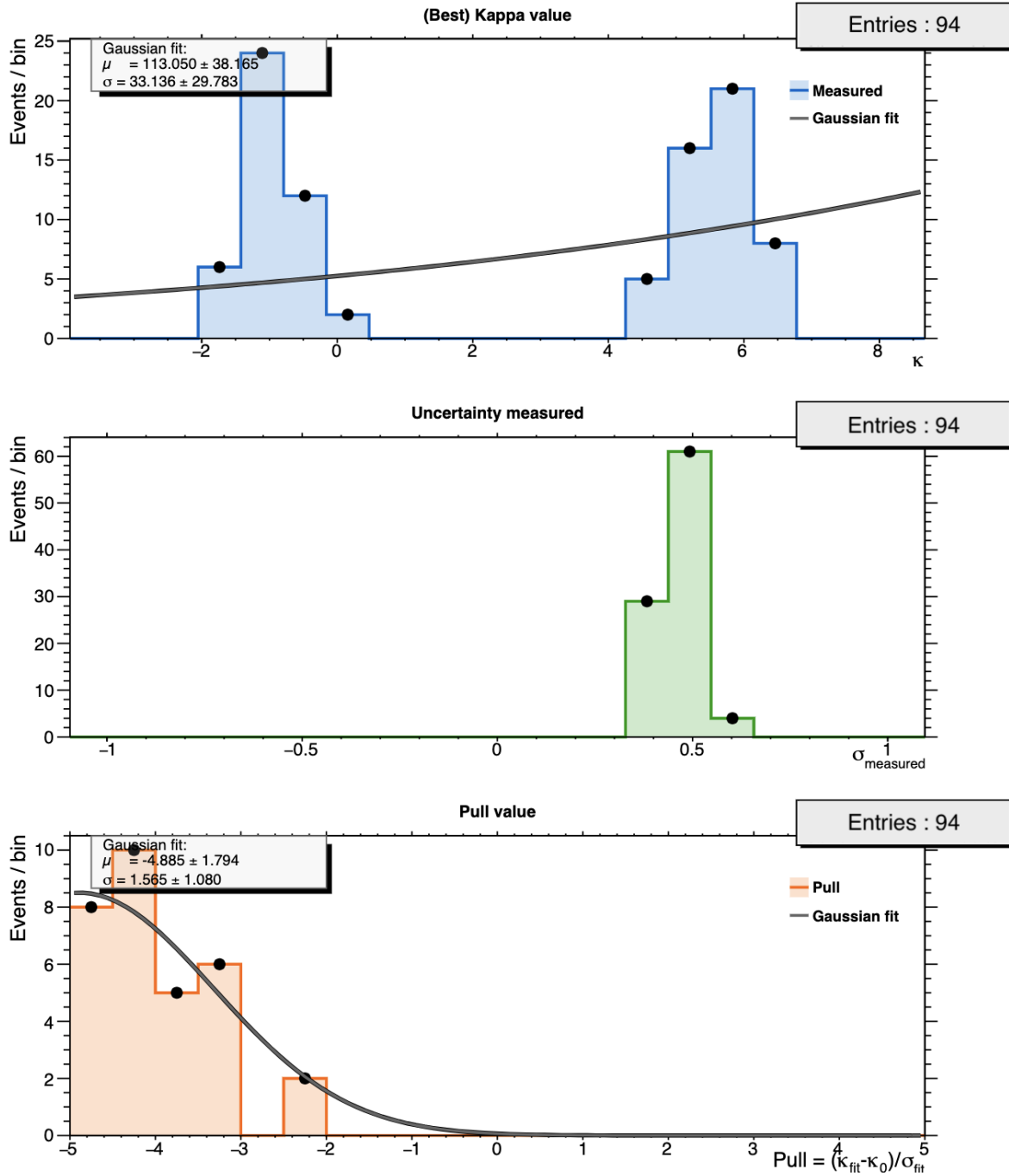


Figure 28: Likelihood scan with $t\bar{t}H$ background included, for boosted NLO events.

B.2 Main Block M

We will discuss the first attempt of a NLO Main Block we tried, that we called Main Block M (cf. Figure 29).

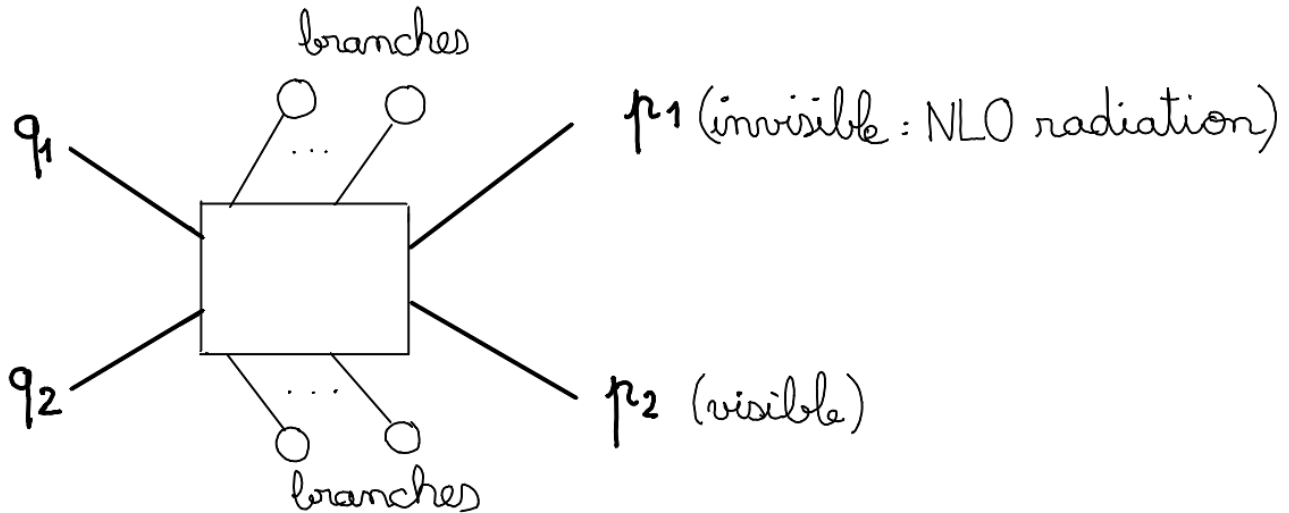


Figure 29: Schematic representation of Block M, following the conventions used by MoMEMTA.

The main idea is to remove all of the degrees of freedom for the undetected real radiation (denoted as p_1). There are different choices possible for the last degrees of freedom to be removed from the conservation equations. One can think about removing one of the Bjorken parameter, as it is a parameter we do not measure directly and most Main Blocks actively try to remove them.

To avoid any unwanted bias, or any asymmetry from choosing one Bjorken to remove over the other, we decided to remove the extra degree of freedom from one of the visible final state particle (denoted as p_2 in Figure 29).

The corresponding transformation of the phase-space reads:

$$dq_1 dq_2 \frac{d^3 \vec{p}_1}{(2\pi)^3 2E_1} \frac{d^3 \vec{p}_2}{(2\pi)^3 2E_2} (2\pi)^4 \delta^{(4)}(I_n - Q_{\text{out}}) \longrightarrow \frac{1}{16\pi^2} \frac{1}{E_1 E_2} dq_1 dq_2 d\Omega_2 d\psi_2 \cdot |\det(J)|$$

where the determinant of the Jacobian $|\det(J)|$ is equal to:

$$|\det(J)| = \frac{|\vec{p}_2|^2 \sin \theta_2 E_1 E_2}{| |\vec{p}_2| - E_2 (p_{1x} \sin \theta_2 \cos \varphi_2 + p_{1y} \sin \theta_2 \sin \varphi_2 + p_{1z} \cos \theta_2) |} \quad (.3)$$

Derivation of the Jacobian Starting from this set of equations:

$$(a) \quad p_{1x} + p_{2x} = -P_x \quad (.4)$$

$$(b) \quad p_{1y} + p_{2y} = -P_y \quad (.5)$$

$$(c) \quad p_{1z} + p_{2z} = (E_{g1} - E_{g2}) - P_{bz} = P_{z,\text{tot}} \quad (.6)$$

$$(d) \quad E_1 + E_2 = (E_{g1} + E_{g2}) - E_{0z} = E_{\text{tot}} \quad (.7)$$

$$(e) \quad E_1^2 - p_{1x}^2 - p_{1y}^2 - p_{1z}^2 = m_1^2 = 0 \quad (.8)$$

$$(f) \quad E_2^2 - |\vec{p}_2|^2 = m_2^2 \quad (.9)$$

One can rewrite the system of equations a,b,c,d with respect to the $p_{1x}, p_{1y}, p_{1z}, |\vec{p}_2|$ with $|\vec{p}_2|$ being the norm of the visible p_2 3-momenta (the degree of freedom chosen for removal).

The new system is:

$$\begin{aligned} p_{1x} + |\vec{p}_2| \sin \theta_2 \cos \varphi_2 &= -P_x \\ p_{1y} + |\vec{p}_2| \sin \theta_2 \sin \varphi_2 &= -P_y \\ p_{1z} + |\vec{p}_2| \cos \theta_2 &= P_{z,\text{tot}} \\ p_{1x}^2 + p_{1y}^2 + p_{1z}^2 + m_2^2 + |\vec{p}_2|^2 &= E_{\text{tot}} \end{aligned}$$

with the associated Jacobian matrix:

$$J^{-1} = \begin{bmatrix} \frac{\partial P_x}{\partial p_{1x}} & \frac{\partial P_x}{\partial p_{1y}} & \frac{\partial P_x}{\partial p_{1z}} & \frac{\partial P_x}{\partial |\vec{p}_2|} \\ \frac{\partial P_y}{\partial p_{1x}} & \frac{\partial P_y}{\partial p_{1y}} & \frac{\partial P_y}{\partial p_{1z}} & \frac{\partial P_y}{\partial |\vec{p}_2|} \\ \frac{\partial P_{z,\text{tot}}}{\partial p_{1x}} & \frac{\partial P_{z,\text{tot}}}{\partial p_{1y}} & \frac{\partial P_{z,\text{tot}}}{\partial p_{1z}} & \frac{\partial P_{z,\text{tot}}}{\partial |\vec{p}_2|} \\ \frac{\partial E_{\text{tot}}}{\partial p_{1x}} & \frac{\partial E_{\text{tot}}}{\partial p_{1y}} & \frac{\partial E_{\text{tot}}}{\partial p_{1z}} & \frac{\partial E_{\text{tot}}}{\partial |\vec{p}_2|} \end{bmatrix} = \begin{bmatrix} 1 & 0 & 0 & \cos \varphi_2 \sin \theta_2 \\ 0 & 1 & 0 & \sin \varphi_2 \sin \theta_2 \\ 0 & 0 & 1 & \cos \theta_2 \\ \frac{p_{1x}}{E_1} & \frac{p_{1y}}{E_1} & \frac{p_{1z}}{E_1} & \frac{|\vec{p}_2|}{E_2} \end{bmatrix}$$

and

$$\begin{aligned} \det(J^{-1}) &= \left| \frac{|\vec{p}_2|}{E_2} \left(\frac{p_{1x} \sin \theta_2 \cos \varphi_2}{E_1} + \frac{p_{1y} \sin \theta_2 \sin \varphi_2}{E_1} + \frac{p_{1z} \cos \theta_2}{E_1} \right) \right| \\ &= \frac{1}{E_1 E_2} |E_1 |\vec{p}_2| - E_2 (p_{1x} \sin \theta_2 \cos \varphi_2 + p_{1y} \sin \theta_2 \sin \varphi_2 + p_{1z} \cos \theta_2)| \end{aligned}$$

$$\Rightarrow \det(J) = E_1 E_2 \cdot \frac{1}{|E_1 |\vec{p}_2| - E_2 (p_{1x} \sin \theta_2 \cos \varphi_2 + p_{1y} \sin \theta_2 \sin \varphi_2 + p_{1z} \cos \theta_2)|}$$

Issue with Main Block M The main issue with this Main Block is the almost systematic failure of integration for most of the events, with the phase-space exploration taking a very long time before failing.

This is very likely due to the use of the Bjorken variables as being bad variables of integration. It might be the reason why most of the official Main Blocks defined in the MOMEMTA software remove them almost every time.

B.3 Improving the Transfer Function for ATLAS Simulation: Application on ATLAS simulated n-tuples

We will present in this Appendix the results obtained after improving the W transfer function in Eq.(8.5) to better account for more realistic samples.

This has been used on the ATLAS simulated n-tuples, which have been generated for the non-resonant $HH \rightarrow b\bar{b}\gamma\gamma$ analysis group.

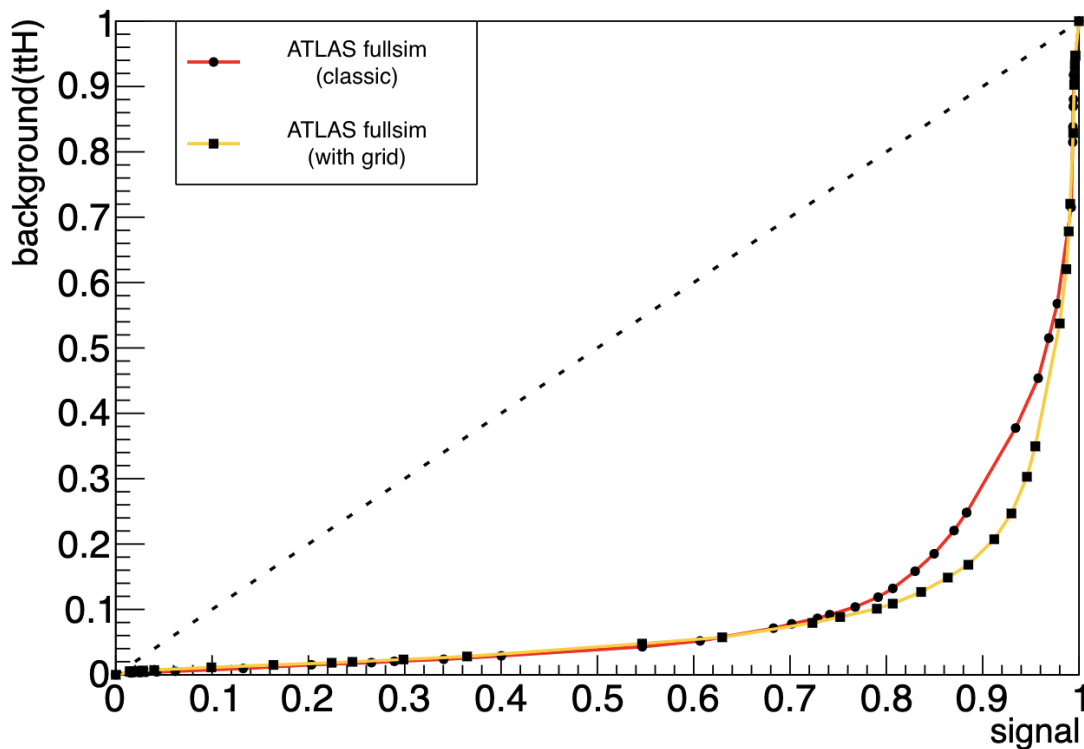


Figure 30: ROC curves of the same ATLAS simulated n-tuples (gluon-fusion signal and $t\bar{t}H$ background under different transfer function W using the MEM@NLO.)

[$t\bar{t}H$ Background]	AUC (%)	signal rejected (%)	% background rejected (%)
ATLAS_SIMU (classic, in red)	9.69	0.31	0.37
ATLAS_SIMU (with grid, in orange)	8.43	0.22	0.37

Table 18: Table for the values of interest hidden in Fig. 30. The MEM integration algorithm is (DIVONNE). Are indicated in this table: the area under the curve (AUC) (in %); the number of signal events that have zero weights values for **both** hypothesis at the same time (in %); and the number of background events that have zero weights values for **both** hypothesis at the same time (in %).

ROC curve The discrimination power of the MEM@NLO on the ATLAS simulated n-tuples slightly increased by using the new grid formalism for the MEM transfer function W , and a slight decrease of the number of weights with zero value for **both** hypothesis (cf. Table 18). There is no significant improvement to report on the discrimination power.

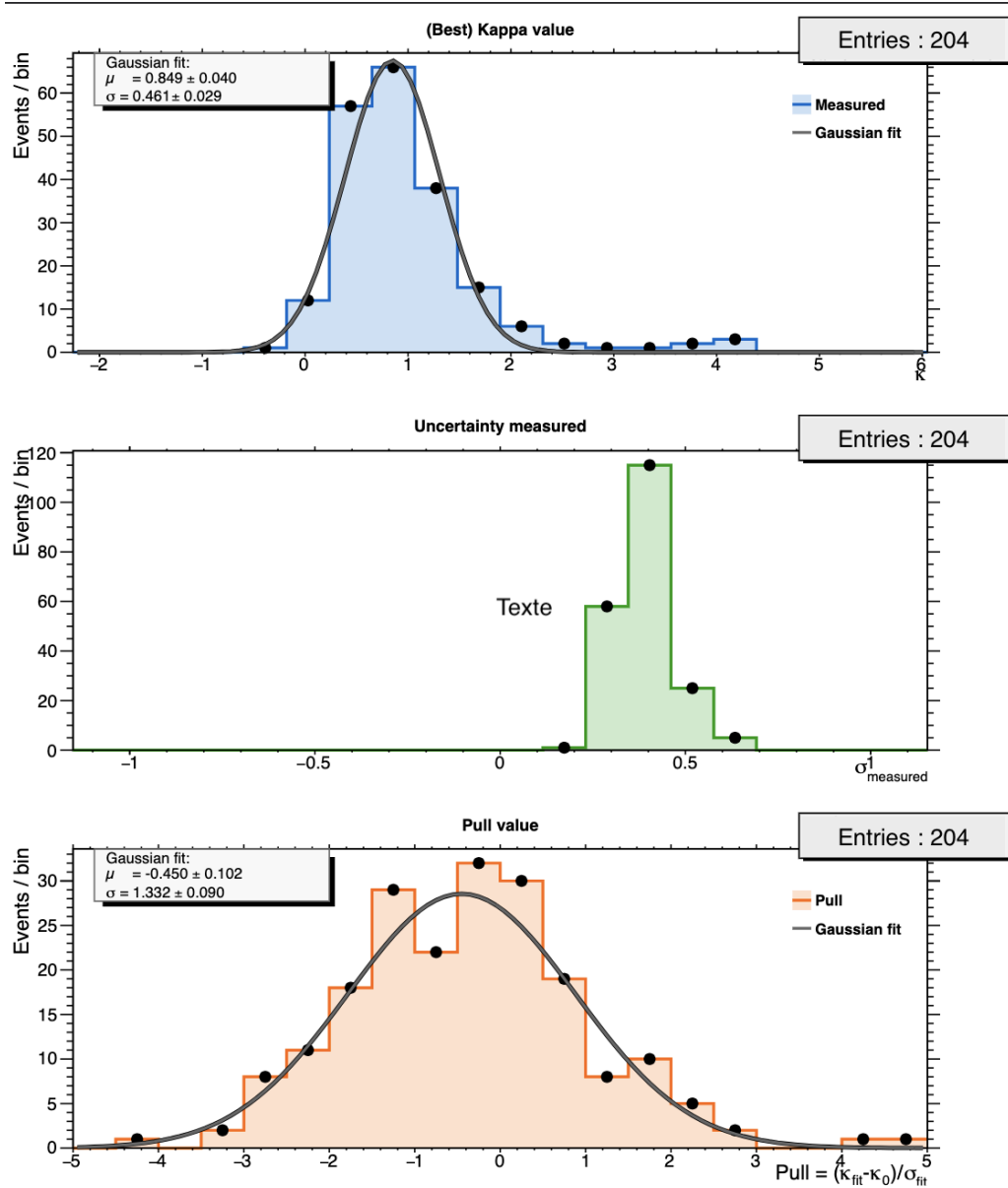


Figure 31: Likelihood scan with $t\bar{t}H$ background included, for NLO events using the MEM@NLO and the grid W transfer function.

Processes	Number events flagged as ill (%)
signal ggF ($\kappa_\lambda = 1.00$)	1.78
$t\bar{t}H$ background	1.44

Table 19: Fraction of "ill" events (zero weight for their own hypothesis) removed before the likelihood scan of Fig. 31.

Likelihood scans The measurement of the κ_λ value by using the new grid formalism for the MEM transfer function W is approximately the same as before with the best-fit value histogram mean at around 0.849 (to be compared to Figure 17.15 without the grid where the mean is around 0.96).

Conclusion No significant improvement has been observed using the new grid implementation on ATLAS simulated n-tuples. A slight decrease in the number of ill-events is still observed.

Any future improvement of the MEM@NLO should start on improving the other ingredients from Eq.(8.5), as the simple version of transfer function W already provides a very good approximation on more realistic data samples (i.e the ATLAS simulated n-tuples).

C Set-up for our work environment at CC-IN2P3

```

module load Compilers/gcc/13.2.0;
module load Analysis/root/6.30.06
module load Production/cmake/3.25.0

#Commande pour MoMEMta (cmake)
export BOOST_INCLUDEDIR=/pbs/software/redhat-9-x86_64/boost/1.79.0/include/
export BOOST_LIBRARYDIR=/pbs/software/redhat-9-x86_64/boost/1.79.0/lib/

#Commandes pour Fortran:
module load Programming_Languages/python/3.9.1
export CXX=/pbs/software/redhat-9-x86_64/gcc/13.2.0/bin/g++
export CC=/pbs/software/redhat-9-x86_64/gcc/13.2.0/bin/gcc
export FC=/pbs/software/redhat-9-x86_64/gcc/13.2.0/bin/gfortran

export LD_LIBRARY_PATH=/pbs/software/redhat-9-x86_64/gcc/13.2.0/lib64:
    $LD_LIBRARY_PATH

#module load Programming_Languages/python/2.7.18 #python3 is not supported
#    by MadGraph

export PATH=/sps/l2it/mtartari/pythia8235/bin:$PATH
export PATH=/sps/l2it/mtartari/fastjet-3.4.0/Build/bin:$PATH
export PATH=/sps/l2it/mtartari/LHAPDF-6.4.0/build_test/bin:$PATH
export LD_LIBRARY_PATH=/sps/l2it/mtartari/LHAPDF-6.4.0/build_test/lib:
    $LD_LIBRARY_PATH
export LD_LIBRARY_PATH=/sps/l2it/mtartari/HepMC-2.06.11/hepmc2-install/lib:
    $LD_LIBRARY_PATH

#Probleme avec nouvelle version POWHEG/ggHH (14 Novembre 2023)
export PYTHONPATH=/sps/l2it/mtartari/LHAPDF-6.4.0/build_test/lib/python3.9/
    site-packages:$PYTHONPATH #(to solve issue with import lhapdf)

echo "*****"
echo -e "\033[0;34m[INFO]\033[0mConfiguration de l'environnement avec ccenv
    :"
echo -e "\033[0;34m[INFO]\033[0m----- gcc: 13.2.0 ;"
echo -e "\033[0;34m[INFO]\033[0m----- cmake: 3.25.0 ;"
echo -e "\033[0;34m[INFO]\033[0m----- root: 6.30.06 ;"
echo -e "\033[0;34m[INFO]\033[0m----- python: 3.9.1;"
echo -e "\033[0;34m[INFO]\033[0m----- pythia: 8235 ;"
echo -e "\033[0;34m[INFO]\033[0m----- fastjet: 3.4.0 ;"
echo -e "\033[0;34m[INFO]\033[0m----- LHAPDF: 6.4.0 ;"
echo -e "\033[0;34m[INFO]\033[0m----- HepMC: 2.06.11 ;"
echo -e "\033[0;34m[INFO]\033[0m(version du 17/09/24)"
echo "*****"

```

As already mentioned several times throughout this manuscript, and in spirit of transparency and reproducibility, the code developed during this thesis has been made publicly available at https://gitlab.com/mtartarin/phd_share_public.

The repository provides all necessary files, together with a list of explicit software dependencies, to run the new MEM@NLO framework and reproduce the main results already presented.

Résumé de la thèse obligatoire en français - Mandatory french summary [20 pages]

La présente section constitue un résumé d'environ vingt pages de la thèse, rédigé en français, conformément aux exigences de l'école doctorale ED SdM (École Doctorale Science de la Matière, Toulouse). Il ne vise en aucun cas à remplacer le manuscrit complet.

En raison de cette limitation de format, de nombreux développements conceptuels, techniques et expérimentaux ne peuvent pas être présentés entièrement. Les explications fournies ici suffisent pour donner une vision générale du travail, mais elles ne permettent pas de saisir pleinement la richesse des méthodes et des résultats.

Le lecteur intéressé est donc invité à se reporter systématiquement aux chapitres correspondants du manuscrit complet, où les notions sont développées de manière plus détaillée et rigoureuse.

Les figures présentées dans ce résumé sont directement réutilisées à partir du manuscrit original. Leurs légendes ont été simplifiées pour en faciliter la lecture, et l'ensemble des informations détaillées (sources de données, outils logiciels, références internes et bibliographiques,...) sont disponible dans les versions complètes de ces figures au sein du manuscrit principal.

0. Introduction

Le boson de Higgs est une particule élémentaire dont la découverte a été prononcée en 2012 au LHC (Large Hadron Collider). Cette particule est associée à un champ scalaire fondamental, le champ de Higgs, dont le rôle central dans le Modèle Standard est d'expliquer l'origine de la masse des particules élémentaires.

Le Modèle Standard de la physique des particules est la théorie qui décrit, à l'aide de champs quantiques, les constituants élémentaires de la matière ainsi que les interactions fondamentales qui les régissent, à l'exception de la gravitation. Il fournit un cadre cohérent et extrêmement précis pour l'interprétation des phénomènes observés dans les expériences de physique des hautes énergies.

La dynamique du champ de Higgs est entièrement décrite par un potentiel, dont la forme encode la structure du mécanisme de brisure spontanée de la symétrie électrofaible. La reconstruction expérimentale du potentiel du champ de Higgs constitue ainsi un objectif fondamental de la physique des hautes énergies. Elle permet de tester si la structure du mécanisme de Brisure Spontanée de la Symétrie Électrofaible est effectivement celle prédite par le Modèle Standard, ou si elle est modifiée par de nouvelles dynamiques encore inconnues.

La mesure précise de l'auto-couplage trilineaire du boson de Higgs λ_{3H} figure parmi les objectifs majeurs du programme du LHC au CERN. Ce paramètre contrôle directement l'intensité de l'interaction du boson de Higgs avec lui-même, et fixe la courbure du potentiel du champ de Higgs autour de son minimum. Toute déviation mesurable de λ_{3H} par rapport à sa valeur prédite serait donc un signe clair de nouvelle physique au-delà du Modèle Standard.

Les mesures actuelles des collaborations ATLAS et CMS autorisent encore des déviations substantielles par rapport à la prédiction du Modèle Standard, en raison de la difficulté expérimentale intrinsèque associée à la production de paires de bosons de Higgs.

Au LHC, l'auto-couplage du Higgs est principalement recherché via la production simultanée de deux bosons de Higgs HH . Parmi les canaux accessibles, le canal $HH \rightarrow b\bar{b}\gamma\gamma$ offre un compromis favorable entre le taux de branchement très élevé de la désintégration du Higgs en deux quarks-b ($H \rightarrow b\bar{b}$) et l'excellente résolution en masse associée au canal Higgs en deux photons ($H \rightarrow \gamma\gamma$). Cette combinaison permet une identification efficace du signal malgré un environnement expérimental complexe, au prix toutefois d'un taux de production global relativement faible.

Dans ce régime de statistiques limitées, le défi expérimental est de maximiser l'information extraite de chaque événement individuel, tout en limitant les biais issus de la chromodynamique quantique (QCD), en particulier ceux liés à l'émission de radiation supplémentaire dans l'état final.

La *Méthode des Éléments de Matrice* (MEM) répond précisément à ces enjeux. Elle repose sur l'utilisation directe des prédictions théoriques, calculées à partir des

éléments de matrice des processus étudiés. Ces prédictions sont évaluées événement par événement et intégrées sur l'espace des phases. On obtient ainsi, pour chaque événement, une vraisemblance (c'est-à-dire une probabilité associée à une hypothèse). Chaque événement est ainsi utilisé de manière optimale pour contraindre les paramètres du modèle physique considéré.

Historiquement, la MEM a permis d'obtenir plusieurs mesures de référence portant sur des processus rares, avec une précision inégalée, notamment pour la masse du quark top, les corrélations de spin dans la production $t\bar{t}$ ou les propriétés de spin et de parité du boson de Higgs. Cependant, la plupart des implémentations existantes reposent sur des amplitudes calculées à l'ordre dominant (LO), ce qui limite leur capacité à décrire fidèlement la structure cinématique des événements au LHC, où les effets de radiation QCD jouent un rôle majeur.

L'objectif de cette thèse est de lever cette limitation. Nous présentons la première implémentation d'une **Méthode des Éléments de Matrice à l'ordre Next-to-Leading Order (MEM@NLO)** appliquée au processus $gg \rightarrow HH \rightarrow b\bar{b}\gamma\gamma$. Cette implémentation a été intégrée dans le logiciel **MoMEMta** et repose sur une interface avec le générateur **POWHEG-BOX-V2**, permettant un accès cohérent aux différentes contributions de l'élément de matrice NLO : Born, virtuelles et réelles.

La MEM@NLO a été validée à l'aide de deux jeux de pseudo-données réalistes : un ensemble produit dans le cadre de cette thèse (pseudo-données NLO ISR), et un ensemble officiel utilisé par la collaboration ATLAS (full simulation ATLAS). Ces jeux de données incluent les principaux bruits de fond pertinents ($t\bar{t}H$, production QCD di-photon et production de Higgs simple). Les résultats emblématiques obtenus sont :

$$\kappa_\lambda = 1.14 \pm 0.50 \quad (\text{pseudo-données NLO ISR}), \quad \kappa_\lambda = 1.223 \pm 0.41 \quad (\text{full simulation ATLAS})$$

Le paramètre κ_λ désigne le rapport entre la valeur mesurée de l'auto-couplage du boson de Higgs λ_{3H} , et sa valeur prédite dans le Modèle Standard λ_{3H}^{SM} . Par construction, une prédiction correcte sur le potentiel de Higgs par le Modèle Standard correspond donc à $\kappa_\lambda = 1$.

Les valeurs obtenues par notre MEM@NLO sont donc compatibles avec la mesure de cette quantité, et sont associées à des incertitudes réduites. Elles illustrent ainsi la capacité de l'approche MEM@NLO à contraindre efficacement l'auto-couplage du Higgs dans un environnement expérimental réaliste, et illustrent le gain de précision et la robustesse de l'approche MEM@NLO, dans un cadre expérimental réaliste proche de celui de l'expérience ATLAS.

I. Cadre théorique et production di-Higgs

Un aperçu du Modèle Standard

Le Modèle Standard (MS) de la physique des particules décrit l'ensemble des constituants élémentaires de la matière ainsi que les interactions fondamentales (forte, faible et électromagnétique) qui les régissent. Il s'articule autour de trois grandes familles de particules :

- les fermions de matière (particules de spin $\frac{1}{2}$: quarks et leptons), qui constituent la matière visible;
- les bosons vecteurs (particules de spin 1 : gluons g , bosons W^\pm , boson Z et photon γ), médiateurs d'interactions fondamentales;
- et le boson scalaire de Higgs H (particule de spin 0), associé au champ responsable de la génération des masses.

Découvert en 2012 au LHC par les collaborations ATLAS et CMS, le boson de Higgs occupe une place centrale dans ce cadre théorique. Il fournit le mécanisme par lequel les bosons W et Z acquièrent une masse, et, par extension, permet également aux fermions de devenir massifs via leurs couplages au champ de Higgs : un processus connu sous le nom de mécanisme de Brout–Englert–Higgs.

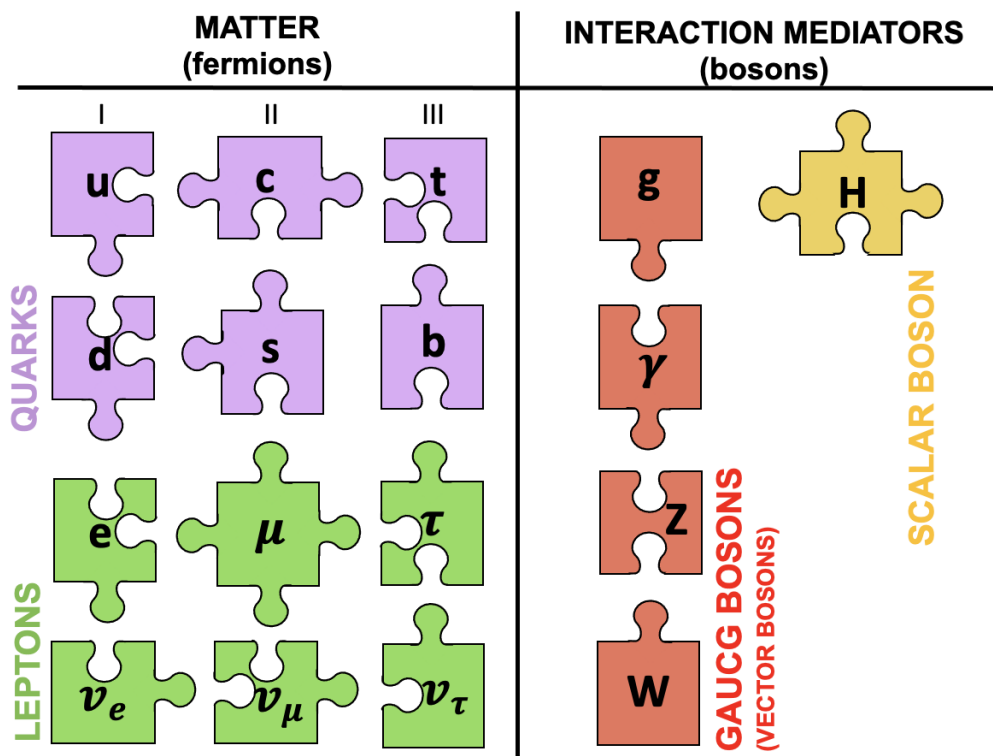


Figure 32: Représentation schématisée du Modèle Standard des particules sous la forme de pièces de puzzle (adapté de la Figure 1.1 de la thèse).

Le potentiel de Higgs et les auto-couplages

Dans le cadre du Modèle Standard, la dynamique du champ scalaire de Higgs est décrite par un potentiel auto-interactif responsable de la brisure spontanée de la symétrie électrofaible. Après cette brisure, le champ physique H peut être développé autour de sa valeur moyenne dans le vide, notée $v \simeq 246$ GeV.

Le potentiel effectif prend alors la forme :

$$V(H) = \frac{1}{2}m_H^2 H^2 + \lambda_{3H} v H^3 + \frac{1}{4}\lambda_{4H} H^4. \quad (.10)$$

Ce qui permet de mettre en évidence respectivement:

- la masse du boson de Higgs m_H ,
- l'auto-couplage trilinéaire λ_{3H} ,
- et l'auto-couplage quadrilinéaire λ_{4H} .

Ces deux derniers paramètres décrivent la forme du potentiel autour de son minimum et caractérisent les interactions du champ de Higgs avec lui-même. Dans le Modèle Standard, ils sont fixés par la masse mesurée du boson de Higgs m_H et par la valeur de v , ce qui rend toute déviation expérimentale un indicateur direct de nouvelle physique.

On a les relations :

$$m_H^2 = 2\lambda v^2, \quad \lambda_{3H} = \frac{3m_H^2}{v}, \quad \lambda_{4H} = \frac{3m_H^2}{v^2}.$$

où le paramètre λ est un coefficient fondamental du potentiel du champ de Higgs ϕ (à ne pas confondre avec le boson de Higgs H , qui correspond à la perturbation du champ autour de sa valeur moyenne v).

Avec $m_H = 125.09 \pm 0.21$ (stat) ± 0.11 (syst) GeV et $v \simeq 246$ GeV, on obtient une prédiction du MS pour l'auto-couplage trilinéaire $\lambda_{3H}^{SM} = 3m_H^2/v \simeq 190$ GeV.

Production di-Higgs au LHC et rôle de κ_λ

La production non résonante de paires de bosons de Higgs au LHC est dominée par la fusion de gluons (ggF), illustrée par les diagrammes de Feynman de la Figure 33. Ce processus est possible à l'aide de boucles virtuelles de quarks lourds, principalement le quark top.

À l'ordre dominant (Leading Order, LO), deux types de diagrammes interfèrent destructivement : le "triangle", sensible à l'auto-couplage λ_{3H} , et la "boîte", qui ne dépend pas de ce couplage.

Cette interférence confère à la section efficace une forte dépendance au paramètre $\kappa_\lambda = \lambda_{3H}/\lambda_{3H}^{SM}$

Par exemple la structure différentielle en fonction de la masse du système di-Higgs m_{HH} , comme dans la Figure 34, reflète ce jeu d'interférences. Le triangle domine à basse valeur m_{HH} et la boîte à grande valeur de m_{HH} .

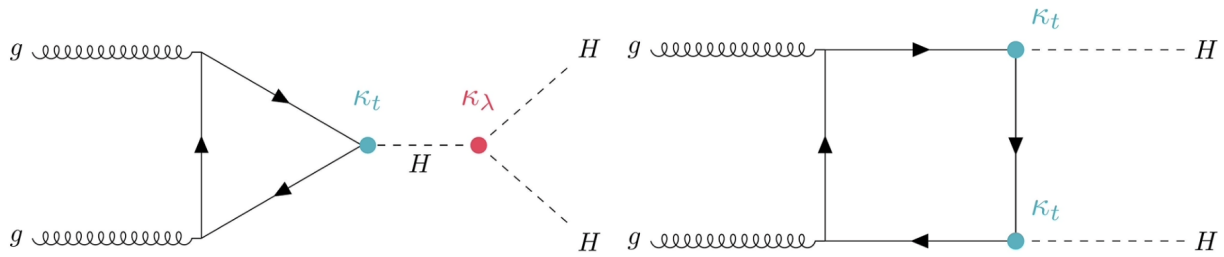


Figure 33: Diagrammes dominants pour $gg \rightarrow HH$: triangle (gauche, sensible à κ_λ) et boîte (droite) (adapté de la Figure 3.1 de la thèse).

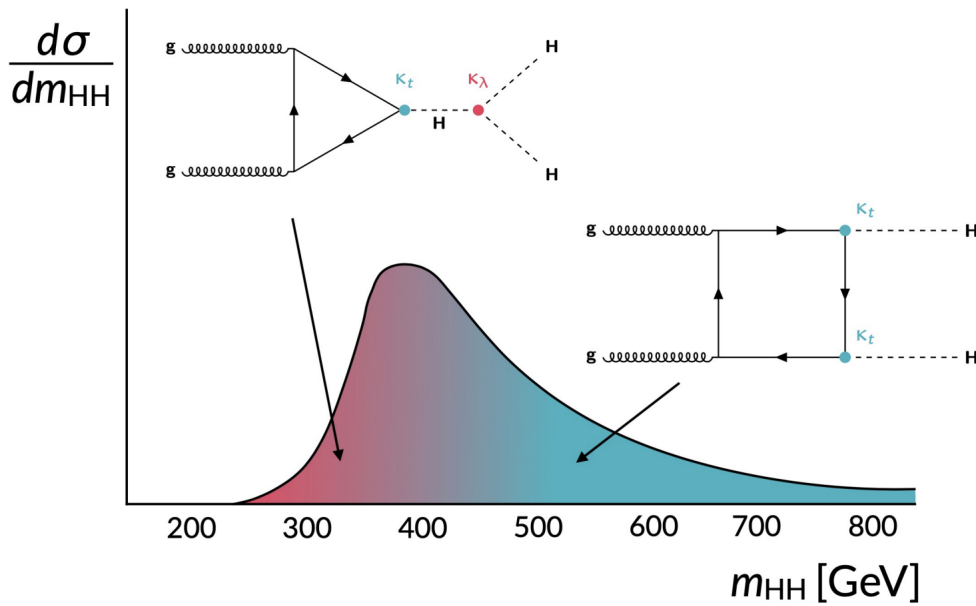


Figure 34: Section différentielle $d\sigma/dm_{HH}$ séparant triangle, boîte et interférence (adapté de la Figure 3.2 de la thèse).

Les prédictions théoriques font apparaître des corrections importantes au-delà du LO. À $\sqrt{s} = 14$ TeV, la section efficace pour le processus ggF passe typiquement de ~ 20 fb (LO) à ~ 33 fb (Next-to-Leading Order [NLO], théorie complète).

Contraintes expérimentales et courbe $\sigma(\kappa_\lambda)$

Le processus di-Higgs est extrêmement rare au LHC, avec un taux de production environ 1800 fois plus faible que celui de la production de Higgs simple. Dans ce régime dominé par de faibles statistiques, chaque événement compte : la sensibilité dépend directement de la capacité à exploiter au maximum l'information contenue dans les observables reconstruites.

Les combinaisons ATLAS+CMS (Run 2) donnent un intervalle d'incertitude autour de la valeur mesurée relativement large:

$-1.2 < \kappa_\lambda < 7.2$ (95% CL). Cette incertitude traduit la difficulté pour mesurer la production d'une paire de boson de Higgs, ainsi qu'une dégénérescence des solu-

tions (*i.e.* la présence d'une solution miroir, par symétrie de la courbe de la section efficace).

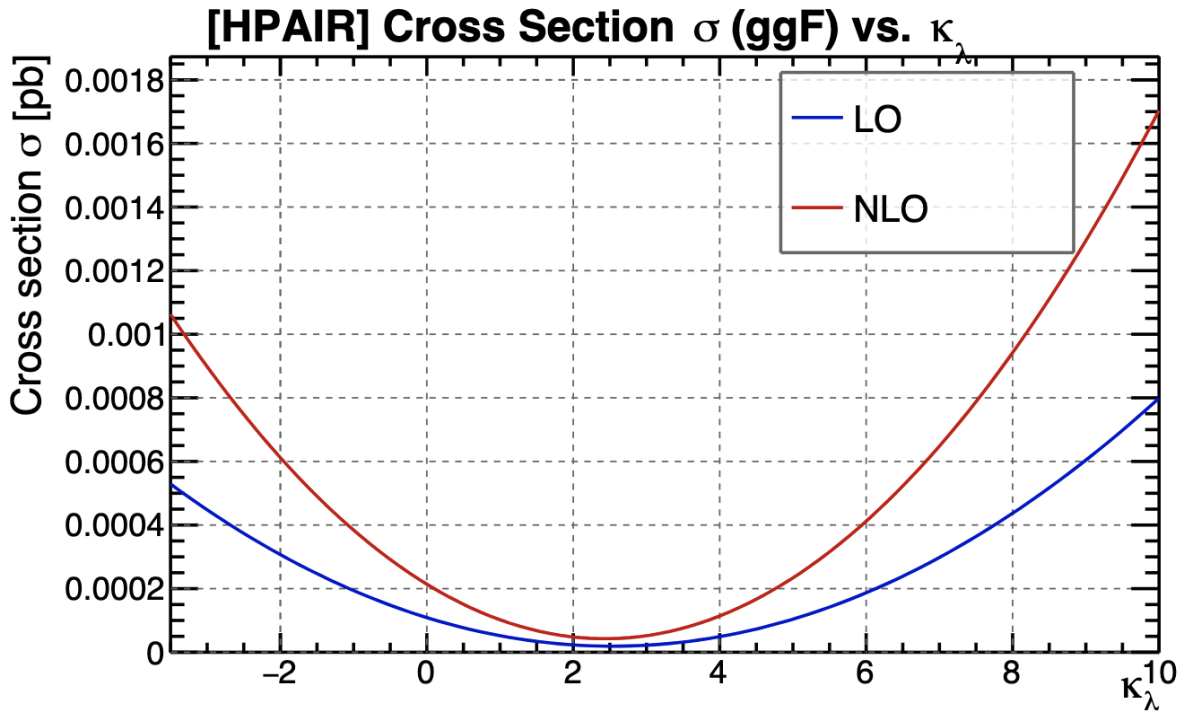


Figure 35: Section efficace totale $gg \rightarrow HH$ en fonction de κ_λ , prédictions HPAIR LO/NLO (adapté de la Figure 6.1 de la thèse).

Cette dépendance de $\sigma_{HH}(\kappa_\lambda)$ est très utilisée dans les analyses de type *yield-based*. Dans le travail que nous présentons ici, cette information est aussi incorporée via une vraisemblance de rendement $L_{yield}(\kappa_\lambda)$, combinée à la vraisemblance cinématique de la MEM que nous introduirons plus tard.

II. Le détecteur ATLAS et le canal $HH \rightarrow b\bar{b}\gamma\gamma$

Aperçu et objets de physique

Le détecteur de particules ATLAS est un dispositif polyvalent composé de plusieurs sous-détecteurs complémentaires. Il comprend un trajectographe interne équipé de la couche à pixels IBL, des calorimètres électromagnétiques à argon liquide (LAr) à haute granularité, une calorimétrie hadronique, un spectromètre à muons, ainsi qu'un système de déclenchement à deux niveaux (L1 et HLT).

Les performances essentielles pour les analyses avec comme particules finales $b\bar{b}\gamma\gamma$ concernent donc la reconstruction des photons γ et des b-jets.

Photons. Les énergies ECAL brutes sont corrigées (matériau amont, fuites) puis raffinées.

Jets et b-tagging. La reconstruction de jets utilise l'algorithme anti- k_t et des calibrations précises.

Amélioration de m_{bb} . Une *b-calibration* largement utilisée ajoute un muon interne au jet et corrige la perte due au neutrino qui en résulte. La résolution de m_{bb} est améliorée d'environ 10%.

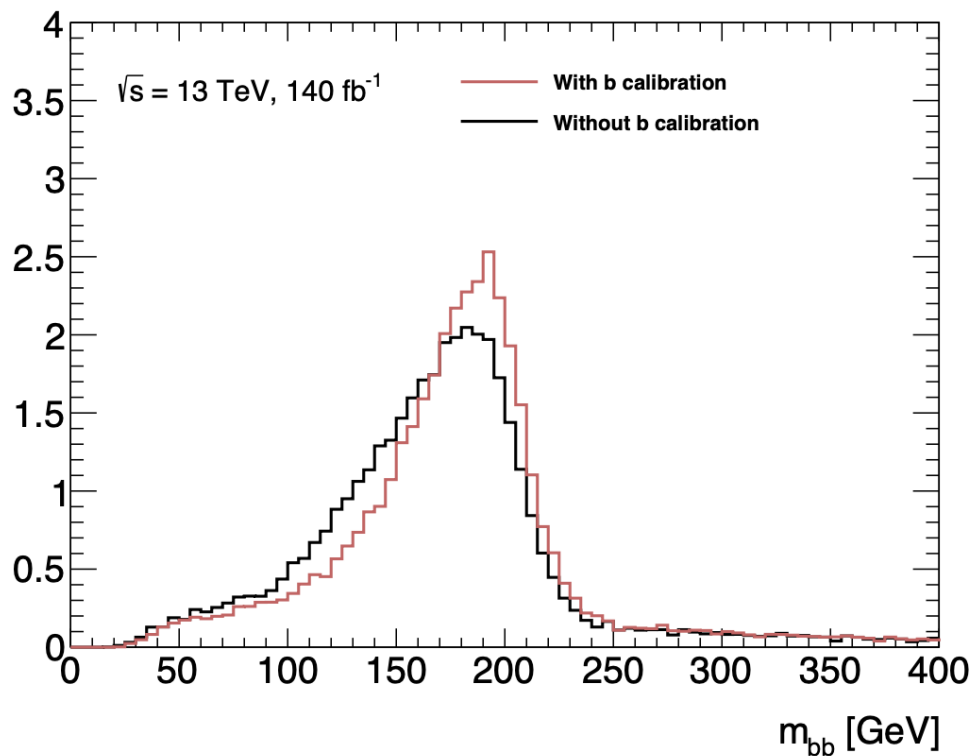


Figure 36: Distribution reconstruite m_{bb} avec et sans *B-calibration* (adapté de la Figure 5.8 de la thèse).

III. La Methode des Elements de Matrice

Principe général

La MEM s'appuie sur le lemme de Neyman–Pearson, garantissant l'optimalité statistique du rapport de vraisemblances utilisé, et donc de la méthode.

Intuitivement, la MEM quantifie à quel point la configuration mesurée d'un événement ressemble à ce que prédit la théorie, en tenant compte des degrés de liberté non mesurés et de la résolution du détecteur.

En physique des particules, l'idée est de calculer pour chaque événement observé la probabilité d'observer les variables mesurées \mathbf{x} , sachant une hypothèse de processus \mathbf{h} . Cette probabilité est reliée à l'élément de matrice au carré du processus p étudié $|\mathcal{M}_p(\mathbf{y})|^2$.

La vraisemblance pour un événement est donnée par :

$$L(\mathbf{x}|h) = \frac{1}{\sigma_{HH}^p} \int d\Phi |\mathcal{M}_p(\mathbf{y})|^2 W(\mathbf{x}, \mathbf{y}) f_{\text{PDF}}(x_1) f_{\text{PDF}}(x_2). \quad (.11)$$

Ici \mathbf{y} sont les variables à l'état partonique, $d\Phi$ est l'espace des phases sur lequel intégrer, $W(\mathbf{x}, \mathbf{y})$ est la fonction de transfert reliant partons et objets reconstruits, et f_{PDF} les densités partoniques.

Sommer les différentes probabilités (ou leur logarithme) sur un échantillon donne un estimateur efficace de l'hypothèse physique \mathbf{h} .

Observables dérivées

A partir de la sortie de la MEM, on peut produire différents résultats:

Courbes ROC. Elles comparent le pouvoir discriminant d'une observable pour séparer un signal d'un bruit de fond. L'aire sous la courbe (AUC) mesure la performance.

Avec nos conventions, plus la courbe épouse l'angle en bas à droite, plus la méthode est efficace pour discriminer les événements (*i.e.* distinguer le signal du bruit de fond).

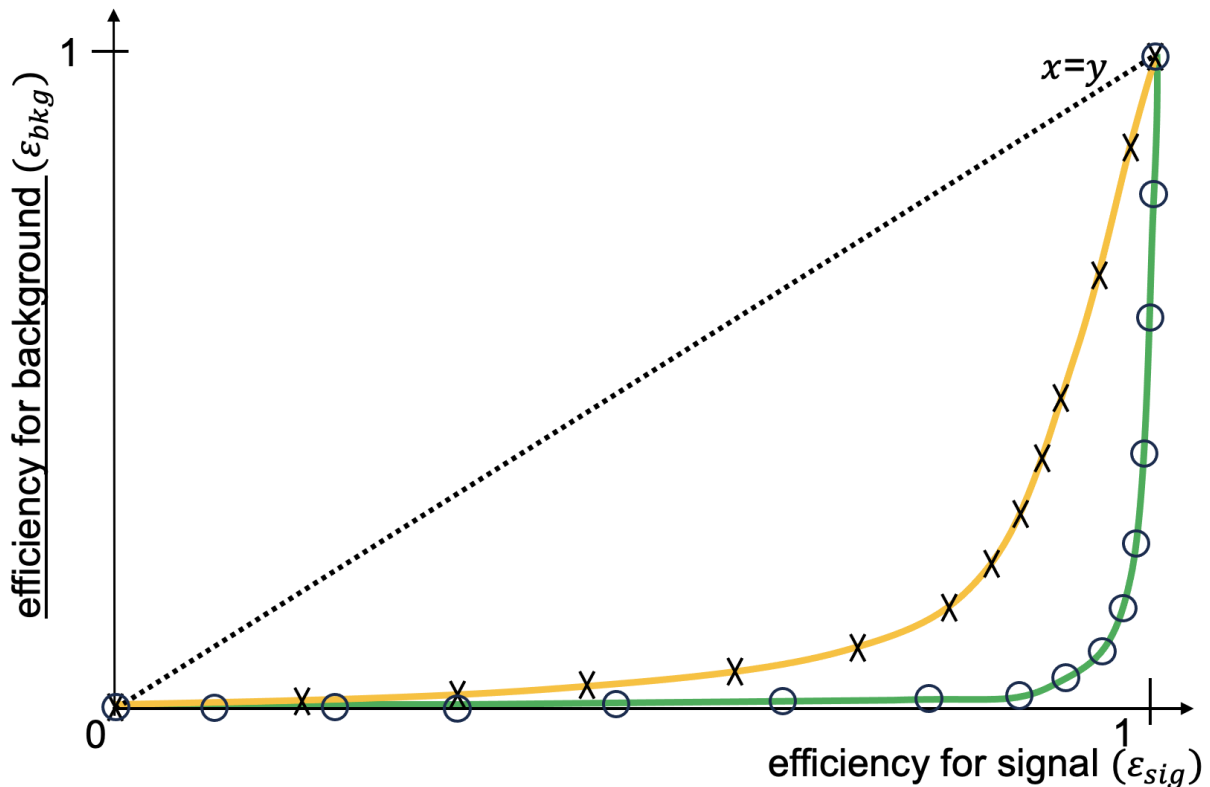


Figure 37: Exemple schématique de deux courbes ROC : cas où les événements sont bien discriminés entre l'hypothèse signal et l'hypothèse bruit de fond (en vert) ; cas où la discrimination est plus faible (en orange). Différents points sur une courbe ROC correspondent à des coupures différentes appliquées à la variable discriminante. La ligne $x = y$ représente la performance d'une classification aléatoire (adapté de la Figure 8.2 de la thèse).

Scan de vraisemblance. On retrouve la meilleure valeur de l'hypothèse sur κ_λ par le minimum de la courbe NLL tracée: $\hat{\kappa}$ (*cf.* Figure 38). Autour de ce minimum, on définit :

$$\Delta(-\ln \mathcal{L}) \equiv -\ln \mathcal{L}(\kappa) - (-\ln \mathcal{L}(\hat{\kappa})) = 0.5 \quad (.12)$$

Ce test permet de donner une estimation de l'incertitude (l'intervalle de confiance de 1σ) autour de la meilleure valeur de \hat{h} .

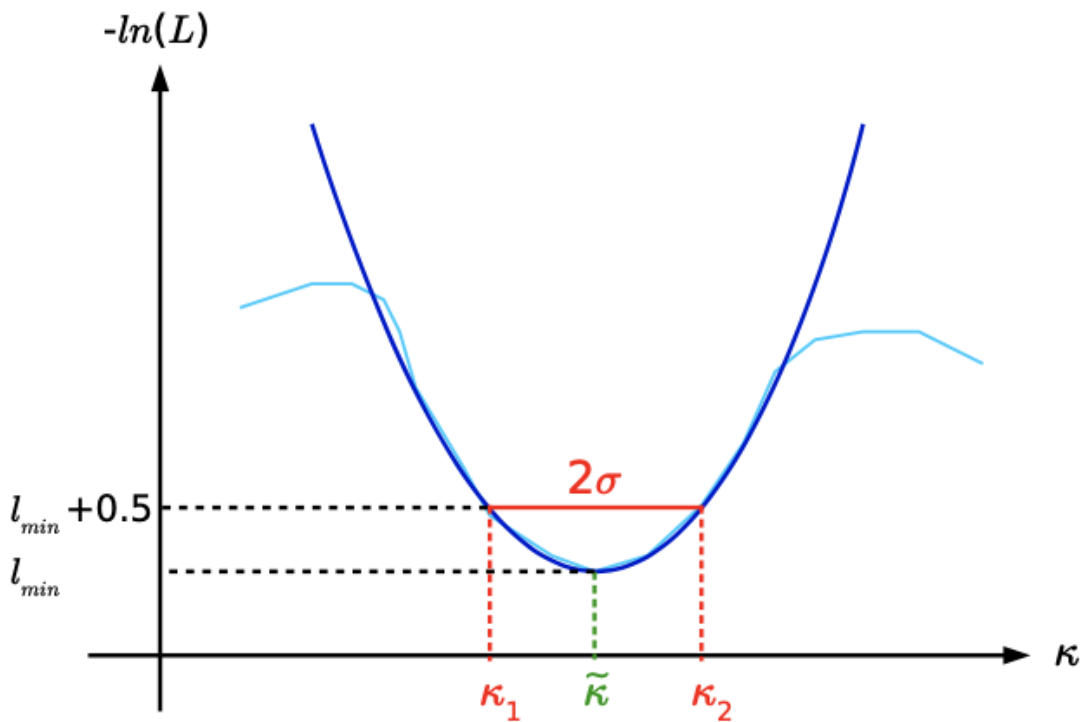


Figure 38: Méthode du minimum de log-vraisemblance négatif : fonction de log-vraisemblance négatif (NLL) en fonction du paramètre κ . La courbe en cyan montre les valeurs observées de la NLL, tandis que la parabole en **bleu** représente l'ajustement quadratique autour du minimum. La ligne verticale en **vert** indique la valeur du paramètre au meilleur ajustement $\tilde{\kappa}$, et les lignes en **rouge** délimitent l'intervalle d'incertitude à 1σ , défini par $\sigma_\kappa = (\kappa_2 - \kappa_1)/2$, où κ_1 et κ_2 sont les points d'intersection de la courbe NLL avec $\Delta\text{NLL} = 0.5$ (ligne horizontale en pointillés). L'approximation parabolique (**bleu**) devient exacte dans la limite asymptotique autour de $\tilde{\kappa}$, conformément au théorème de Wilks (adapté de la Figure 8.3 de la thèse).

IV. Implémentation à Leading Order (LO) et limites

Construction LO

La construction d'une MEM à l'ordre dominant (MEM@LO) a été initialement réalisée par F. Eble et J. Stark dans le cadre d'un stage de master en 2019. Ce développement a constitué la base du présent travail de thèse. À partir de ce travail, nous avons mis en évidence la nécessité de généraliser la méthode à l'ordre supérieur (NLO).

La mise en œuvre à l'ordre dominant (Leading Order, LO) s'appuie sur des événements générés à partir des diagrammes de Feynman et des règles de calcul limitées à cet ordre. Les intégrales de vraisemblance sont alors construites via une interface entre

le générateur MadGraph5_aMC@NLO et le cadre MoMEMta.

Avant d'aborder le développement à NLO, nous avons entièrement reconstruit la MEM@LO *from the ground up*, en réimplémentant chaque composant de la chaîne (depuis la génération des événements, par la construction de la MEM, jusqu'à l'évaluation des intégrales de vraisemblance) afin d'en maîtriser pleinement les mécanismes, les approximations et les limitations.

Performances LO

À LO, les distributions MEM@LO montrent un fort pouvoir séparateur entre le signal (ggF) et le bruit de fond $t\bar{t}H$. Cela se voit dans les courbes ROC qui en résultent (cf. Figure 39, courbe en noir). Cependant, la méthode LO échoue dès qu'une radiation QCD est présente. En présence de radiation additionnelle, un grand nombre d'événements reçoivent un poids nul (cf. Figure 39, courbe en rouge). Cela limite fortement l'usage de la MEM LO en environnement réaliste.

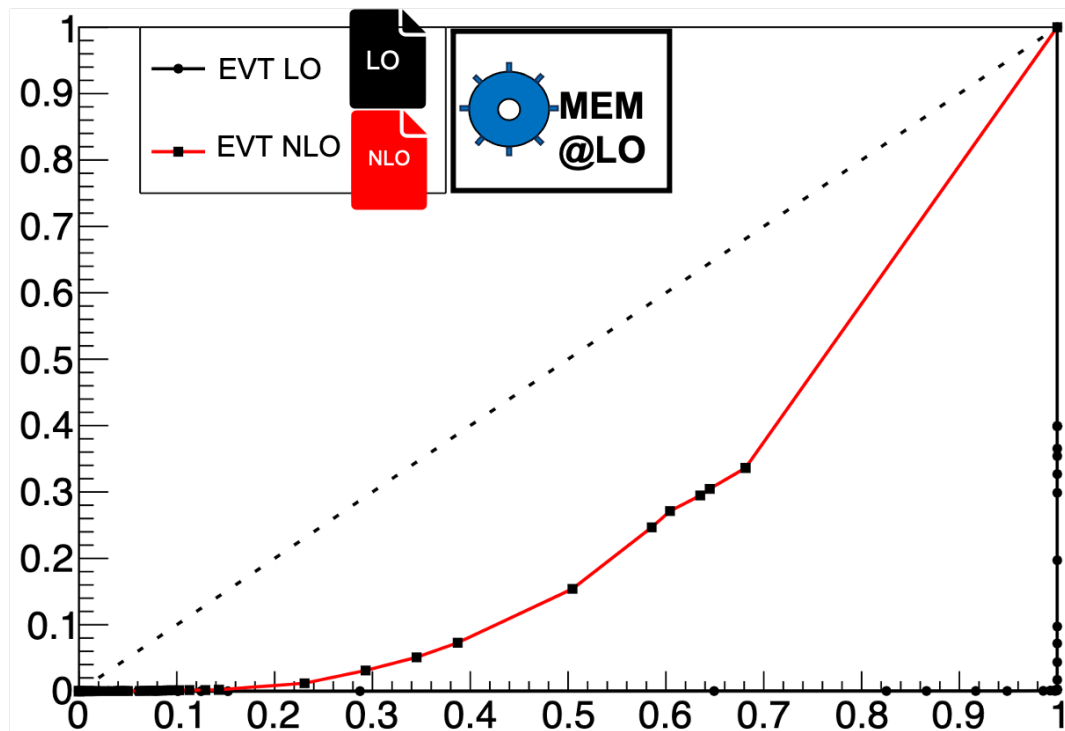


Figure 39: Comparaison des ROC pour des événements LO (en noir) et NLO (en rouge) avec une MEM@LO, avec un bruit de fond $t\bar{t}H$ (adapté de la Figure 12.3 de la thèse).

V. Développement du formalisme MEM@NLO

Motivation

À l'ordre NLO, la probabilité différentielle contient (de manière simplifiée) trois contributions majeures :

$$d\sigma^{\text{NLO}} = d\sigma^{\text{Born}} + d\sigma^{\text{Virtual}} + d\sigma^{\text{Real}}.$$

Une MEM@LO n'incorpore que la première : $d\sigma^{\text{Born}}$. Cela crée un décalage systématique lorsque l'on compare à des événements générés avec radiation QCD.

Le défi est donc d'exploiter les contributions Virtual et Real dans le calcul de vraisemblance, tout en gardant une intégration stable et efficace.

Chaîne logicielle

Nous avons développé un interface entre les logiciels POWHEG-BOX-V2 et MoMEMta, et apporté des modifications majeures. Cela permet d'extraire point-par-point les amplitudes Born, Virtual et Real. Ces contributions sont stockées et transmises au moteur d'intégration de MoMEMta. Une connaissance très précise de ces deux logiciels est cruciale pour réaliser ces manoeuvres.

Du côté génération, nous avons aussi modifié POWHEG-BOX-V2 pour $ggHH$ (ggF di-Higgs) et $t\bar{t}H$. Du côté de l'intégration de la MEM, nous avons construit et intégré dans MoMEMta de nouveaux blocs (comme le bloc N).

Nouveau bloc N

Le Main Block N est une nouvelle implémentation que nous avons développée afin de combler une limitation présente dans les blocs existants de MoMEMta. Ce nouveau bloc supprime les degrés de liberté q_1 , q_2 et p_T^{rad} , mais conserve p_z^{rad} . Cela assure une couverture stable du spectre de la radiation du glon supplémentaire.

Le jacobien correspondant a été calculé et introduit pour corriger le changement de variables correspondant.

Module ExtraRadiation_3DOF

Pour les processus qui comportent déjà des particules invisibles à LO (*e.g.* $t\bar{t}H$), un module ExtraRadiation_3DOF a été développé. Il introduit trois degrés de liberté supplémentaires liés uniquement à la radiation.

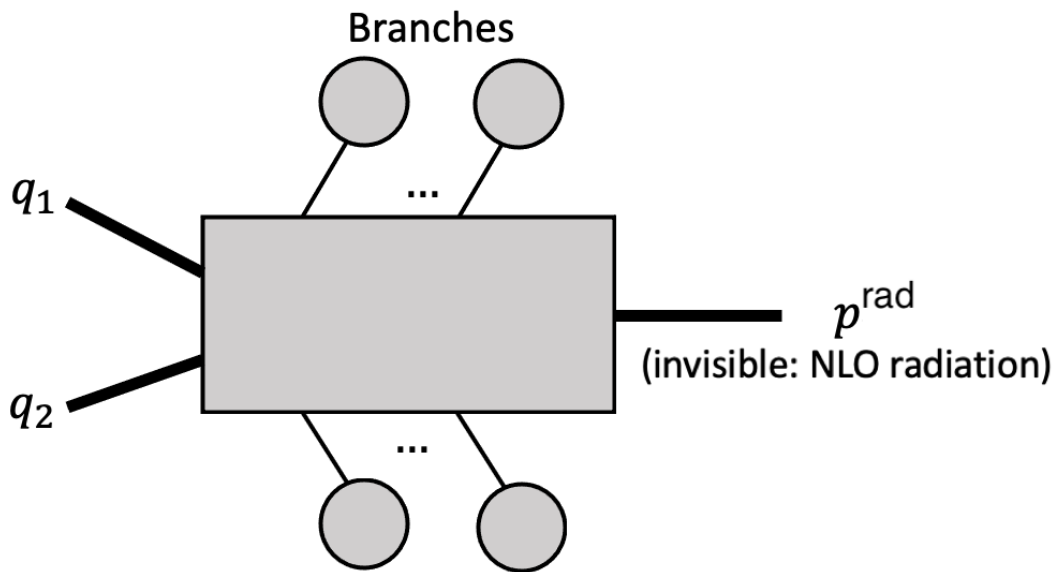


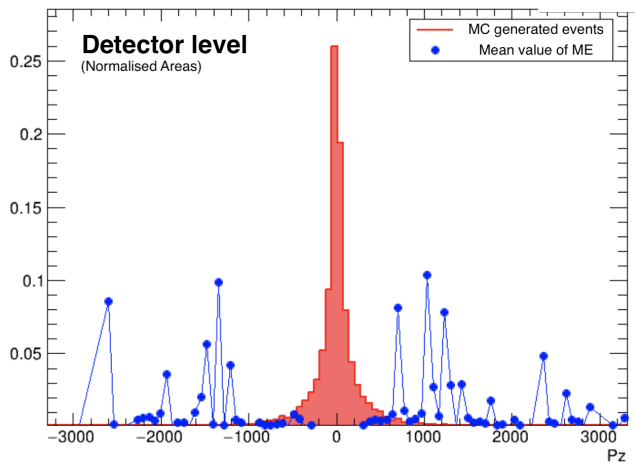
Figure 40: Structure du Main Block N et variables intégrées (adapté de la Figure 14.5 de la thèse).

Validation et stabilité numérique

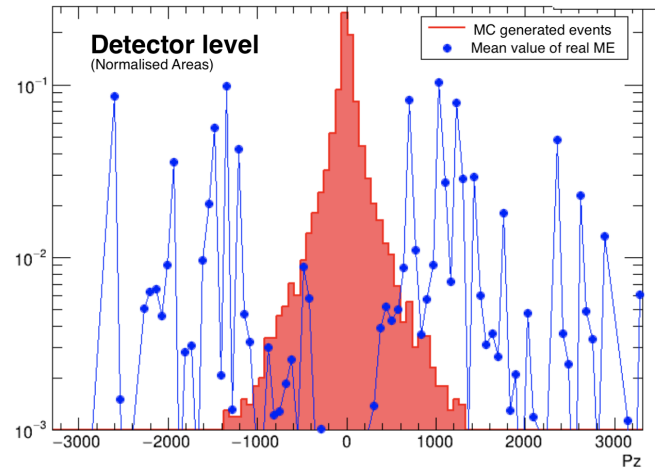
La validation des nouveaux blocs développés dans le cadre de cette thèse, et en particulier du bloc N, a été réalisée suivant une procédure progressive en trois étapes, conçue pour isoler et tester successivement les différentes composantes de l'implémentation.

Dans un premier temps, seuls les termes réels (*Real*) fournis par l'interface ont été considérés. Les densités de partons (PDF) ont ensuite été incluses, avant de construire l'intégrande complet de la MEM.

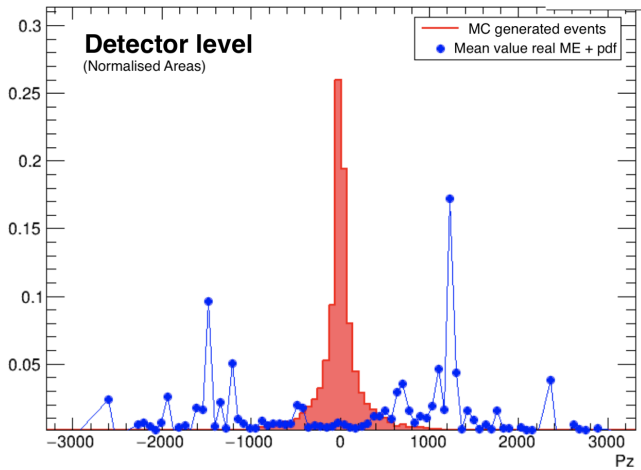
À chaque étape de cette procédure, les distributions obtenues convergent vers les références attendues, ce qui atteste à la fois de la stabilité numérique de l'implémentation et de la cohérence de l'intégration progressive des différents ingrédients (cf. Figure 14.6).



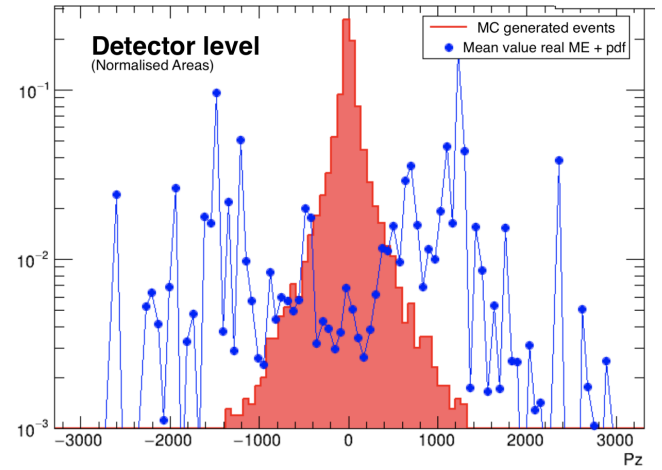
(a) Élément de matrice réelle uniquement



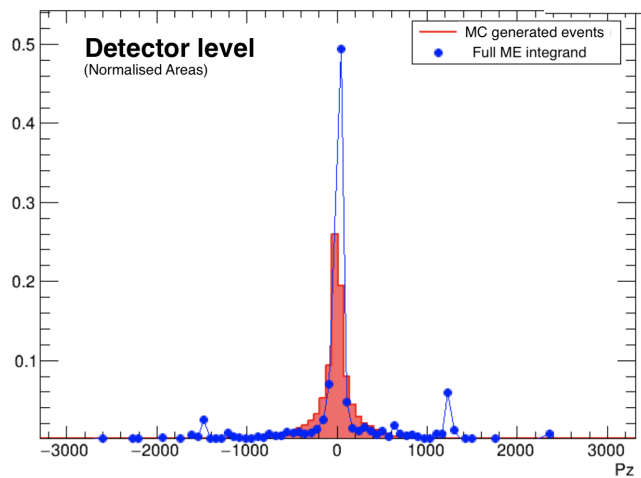
(b) avec axe vertical en log



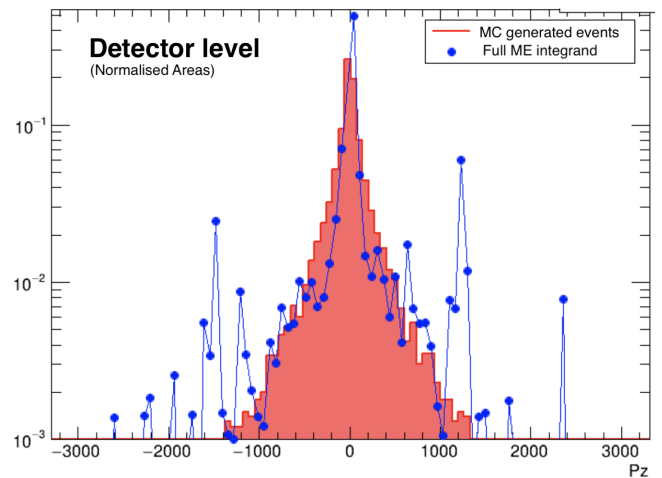
(c) Élément de matrice réelle + Parton Density Functions



(d) avec axe vertical en log



(e) Intégrand (réel) complet de la MEM



(f) avec axe vertical en log

Figure 41: Validation progressive du Bloc N (adapté de la Figure 14.6 de la thèse).

VI. Jeux de données, présélections et automatisation

Jeux de données utilisés

Deux types d'échantillons ont été utilisés pour tester et valider notre nouvelle implémentation de la MEM@NLO au cours de cette thèse:

1. **Pseudo-données NLO.** Générées avec POWHEG-BOX-V2 ou MADGRAPH5. Différents modes de radiation sont définis lorsque le logiciel POWHEG-BOX-V2 est utilisé: ISR (Initial State Radiation), FSRdr (Final State Radiation avec radiation dans cône ΔR) et FSRender (Final State Radiation, fin de chaîne). Le mode ISR est celui que nous avons considéré en priorité dans ce manuscrit pour valider notre méthode.
2. **n-tuples fullsim ATLAS.** Produits avec la chaîne officielle de simulation et reconstruction de la collaboration ATLAS.

Présélections et smearing

Comme dans toute analyse de physique des particules, des critères de présélection sont appliqués afin de définir une région cinématique compatible avec la topologie du processus étudié. Dans le cadre de la MEM, ces coupes sont volontairement maintenues aussi peu restrictives que possible, afin de préserver un maximum d'information cinématique pour l'évaluation des vraisemblances événement par événement.

À titre d'exemple, les photons reconstruits sont requis d'avoir des impulsions transverses supérieures à 30 et 25 GeV respectivement, et d'être situés dans la région centrale du détecteur ($|\eta| < 2.37$). Les jets sont sélectionnés avec $p_T > 25$ GeV et $|\eta| < 2.5$, et les masses invariantes reconstruites $m_{\gamma\gamma}$ et m_{bb} sont requises d'être compatibles avec la masse du boson de Higgs.

Afin de reproduire de manière réaliste les effets de résolution du détecteur, un smearing gaussien est aussi appliqué aux énergies des photons et des jets identifiés comme provenant de quarks b .

Ces choix assurent que l'évaluation de la MEM est effectuée dans une région cinématique où la reconstruction est fiable et où les fonctions de transfert restent représentatives, sans introduire de sélection artificiellement agressive qui réduirait la statistique utile.

Automatisation de la chaîne MEM

Une automatisation complète de la zone de travail a été mise en place. Ce travail conséquent a permis d'optimiser l'utilisation de la MEM et l'exploitation de ses résultats, rendant possible la production d'un grand volume de résultats dans le cadre de cette thèse.

Les principales automatisations réalisées sont les suivantes :

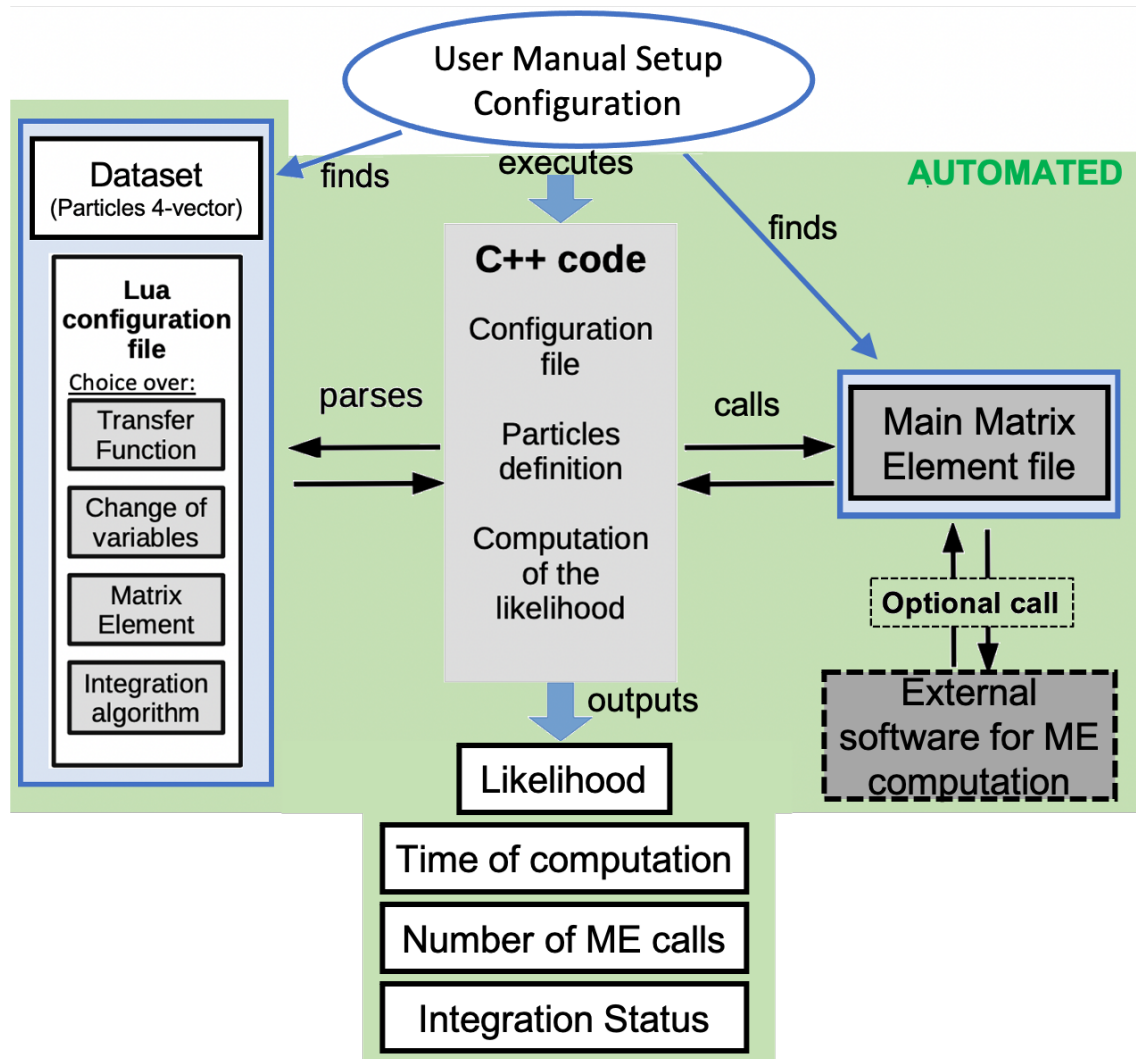


Figure 42: Schéma de la chaîne d'interface POWHEG-BOX-V2 ↔ MoMEMta (adapté de la Figure 15.8 de la thèse).

- la génération des événements, incluant le *smearing* et l'application automatique des coupes cinématiques ;
- l'envoi des calculs MEM sur les fermes de calcul du CC-IN2P3, ainsi que la récupération et la mise en forme automatiques des sorties ;
- le traitement des résultats et la phase de vérification, entièrement systématisés pour garantir la fiabilité des poids calculés ;
- la production des résultats finaux (courbes ROC, scans de vraisemblance et résumés statistiques, ...) via un ensemble de macros dédiées et automatiques.

VII. Résultats expérimentaux et interprétation

Courbes ROC

La MEM@NLO a été confrontée aux principaux bruits de fond : $t\bar{t}H$, QCD diphoton et single-Higgs. Les courbes ROC des événements NLO montrent une nette amélioration avec la nouvelle MEM@NLO, par rapport à la MEM@LO.

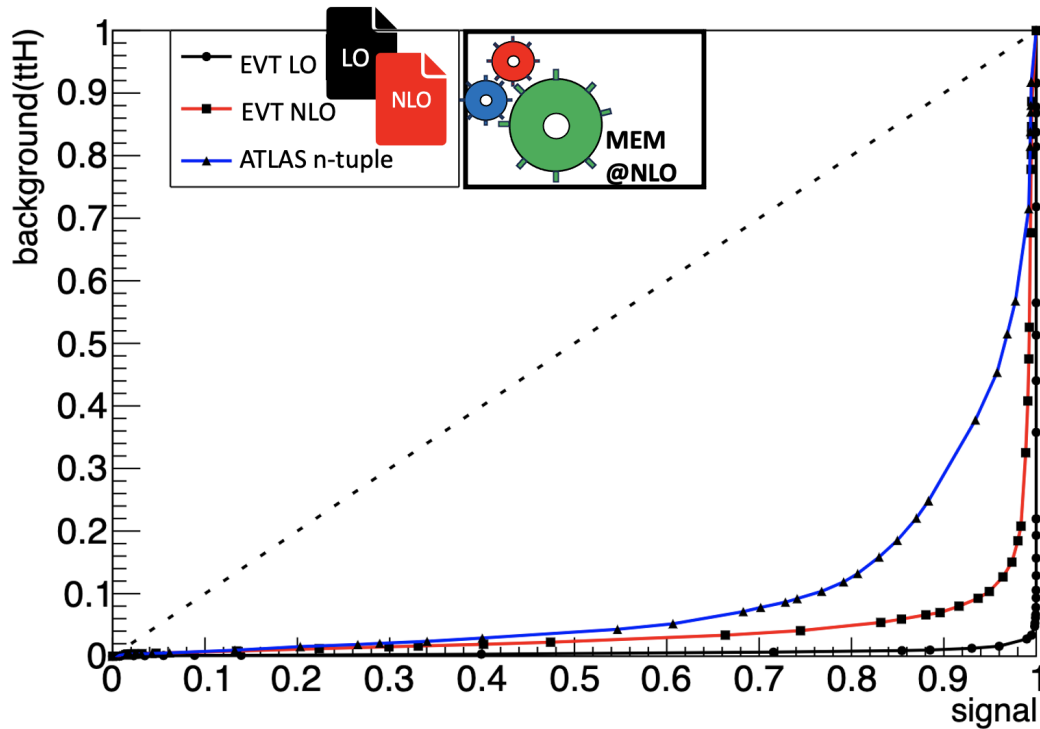


Figure 43: Courbes ROC MEM@NLO contre le bruit de fond $t\bar{t}H$ (LO en noir; NLO en rouge; ATLAS n-tuple en blue). (adapté de la Figure 17.1 de la thèse).

Scans de vraisemblance

Les paramètres de couplage κ_λ ont été estimés en effectuant des scans de vraisemblance (cf. Figure 44).

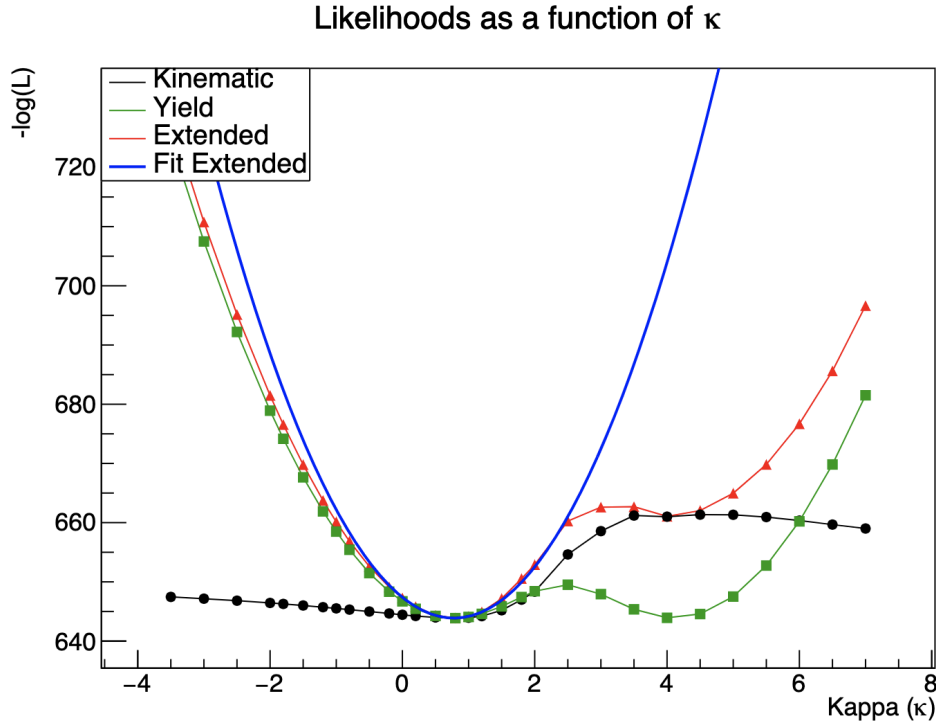


Figure 44: Exemple de scan de vraisemblance pour un pseudo-jeu de données constitué d'événements signal NLO ISR ($\kappa_\lambda = 1.00$) analysés avec la MEM@NLO.

Le graphe montre $-\log \mathcal{L}$ en fonction du modificateur de couplage κ_λ pour plusieurs composantes de vraisemblance :

Noir : composante cinématique seule (\mathcal{L}_{Kin}). **Vert** : terme de rendement ($\mathcal{L}_{\text{yield}}$). **Rouge** : vraisemblance étendue (\mathcal{L}_{ext}). **Bleu** : ajustement quadratique de $-\log \mathcal{L}_{\text{ext}}$, utilisé pour extraire la valeur au meilleur ajustement et son incertitude statistique.

Pseudo-données NLO ISR avec bruits de fond combinés. Le scan reconstruit correctement la valeur injectée $\kappa_\lambda = 1.0$. On obtient un estimateur :

$$\hat{\kappa}_\lambda = 1.14 \pm 0.50 \quad (\text{NLO ISR} + \text{fonds combinés}).$$

Le tableau 20 résume les résultats numériques détaillés. La valeur centrale proche de l'unité indique que la méthode reconstruit correctement la valeur injectée dans les pseudo-données. L'incertitudes obtenue illustre l'apport de la formulation NLO, dans un contexte où la rareté du signal et la complexité expérimentale limitent fortement la précision atteignable.

Likelihood Scan Performance

MEM@NLO, $\sqrt{s}=14$ TeV, $b\bar{b}\gamma\gamma$ final state, with 300 fb^{-1}

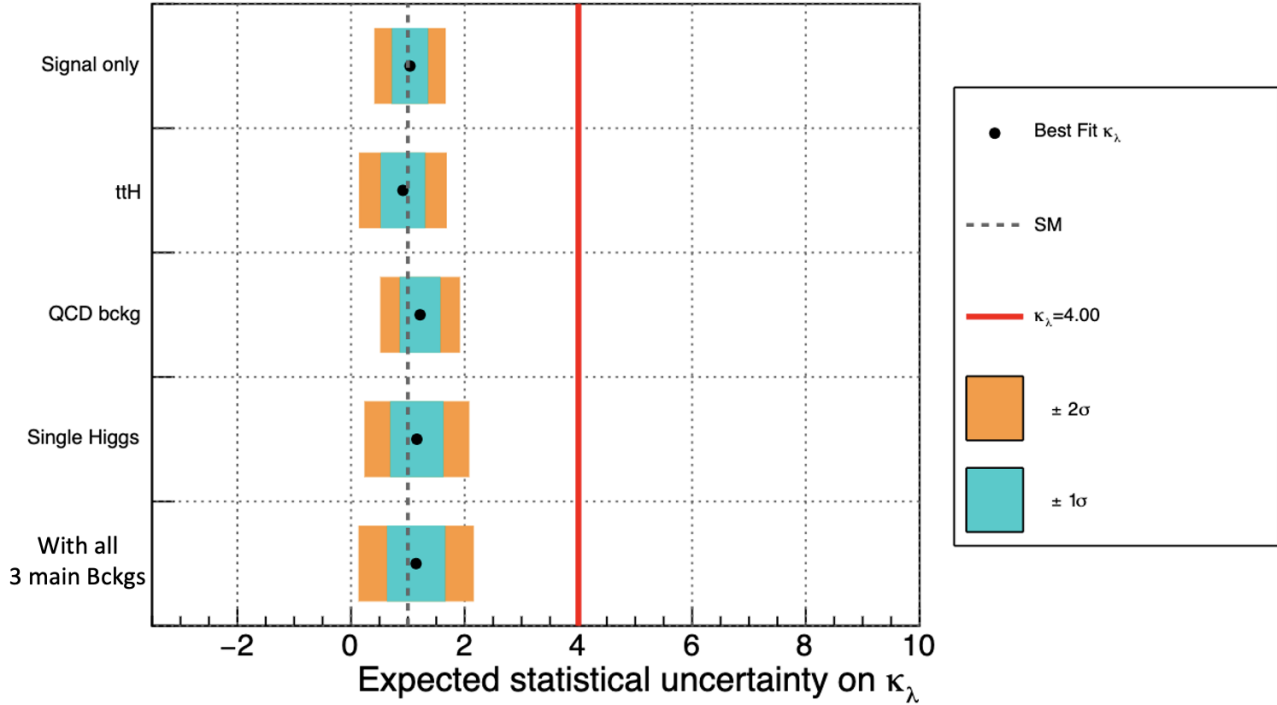


Figure 45: Résumé des performances de la vraisemblance de la MEM@NLO pour l'état final $b\bar{b}\gamma\gamma$ à $\sqrt{s} = 14$ TeV et pour une luminosité intégrée de 300 fb^{-1} en NLO ISR. Pour chaque ensemble de pseudo-jeux de données, le point noir indique la valeur mesurée du modificateur d'auto-couplage du Higgs κ_λ , tandis que la ligne grise en pointillés marque la valeur du Modèle Standard ($\kappa_\lambda = 1.00$). Les bandes turquoise (orange) représentent les intervalles attendus à $\pm 1\sigma$ ($\pm 2\sigma$) (adapté de la Figure 17.20 de la thèse).

Process	Best fit		Measured uncertainty	Pull distribution	
	κ_{mean}	σ_κ		ω_{mean}	σ_{pull}
Signal seul	1.037 ± 0.012	0.309 ± 0.008	0.302 ± 0.030	0.123 ± 0.039	1.020 ± 0.026
ttH	0.913 ± 0.042	0.441 ± 0.026	0.381 ± 0.087	-0.391 ± 0.113	1.422 ± 0.092
QCD ($b\bar{b}\gamma\gamma$)	1.215 ± 0.040	0.354 ± 0.027	0.345 ± 0.030	0.555 ± 0.126	1.023 ± 0.103
Single Higgs	1.158 ± 0.039	0.478 ± 0.030	0.418 ± 0.088	0.296 ± 0.085	1.044 ± 0.058
All bckg	1.144 ± 0.066	0.502 ± 0.048	0.485 ± 0.142	-0.185 ± 0.121	1.013 ± 0.096

Table 20: Résumé des performances des scans de vraisemblance pour chaque processus, à partir des événements NLO ISR générés et analysés avec MEM@NLO.

n-tuples ATLAS. Une seconde étude est menée avec des n-tuples produits dans la chaîne de simulation ATLAS, avec l'ensemble des bruits de fond. La vraisemblance atteint une très bonne précision ici aussi. On obtient :

$$\hat{\kappa}_\lambda = 1.223 \pm 0.41 \quad (\text{n-tuples ATLAS} + \text{fonds combinés}).$$

Le tableau 21 présente les résultats correspondants. Ici encore, la valeur centrale proches de l'unité indique que la méthode reconstruit correctement la valeur injectée dans les pseudo-données.

Likelihood Scan Performance

MEM@NLO, $\sqrt{s}=14$ TeV, $b\bar{b}\gamma\gamma$ final state, with 300 fb⁻¹

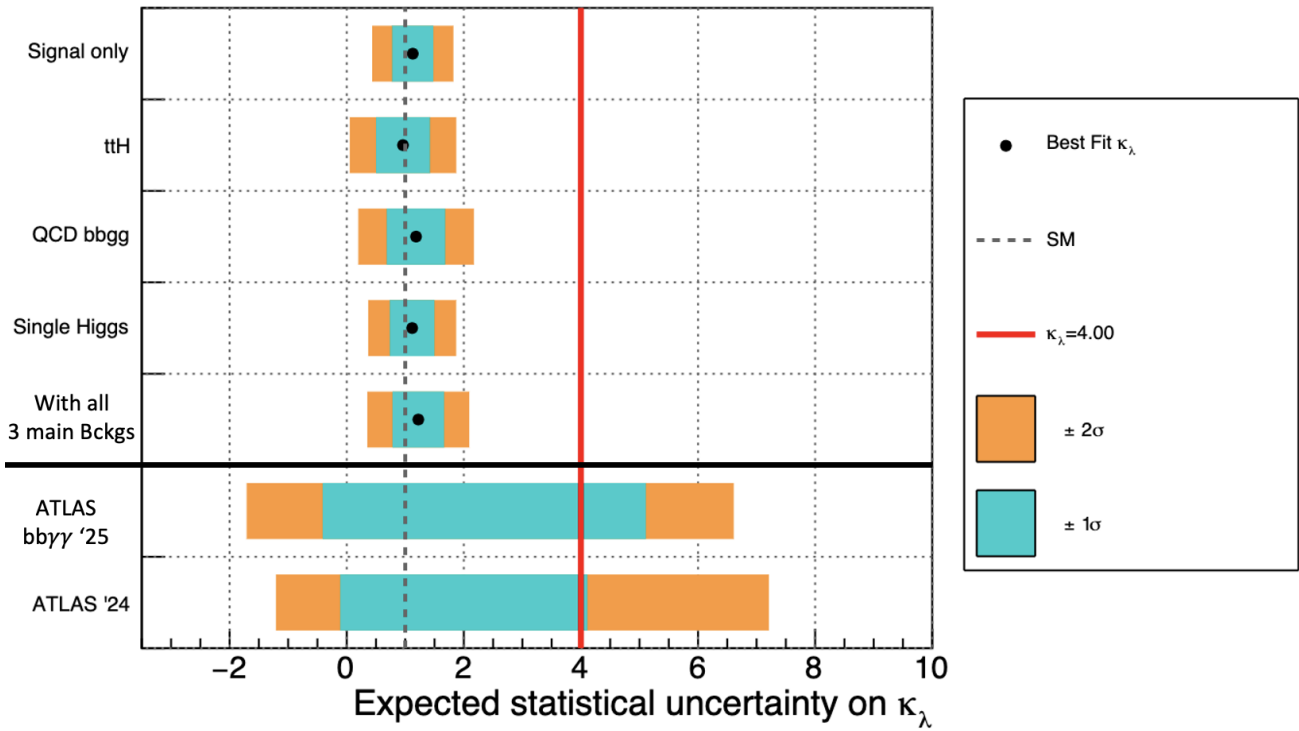


Figure 46: Résumé des performances de la vraisemblance profilée MEM@LO pour l'état final $b\bar{b}\gamma\gamma$ à $\sqrt{s} = 14$ TeV et pour une luminosité intégrée de 300 fb⁻¹, pour des événements n-tuples ATLAS fullsim. La même convention que celle de la Figure 45 est utilisée. (adapté de la Figure 17.21 de la thèse).

Process	Best fit		Measured uncertainty	Pull distribution	
	κ_{mean}	σ_{κ}		ω_{mean}	σ_{pull}
Signal seul	1.128 ± 0.013	0.342 ± 0.011	0.307 ± 0.031	0.355 ± 0.040	1.029 ± 0.029
$t\bar{t}H$	0.961 ± 0.040	0.450 ± 0.031	0.383 ± 0.068	-0.211 ± 0.100	1.293 ± 0.079
QCD ($b\bar{b}\gamma\gamma$)	1.184 ± 0.059	0.489 ± 0.053	0.401 ± 0.076	0.384 ± 0.133	1.104 ± 0.127
Single Higgs	1.118 ± 0.034	0.371 ± 0.030	0.386 ± 0.071	0.303 ± 0.076	0.905 ± 0.060
All bckg	1.223 ± 0.048	0.411 ± 0.044	0.443 ± 0.068	0.453 ± 0.099	0.806 ± 0.069

Table 21: Résumé des performances des scans de vraisemblance pour les échantillons $b\bar{b}\gamma\gamma$ simulés par ATLAS et analysés avec MEM@NLO.

Les valeurs de meilleur ajustement correspondent à la moyenne gaussienne et à la largeur de la distribution de $\hat{\kappa}_{\lambda}$.

L'incertitude mesurée est donnée par la valeur moyenne de l'histogramme vert dans le panneau central.

Les paramètres de *pull* sont obtenus à partir de l'ajustement gaussien de la distribution de *pull* dans le panneau inférieur.

VIII. Conclusions et perspectives

La mesure de l'auto-couplage trilinéaire du boson de Higgs, λ_{3H} , constitue un test fondamental du Modèle Standard en physique des particules.

Ce travail présente la première implémentation complète de la **Matrix Element Method à l'ordre NLO (MEM@NLO)** appliquée à la production di-Higgs $gg \rightarrow HH \rightarrow b\bar{b}\gamma\gamma$.

Le formalisme développé combine des amplitudes NLO avec dépendance complète en masse du quark top, un traitement infrarouge des émissions réelles, et une automatisation du travail, formant une véritable *MEM factory* capable de produire des résultats à grande échelle. L'interface entre POWHEG-BOX-V2 et MoMEMta permet d'exploiter directement les amplitudes NLO dans le calcul de vraisemblance événement-par-événement.

Validée sur des échantillons Monte Carlo NLO et sur des n -tuples fullsim d'ATLAS, la MEM@NLO atteint une précision compétitive avec :

- $\kappa_\lambda = 1.14 \pm 0.50$ pour les pseudo-données NLO ISR ;
- et $\kappa_\lambda = 1.223 \pm 0.41$ pour les données simulées complètes ATLAS.

Elle permet également la **levée de la dégénérescence miroir** autour de $\kappa_\lambda \simeq 4.0$, encore non résolue par les approches d'analyses classiques, grâce à l'exploitation complète de l'information cinématique dans la MEM.

Ces résultats positionnent la MEM@NLO comme une stratégie robuste et performante pour la mesure de l'auto-couplage du Higgs, offrant des vraisemblances nettes et non ambiguës.

Perspectives. Le cadre développé est conçu pour être compatible avec les conditions du Run 3 et pourrait (après validation approfondie) être intégrées dans les analyses combinées d'ATLAS sur la production di-Higgs. Sa conception générale permettrait par ailleurs une extension à d'autres états finaux ($b\bar{b}\tau^+\tau^-$, $b\bar{b}b\bar{b}$, etc.) et à des interprétations dans le cadre du SMEFT à précision NLO.

Grâce à sa conception générale, l'implémentation développée dans cette thèse pourrait servir de référence pour l'étude de processus rares, et ouvre la voie à des mesures de haute précision du boson de Higgs au LHC comme dans l'ère du futur HL-LHC.

Bibliography

- [1] *The Higgs Boson Explained*, Youtube video.
<https://www.youtube.com/watch?v=IqAWqwh3Etw>. From "Piled Higher and Deeper", Uploaded 30 July 2012.
- [2] S. L. Glashow, *Partial-symmetries of weak interactions*, Nuclear Physics **22** (1961) 579–588, <https://www.sciencedirect.com/science/article/pii/0029558261904692>.
- [3] S. Weinberg, *A Model of Leptons*, Phys. Rev. Lett. **19** (1967) 1264–1266, <https://link.aps.org/doi/10.1103/PhysRevLett.19.1264>.
- [4] A. Salam and J. Ward, *Electromagnetic and weak interactions*, Physics Letters **13** (1964) 168–171, <https://www.sciencedirect.com/science/article/pii/0031916364907115>.
- [5] ATLAS Collaboration, *Observation of a new particle in the search for the Standard Model Higgs boson with the ATLAS detector at the LHC*, Physics Letters B **716** (2012) 1–29, <https://www.sciencedirect.com/science/article/pii/S037026931200857X>.
- [6] CMS Collaboration, *Observation of a new boson at a mass of 125 GeV with the CMS experiment at the LHC*, Physics Letters B **716** (2012) 30–61, <https://www.sciencedirect.com/science/article/pii/S0370269312008581>.
- [7] ATLAS Collaboration, *The ATLAS Experiment at the CERN Large Hadron Collider*, Journal of Instrumentation **3** (2008) S08003–S08003, <http://dx.doi.org/10.1088/1748-0221/3/08/S08003>.
- [8] CMS Collaboration, *The CMS experiment at the CERN LHC*, Journal of Instrumentation **3** (2008) S08004–S08004, <http://dx.doi.org/10.1088/1748-0221/3/08/S08004>.
- [9] F. Halzen and A. D. Martin, *Quarks and Leptons: An Introductory Course in Modern Particle Physics*. Wiley, New York, 1984.
- [10] Particle Data Group, *Review of Particle Physics*, Phys. Rev. D **98** (2018) 030001.
- [11] Y. Fukuda et al., *Evidence for Oscillation of Atmospheric Neutrinos*, Phys. Rev. Lett. **81** (1998) 1562–1567.

- [12] Q. R. Ahmad et al., *Direct Evidence for Neutrino Flavor Transformation from Neutral-Current Interactions in the Sudbury Neutrino Observatory*, Phys. Rev. Lett. **89** (2002) 011301.
- [13] Particle Data Group, *Review of Particle Physics*, Progress of Theoretical and Experimental Physics **2022** (2022), <http://dx.doi.org/10.1093/ptep/ptac097>, Full author list available at the URL; shortened here for readability.
- [14] Wikipedia, *Standard Model of Elementary Particles*, https://en.wikipedia.org/wiki/File:Standard_Model_of_Elementary_Particles.svg.
- [15] E. Noether, *Invariante Variationsprobleme*, Nachrichten von der Gesellschaft der Wissenschaften zu Göttingen, Mathematisch-Physikalische Klasse (1918) 235–257, <http://eudml.org/doc/59024>.
- [16] J. H. Christenson, J. W. Cronin, V. L. Fitch, and R. Turlay, *Evidence for the 2π Decay of the K_2^0 Meson*, Phys. Rev. Lett. **13** (1964) 138–140, PhysRevLett.13.138.
- [17] *The BABAR detector*, Nuclear Instruments and Methods in Physics Research Section A: Accelerators, Spectrometers, Detectors and Associated Equipment **479** (2002) 1–116, [http://dx.doi.org/10.1016/S0168-9002\(01\)02012-5](http://dx.doi.org/10.1016/S0168-9002(01)02012-5).
- [18] *The Belle detector*, Nuclear Instruments and Methods in Physics Research Section A: Accelerators, Spectrometers, Detectors and Associated Equipment **479** (2002) 117–232, [http://dx.doi.org/10.1016/S0168-9002\(01\)02013-7](http://dx.doi.org/10.1016/S0168-9002(01)02013-7).
- [19] F. Englert and R. Brout, *Broken Symmetry and the Mass of Gauge Vector Mesons*, Phys. Rev. Lett. **13** (1964) 321–323, <https://link.aps.org/doi/10.1103/PhysRevLett.13.321>.
- [20] G. S. Guralnik, C. R. Hagen, and T. W. B. Kibble, *Global Conservation Laws and Massless Particles*, Phys. Rev. Lett. **13** (1964) 585–587, <https://link.aps.org/doi/10.1103/PhysRevLett.13.585>.
- [21] P. W. Higgs, *Broken Symmetries and the Masses of Gauge Bosons*, Phys. Rev. Lett. **13** (1964) 508–509, <https://link.aps.org/doi/10.1103/PhysRevLett.13.508>.
- [22] J. Ellis, *Higgs Physics*, arXiv:1312.5672, <https://cds.cern.ch/record/1638469>, 52 pages, 45 figures, Lectures presented at the ESHEP 2013 School of High-Energy Physics, to appear as part of the proceedings in a CERN Yellow Report.
- [23] M. Bonanomi, *The Higgs Boson and the Standard Model of Particle Physics*. Springer Nature Switzerland, 2023. https://doi.org/10.1007/978-3-031-26833-5_1.

- [24] J. Goldstone, A. Salam, and S. Weinberg, *Broken Symmetries*, Phys. Rev. **127** (1962) 965–970, <https://link.aps.org/doi/10.1103/PhysRev.127.965>.
- [25] ATLAS and CMS Collaboration, *Combined Measurement of the Higgs Boson Mass in pp Collisions at $\sqrt{s} = 7$ and 8 TeV with the ATLAS and CMS Experiments*, Phys. Rev. Lett. **114** (2015) 191803, [arXiv:1503.07589](https://arxiv.org/abs/1503.07589) [hep-ex].
- [26] Particle Data Group, *Review of Particle Physics*, PTEP **2022** (2022) 083C01.
- [27] L. H. C. S. W. Group, *Handbook of LHC Higgs Cross Sections: 3. Higgs Properties: Report of the LHC Higgs Cross Section Working Group*. CERN Yellow Reports: Monographs. 2013. <https://cds.cern.ch/record/1559921>.
- [28] M. Reichert, A. Eichhorn, H. Gies, J. M. Pawłowski, T. Plehn, and M. Scherer, *Probing baryogenesis through the Higgs boson self-coupling*, Physical Review D **97** (2018), <http://dx.doi.org/10.1103/PhysRevD.97.075008>.
- [29] Y. Zhang, *Constraints on the Higgs self-coupling at the LHC with $\sqrt{s} = 13$ TeV and long-lived particle searches with a future lepton collider*. Ph.d. thesis, Université Paris Cité and Shanghai Jiao Tong University, Dec., 2023. <https://theses.hal.science/tel-04874807>. Defended on: 19/09/2023.
- [30] F. Montereali, *HH Searches and Higgs-Self Couplings Measurements by ATLAS+CMS*, Conference slides, *Weak Interactions and Neutrinos (WIN 2025)*, brighton, united kingdom, June, 2025. <https://cds.cern.ch/record/2935979/files/ATL-PHYS-SLIDE-2025-276.pdf>. ATL-PHYS-SLIDE-2025-276.
- [31] E. W. N. Glover and J. J. van der Bij, *Higgs Boson Pair Production via Gluon Fusion*, Nucl. Phys. B **309** (1988) 282–294.
- [32] S. Dawson, S. Dittmaier, and M. Spira, *Neutral Higgs Boson Pair Production at Hadron Colliders: QCD Corrections*, Phys. Rev. D **58** (1998) 115012, [arXiv:hep-ph/9805244](https://arxiv.org/abs/hep-ph/9805244) [hep-ph].
- [33] D. de Florian, M. Grazzini, C. Hänga, S. Kallweit, J. M. Lindert, P. Maierhöfer, J. Mazzitelli, and D. Rathlev, *Differential Higgs Boson Pair Production at Next-to-Next-to-Leading Order in QCD*, JHEP **09** (2016) 151, [arXiv:1606.09519](https://arxiv.org/abs/1606.09519) [hep-ph].
- [34] M. Grazzini, G. Heinrich, S. Jones, S. Kallweit, M. Kerner, J. M. Lindert, and J. Mazzitelli, *Higgs Boson Pair Production at NNLO with Top-Quark Mass Effects*, JHEP **05** (2018) 059, [arXiv:1803.02463](https://arxiv.org/abs/1803.02463) [hep-ph].
- [35] F. Maltoni, E. Vryonidou, and M. Zaro, *Top-Quark Mass Effects in Double and Triple Higgs Production in Gluon–Gluon Fusion at NLO*, JHEP **11** (2014) 079, [arXiv:1408.6542](https://arxiv.org/abs/1408.6542) [hep-ph].

- [36] S. Borowka, N. Greiner, G. Heinrich, S. Jones, M. Kerner, J. Schlenk, U. Schubert, and T. Zirke, *Higgs Boson Pair Production in Gluon Fusion at Next-to-Leading Order with Full Top-Quark Mass Dependence*, Phys. Rev. Lett. **117** (2016) 012001, [arXiv:1604.06447 \[hep-ph\]](#).
- [37] CERN, *CERN Yellow Reports: Monographs, Vol 2 (2017): Handbook of LHC Higgs cross sections: 4. Deciphering the nature of the Higgs sector*, 2017. <https://e-publishing.cern.ch/index.php/CYRM/issue/view/32>.
- [38] K. Leney, *Overview of ATLAS Non-Resonant HH Results*, Talk at *Higgs Pairs 2025*: Isola d'Elba, Italy, 12 May 2025, on behalf of the ATLAS Collaboration, 2025.
- [39] ATLAS and CMS Collaborations, *Highlights of the HL-LHC physics projections by ATLAS and CMS*, 2025. <https://arxiv.org/abs/2504.00672>.
- [40] P. Huang, A. J. Long, and L.-T. Wang, *Probing the Electroweak Phase Transition with Higgs Factories and Gravitational Waves*, Phys. Rev. D **94** (2016) 075008, [arXiv:1608.06619 \[hep-ph\]](#).
- [41] M. J. Ramsey-Musolf, T. V. I. Tenkanen, and V. Q. Tran, *Refining Gravitational Wave and Collider Physics Dialogue via Singlet Scalar Extension*, 2024. Preprint.
- [42] Y. Aoki, G. Endrödi, Z. Fodor, S. D. Katz, and K. K. Szabó, *The Order of the Quantum Chromodynamics Transition Predicted by the Standard Model of Particle Physics*, Nature **443** (2006) 675–678, [arXiv:hep-lat/0611014 \[hep-lat\]](#).
- [43] O. S. Brüning, J. Poole, P. Collier, P. Lebrun, R. Ostojic, S. Myers, and P. Proudlock, *LHC Design Report*, 2004. <http://cds.cern.ch/record/782076>.
- [44] E. Lopienska, *The CERN accelerator complex, layout in 2022. Complexe des accélérateurs du CERN en janvier 2022*, <https://cds.cern.ch/record/2800984>, General Photo.
- [45] I. Veliscek, *The search for pair production of Higgs bosons at the ATLAS experiment*. Ph.d. thesis, University of Oxford, CERN Document Server, Sept., 2023. <https://cds.cern.ch/record/2905691>. Supervisors: Brian Todd Huffman and James Alexander Frost.
- [46] Y. Zhang, *Constraints on the Higgs self-coupling at the LHC with $\sqrt{s} = 13$ TeV and Long-Lived Particles searches with a future lepton collider*. Ph.d. thesis, Université Paris-Est, CERN Document Server, Dec., 2023. <https://cds.cern.ch/record/2913609>. Supervisors: Gregorio Bernardi and Liang Li.

- [47] The LHCb Collaboration, *The LHCb Detector at the LHC*, Journal of Instrumentation **3** (2008) S08005–S08005, <http://dx.doi.org/10.1088/1748-0221/3/08/s08005>.
- [48] The ALICE Collaboration, *The ALICE experiment at the CERN LHC*, Journal of Instrumentation **3** (2008) S08002–S08002, <http://dx.doi.org/10.1088/1748-0221/3/08/s08002>.
- [49] CERN, *The HL-LHC project*, <https://hilumilhc.web.cern.ch/content/hl-lhc-project>, 2025. Accessed 25 June 2025.
- [50] ATLAS Collaboration, *Online Luminosity Summary Plots for Run 3*, <https://twiki.cern.ch/twiki/bin/viewauth/AtlasPublic/LuminosityPublicResultsRun3?t=1673270563>.
- [51] ATLAS Collaboration, S. Mehlhase, *ATLAS detector slice (and particle visualisations)*, <https://cds.cern.ch/record/2770815>.
- [52] Izaak Neutelings, *CMS coordinate system*, https://tikz.net/axis3d_cms/.
- [53] ATLAS Collaboration, *ATLAS Inner Detector: Technical Design Report. Vol. 1*, tech. rep., CERN, Apr., 1997. <https://cds.cern.ch/record/331063>.
- [54] P. Krieger, *The ATLAS liquid argon calorimeter: construction, integration, commissioning and performance from selected particle beam test results*, in *IEEE Nuclear Science Symposium Conference Record, 2005*. 10.1109/NSSMIC.2005.1596428.
- [55] ATLAS Collaboration, *ATLAS b -jet identification performance and efficiency measurement with $t\bar{t}$ events in pp collisions at $\sqrt{s} = 13$ TeV*, <https://arxiv.org/abs/1907.05120>.
- [56] ATLAS Outreach, *ATLAS Fact Sheet: To raise awareness of the ATLAS detector and collaboration on the LHC*, 2012. <http://cds.cern.ch/record/1457044>.
- [57] ATLAS Collaboration, P. Jenni, M. Nessi, M. Nordberg, and K. Smith, *ATLAS high-level trigger, data-acquisition and controls: Technical Design Report*. CERN, Geneva, 2003. <https://cds.cern.ch/record/616089>.
- [58] ATLAS Collaboration, *Measurement of the photon identification efficiencies with the ATLAS detector using LHC Run 2 data collected in 2015 and 2016*, <https://arxiv.org/abs/1810.05087>.
- [59] ATLAS Collaboration, *Electron and photon efficiencies in LHC Run 2 with the ATLAS experiment*, Journal of High Energy Physics **2024** (2024), [http://dx.doi.org/10.1007/JHEP05\(2024\)162](http://dx.doi.org/10.1007/JHEP05(2024)162).

- [60] M. Cacciari, G. P. Salam, and G. Soyez, *The anti-kt jet clustering algorithm*, Journal of High Energy Physics **2008** (2008) 063, <https://dx.doi.org/10.1088/1126-6708/2008/04/063>.
- [61] ATLAS Collaboration, *ATLAS b -jet identification performance and efficiency measurement with $t\bar{t}$ events in pp collisions at $\sqrt{s} = 13$ TeV*, <https://arxiv.org/abs/1907.05120>.
- [62] ATLAS Collaboration, *ATLAS flavour-tagging algorithms for the LHC Run 2 pp collision dataset*, <https://arxiv.org/abs/2211.16345>.
- [63] C. Rougier, *Trajectographie de particules chargées à l'aide d'un nouvel algorithme d'apprentissage géométrique profond et recherche de particules supplémentaires de type boson de Higgs dans les données d'ATLAS Run 2*. Thèse de doctorat en physique, Université Toulouse III - Paul Sabatier, France, Sept., 2023. Soutenance le 19 septembre 2023. Document en cours de traitement par l'établissement de soutenance.
- [64] ATLAS Collaboration, *Combination of Searches for Higgs Boson Pair Production in pp Collisions at $\sqrt{s} = 13$ TeV with the ATLAS Detector*, Phys. Rev. Lett. **133** (2024) 101801, [arXiv:2406.09971](https://arxiv.org/abs/2406.09971) [hep-ex].
- [65] CMS Collaboration, *Combination of searches for nonresonant Higgs boson pair production in proton-proton collisions at $\sqrt{s} = 13$ TeV*, tech. rep., CERN, Geneva, 2024. <https://cds.cern.ch/record/2917252>.
- [66] ATLAS Collaboration, *Study of Higgs boson pair production in the $HH \rightarrow b\bar{b}\gamma\gamma$ final state with 308 fb^{-1} of data collected at $\sqrt{s} = 13$ TeV and 13.6 TeV by the ATLAS experiment*, 2025. <https://arxiv.org/abs/2507.03495>.
- [67] T. Sjöstrand, S. Ask, J. R. Christiansen, R. Corke, N. Desai, P. Ilten, S. Mrenna, S. Prestel, C. O. Rasmussen, and P. Z. Skands, *An Introduction to PYTHIA 8.2*, Comput. Phys. Commun. **191** (2015) 159–177, [arXiv:1410.3012](https://arxiv.org/abs/1410.3012) [hep-ph].
- [68] J. Bellm, S. Gieseke, D. Grellscheid, A. Papaefstathiou, S. Platzer, P. Richardson, C. Rohr, T. Schuh, P. Schichtel, M. H. Seymour, A. Siodmok, P. Stephens, B. Waugh, and S. Webster, *Herwig 7.0/Herwig++ 3.0 release note*, Eur. Phys. J. C **76** (2016) 196, [arXiv:1512.01178](https://arxiv.org/abs/1512.01178) [hep-ph].
- [69] E. Bothmann et al., *Event Generation with Sherpa 2.2*, SciPost Phys. **7** (2019) 034, [arXiv:1905.09127](https://arxiv.org/abs/1905.09127) [hep-ph].
- [70] ATLAS Collaboration, *The ATLAS Simulation Infrastructure*, Eur. Phys. J. C **70** (2010) 823–874, [arXiv:1005.4568](https://arxiv.org/abs/1005.4568) [physics.ins-det].
- [71] S. Agostinelli et al., *Geant4 - a simulation toolkit*, Nucl. Instrum. Meth. A **506** (2003) 250–303.

- [72] ATLAS Collaboration, *AtlFast3: The Next Generation of Fast Simulation in ATLAS*, Comput. Softw. Big Sci. **6** (2022) 7, [arXiv:2109.02551 \[hep-ex\]](#).
- [73] ATLAS Collaboration, *Combined Measurement of the Higgs Boson Mass from the $H \rightarrow \gamma\gamma$ and $H \rightarrow ZZ^* \rightarrow 4\ell$ Decay Channels with the ATLAS Detector Using $\sqrt{s} = 7, 8$, and 13 TeV pp Collision Data*, Phys. Rev. Lett. **131** (2023) 251802, [arXiv:2308.04775 \[hep-ex\]](#).
- [74] ATLAS Collaboration, *Expected tracking and related performance with the updated ATLAS Inner Tracker layout at the High-Luminosity LHC*, tech. rep., CERN, Geneva, 2021. <https://cds.cern.ch/record/2776651>.
- [75] ATLAS Collaboration, *Technical Design Report for the ATLAS Inner Tracker Strip Detector*, tech. rep., CERN, Geneva, 2017. <https://cds.cern.ch/record/2257755>.
- [76] ACTS Collaboration, *A Common Tracking Software Project*, <https://arxiv.org/abs/2106.13593>, Full author list available at the URL; shortened here for readability.
- [77] ATLAS Collaboration, *ATLAS Software and Computing HL-LHC Roadmap*, tech. rep., CERN, Geneva, 2022. <https://cds.cern.ch/record/2802918>.
- [78] M. Tartarin, *ACTS Kalman Filter cluster calibration for refitting*, tech. rep., CERN, Geneva, 2023. <https://cds.cern.ch/record/2878239>. ATLAS Note draft for my QP project under the supervision of Paul Gessinger-Befurt, Louis-Guillaume Gagnon and Alexis Vallier.
- [79] R. E. Kalman, *A New Approach to Linear Filtering and Prediction Problems*, Journal of Basic Engineering **82** (1960) 35–45, <http://dx.doi.org/10.1115/1.3662552>.
- [80] ATLAS Collaboration, *Projected sensitivity of searches for Higgs boson pair production in final states with light leptons, taus, and photons with the ATLAS detector at the HL-LHC*, tech. rep., CERN, Geneva, 2025. <https://cds.cern.ch/record/2925675>.
- [81] Alamy Stock Photo, *Medieval writing desk*, <https://www.alamy.com/stock-photo/medieval-writing-desk.html>, n.d. Image ID C45WYM, accessed on June 26, 2025.
- [82] Philosophical Transactions of the Royal Society of London. Series A, Containing Papers of a Mathematical or Physical Character **231** (1933) 289–337, <http://dx.doi.org/10.1098/rsta.1933.0009>.
- [83] DØ Collaboration, *Measurement of the Top Quark Mass Using Dilepton Events*, <https://arxiv.org/abs/hep-ex/9706014>.
- [84] F. Canelli, *Helicity of the W boson in single - lepton $t\bar{t}$ events*. PhD thesis, Rochester U., 2003.

- [85] DØ Collaboration Nature **429** (2004) 638, [arXiv:hep-ex/0406031](https://arxiv.org/abs/hep-ex/0406031).
- [86] F. Kling, T. Plehn, and P. Schichtel, *Mad-Maximized Higgs Pair Analyses*, <https://arxiv.org/abs/1607.07441>.
- [87] Wikipedia, *RoC*, <https://fr.wikipedia.org/wiki/RoC>.
- [88] S. Wilks, *The Large-Sample Distribution of the Likelihood Ratio*, Annals of Mathematical Statistics **9** (1938) 60–62, <https://doi.org/10.1214/aoms/1177732360>.
- [89] J. F.Eble, *Prospective study for the development of an analysis to measure the tri-linear Higgs coupling using the Matrix Element Method with the ATLAS experiment at the HL-LHC*. Ph.d. thesis, KTH Royal Institute of Technology, 2020. <https://urn.kb.se/resolve?urn=urn:nbn:se:kth:diva-291100>.
- [90] J. Alwall, R. Frederix, S. Frixione, V. Hirschi, F. Maltoni, O. Mattelaer, H.-S. Shao, T. Stelzer, P. Torrielli, and M. Zaro, *The automated computation of tree-level and next-to-leading order differential cross sections, and their matching to parton shower simulations*, J. High Energ. Phys. **2014** (2014) 79, [https://doi.org/10.1007/JHEP07\(2014\)079](https://doi.org/10.1007/JHEP07(2014)079).
- [91] C. Degrande, C. Duhr, B. Fuks, D. Grellscheid, O. Mattelaer, and T. Reiter, *UFO - The Universal FeynRules Output*, Comput. Phys. Commun. **183** (2012) 1201–1214, <https://doi.org/10.1016/j.cpc.2012.01.022>.
- [92] G. P. Lepage, *A New Algorithm for Adaptive Multidimensional Integration*, J. Comput. Phys. **27** (1978) 192–203, [https://doi.org/10.1016/0021-9991\(78\)90004-9](https://doi.org/10.1016/0021-9991(78)90004-9).
- [93] P. Artoisenet, V. Lemaître, F. Maltoni, and O. Mattelaer, *Automation of the matrix element reweighting method*, J. High Energ. Phys. **2009** (2009) 18, <https://doi.org/10.1088/1126-6708/2009/04/018>.
- [94] S. Brochet, C. Delaere, B. François, V. Lemaître, A. Mertens, A. Saggio, M. V. Marono, and S. Wertz, *MoMEMta, a modular toolkit for the Matrix Element Method at the LHC*, <https://arxiv.org/abs/1805.08555>.
- [95] T. Hahn, *Cuba - a library for multidimensional numerical integration*, <https://arxiv.org/abs/hep-ph/0404043>.
- [96] S. Alioli, P. Nason, C. Oleari, and E. Re, *A general framework for implementing NLO calculations in shower Monte Carlo programs: the POWHEG BOX*, J. High Energ. Phys. **2010** (2010) 43, [https://doi.org/10.1007/JHEP06\(2010\)043](https://doi.org/10.1007/JHEP06(2010)043).
- [97] S. Wertz, *The Matrix Element Method in the LHC era*, EPJ Web of Conferences **137** (2017) 11010, <http://dx.doi.org/10.1051/epjconf/201713711010>.
- [98] K. Kondo Journal of the Physical Society of Japan **57** (1988) 4126.

- [99] K. Kondo Journal of the Physical Society of Japan **60** (1991) 836.
- [100] A. Abulencia, *Top Quark Mass Measurement from Dilepton Events at CDF II with the Matrix-Element Method*, <https://arxiv.org/abs/hep-ex/0605118>.
- [101] V. Khachatryan et al. Eur. Phys. J. C **75** (2015) 251, [arXiv:1502.02485](https://arxiv.org/abs/1502.02485).
- [102] G. Aad et al. Eur. Phys. J. C **75** (2015) 349, [arXiv:1503.05066](https://arxiv.org/abs/1503.05066).
- [103] V. Khachatryan et al., 2016. CMS-PAS-HIG-16-038.
- [104] CMS Collaboration, *Observation of $t\bar{t}H$ Production*, Physical Review Letters **120** (2018), <http://dx.doi.org/10.1103/PhysRevLett.120.231801>.
- [105] V. Khachatryan et al., 2016. CMS-PAS-HIG-16-022.
- [106] CMS Collaboration, *Evidence for associated production of a Higgs boson with a top quark pair in final states with electrons, muons, and hadronically decaying τ leptons at $\sqrt{s} = 13$ TeV*, Journal of High Energy Physics **2018** (2018), [http://dx.doi.org/10.1007/JHEP08\(2018\)066](http://dx.doi.org/10.1007/JHEP08(2018)066).
- [107] G. Aad et al. Phys. Lett. B **740** (2015) 118, [arXiv:1410.0647](https://arxiv.org/abs/1410.0647).
- [108] V. Khachatryan et al., 2013. CMS-PAS-TOP-13-009.
- [109] G. Aad et al. Phys. Lett. B **756** (2016) 228, [arXiv:1511.05980](https://arxiv.org/abs/1511.05980).
- [110] ATLAS Collaboration, *Measurement of single top-quark production in the s -channel in proton–proton collisions at $\sqrt{s} = 13$ TeV with the ATLAS detector*, Journal of High Energy Physics **2023** (2023), [http://dx.doi.org/10.1007/JHEP06\(2023\)191](http://dx.doi.org/10.1007/JHEP06(2023)191).
- [111] V. Khachatryan et al. Phys. Lett. B **758** (2016) 321, [arXiv:1511.06170](https://arxiv.org/abs/1511.06170).
- [112] S. Chatrchyan et al. Phys. Lett. B **716** (2012) 30, [arXiv:1207.7235](https://arxiv.org/abs/1207.7235).
- [113] G. Aad et al. Phys. Rev. D **91** (2015) 012006, [arXiv:1408.5191](https://arxiv.org/abs/1408.5191).
- [114] S. Chatrchyan et al. Phys. Rev. D **89** (2014) 092007, [arXiv:1312.5353](https://arxiv.org/abs/1312.5353).
- [115] G. Aad et al. Eur. Phys. J. C **75** (2015) 476, [arXiv:1506.05669](https://arxiv.org/abs/1506.05669), [Erratum: Eur. Phys. J. C76, no.3, 152 (2016)].
- [116] G. Aad et al., 2016. ATLAS-CONF-2016-079.
- [117] V. Khachatryan et al. Phys. Lett. B **759** (2016) 672, [arXiv:1602.04305](https://arxiv.org/abs/1602.04305).
- [118] S. Chatrchyan et al., 2016. CMS-PAS-HIG-16-033.
- [119] G. Heinrich, *Higgs Pairs Workshop 2025*, Presentation powerpoint on indico, May, 2025. Isola d’Elba, Italy, 11–17 May 2025. Slides at <https://indico.cern.ch/event/1399335/>.
- [120] S. Eales, *Man generating power for machine*,. CartoonStock ID, at <https://www.cartoonstock.com/cartoon?searchID=CS188833>.

- [121] T. Martini, *The Matrix Element Method at next-to-leading order QCD using the example of single top-quark production at the LHC*, <https://arxiv.org/abs/1807.06859>.
- [122] J. Alwall, A. Freitas, and O. Mattelaer, *The Matrix Element Method and QCD Radiation*, <https://arxiv.org/abs/1010.2263>.
- [123] T. Martini, T. Nuraliyev, and P. Uwer, *Determination of the top-quark mass from top-quark pair events with the matrix element method at next-to-leading order: Potential and prospects*, <https://arxiv.org/abs/2301.03280>.
- [124] R. Baumeister and S. Weinzierl, *The matrix element method at next-to-leading order for arbitrary jet algorithms*, <https://arxiv.org/abs/1612.07252>.
- [125] J. M. Campbell, W. T. Giele, and C. Williams, *The Matrix Element Method at Next-to-Leading Order*, <https://arxiv.org/abs/1204.4424>.
- [126] W. T. Giele, G. C. Stavenga, and J.-C. Winter, *A Forward Branching Phase-Space Generator*, 2011. <https://arxiv.org/abs/1106.5045>.
- [127] G. Heinrich, S. P. Jones, M. Kerner, G. Luisoni, and E. Vryonidou, *NLO predictions for Higgs boson pair production with full top quark mass dependence matched to parton showers*, <https://arxiv.org/abs/1703.09252>.
- [128] G. Heinrich, S. P. Jones, M. Kerner, G. Luisoni, and L. Scyboz, *Probing the trilinear Higgs boson coupling in di-Higgs production at NLO QCD including parton shower effects*, JHEP **06** (2019) 066, [arXiv:1903.08137](https://arxiv.org/abs/1903.08137) [hep-ph].
- [129] H. Murayama, I. Watanabe, and K. Hagiwara, *HELAS: HELicity amplitude subroutines for Feynman diagram evaluations*,.
- [130] Wolfram Research, Inc., *Mathematica, Version 14.0*, <https://www.wolfram.com/mathematica>.
- [131] R. Munroe. Hypothesis Generation <https://xkcd.com/2569/>.
- [132] CERN, *Handbook of LHC Higgs Cross Sections: 4. Deciphering the Nature of the Higgs Sector*, <https://arxiv.org/abs/1610.07922>.
- [133] M. Tartarin and J. Stark, *COMETA Workshop 2025*, Presentation powerpoint on indico, 2025. Paris, France, 17 March 2025. Slides at <https://indico.cern.ch/event/1484269/timetable/?view=standard#18-a-novel-implementation-of-t>.
- [134] M. Tartarin and J. Stark, *A Novel Implementation of the Matrix Element Method at Next-to-Leading Order for Measuring the Higgs Tri-Linear Coupling in Di-Higgs Production at the LHC*, Presentation powerpoint on indico, May, 2025. Higgs Pairs Workshop 2025, Isola d'Elba, Italy, 16 May 2025. Slides at <https://indico.cern.ch/event/1399335/timetable/?view=standard#25-a-novel-implementation-of-t>.

- [135] M. Tartarin and J. Stark, *HHb \bar{b} $\gamma\gamma$ with a Matrix Element Method at Next-to-Leading Order*, Presentation powerpoint on indico, May, 2025. Physique ATLAS France (PAF) 2025, Annecy, France, 27 May 2025. Slides at <https://indico.cern.ch/event/1474401/>.
- [136] M. Tartarin and J. Stark, *A Novel Implementation of the Matrix Element Method at Next-to-Leading Order for Measuring the Higgs Tri-Linear Coupling in Di-Higgs Production at the LHC*, Presentation powerpoint on indico, July, 2025. EPS-HEP 2025, Marseille, France, 8 Jul 2025. Slides at <https://indico.in2p3.fr/event/33627/timetable/?view=standard#175-a-novel-implementation-of>.

Titre : Étude de l'auto-couplage du boson de Higgs dans le canal $HH \rightarrow b\bar{b}\gamma\gamma$ à l'aide de la Méthode des Éléments de Matrice à NLO avec l'expérience ATLAS auprès du collisionneur LHC au CERN

Mots clés : physique des particules expérimentale, grand collisionneur de hadrons (LHC), expérience ATLAS, Méthode des Éléments de Matrice, NLO, Higgs

Résumé : La découverte du boson de Higgs en 2012 a marqué une étape fondamentale dans la validation du Modèle Standard (MS) de la physique des particules, en confirmant le mécanisme de Brout-Englert-Higgs responsable de la rupture spontanée de symétrie électrofaible. Néanmoins, malgré son succès empirique, le MS est remis en question.

Parmi les paramètres fondamentaux encore peu contraints expérimentalement figure l'auto-couplage du boson de Higgs, noté λ_{3H} . Ce paramètre, directement lié à la forme du potentiel de Higgs, n'est accessible qu'à travers l'étude du processus de production double du boson de Higgs (di-Higgs). Ce processus, extrêmement rare dans le cadre du MS, possède un taux de production environ 500 fois plus faible que celui de la production simple de Higgs, et n'a pas encore été observé expérimentalement.

Dans cette thèse, nous avons développé une approche innovante pour contribuer à la mesure de λ_{3H} dans le canal $gg \rightarrow HH \rightarrow b\bar{b}\gamma\gamma$, qui combine une sensibilité élevée grâce à un fort taux de branchement pour $H \rightarrow b\bar{b}$ et une excellente résolution de reconstruction pour $H \rightarrow \gamma\gamma$. Notre travail repose sur l'implémentation de la Méthode des Éléments de Matrice (MEM), une technique multivariée fondée sur le calcul de rapports de vraisemblance à partir d'éléments de matrice issus de la théorie quantique des champs.

La MEM est connue pour sa puissance statistique, en particulier dans les situations où les événements sont rares et les signaux faiblement séparables des bruits de fond. Elle a joué un rôle clé dans plusieurs analyses de précision, comme la mesure de la masse du quark top au Tevatron ou la mise en évidence de la production de top unique au LHC. Son application au canal $HH \rightarrow b\bar{b}\gamma\gamma$ et à Next-to-Leading order (NLO) n'avait encore jamais été réalisée, notamment en raison des difficultés techniques liées à sa mise en œuvre au-delà du niveau de précision Leading Order (LO).

Dans ce contexte, nous avons conçu un cadre MEM opérationnel à l'ordre Next-to-Leading Order (NLO), en intégrant des éléments de matrice calculés à NLO à l'aide des outils POWHEG-BOX-V2 et MG5_aMC@NLO. Cette infrastructure a été intégrée dans une version modifiée du logiciel MoMEMta, adaptée aux exigences du calcul NLO, notamment en termes de prise en compte des contributions réelles et virtuelles et de la structure complexe de l'espace des phases.

À notre connaissance, il s'agit de la première application de la MEM à l'ordre NLO pour la recherche du processus di-Higgs et la mesure de λ_{3H} . Nous avons validé notre approche sur des échantillons simulés par Monte Carlo, et démontré que cette méthode permet d'extraire une information sensible sur λ_{3H} .

Ce travail constitue ainsi une avancée dans l'outillage méthodologique disponible pour l'analyse de données du LHC, et établit la faisabilité de la MEM à NLO pour l'étude de processus rares. Il ouvre la voie à des applications plus larges dans la physique de précision et les recherches de nouvelle physique au-delà du Modèle Standard.

Title: Contribution to the study of the Higgs boson self-coupling in the $HH \rightarrow b\bar{b}\gamma\gamma$ channel using the Matrix Element Method at NLO with the ATLAS experiment at LHC, CERN

Key words: particle physics, Large Hadron Collider LHC, ATLAS experiments, Matrix Element Method, NLO, Higgs coupling

Abstract: The discovery of the Higgs boson in 2012 marked a major milestone in the validation of the Standard Model (SM) of particle physics, by confirming the Brout-Englert-Higgs mechanism responsible for the spontaneous breaking of electroweak symmetry. Nevertheless, despite its empirical success, the SM remains challenged.

Among the fundamental parameters still poorly constrained experimentally is the Higgs boson self-coupling, denoted λ_{3H} . This parameter, directly related to the shape of the Higgs potential, can only be accessed through the study of Higgs boson pair production (di-Higgs). This process, extremely rare within the SM, has a production rate approximately 500 times smaller than that of single Higgs production and has not yet been observed experimentally.

In this thesis, we developed an innovative approach to contribute to the measurement of λ_{3H} in the $gg \rightarrow HH \rightarrow b\bar{b}\gamma\gamma$ channel, which combines high sensitivity due to the large branching ratio of $H \rightarrow b\bar{b}$ and the excellent reconstruction resolution of $H \rightarrow \gamma\gamma$. Our work is based on the implementation of the Matrix Element Method (MEM), a multivariate technique relying on the calculation of likelihood ratios from matrix elements derived from quantum field theory.

The MEM is known for its strong statistical power, particularly in situations where events are rare and signals are barely distinguishable from backgrounds. It has played a key role in several precision analyses, such as the measurement of the top quark mass at the Tevatron or the observation of single top production at the LHC. Its application to the $HH \rightarrow b\bar{b}\gamma\gamma$ channel and at Next-to-Leading Order (NLO) had not yet been performed, mainly due to the technical challenges associated with implementing the method beyond Leading Order (LO) accuracy.

In this context, we developed a fully operational MEM framework at NLO, integrating matrix elements computed at NLO using the POWHEG-BOX-V2 and MG5_aMC@NLO tools. This framework was incorporated into a modified version of the MoMEMta software, adapted to the demands of NLO calculations, including the treatment of real and virtual contributions and the complex structure of the phase space.

To our knowledge, this represents the first application of the MEM at NLO for the search of the di-Higgs process and the measurement of λ_{3H} . We validated our approach using Monte Carlo simulated samples and demonstrated that this method can extract meaningful information about λ_{3H} .

This work thus represents a step forward in the methodological tools available for LHC data analysis and establishes the feasibility of applying MEM at NLO to the study of rare processes. It opens the way for broader applications in precision physics and searches for physics beyond the Standard Model.